A Novel Reconfigurable Induction Machine Drive for Hybrid Vehicles

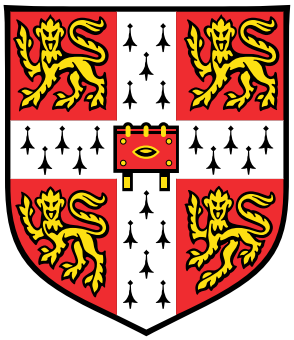

Saikat Subhra Ghosh

Department of Engineering

University of Cambridge

This dissertation is submitted for the degree of

Doctor of Philosophy

Girton College

September, 2019

I would like to dedicate this thesis to my loving parents.

Declaration

I hereby declare that except where specific reference is made to the work of others, the contents of this thesis is the result of my own work and includes nothing which is the outcome of work done in collaboration except as declared in the Preface and specified in the text. It is not substantially the same as any that I have submitted, or, is being concurrently submitted for a degree or diploma or other qualification at the University of Cambridge or any other University or similar institution except as declared in the Preface and specified in the text. I further state that no substantial part of my thesis has already been submitted, or, is being concurrently submitted for any such degree, diploma or other qualification at the University of Cambridge or any other University or similar institution except as declared in the Preface and specified in the text. It does not exceed the prescribed word limit for the relevant Degree Committee.

Saikat Subhra Ghosh
September, 2019

Publications

The following publications have been produced during the course of this research:

- Integrated starter alternator sizing for micro / mild hybrid vehicle using Monte Carlo simulation, Ghosh SS, Flack TJ, Long T, Transportation Electrification Conference (ITEC-India), 2017 IEEE, 12 Dec 2017 - 15 Dec 2017
- Independent Phase Belt Controlled Phase Pole Modulated Induction Machine for Integrated Starter Alternator Application, Ghosh S, Flack T, Long T, The 9th International Conference on Power Electronics, Machines and Drives, 17 Apr 2018 - 19 Apr 2018. The Journal of Engineering (JoE)

Acknowledgements

I would like to express my sincere gratitude to my supervisor, Dr Timothy J. Flack, for his help and support throughout my PhD research, and for his advice and guidance during my PhD. I would like to thank him for his sincere efforts in proofreading my papers, as well as this thesis.

I am deeply grateful to my advisor Dr Teng Long for his invaluable guidance, advice and encouragement in undertaking this research and creating a pleasant environment to work. His kind offer of proofreading this dissertation is very much appreciated.

I would also like to acknowledge the support I received from Commonwealth Scholarship Commission in the UK (CSCUK) for kindly sponsoring my PhD studies through Commonwealth Scholarship. Also, a special mention to Dr Tim Flack for arranging my fourth-year funding. This PhD study at Cambridge has significantly transformed me academically, professionally and personally. This impactful journey would not have realised without your support.

I am grateful to my first supervisor (only for a month though) Dr Richard McMahon, who kept trust in my capabilities and enabled my admission to Cambridge as well as recommending me for Commonwealth Scholarship.

I am extremely grateful to Mr John Grundy for his help and hard work in assisting in the construction of the machine test-rig and all the other mechanical systems, and for the dedication, he shows to the power group students. I also want to thank Mrs Sarah Stone for her administrative assistance for the duration of my studies in Cambridge.

Thanks are also due to all my colleagues in the EPEC group past and present, particularly to Dimitrios, Kumaran, Aaron, Daniel, Hao and Luke. It has been a very pleasant working environment around you. I have learned a lot from you through endless stimulating technical discussions, brainstorming sessions, and encouragement as support in lab. I am lucky to have you as friends. Apart from work, our chit chats in the lab have made this journey much enjoyable.

I would like to thank my friends in Cambridge, for their understanding and support, and making my stay at Cambridge enjoyable. A special mention goes to another fellow CSC

scholar at Cambridge from my home town – Arko. I would also like to thank my friends from Girton -Thejesh, Shreyashi and Ram. You ensured I'd come home every night to a flat full of supporting friends. I would also like to especially acknowledge Dr. Hirak Patra, for being a great mentor and an elder brother like figure, whom I often looked for many advises during this journey.

To the other incredibly special person I've met here – you know who you are. I am very lucky to meet you in this historic city, and I am glad our path crossed here. My life is definitely enriched having had you in it. We've made countless incredible memories and I can't wait to see what the future has in store for us.

I have also been lucky to have many other friends from different walks of life. I would like to acknowledge their friendly support in my journey. There is one person who merits a special mention - Dr Debatnu Maiti - for building up a strong friendship through our long calls and always being there for a friendly chat.

Finally, I would like to express my deep gratitude to my parents for their faith in me. I thank them for being with me always, supporting and encouraging me to dream higher.

A Novel Reconfigurable Induction Machine Drive for Hybrid Vehicles

Saikat Subhra Ghosh

Abstract

With the growing concerns over global warming and depleting oil reserves, full and hybrid electric vehicles (EVs) are gaining significant attention from commercial bodies as well as government policymakers. Considering the high cost and range anxiety of full EVs, hybrid EVs are expected to be the immediate solution. The electric drive train of the hybrid vehicle needs to have four main functions, high torque low-speed motoring for engine starting,low torque high speed generating for charging the onboard battery as the vehicle alternator, medium torque medium speed motoring for torque boost, and medium torque medium speed generating for regenerative braking. Two electric machine drives are normally required to meet the above requirements, resulting in a complex system and higher cost. In this thesis, a novel induction machine drive, reconfigurable induction machine drive (RIMD) is proposed to achieve a modified torque-speed envelope, so the drive train of hybrid EVs can be replaced by one single machine drive.

The reconfigurable induction machine drive is based on the principle of pole phase modulation. A novel concept of independent phase belt controlled pole-phase modulation is developed. The proposed pole-phase modulation technique offers higher reconfigurability compared to the previously reported literature. As an example, a toroidally wound machine with 36 stator slots can be reconfigured to 2/4/6/8/10 pole operation by using a 12-phase inverter. The proposed concept is analysed by using Finite Element Analysis (FEA) method and the equivalent circuit and parameters of the reconfigurable induction machine are obtained.

To validate the proposed machine, a scaled-down 1.5 kW prototype has been developed which is capable of 2/4/6/8/10 pole operation. A 12-phase inverter has been developed as well to drive the machine. Results from open and short circuit tests have validated the design and equivalent circuit model of the machine. A circulating power test bench has been developed. The torque-speed characteristics of the developed machine have been obtained from the test bench.

Finally, a dynamic model of the proposed RIMD has been developed based on the d-q model theory. The model has been then used to develop an online pole transition control scheme, which ensures there is no significant oscillation in speed and current. The scheme allows online pole transition in only 0.1 s. The dynamic model along with with the proposed control scheme has been simulated in Matlab – Simulink platform. Finally the online pole changing control scheme has been implemented in the hardware and the experimental results are reported.

Contents

List of Figures

List of Tables

Nomenclature

Acronyms / Abbreviations

BLDC	Brush Less DC
DTC	Direct torque control
EMF	Electro Motive Flux
EV	Electric Vehicle
FEA	Finite Element Analysis
FOC	Flux Oriented Control
HEV	Hybrid Electric Vehicle
ICE	Internal Combustion Engine
IM	Induction Machine
IPM	Interior Permanent Magnet
ISA	Integrated Starter Alternator
MMF	Magneto Motive Flux
Mtoe	Million tonnes of oil equivalent
PAM	Phase Amplitude Modulation
PM	Permanent Magnet
PPM	Pole Phase Modulated
PPMIM	Pole Phase Modulated Induction Machine

PWM	Pulse Width Modulation
SOC	State of Charge
SPM	Surface Permanent Magnet
SRM	Switch Reluctance Machine
SVPWM	Space vector pulse width modulation
THD	Total Harmonic Distortion
VSC	Voltage Source Converter
VVVF	Variable Voltage Variable Frequency

Symbols

α	Stator slot angle
λ	Flux Linkage
λ_{rr}	Rotor self flux linkage
λ_{rs}	Rotor to stator mutual flux linkage
λ_{r}	Rotor flux linkage
λ_{sr}	Stator to rotor mutual flux linkage
λ_{ss}	Stator self flux linkage
λ_{s}	Stator flux linkage
$\mathscr{F}_r$	Rotor MMF function
$\mathscr{F}_s$	Stator MMF function
$\mathscr{N}_r$	Rotor winding function
$\mathscr{N}_s$	Stator winding function
ω_{sl}	Slip frequency
ω_{s}	Electrical excitation frequency

ρ_{bar}	Resistivity of the rotor bar material
ρ_s	Resisitivity of the stator winding material - copper
θ_r	Rotor angle
θ_s	Stator angle
A_{bar}	Cross sectional area of the rotor bar
A_c	Cross sectional area of a single strand
D	Diameter of the air-gap
g	Length of the air-gap
l	Length of the machine
l_{bar}	Length of the rotor bar
L_{lr}	Rotor leakage inductance - referred to rotor
L_{ls}	Stator leakage inductance
L_m	Magnetising inductance
L_{rr}	Rotor magnetising inductance
L_{rs}	Rotor to stator mutual inductance
$L_r^{'}$	Rotor leakage inductance - referred to stator
L_{sr}	Stator to rotor mutual inductance
L_{ss}	Stator magnetising inductance
L_s	Stator leakage inductance
m	Number of phases
N_c	Number of strands in the stator winding
N_s	Number of turns in one stator slot coil
p	Number of pole pairs

q	Phase belt
Q_r	Total number of rotor bars
Q_s	Total number of stator slots
r	Radius of the air-gap
r_g	Radius of the air-gap
R_{bar}	Resistance of a single rotor bar
R_{er}	Resistance of the end ring
R_{leg}	Stator winding resistance of the phase belt
R_m	Core loss resistance
R_r	Rotor resistance (not refered to stator)
$R_r^{'}$	Rotor resistance - referred to stator
R_{sl}	Resistance of a coil in one stator slot
R_s	Stator winding resistance
s	Slip
T_{em}	Electromagnetic Torque

Chapter 1

Introduction

This chapter starts with looking into the automobile sector, in terms of energy consumption and contribution to global greenhouse gas emission, setting the context for the need of automobile electrification and hybridisation. The chapter then provides a brief overview of the vehicle architectures for electrification and hybridisation, followed by literature survey on the electric drives for automobile application, and concluding with the pole changing induction machine drive as the main focus of this thesis. The chapter finally concludes with a brief outline of the structure of this thesis

1.1 Motivation

The global demand for energy has been increasing ever since mankind has learnt to harness fossil fuel as a source of energy. However the rate of increase of the energy demand has increased significantly in recent past. The net energy consumption almost doubled from 4294 Mtoe to 9173 Mtoe from 1971 to 2013 [7]. In the same time frame energy consumption in the transport sector increased at an even higher rate, from 977 Mtoe in 1971 to 2568 Mtoe in 2013 - resulting in more than 2.5 times increase. This results in a similar contribution in the greenhouse gas emission as well, the transport sector being responsible for 14.3% of the global greenhouse gas emission [8]. Most of this contribution is made by the road transport (10.5% of the global greenhouse gas emission) [9].

With such an impact in global energy consumption and the greenhouse gas emission, the improvement of the fuel economy of road transport is of interest. Further, in accordance with the increasing level of pollution and concern over depleting oil storage, the rising level of regulatory restriction requires more fuel efficient and low emission automobiles. Electric vehicle (EV) and hybrid electric vehicles (HEV) seem to provide a solution for

this challenge, with a price for the additional weight and the cost of the electric powertrain components [10, 11]. In order to achieve an optimized weight, cost and fuel efficiency, several vehicle powertrain architectures with different level of electrification, such as micro, mild, full, and plug-in hybrid and full electric options (discussed in detail in section 1.2) are available [12–15]. However, due to the inherent problem of cost and volume of the battery pack, along with range anxiety, the electric vehicle is yet to gain major market share [12], whereas hybrids have gained popularity, in both high-end and low-end automobiles. Micro and Mild hybrid vehicles offer the most attractive option in terms of fuel economy and component cost of extra electric powertrain [11], which can be argued as the major driving force behind their larger market share amongst all other alternate architectures[12]. Several market analysis reports also indicate [16] a growth of the hybrids until there is a significant breakthrough in energy storage causing affordable and smaller battery systems.

Further, with the growing concern over electric and hybrid vehicles, there is a need to meet improved performance and design specifications, such as efficiency, torque density, weight, volume and cost [17]. This requirement has triggered studies towards different possible motor technologies as well as revisiting existing motor technologies [18]. In this context, a study to design an electric drive for micro / mild hybrid automobiles by combining the knowledge of power electronics and electric machine design to meet this challenge is of relevance.

1.2 Electric and Hybrid Vehicle Architectures

There have been several vehicle architectures proposed and developed for electrification and hybridisation of automobiles, as shown in Fig. 1.1. Full electric vehicle, as shown in Fig. 1.1a completely removes the internal combustion engine (ICE), and replaces it with an electric machine. The machine is driven by a power electronic inverter, from the energy stored in the battery. The battery is recharged through the onboard charger / off-board charger using mains electricity.

Unlike full electric vehicle, hybrid architecture keeps the ICE, along with an electric machine. For the series hybrid, the vehicle is again driven fully by an electric machine from the battery through a power electronic converter. However, as shown in Fig. 1.1b, the engine is operated at its most efficient point (torque, speed) to charge the battery through the generator when the battery state of charge (SOC) is low. The plug-in hybrid has the option to charge the battery also from the onboard charger before the start of the journey. This arrangement allows reduction in size of the battery, as the battery need not store the energy

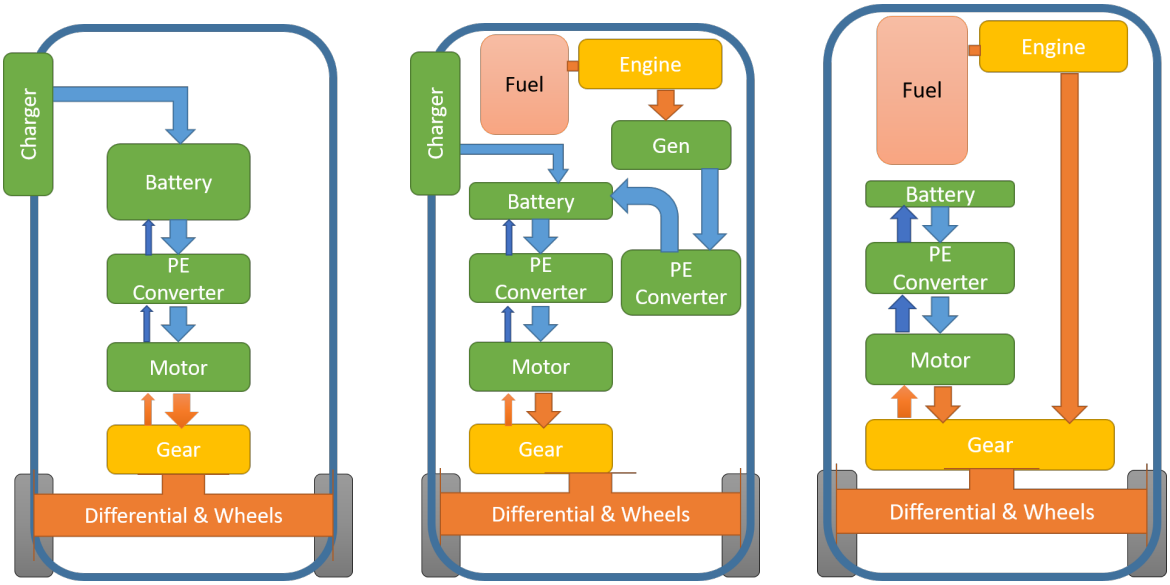

(a) Full electric (b) Plug-in series hybrid (c) Parallel hybrid

Figure 1.1: Electric and hybrid vehicle architecture

for the full range of the vehicle, while addressing the issue of the range anxiety of electric vehicles. Although this architecture reduces the size of the costly battery needed, compared to that of the EV, the vehicle consists of two full-sized machines (the generator and the drive motor), thus increasing the cost, weight and volume of the powertrain. However, the parallel hybrid solves this challenge, by adding/subtracting necessary torque directly with the engine, as shown in Fig. 1.1c [19]. This architecture reduces both the size of the battery as well as the electric machine needed for hybridisation, thus offering the most optimised solution.

In the conventional automobiles a starter motor (usually a DC motor) [20], is used to start the combustion engine, operating at low speed high torque range intermittently (only to start the engine, with a maximum duration of 20-30s). Further, there is a separate electric machine (usually a Lundell Alternator) [21] to generate electricity (wide speed range operation), which supplies power to the vehicle power network and charges the battery. The arrangement is shown in Fig. 1.2a.

Th Integrated Starter Alternator (ISA) [22, 23] makes the first step towards a micro or mild hybrid automobile, where a single electrical machine is used for starting an internal combustion engine from a standstill, generating electrical energy when the engine is running as shown in Fig. 1.2b. The ISA can be directly used to replace the starter motor and alternator, in the position of the alternator, keeping it coupled with the engine by pulley

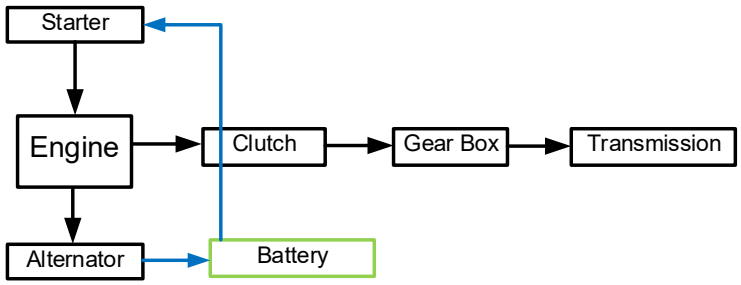

(a) Engine with starter motor and alternator

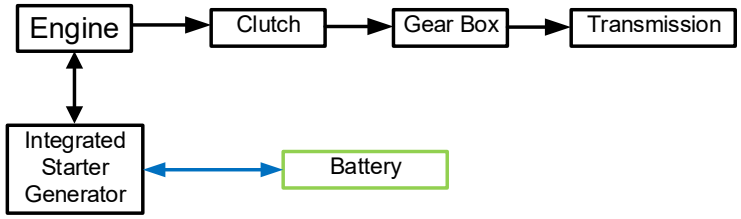

(b) Engine with belt driven ISA

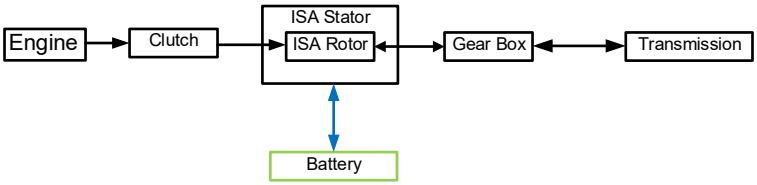

(c) ISA with regenerative braking

Figure 1.2: Schematic arrangement of starter, alternator and ISA

and belt, as shown in Fig. 1.2b. However, this arrangement allows starting, generation, and torque boost functionality only. To achieve regenerative braking, the system has to be modified as shown in Fig. 1.2c [19]. The stator of the machine is energised only when torque is to be added (motoring mode) or subtracted (generating mode) from the torque produced by the engine. Otherwise, the rotor of the machine only transmits the torque from the engine to the transmission. When the brake is applied, the clutch is disengaged, and the ISA can be used for regenerative braking. The black arrowheads in the figures 1.2a, 1.2b and 1.2c, shows the direction of torque transmission, whereas the blue arrowheads show the direction of electrical power transmission.

It is clear the ISA needs to operate in different operating modes such as high torque - low speed for cranking, and high speed - low torque for alternator mode in cruising. Further,

the intermediate range of torque and speed will allow other hybrid functionality such as regeneration and torque boost. These different applications of a single machine demand a very wide torque and speed range of operation in both motoring and generating mode [20, 22].

Different types of electric machines [17, 24, 25], induction machine (IM) [26–30], permanent magnet (PM) machine [19, 20, 31–37], Lundell Alternator [38], Switched Reluctance Motor (SRM) [23, 39–43] have been discussed as potential candidates, with each of them having some advantages and disadvantages. As discussed by *Chan* in [44] IM and PM was being researched extensively for electric and hybrid automotive application. DC motor, although had a simpler control scheme, due to the inherent problem of commutator and brush, was not a suitable choice for this application[11, 44]. Further, as pointed out in [11, 17, 22, 44] SRM was also being considered for this application. Although SRM has the advantage of robust construction, the difficulty of control, torque ripple and acoustic noise are major problems to be addressed. Further, in recent years SRM has drawn attention in research field [18] to find the alternative of PM motors, which depend on costly rare-earth material [17]. The next section presents a literature survey on the various type of electric drives proposed for ISA.

1.3 Electric Drive for ISA

In this section, the advantages and disadvantages along with recent research on three major drives for electric and hybrid automobile application, (a) PM machine and (b) SRM, and (c) IM, have been discussed. Further, in micro and mild hybrid automobile application, the electric machine also replaces the alternator of the vehicle. Hence recent research and possible options for automotive alternators [21, 24, 25] is also discussed along with the existing literature [15, 21, 25, 45–49] on use of 42V system along with suitable power electronic controller for bi-directional power flow and control.

1.3.1 Permanent Magnet Motor

Amongst different possible candidates, PM machines offer maximum torque and power density, leading to the first choice for major automobile manufacturers for the initial period [17, 44].

Sensor-less control (speed sensor) of Interior PM machine (IPM) [31] has been reported for ISA application. Further, different approaches have been proposed to overcome the chal-

lenge of field-weakening control of IPM motor, at a higher speed of operation. Optimized machine design [34–36] along with the control scheme for the power electronic converter [32, 34, 37] has been reported. PM assisted Synchronous Reluctance Motor has been explored for ISA application [19]. Further, doubly excited PM motor has been reported in [33], where another excitation winding has been introduced to control the field. A similar concept has been extended to the machine reported in [19] resulting in the Biaxial Excitation Generator [20] for ISA application. Research has been reported on reconfigurable winding [50] and open winding [51] configured IPM motor also. 4 different topologies, a) series-parallel, b) boosted inverter, c) tapped winding and d) $Y-\Delta$ configuration has been studied both with simulation results and experimentally (*option a-c only*) in [50]. The study concludes based on cost, size, power, efficiency, machine leads and torque disturbance tapped winding is an optimized choice. *Gerrits et al* report a reconfigurable winding surface PM machine (SPM) in [51]. The described machine uses 4 inverter modules (3 leg bridge converter) to feed 6 phase open winding configuration. The described machine has the option to reconfigure in series and parallel mode also.

Although significant research has been reported on PM machines for ISA application, recent uncertainty in rare earth material pricing [17] has drawn attention towards machines without rare earth materials [18]. Further, the temperature sensitivity of the permanent magnet material makes it less attractive for an automotive application and SPM motors are not suitable for very high speed [30].

1.3.2 Switched Reluctance Motor

Due to rugged rotor construction and constant power over a wide speed range [23], SRM has been considered as a potential candidate for electric and hybrid electric vehicle application.

A 6 kW Switched Reluctance Generator automotive ISA application is discussed by *Torrey* in [39]. The paper discusses the general principle of operation and control of switched reluctance generators in detail, along with a discussion of SRM's spatial and magnetic nonlinearity. *Schofield et al* discuss an SRM for ISA application with a light truck engine in [40]. Simulation based design and some experimental results of a 42V 6 kW SRM for ISA application have been reported in [41]. In [42] *Kiyota et al* report design, simulation and experimental results of a 60 kW SRM, to match the dimension and performance of IPM used in the Toyota Prius. These results [40–42] report machine performance comparable to that of PM motors, even, with some cases improved peak efficiency and torque. *Hu et al*

report a new SRM Drive for series plug-in Hybrid Electric Vehicles (PHEV) in [43], where the machine winding is also used for battery charging from the grid. [52] reports use of a three phase inverter for driving six phase inverter, however, extra diodes are needed in series of each winding.

SRM has the potential to reach almost similar power and torque densities of IPM, and without the use of costly rare-earth permanent magnet materials [42]. Hence, recently as an alternative candidate for EV and HEV application, this is being researched significantly[18]. However, the disadvantages of SRM, such as a unique power converter, or extra power electronic componentand high level of vibration and noise, along with difficulty of control, have not allowed major adoption of this technology.

1.3.3 Induction Motor

With the advent of power electronic controllers, variable speed control of IM became easy [44]. Extensive application of IM and Space Vector control, also known as Flux Oriented Control (FOC) in other industrial applications led to extensive research in this field, making one of the most mature electric drive technologies.

ISA application of IM has been reported by several authors [26, 28], where the motor is controlled by vector control along with sensor less control[28]. Further, a novel topology using a fractionally rated inverter to feed the reactive power only for generator application has been reported in [27]. Direct flux vector control scheme has been proposed by *Zhang et al* in [29] , which is derived from the direct torque control principle. In the recent paper [30] *Jurkovic et al* describe the technology for a commercially available vehicle from General Motors. The effect of machine design, use of stator bar conductor and rotor bar selection in machine performance and noise reduction has been reported. *Martin et al* describes a reconfigurable-winding IM for the ISA application in [53]. The research reports result for a reconfigurable winding IM (4 pole / 8 Pole) using simple V/f control. To implement the reconfigurable winding topology, individual stator leads are brought outside, and connected by an electrically controlled switch network. Although some interesting improvement in torque-speed characteristics has been reported, in both motoring and generating mode, application of these many switches makes it difficult for practical implementation in an automobile. In [2], *Miller et al* discuss pole phase modulated (PPM) ISA, using toroidally wound IM, which brings similar enhancement in torque-speed characteristic as in the previous paper, with a smaller number of switches, which offers a wide torque-speed characteristic by changing the pole number of the IM.

Although for initial years of electric and hybrid vehicles, PM machine was the first choice for a commercial solution [17] due to their higher torque and power density, IM still stood as next choice. Robust construction, matured manufacturing process along with established FOC control are several advantages of IM for xEV application. However, the power density and efficiency of IM is slightly lower than PM machines [17]. However PM machines with high flux density, are dependent on rare-earth material, and price hike of rare-earth materials in 2011-12, caused a total shift towards IM [17] by all major manufacturers. Further, special precaution need to be taken for PM materials against high temperature and shock due to vehicle vibration in automotive application. These restrictions make PM material free drives such as IM an attractive choice for xEV application.

1.3.4 Automotive Alternators and Power Network

The previous sections (Sec. 1.3.1 -1.3.3) mostly focus on the literature only related to ISA application of electric drives. However, as ISA also need to meet the requirements of existing automobile alternator and power network, in this section few recent studies on the alternator of the conventional automobiles - Lundell alternator, the challenges in modern automobile power generation and scope of power electronics and control to address them will be discussed.

In [21] *Perreault et al* introduce a Switched Mode Rectifier (SMR) with Lundell Alternator to enhance the output capability of the machine almost by 100% by load matching. *Lorilla et al* report a comparative study of 4 electrical machines for automotive alternator application in [24, 25]. The papers report analytical results in [24]. FEM simulation based optimization study to find the advantages of different machines when being used with the SMR are described in [21]. The study concludes that the Lundell Alternator as the most effective solution, and hence the choice of future application. The concept discussed in [21] is further taken forward in [38] by *Tang et al*, by introducing a modular cell like interleaved winding. The interleaved winding reduces output voltage ripple significantly, hence the requirement of the capacitor on the output. In [54] *Sarafianos et al* discuss the scope of alternate diode bridges to improve the Lundell alternator performance. In [55] a MATLAB based model of Lundell alternator has been developed from simple characterisation tests and experimentally validated. In [56] *Neugebauer et al* describe a computer aided optimized design of the 42-14V DC/DC converter for future dual voltage automobile systems.

The challenges of voltage transients and sensitivity in automobile power networks has

been discussed in [57–59]. Further different control and load management strategies have been discussed to address them [60–62].

1.3.5 Commercial Cases

Having discussed the recent trend in research on electrical drives for ISA application, it is worthwhile to look briefly into different commercially available technologies in the market from different automobile manufacturers. This gives an idea of industry adaptation of various technologies discussed in previous sections.

In [44] several hybrid technologies from the major automobile manufacturer is reported, including both commercial as well as technology demonstration models which are reported here. Toyota Prius is one of the earliest Hybrid Electric Vehicles, which used 33 kW PM Brush Less DC (BLDC) machine for its first generation. Honda Civic used a 10 kW PM machine as its hybrid drive. Saturn Vue from General Motors is another commercial model which used a 5kW belt driven IM as a starter-alternator in a micro-hybrid system. Further, [30] reports the IM used for e-assist technology available in 2012 Buick Lacrosse and Chevy Malibu from General Motors. Application of SRM has been also mentioned in [41] for General Motor's E-Commodore technology demonstration model.

1.4 Conclusion

PM machines clearly have shown maximum torque and power density in terms of both volume and weight, and have been the first choice for initial hybrid electric vehicles and drawn a significant amount of research as well. However, the volatile price of rare-earth material has shifted the trend in research towards rare-earth material free machines [18]. IM, particularly copper bar rotor machines have been used for this application mostly, where matured space vector pulse width modulation (SVPWM) or direct torque control (DTC) based control strategy is utilised. Further, due to some major technical challenges of torque ripple, difficulty of control and requirement of special converter topology, SRM has remained mostly in research only, although it has been reported to have efficiency, power and torque density close to those of PM machines, and slightly higher than IM. Position sensor less control has special advantage for this application due to increased robustness of the system. Further, it has been clearly reported, to achieve maximum utilization optimized design approach for the machine and converter, as well as a control strategy is important, as the application is highly sensitive to cost. Although the size of the electric machines being used in

automobiles has increased steadily, the research papers, as well as business analysis reports indicate micro and mild hybrid will play a significant role in the automobile industry, until major improvements in energy storage technology are realised.

As discussed in the previous section, pole phase modulated IM (PPMIM), offers several advantages for being used as an ISA. PPM allows achieving wide torque-speed characteristics, which is very useful for ISA application, as well as other electric and hybrid vehicles. Based on the literature survey, reported in the previous section, a study to enhance the performance of PPMIM has been pursued in this thesis. The next section presents a summary of this thesis along with the key contributions made.

1.5 Thesis Summary and key contributions

The thesis is organised in seven chapters. The content of each chapter is outlined here.

Chapter 1 starts with looking into the automobile sector, in terms of energy consumption and contribution to global greenhouse gas emissions, setting the context for the need for automobile electrification and hybridisation. The chapter then provides a brief overview of the vehicle architectures for electrification and hybridisation, followed by literature survey on the electric drives for automobile application, and concluding on pole changing IM drive as the main focus of this thesis. The chapter finally concludes with a brief outline of the structure of this thesis

Chapter 2 presents the operating principle and previous research on reconfigurable IM. It has also been shown that PPM strategy allows maximum flexibility on torque-speed characteristics of the machine. The electronic method to achieve PPM, using power electronic converter is briefly discussed next. The chapter finally concludes that a toroidally wound PPMIM has maximum flexibility on pole changing, and thus achieves wide torque-speed characteristics.

Chapter 3 introduces a novel independent phase belt controlled PPMIM. As an example case, a 12 phase PPMIM has been studied, which is capable of reconfiguring into 2/4/6/8/10 pole machine. Finite element analysis (FEA) of the proposed machine has been performed to investigate the air gap flux profile of the machine under different pole configurations. The equivalent circuit parameters of the machine under different pole configurations has been extracted from the FEA analysis as well. Further, the analytical expressions of the equivalent circuit parameters of the machine have been derived, which can be used for faster calculation, and machine design optimisation. The chapter concludes with the comparison of the equivalent circuit parameters of the machine obtained from the analytical model and

FEA model, which matches well with each other.

The next chapter reports the hardware prototype developed for experimental verification of the proposed concept. Details of the 12 phase inverter design, along with circulating power test bench design have been reported in this chapter. Further, the software to control the embedded processor which controls the 12 phase inverter, and user interface designed for the experiment is presented.

Chapter 5 reports the experimental results of the developed hardware prototype. At first, the equivalent circuit parameters of the machine have been extracted from the no load test at synchronous speed and blocked rotor short circuit test. Next, load testing of the machine has been performed to obtain the torque-speed characteristics of the machine under different pole configuration. It has been shown the machine T-S characteristics derived from analytical and FEM model is in good agreement with the experimental results obtained in this chapter.

Having discussed the theory of the proposed independent phase belt controlled PPMIM, Chapter 6 focusses on development of a dynamic model of the machine for closed-loop control and online pole changing. A generalised model of PPMIM has been developed with special attention to model the cage rotor - which is essential for pole reconfigurability. The developed model covers different possible pole configurations of the PPMIM. The model has been used to develop an online pole changing control strategy, which optimises the torque and current oscillation during pole changing. The experimental results of online pole changing have been reported as well.

Finally chapter 7 concludes the thesis with a brief summary and finishes with several possible future works, based on the contribution of this thesis.

The key contributions of this thesis can be summarised as below:

- A novel independent phase belt controlled PPMIM concept has been developed. The developed concept has been validated with the finite element analysis. The proposed model shows wider reconfiguring ability compared to that reported in the literature, thus achieving wider torque-speed characteristics. The wider torque-speed characteristics is particularly useful for ISA application for micro / mild hybrid application. Further, the proposed machine design is scalable to cater to the electric drive of a full electric vehicle. As an example case 12 phase PPMIM has been studied, which is capable of reconfiguring into 2/4/6/8/10 pole machine.

- A mathematical model of the proposed independent phase belt controlled PPMIM has been developed, which specifically takes care of the toroidal winding machine.

The analytical model provides closed-form equation for evaluation of the equivalent circuit parameters under different phase-pole configuration, which matches very well with the same parameters obtained from the FEA.

- The proposed concept is verified by experimental verification, by fabricating a 1.5 kW prototype, along with a circulating power test bench. The machine parameters are extracted from no load test and short circuit test. Further, the torque-speed characteristics of the machine have been obtained for different pole configurations.
- A dynamic model of the proposed independent phase belt controlled PPMIM has been developed for closed-loop control, and online pole changing. A control scheme has been developed and experimentally verified to optimise the torque and current oscillation during pole changing.

Chapter 2

Pole Changing Induction Machine

The last chapter concluded with a discussion of the benefits of the pole changing induction machine for ISA. This chapter starts with revisiting the IM operating equations and variable voltage variable frequency IM drive. Then, the operating principle and previous research on reconfigurable IMs is discussed. It is shown that the PPM strategy allows high flexibility on torque-speed characteristics of the machine. The electronic method to achieve PPM, using power electronic converter is briefly discussed next. The chapter concludes that a toroidally wound PPMIM has higher flexibility on pole changing, and thus achieves wide torque-speed characteristics.

2.1 Induction Machine Drive

Before the advent of power electronics, electrical machines used to be directly fed from line sources, either grid-connected three phase supply, DC source or single phase supply for smaller machines. The IM has been the workhorse of the industry for several decades, owing to its simple construction, good efficiency and ease of maintenance compared to DC machines. However, a line fed IM (fixed voltage and frequency) has the shortcoming of its inability to operate efficiently away from its synchronous speed. Further due to fixed torque-speed characteristics, the operating point is decided by the cross over point of the load torque-speed characteristics and machine torque-speed characteristics [3]. The next section discusses the machine model and torque-speed characteristics of an IM, when fed with a constant voltage and frequency, which will be the case when the machine is driven directly from the grid.

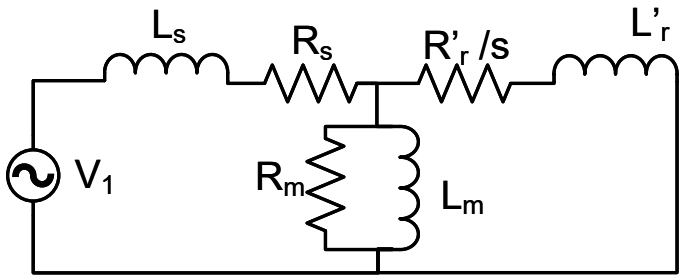

Figure 2.1: IM per phase equivalent circuit

2.1.1 Induction Machine Characteristics

The three phase IM fed with fixed voltage and frequency supply can be studied by using a per phase equivalent circuit as shown in Fig. 2.1. The circuit consists of stator winding resistance (R_s), stator leakage inductance (L_s), rotor winding resistance - referred to the stator ($R_r^{'}$), rotor leakage inductance - referred to the stator ($L_r^{'}$), magnetising inductance (L_m), and core loss resistance (R_m). The torque of an IM (T_{em}) is given as

$$T_{em} = \frac{V_1^2}{(R_s + \frac{R_r^{'}}{s})^2 + (X_S + X_r^{'})^2} * \frac{pR_r^{'}}{s\omega_s} \tag{2.1}$$

where s is the slip of the machine and p is the pole pair number. The derivation is shown in Appendix A. The torque-speed characteristics of an example IM is shown in Fig. 2.2 from Appendix A.

The torque-speed zone in the left side of the peak point is not stable for operation (because of positive $\frac{dT_{em}}{d\omega_r}$), hence the only useful zone is the right side of the peak torque. Depending on the exact machine characteristics the rated slip varies between 1%-13% (NEMA design A,B,C,D) [6]. Hence the available uncontrolled speed range from a fixed voltage and frequency is limited. The wound rotor IM characteristics can be changed, by introducing additional resistance in the rotor, at the cost of lower efficiency. The presence of brush-slip ring assembly poses a challenge in maintenance and reliability. Hence wound rotor IM will not be suitable for target ISA application and not discussed any further here.

Power electronic converter allows the IM to be fed with variable voltage and variable frequency (VVVF) supply, which in turn changes the torque-speed characteristics of the machine. This allows multiple possible operating points for the same load torque-speed characteristics and thus widening torque-speed characteristics of the drive. The next section

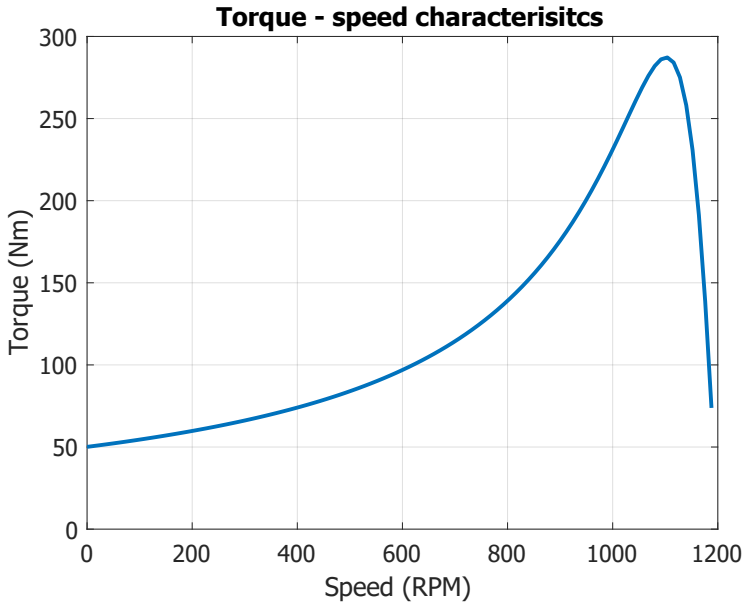

Figure 2.2: IM torque-speed characteristics

discusses VVVF IM drive using a voltage source converter (VSC).

2.1.2 VVVF Induction Machine Drive

Early IM drives used to be current source converter due to the application of thyristors. However, advances in power electronic devices e.g MOSFETs and IGBTs allows building voltage source converters (VSC) easily. VSCs allow better flexibility and ease of control in inverter application, which is mostly used for all such applications, except few very high power applications. As for the target ISA application, VSC will be the most suitable. A schematic diagram of a 3 phase voltage source inverter fed IM is shown in Fig. 2.3. The gates of the shown MOSFETs are usually controlled by a microcontroller or similar embedded controller platform. Pulse width modulation (PWM) is used to generate desired balanced 3 phase voltage and frequency across three phases shown as R, Y, *and* B. Different PWM techniques can be used such as Sine PWM, Space Vector PWM, Bus Clamped PWM, etc.

The peak line voltage is limited to the DC bus voltage V_{dc} (using third harmonic injected sine PWM / SVPWM). The fundamental frequency is also limited by the power electronic devices switching frequency, machine frequency, and total harmonic distortion (THD). Within these limits, the 3 phase inverter can be used to control the voltage and

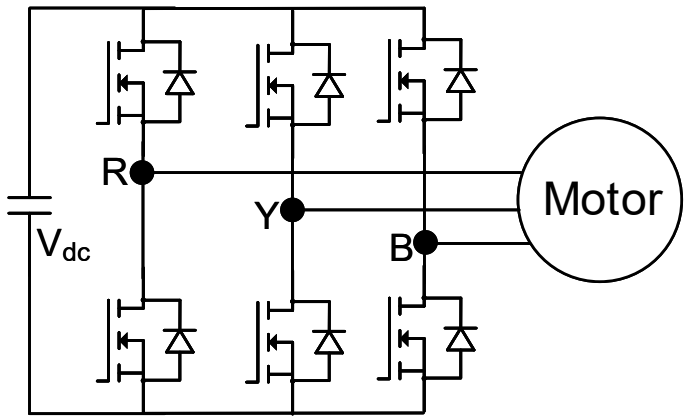

Figure 2.3: 3 Phase Voltage Source Converter

frequency fed to the machine independently.

A control strategy needs to be decided to utilise the variable voltage and frequency for speed control of IM. To maximise the torque-speed operating zone the machine should be operated at the rated flux [3], when possible. Operating lower than rated flux will lead to lower torque output, whereas operating at higher than rated flux will lead to saturation of the core. The flux of the machine is represented by the magnetising branch L_m, in the circuit shown in Fig. 2.1. The flux ϕ is given as:

$$\phi = L_m I_m \tag{2.2}$$

where I_m is the current through the magnetising branch. Neglecting the voltage drop in the stator winding resistance (R_s) and leakage inductance (L_m) $I_m$can be expressed as

$$I_m = \frac{V_1}{\omega_s L_m} \tag{2.3}$$

Combining Eqn. 2.2 and Eqn. 2.3,

$$\phi = \frac{V_1}{\omega_S} \tag{2.4}$$

Hence to operate the machine at rated flux, the voltage is kept proportional to frequency, which is known as constant v/f control. However, this can not be achieved at higher than a certain frequency (known as base speed), due to the limitation of available voltage and insulation of the machine. Hence for higher than base speed, the voltage is kept constant,

while the frequency is increased. This essentially leads to lower flux in the machine, and hence lower torque output. This operation is known as flux weakening.

Eqn. A.6 can be interpreted to state that the torque of the machine is proportional to the power dissipated in the resistance $\frac{R_r^{'}}{s}$, in the circuit shown in Fig. 2.1, for a given frequency [6]. Hence the maximum torque condition can be found by finding the condition of maximum power transfer to this resistance. Using maximum power transfer theorem this can be given as [6]:

$$\frac{R_r^{'}}{s} = \sqrt{R_s^2 + (X_S + X_r^{'})^2} \tag{2.5}$$

X_S and $X_r^{'}$ are defined for ω_s. For any arbitrary frequency ω, Eqn. 2.5 can be generalised as below:

$$\frac{R_r^{'}}{s} = \sqrt{R_s^2 + \left((X_S + X_r^{'}) * (\frac{\omega}{\omega_s})\right)^2} \tag{2.6}$$

Using this the peak torque, also known as the breakdown torque can be expressed as:

$$T_{max} = \frac{3pV^2}{\omega} * \frac{\sqrt{R_s + \left((X_S + X_r^{'}) * (\frac{\omega}{\omega_s})\right)^2}}{\left((X_S + X_r^{'}) * (\frac{\omega}{\omega_s})\right)^2 + \left(R_s + \sqrt{R_s + \left((X_S + X_r^{'}) * (\frac{\omega}{\omega_s})\right)^2}\right)^2} \tag{2.7}$$

where V and ω are the applied voltage and frequency of the supply from the VSC. Eqn. 2.7 can be simplified by neglecting the stator resistance R_s as:

$$T_{max} = \frac{3pV^2}{2\omega} * \frac{1}{(X_S + X_r^{'}) * (\frac{\omega}{\omega_s})} = \frac{3pV^2}{2\omega^2} * \frac{\omega_s}{X_S + X_r^{'}} = \frac{3pV^2}{2\omega^2} * \frac{1}{L_s + L_r^{'}} \tag{2.8}$$

From Eqn. 2.8, keeping $(\frac{V}{f})$ constant ensures the same peak torque is available at a lower speed. However, in the flux weakening control when the voltage is kept constant, breakdown torque is inversely proportional to square of ω. Thus the maximum power output of the machine will be reduced with high speed operation due to field weakening. Fig. 2.4a shows the machine (specified in Table. A.1) characteristics under VVVF control. By extending the operation of the IM to the super-synchronous speed range ($\omega_{re} > \omega$), the machine can be used as a generator. Fig. 2.4b shows inverter controlled IM characteristics for an ISA application reported in [22].

To achieve dynamic control, closed-loop control has to be implemented. The torque of the machine is controlled with a faster inner loop, whereas speed is controlled with the

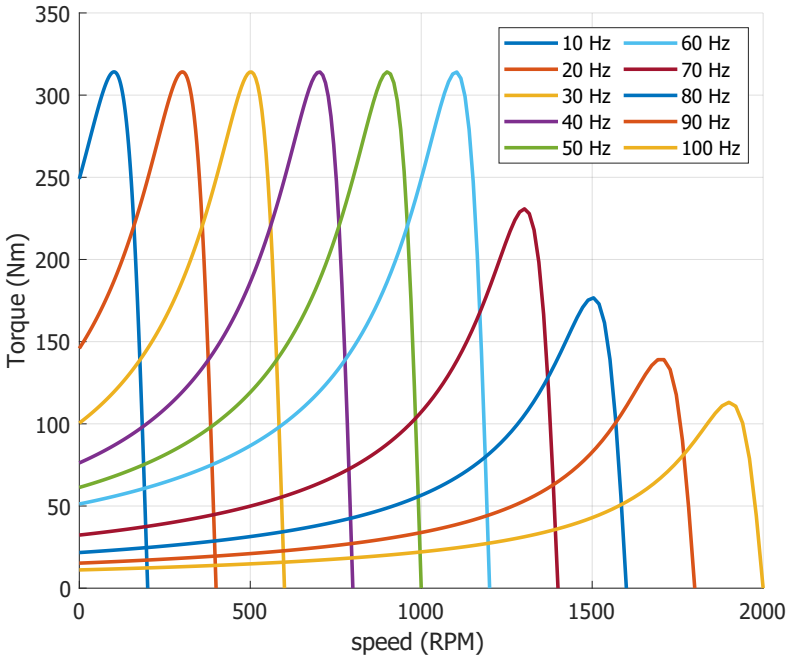

(a) IM torque-speed characteristics under VVVF

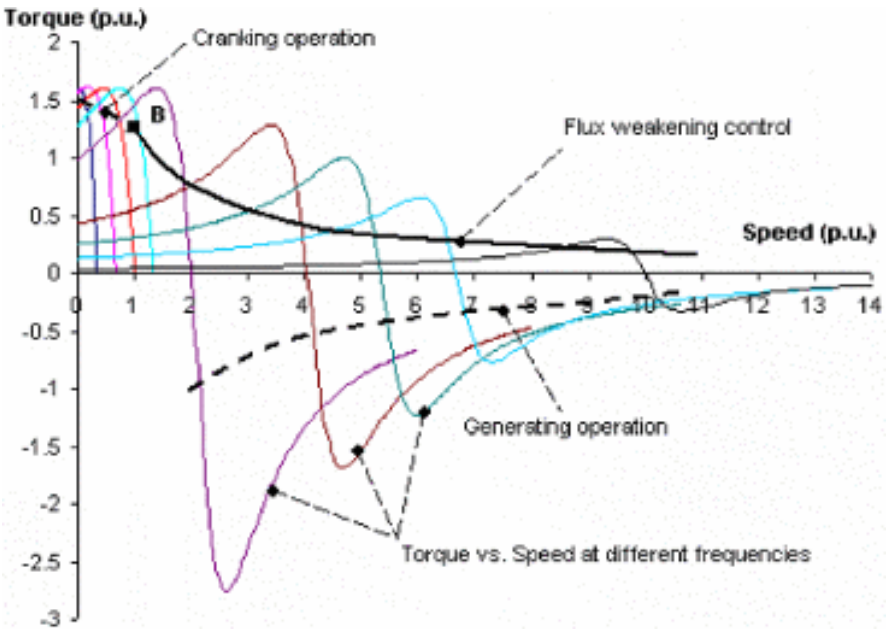

(b) IM Torque-Speed Characteristics for ISA Application[22]

Figure 2.4: IM characteristics under VVVF

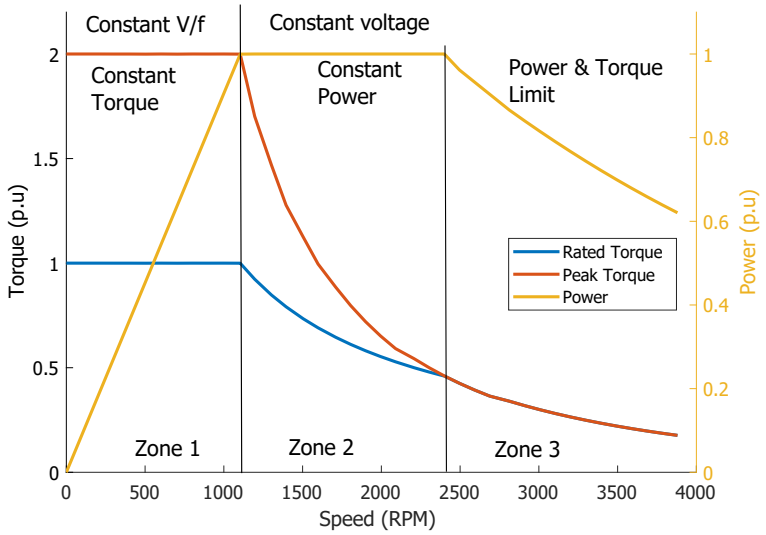

Figure 2.5: IM torque-speed operation envelope under VVVF

slower external loop. Dynamic control of IM with DQ0 model of the machine allows this type of independent control of the torque and speed of the machine.

Eqn. 2.8 sets the limit of the maximum torque of the machine under VVVF operation. However, the peak torque is higher than the rated continuous torque of the machine. It's reasonable to assume that the peak torque to be 2 p.u, where the rated torque is 1.pu [6, pp 54-55]. Further, the drive operation is limited by both the IM and the inverter. Fig. 2.5 shows the the torque-speed envelope of operation under VVVF control.

In the constant V/f region shown as zone 1 in Fig. 2.5, the torque output is limited by the current rating of the inverter. As the voltage to the machine increases linearly with the speed (constant v/f), the power input to the machine also increases linearly. Hence the rated torque of the machine remains constant. It has been already shown from Eqn. 2.8 that the peak torque also remains constant in this region. In the flux weakening region, the inverter operates at maximum voltage output, hence the power is limited by the current rating of the inverter, leading to constant power operation. Power being constant, the rated torque of the machine decrease with the inverse of ω. However, as per Eqn. 2.8, the peak torque starts decreasing at inverse of ω^2. Hence at a certain speed point (which will be $\frac{peak\ torque}{rated\ torque}$ times base speed) the peak torque of the machine limits the output. In this region, shown as zone 3 in Fig. 2.5, the torque of the machine is inversely proportional to ω^2, hence the power of the machine is proportional to $\frac{1}{\omega}$. Although VSC fed IM drive with VVVF achieves more flexibility in the operating torque-speed characteristics, compared to line fed machine,

VVVF control has its limits too. For a machine with the peak torque twice of its rated torque constant power operation is available only from rated speed to twice the rated speed.

2.2 Reconfigurable Induction Machine Drive

It has been shown in the previous section significant flexibility is obtained by using a power electronic converter to drive the IM. However, the constant power operation zone is limited mostly due to the current limit of the power electronic converter, as the machine can withstand short term higher current. It can be further argued that the magnetic pole count is the single most controlling factor of torque-speed characteristics of an IM [63]. Only few literature [64, 65] has reported the use of winding reconfiguration (high-speed winding / low-speed winding) to achieve increased speed range, while keeping the phase and pole count same. Compared to pole changing stator winding reconfiguration, these types of winding reconfiguration has either lower torque-speed range and/or lower utilization of inverter DC bus voltage, hence these techniques are not discussed here any further.

Before the advent of power electronics to effectively control the machine torque-speed characteristics, different techniques were developed, such as phase amplitude modulation (PAM), pole changing configuration using mechanical switches to manipulate effective pole count of the machine. Further, coupled with power electronic converter, these techniques allow to improve the torque-speed characteristics of the machine. In this section some of these techniques to achieve stator winding reconfiguration for pole changing are discussed below.

2.2.1 Pole Changing Induction Machine

Several ideas were developed to use mechanical switches to change the pole numbers of the machine before the advent of Power Electronics. Detailed research on 2:1 pole changing IM is reported in [66]. Further, a 3:1 pole changing technique is reported in [67] . Fig. 2.6 shows torque-speed characteristics of the machine under two different configuration. Poly phase winding for an alternator - motor set up, such as diesel traction engine was also reported [68]. This paper discusses the application of poly-phase winding machine to achieve consequential pole changing.

Power electronics allows implementing pole changing techniques electronically at the inverter side. A 2:1 electronic pole changing configuration using power electronics is reported in [1]. It can be noted from Fig.2.7, electronic pole changing allows higher flexibility on

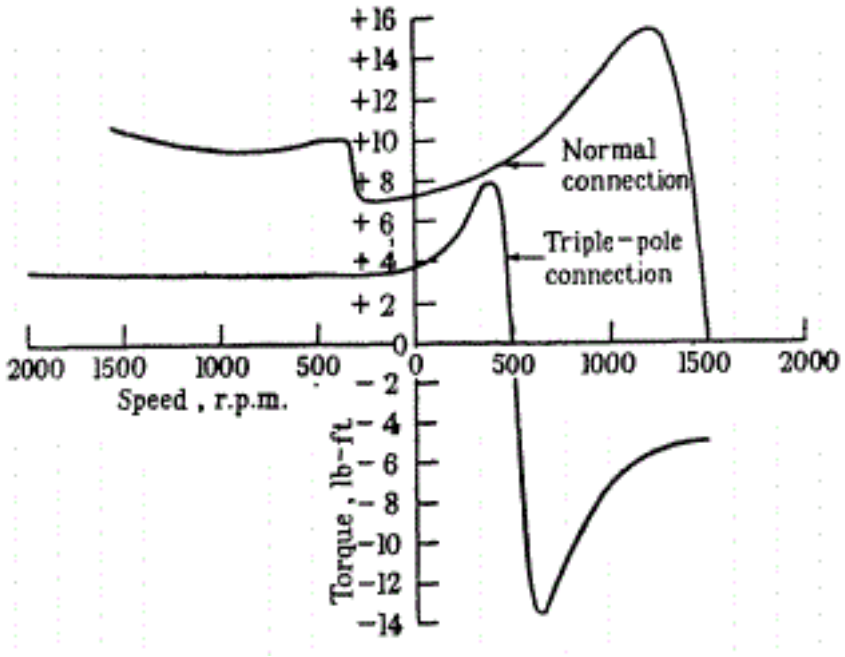

Figure 2.6: torque-speed characteristics of 3:1 pole configuration []

torque-speed characteristics. Further, it should be also emphasized that the electronic pole changing allows changeover of winding configuration without de-energizing the machine.

2.2.2 Phase Amplitude Modulation (PAM)

Although the above mentioned techniques allows change of the pole configuration, but only in multiple order of the base configuration, such as 2:1 , 3:1 etc. Phase Amplitude Modulation (PAM) as discussed in [69], allows pole changing in fractional order. In this method the stator winding of a given pole configuration is excited (reconfigured stator connection using switches), in such a way to create resultant MMF of a set of two other pole configuration. Then, utilising the spacing of the three phase winding, it is made sure that one of the pole configuration is cancelled, giving one desired pole configuration only. The study reports the experimental result of an 8 pole machine, which can be reconfigured to 10 pole as well (PAM creates 6-pole and 10-pole excitation, 6-pole MMF is cancelled, leaving 10-pole MMF).

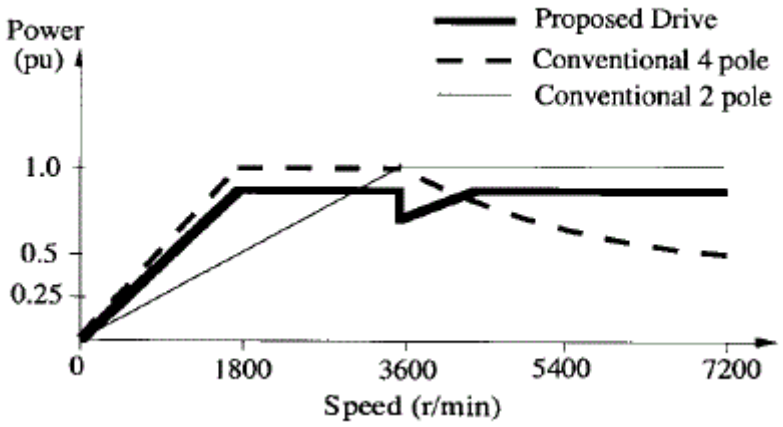

Figure 2.7: Power capability comparison between proposed IM drive and conventional four-pole and two-pole machines having the same outer dimensions [1]

2.2.3 Phase Pole Modulation (PPM)

It can be noted, only a specific set of pole reconfiguration (set of two different pole numbers) can be obtained only from a specific winding connection by using PAM. However, for PAM, the number of phases remains the same in both configurations. Phase Pole Modulation (PPM) allows further flexibility to change the number of phases as well. In [2] PPM was introduced by Miller et al. To have a balanced machine operation the following equation must be satisfied:

$$Q_s = 2pmq \tag{2.9}$$

Where, Q_s is the number of stator slots, p is the pole pair, m is the number of phases and q is the phase belt or number of stator slots per pole per phase. As for a given stator winding q is fixed, p and m can be chosen arbitrarily satisfying Eqn. 2.9. It has been further argued in [2], compared to conventional winding connection, toroidally wound IM allows maximum flexibility in reconfiguration, when PPM is being used. This paper discusses a 9 leg inverter fed 4 pole , 9 phase / 12 pole 3 phase machine. Further, in [5] a PPMIM drive is reported for a conventional radially wound machine. It is reported in [63], that much of literature on PPMIM is for very few variations of configuration, such as 4 pole / 12 pole and 6 pole / 18 pole. This study reports a generalized analysis of PPM machine. However, in line with initial work on PPM [2], this study also concludes that toroidal winding allows maximum flexibility for utilization of PPM.

It can be concluded from the Fig. 2.8 [2], as PPM along with toroidally wound IM

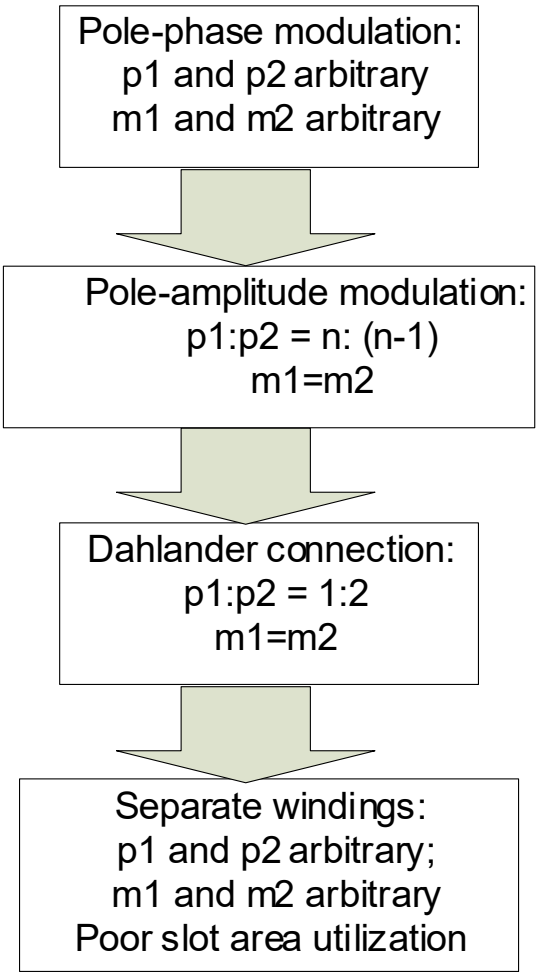

Figure 2.8: Hierarchy of discrete speed control methods for an AC machine (redrawn from [2])

gives maximum flexibility of reconfiguration, it will be the most suitable choice for ISG application. The power electronic converter and control for PPMIM drive is discussed in the next section.

Toroidally wound machine has been previously reported for IM in [70]. This paper reports that, for applications with restricted machine length, i.e electric bikes, electric wheel, toroidally wound machine can have lower losses and a higher efficiency. For such machines with lower axial length, the toroidal machine offers shorter end ring, compared to radially wound machine, thus reduction in stator resistance and increase in efficiency. Further, the paper reports for stator bore circumference the toroidal winding appear as similar to conventional radial winding.

[71] reports a dual rotor toroidally wound machine, where the return side of the toroidally wound stator is also utilized to produce torque by having an external rotor. The machine is reported to have both high efficiency and high torque density due to shorter end ring and torque production by dual rotor. [72] reports a PM machine with with toroidal winding stator, where the end ring side of the stator is utilised by introducing additional axial gap rotor along with the radial gap rotor. The axial gap rotor is used to achieve variable magnetic flux in the machine.Toroidal winding machine for synchronous reluctance machine has been reported in [73], which also reports improvement of efficiency, due to reduction in end ring winding, and better performance compared to fractional slot concentrated winding due to absence of even harmonics. [74] reports a toroidal winding radial flux BLDC machine for high speed flywheel energy storage application. [75] reports a SRM with toroidal winding.

To summarise toroidal winding machine has been reported for different type of machines, e.g PM, SRM BLDC and IM have been reported as well. For IM, Toroidal winding machines have lower utilization of the copper winding due to linkage of the air gap flux in only one side. However, for the machine with restricted axial length, toroidal winding offers shorter end ring winding, and thus better efficiency. For this thesis, like other literature on PPMIM, toroidal winding has been used to achieve greater flexibility of pole reconfiguration, as it will be shown later in this thesis, toroidal winding connection allows ability to excite each of the phase bands independently leading to greater flexibility of reconfiguration of the pole numbers of the machine.

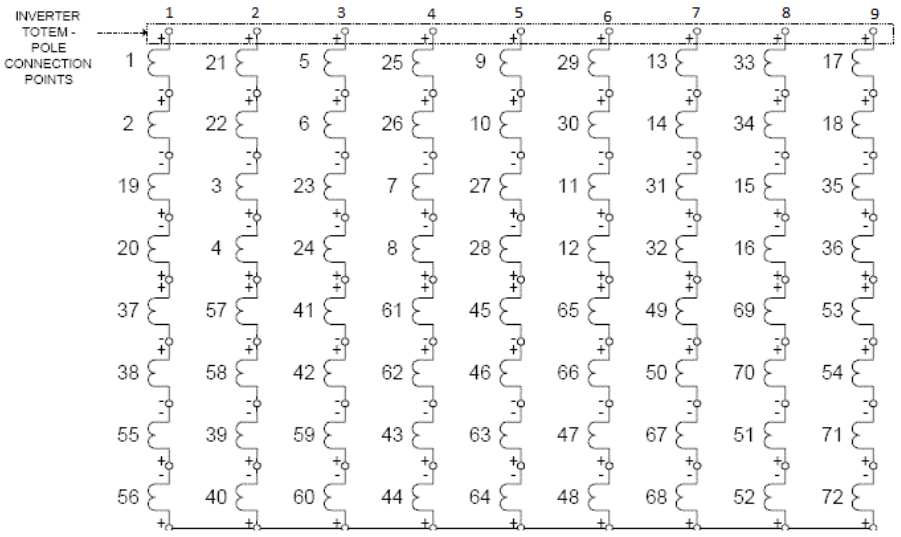

Figure 2.9: Machine winding diagram for PPM - 4pole 9 phase / 12 pole 3 phase [2]

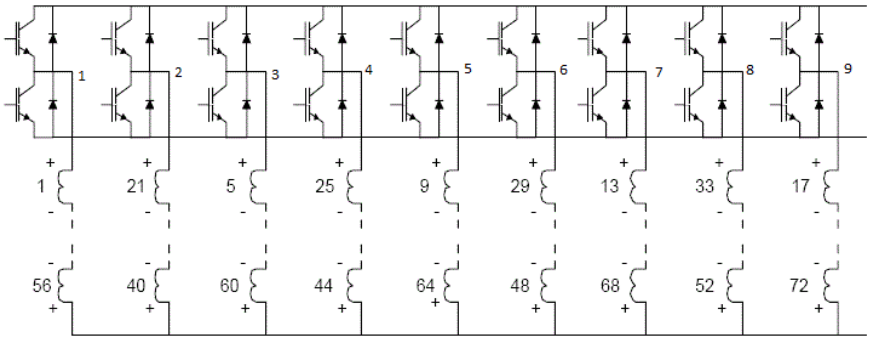

Figure 2.10: Power electronic converter for PPMIM [2]

2.3 Power Electronic Converter for PPM Induction Machine

The winding diagram and the power electronic converter of the 4 pole / 12 pole machine discussed in [2] is shown in Fig. 2.9 and Fig. 2.10 respectively. The phase sequence of the inverter legs for two different configurations are given in Table. 2.1. The phase angle of the phases *A B and C* are given by $0^o, 120^o$ *and* 240^o respectively. Negative of a phase denotes further 180^o phase shift from the original phase.

It can be also noted, although only 3 phases have been used in [2] for 4 pole configuration, there is a possibility to utilise 9 phases as discussed in [5]. Although in lower pole count, there is a scope of application of higher number of phases, (which will lead to more sinusoidal air gap MMF) the number of phases in higher pole count (12 pole in this case) is

Table 2.1: Inverter leg and phase excitation for 4pole / 12 pole PPM [2]

Inverter Leg No.	4 Pole	12 Pole
	Phase	
1	A	A
2	-A	B
3	A	C
4	B	A
5	-B	B
6	B	C
7	C	A
8	-C	B
9	C	C

Table 2.2: Inverter leg and phase excitation for 4pole / 12 pole PPM with carrier shifted PWM [5]

Inverter Leg No.	4 Pole		12 Pole	
	Angle (in degree)			
	Modulation	Carrier	Modulation	Carrier
1	0	0	0	0
2	40	0	120	0
3	80	0	240	0
4	120	0	0	60
5	160	0	120	60
6	200	0	240	60
7	240	0	0	120
8	280	0	120	120
9	320	0	240	120

limited. In [5] another carrier shifted PWM technique for higher pole count is reported for a similar 4 pole / 12 pole PPM machine with 9 leg two-level inverter. The phase angles for inverter legs under two different pole configuration is shown in Table 2.2. It can be seen, for higher pole count the career phase shift is introduced, which leads to the lower harmonic content of the net phase voltage.

2.4 Conclusions

Based on the literature review on IM drives, it can be concluded that VVVF drive allows significant widening of torque-speed operating envelope of the machine. However, pole

changing allows further improvement on the extension of the constant power operation of the machine, which can be applied along with the VVVF control. Hence, given the requirement of wide torque-speed characteristics of ISA [20, 22], a PPMIM, along with additional VVVF control will be suitable.

Although connecting several phase belts in series allows to reduce the number of the power electronic switches, this limits the flexibility of reconfiguration which can be achieved by phase-pole modulation. In this thesis, an independent phase belt controlled phase-pole modulated IM drive has been proposed for ISA application. This ability to provide excitation to each of the phase belts independently allows significant flexibility in producing the air-gap MMF in the machine. The analysis shows a single machine can be reconfigured in 5 different pole-pair configurations, thus achieving significant widening of torque-speed characteristics, which has been explored in details in the next chapters.

Chapter 3

Independent Phase Belt Controlled PPMIM

The last chapter detailed the basic principles of a line fed IM, as well as the VVVF control of IM drive. Further, the concept of pole changing IM was discussed and it was established Phase Pole Modulation on a toroidally wound IM offers maximum flexibility of pole reconfiguration. In this chapter the principle of independent phase belt controlled Pole Phase Modulation scheme is derived, by analysing the air gap MMF of an IM. The proposed scheme of excitation is validated by FEM simulation. An analytical model of the machine is developed and equivalent circuit parameter expressions are found. The equivalent circuit parameters of a specific machine is also obtained from the FEM model and compared against the analytical values.

3.1 Independent Phase Belt Controlled Phase Pole Modulation

The torque of an IM is produced by a rotating stator MMF. The rotating air-gap MMF induces an EMF in the rotor, proportional to the slip speed. The rotor winding is short-circuited hence a current is established in the rotor by this induced EMF. By the interaction of the rotor current and the air-gap MMF, torque is produced in the rotor. In other words, it can be claimed that an excitation scheme, which will generate a rotating sinusoidal MMF in the air-gap, is a valid excitation scheme to operate an IM. For a conventional machine, the excitation scheme is presented by the winding diagram, showing the connection of the

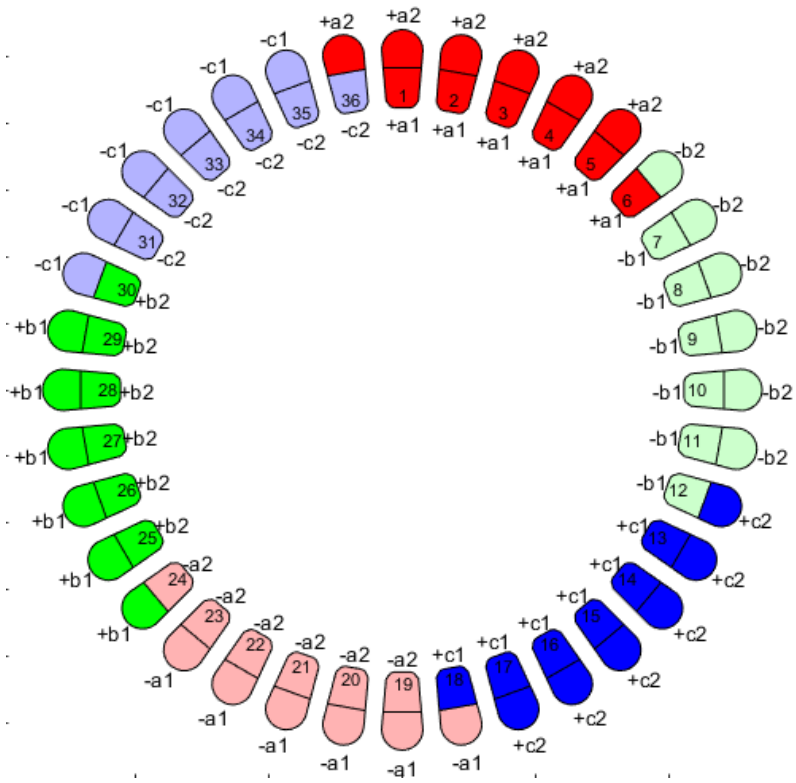

(a) Winding diagram of 2 pole, 3 phase machine

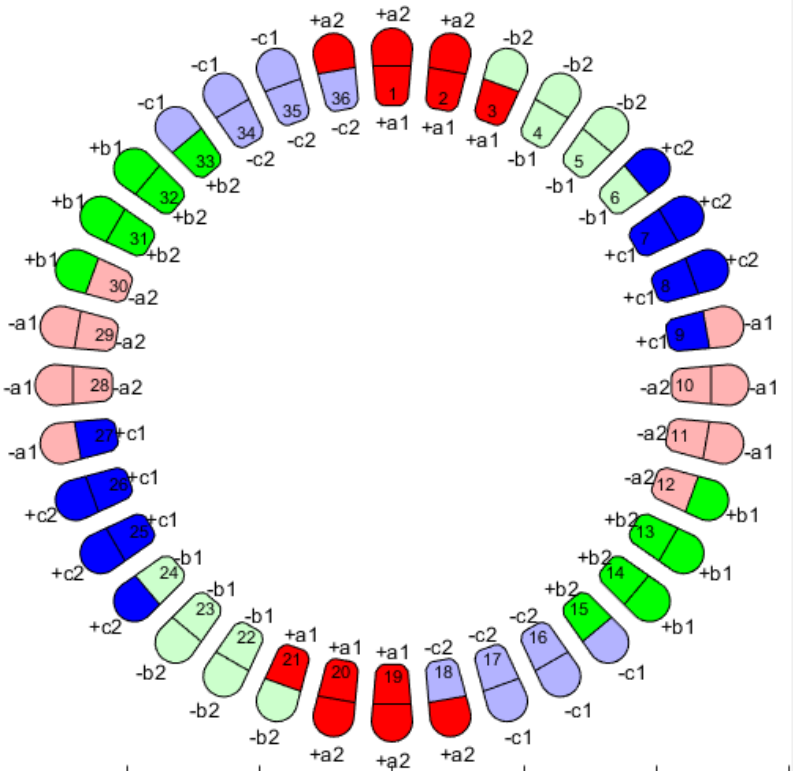

(b) Winding diagram of 4 pole, 3 phase machine

Figure 3.1: Winding diagram of radially wound IM

winding, and direction. The winding diagrams of a 4-pole 3-phase machine and a 2-pole 3-phase machine are shown in Fig. 3.1. The machine has 36 stator slots, and a double layer winding is used for both the pole configurations. The coil is short pitched by one slot in both pole configurations, giving a pole pitch of 17 $\left[\frac{36\ slots}{2\ poles}-1\right]$ for 2 pole, and 8 $\left[\frac{36\ slots}{4\ poles}-1\right]$ for 4 pole. The three phases are indicated as a,b and c respectively. The $\pm$ sign indicates the direction of the coil, and the number afterwards shows the parallel path number. Both 2 pole and 4 pole machine examples are shown for 2 parallel paths. The air-gap radial flux density of these two cases are also plotted in Fig. 3.2b, which has been obtained from an FEM simulation. The north and south poles can be identified from the plots, by positive and negative radial flux density respectively. The notches in the flux distribution is due to the slot and tooth effect of stator and rotor.

The fundamental principle of phase pole modulation, as discussed in the previous chapter, can be viewed as adjusting phase excitation to change the pole numbers. The phase excitation adjustment is achieved by accurately shifting the phase angle of the modulation wave of two consecutive inverter legs. Hence for a PPMIM if particular phase excitation can create a similar MMF distribution across the air gap, as shown in Fig. 3.2a and 3.2b the machine will be configured to 2-pole and 4-pole respectively. To demonstrate the principle, a 36 slot, 12 phase, toroidally wound IM is considered.

The winding diagram of the machine is shown in Fig. 3.3. Each slot is toroidally wound with a coil for a number of turns in the same winding direction, and the coil number is denoted by the slot number. Every 3 consecutive coils are connected in series to form one phase belt, thus giving phase belt (q) to be 3. The end of all 12 phases are connected together to formulate the star point. As the previous literature reports, maximum flexibility in the number of pole configurations, for a PPMIM is achieved when a toroidal winding is used, hence toroidal winding has been used for this thesis as well. The numbers in black in Fig. 3.3 show the coil number, and the numbers in blue in the top denote the inverter leg number (as shown in Fig. 3.4) to be connected for the set of the coils.

This type of connectivity, for the above mentioned 36 slot, 12 phase, toroidally wound IM allows the machine to be configured in 2/4/6/8/10 pole combination. To achieve any particular pole configuration, the following equations has to be satisfied:

$$Q_s = 2pmq \tag{3.1}$$

Where Q_s is the total number of stator slots, p is the pole pair, m is the number of phases per pole and q is the phase belt or the number of consecutive stator slot coils connected in series with one inverter leg. As for the given machine, q is pre-determined and for a

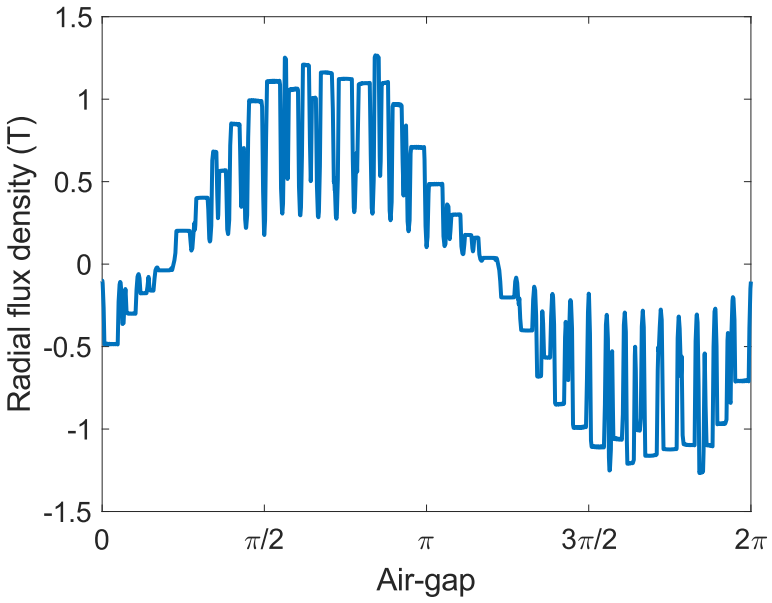

(a) Radial flux distribution of 2 pole, 3 phase machine

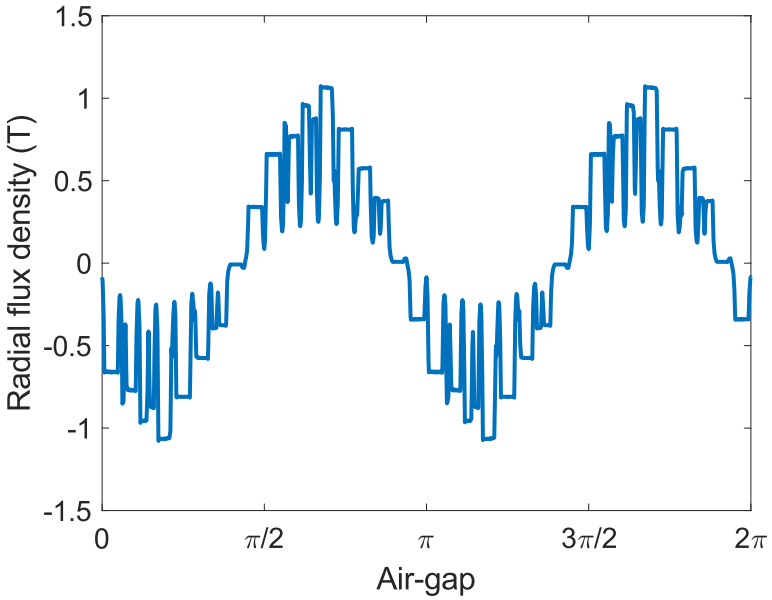

(b) Radial flux distribution of 4 pole, 3 phase machine

Figure 3.2: Air-gap MMF of IM

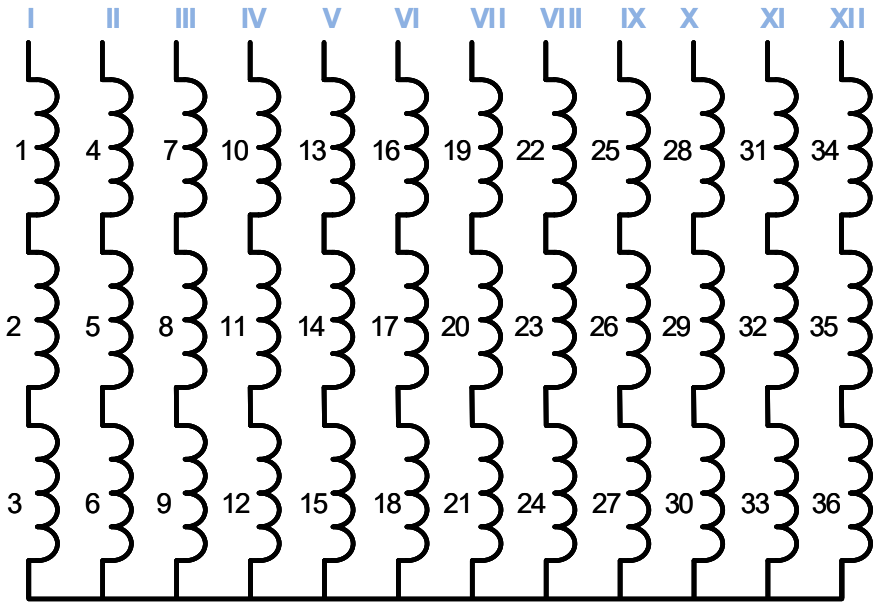

(a) 12 phase winding diagram

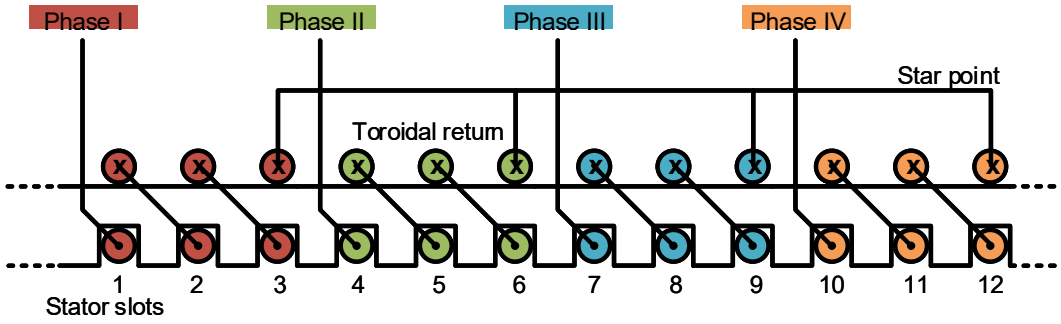

(b) 12 phase winding connection

Figure 3.3: Proposed 12 leg stator PPM winding

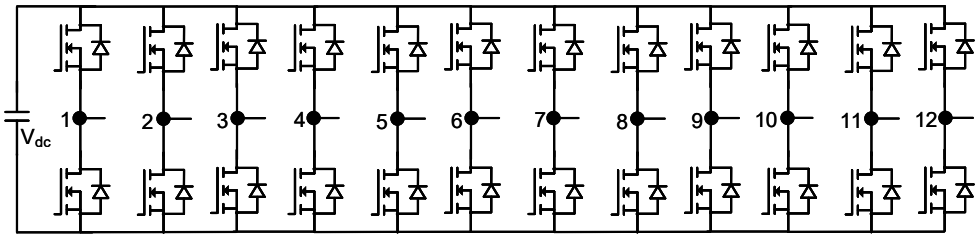

Figure 3.4: 12 leg MOSFET inverter schematic

given pole pair, number of phase per pole has to be decided from the Eqn. 3.1. Applying this equation for 2, 4, and 6 pole configuration, number of phases needs to be 6, 3, and 2 respectively are obtained. However, a further generalised equation can be used to obtain phase difference between the consecutive legs (in degree), given as below:

$$\phi = \frac{p \times 360}{l_n} \tag{3.2}$$

where, l_n is the total number of phase belts, given as below:

$$l_n = \frac{Q_s}{q} = 2pm \tag{3.3}$$

It can be noted that the number of the legs will decide possible phase-pole combinations as well as the number of switches in the inverter. With a large l_n many phase-pole combinations can be achieved at the expense of large number of inverter legs hence switches.

To ensure the star point does not need any return path (as shown in Fig. 3.3), the summation of the currents for all legs has to be zero. Assuming balanced phases and hence phase equivalent circuit model, the current in the n th phase can be given as below:

$$\begin{aligned} i_n &= \widehat{I}\cos(\omega t + (n-1)\theta) \\ &= \widehat{I}\cos(\omega t + (n-1)\tfrac{2p\pi}{l_n}) \end{aligned} \tag{3.4}$$

where $\widehat{I}$ is the peak of the phase current, θ is the phase shift between consecutive inverter legs. The sum of the currents for all legs can be obtained as:

$$\begin{aligned} & \textstyle\sum_{i=1}^{l_n} \widehat{I}\cos(\omega t + (n-1)\tfrac{2p\pi}{l_n}) \\ = \;& \widehat{I}\textstyle\sum_{i=1}^{l_n} \cos(\omega t + (i-1)\tfrac{2p\pi}{l_n}) \\ = \;& 0 \end{aligned} \tag{3.5}$$

Table 3.1: Inverter leg and phase excitation for 2/4/6 pole PPM

	Phase Angle (in degree)				
Pole no →	2	4	6	8	10
Phase angle difference	30	60	90	120	150
Inverter leg no ↓					
1	0	0	0	0	0
2	30	60	90	120	150
3	60	120	180	240	300
4	90	180	270	0	90
5	120	240	0	120	240
6	150	300	90	240	30
7	180	0	180	0	180
8	210	60	270	120	330
9	240	120	0	240	120
10	270	180	90	0	270
11	300	240	180	120	60
12	330	300	270	240	210

The phase angles for the different pole configurations are tabulated in Table. 3.1 using Eqn. 3.2 and 3.3. It should be noted, the phase angle will be 180^o for 12 pole machine, which results in an equivalent single phase IM. Due to the inherent starting torque problem of a single phase machine, this has not been explored any more.

In a conventional 3 phase machine, the north and south poles are constructed by different direction of the coils - as can be seen from the winding diagrams shown in 3.1. Hence, for a conventional machine, the ratio of phase/pole is an integer, as all the phases (a,b, and c) are present under all poles. For the proposed independent phase belt controlled the number of phase per pole is an integer for 2/4/6 pole configuration. However, it should be noted, putting $p = 4$ and 5, which corresponds to 8 pole and 10 pole operation, m is obtained to be 1.5 and 1.2 respectively, indicating fractional phase/pole.

Mathematically the magnetic space phase angle difference is given by $\phi = \frac{\pi}{m}$, and m being an integer ϕ is a submultiple of π for conventional IMs or previously reported PPMIMs. In other view point - this design reports the possibility of removing the constraint of the magnetic space phase angle difference between two consecutive phase belts of a machine to be a submultiple of π or even 2π, which in turn allows fractional slots/pole for an IM at the expense of added harmonic content in the air-gap flux. This can be only achieved by exciting the individual phase belts independently, as conventional winding, with a go and return of the coil will always ensure integral phase per pole. In [63, 76], a 9 leg inverter has

been used to achieve 2/6 pole configurations. However, at the expense of 3 more inverter legs (total 12 leg inverter) it has been shown here up to 5 different pole configurations of the same machine can be achieved.

In conventional radially wound m phase machine as well as previously reported PPMIM [2, 63], as the return paths of different phase belts are connected electrically, the achievable magnetic space phase angle difference between two consecutive phase belts are always a submultiple of π. This constraint limits the possible pole configurations achievable. It can be noted, for the 8 pole configuration, the phase angle difference between two phase belts is $\frac{2\pi}{3}$, not a submultiple of π, which has not been investigated before. Under the pole configuration $p = 5$, even more freedom with respect to the magnetic space phase angle difference has been explored, by making it to be $\frac{5\pi}{6}$ which is not a submultiple of 2π.

In the next section, an analytical model of the machine has been developed from first principles, starting from the analysis of the air-gap MMF created by the phase shifted toroidal winding. The model has been further developed to obtain the machine equivalent circuit parameters from the machine dimensions.

3.2 Equivalent Per-Inverter Leg Circuit Model

The objective of this section is to derive a steady state model for the proposed independent phase belt controlled PPMIM, under different phase and pole configurations. It has been discussed in the previous section (Eqn. 3.3), the choice of phase belt q decides the compromise between the number of electronic switches and phase pole configurations. Hence the effect of q on the steady state model will be also discussed.

The per phase steady state model of the conventional IM is given in Fig. 2.1, where R_s and L_s are the stator resistance and leakage inductances respectively. Similarly $R_r^{'}$ and $L_r^{'}$ represent rotor resistance and leakage inductances referred to stator side, L_m denotes mutual inductance between stator and rotor and s is the slip. In this circuit, the core loss component (R_m) is neglected. However, it should be noted that, for a conventional machine, usually the number of phases and poles are fixed, which is not the case for PPMIM. Hence for this case, it is more useful to obtain a per leg equivalent circuit model of the machine (as the number of inverter legs - or the machine excitation terminal) remains constant. In the following sections each of these 5 parameters of the circuit model has been derived. The analytical results have been verified using finite element method simulation as well.

3.2.1 Stator Resistance

The resistance of the stator winding can be obtained by studying an individual slot coil. As mentioned earlier, a stator coil is made by toroidally winding a wire for a number of turns across a slot, and then number of such coils are connected in series. The resistance of the single stator slot winding can be obtained as the equation given below:

$$R_{sl} = \frac{N_s \rho_s l_c}{A} \tag{3.6}$$

where ρ_s is the resistivity of the stator winding material (copper), A is the cross-sectional area of the conductor, and l_c is the length of a single turn, and N_s is the number of turns in a coil. As it has been shown before, the overhang of the toroidal winding is negligible, the effective length of the stator slot is taken be equal to machine length. Hence for a toroidal winding, the length of the coil l_c can be taken as twice of the machine length l. If multiple-stranded conductors are used A has to be taken as effective cross-section of the stranded wire given by $N_c A_c$, where N_c is the number of strands in a single turn, and A_c is the cross section area of one strand. For the proposed machine, as shown in Fig. 3.3, the phase belt coils are in series. Assuming all stator coils are identical and, the resistance of the leg can be given as

$$R_s = R_{leg} = qR_{sl} = \frac{\rho 2lqN_s}{A} = \frac{\rho 2lqN_s}{N_c A_c} \tag{3.7}$$

where, q is the phase belt - the number of conductor slots per inverter leg connected in series. As discussed in [63, p.59], this gives a per leg model for PPM machine, as the number of the legs l_n is fixed by hardware.

3.2.2 Rotor Resistance

As the rotor is the same as the PPM machine discussed in [63, pp. 60-61], the same derivation is used here too. Assuming stator current sets up a sinusoidal air gap flux, the rotor can be modelled as a polyphase winding with phase belt (q_r) equal to 1 and phase number m_r equal to $\frac{Q_r}{2p}$, where Q_r is the number of rotor bars [3, 63]. The rotor cage is comprised of Q_r rotor bars and $2Q_r$ end ring segments. The resistance of these two components (r_{bar} and r_{er}) may be used to determine rotor resistance [63, pp. 60-61]. The resistance of each bar is given by[63, pp. 60-61]:

$$R_{bar} = \frac{\rho_{bar} l_{bar}}{A_{bar}} \tag{3.8}$$

where ρ_{bar} is the resistivity of the rotor bar conductor, A_{bar} and l_{bar} is the cross-sectional area and length of the rotor bar respectively. The end ring resistance is given by [63, pp. 60-61]

$$R_{er} = \frac{\rho_{er} l_{er}}{A_{er}} \tag{3.9}$$

where ρ_{er}, A_{er} , and l_{er} are similarly defined for end ring. Incorporating the derivation from [3], the effective bar resistance is given as [63, pp. 60-61] :

$$R_{be} = R_{bar} + \frac{R_{er}}{2sin^2(\frac{\pi p}{Q_r})} \tag{3.10}$$

Each rotor phase or closed loop contains two effective bar resistances in series. The per phase rotor resistance is therefore given by

$$R_r = 2R_{be} \tag{3.11}$$

It should be noted this resistance will correspond to rotor per phase model (m_r phases for m_r rotor bars) , hence a suitable transformation should be used to refer this to stator phase which is denoted as $R_r^{'}$. $R_r^{'}$ is given in Eqn. 3.74 in subsection 3.2.4.4, following derivation of equivalent turns ratio of the machine by analysing the rotor and stator MMF. Further, both stator and rotor resistance are obtained for DC. However, incorporating skin depth into the equation (in the cross-section terms), it is possible to obtain slip dependent resistance.

3.2.3 Leakage Inductance

The leakage flux of IM, can be classified into four categories, slot leakage, end winding leakage, differential leakage and skew leakage flux [3, 4, 76]. For the similar reasons mentioned in [63, p.61], here also the differential leakage term and skew leakage term is neglected to obtain a low order air gap flux distribution by the proposed stator winding arrangement. Further, as the proposed winding has negligible end winding connection, this term is also neglected for stator winding. The slot leakage of the conductor is given as [3, 76, pp. 62-63]

$$L_{slot} = \mu_0 l N_s^2 P_s \tag{3.12}$$

where P_s is the specific slot permeability given as below [3]:

$$P_s = \frac{h_4}{3b_2} + \frac{h_3}{b_2} + \frac{h_1}{b_1} + \frac{h_2}{(b_2 - b_1)} ln(\frac{b_2}{b_1}) \tag{3.13}$$

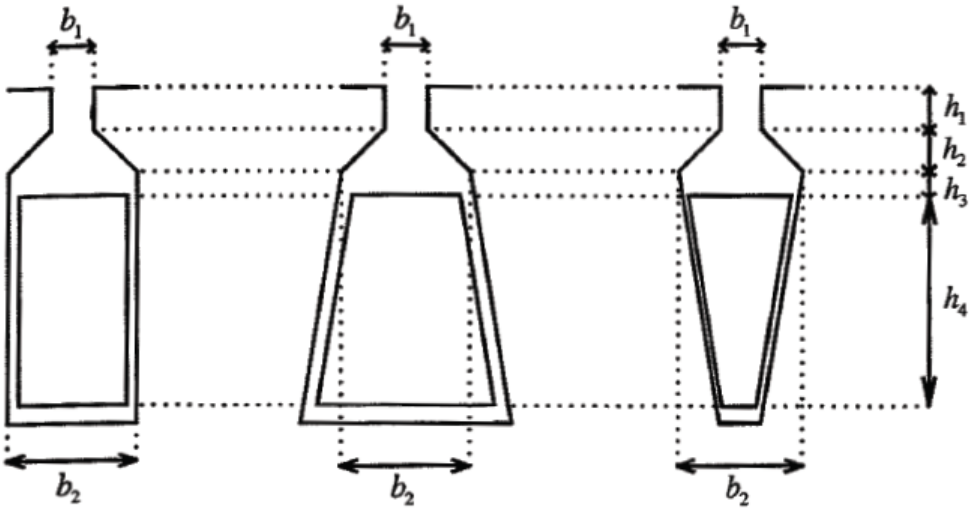

Figure 3.5: Slot shapes with specified dimensions [3]

where, $h_1 - h_4$ and $b_1 - b_4$ are given for different slot geometry in Fig. 3.5. Following similar logic as stator resistance (Eqn. 3.7) phase leakage inductance may be given as

$$L_s = qL_{slot} = \mu_0 q l N_s^2 P_s \tag{3.14}$$

For rotor leakage inductance a similar approach (3.11) can be taken as for rotor resistance. Hence rotor leakage will be given as

$$L_r = 2L_{bar} + \frac{L_{er}}{\sin^2(\frac{\pi p}{Q_r})} \tag{3.15}$$

where L_{bar} and L_{er} are rotor bar and end ring leakage inductance. L_{bar} is given as similar equation as Eqn. 3.12 as below:

$$L_{bar} = \mu_0 l P_r \tag{3.16}$$

where P_r represents rotor bar permittivity, which can be calculated using Eqn. 3.13 and Fig. 3.5, depending on the slot geometry. For end ring leakage the closed form expression from[3] given below can be used.

$$L_{er} = \mu_0 \frac{4}{9}(l_{re} + \kappa \tau_r) \tag{3.17}$$

where l_{re} is the length of the rotor bar extended after end ring, τ_r is the average rotor pole pitch, and κ is an empirical constant based on pole count. Further, once again it should

be kept in mind similar to resistance, this rotor leakage is also with respect to the rotor per phase, hence it should be suitably transformed to the stator phase circuit model.

3.2.4 Mutual Inductance

To derive the expression for mutual inductance of the PPMIM, the flux equations for stator and rotor side need to be given first. Both the stator and rotor have their own leakage and mutual inductances. The flux equations can be given as [63, p.64] :

$$\bar{\lambda}_s = \bar{I}_s L_{ls} + \bar{I}_s L_{ss} + \bar{I}_r L_{sr} \tag{3.18}$$

$$\bar{\lambda}_r = \bar{I}_r L_{lr} + \bar{I}_r L_{rr} + \bar{I}_r L_{rs} \tag{3.19}$$

Where the symbols used are defined as below:
$\bar{\lambda}_s$: Stator flux linkage
$\bar{\lambda}_r$: Rotor flux linkage
$\bar{I}_s$: Stator current
$\bar{\lambda}_r$: Rotor flux linkage
$\bar{I}_r$: Rotor current
L_{ss} : Stator magnetising inductance
L_{ls} : Stator leakage inductance
L_{rr} : Rotor magnetising inductance
L_{lr} : Rotor leakage inductance
L_{rs} : Rotor to stator mutual inductance
L_{sr} : Stator to rotor mutual inductance

All rotor quantities are referred to the rotor frame of reference. The leakage terms have been discussed already in the previous section. Now the expression for two magnetising inductances and two mutual inductances will be derived here.

The rotor quantities are derived in rotor per phase model (where each bar is considered as a phase) and stator quantities are derived in terms of stator number of phases for ease of deriving directly from the first principle. Considering this difference in the number of phases, and turns number in stator (turns number for rotor in cage rotor is 1, if each of the bar is considered as a rotor phase), the derived self and mutual inductances will be different for stator and rotor. Indeed in line with the physical principle, it is shown later in this derivation (section 3.2.4.4), when suitable transformation factor is introduced taking into

account of this number of phase difference, turns ratio and distributed nature of the stator winding the mutual inductance for both - rotor to stator and stator to rotor is the same.

Self inductance can be defined as the flux linkage of a coil due to its own excitation. The definition of self inductance is given as:

$$L_{self} = \frac{1}{\mu I^2} \int_v B^2 dV \tag{3.20}$$

where I is the current in the circuit, and the integration is over the volume enclosed by the circuit. This can be modified by using the concept of winding function and MMF for a cylindrical winding as below [1, 3, 63]:

$$\lambda = LI = \frac{\mu_0 rl}{g} \int_0^{\pi} \mathscr{N}(\theta_e)\mathscr{F}(\theta_e) d\theta_e \tag{3.21}$$

where λ is the flux linkage, $\mathscr{N}$ and $\mathscr{F}$ are winding function and MMF, expressed as a function of electrical angle (over the span of stator or rotor) respectively. r and l are the radius and length of the winding respectively, and g is the length of the air path. It is assumed the iron paths are infinitely permeable, considering MMF drop across the air gap only. Hence Stator self flux linkage will be given as:

$$\lambda_{ss} = \frac{\mu_0 rl}{g} \int_0^{\pi/p} \mathscr{N}_s(\theta_s)\mathscr{F}_s(\theta_s) d\theta_s \tag{3.22}$$

It can be noted in Eqn. 3.22, stator angle θ_s is used, hence the integral limits are 0 to π/p. $\mathscr{N}_s(\theta_s)$ and $\mathscr{F}_s(\theta_s)$ are stator winding function and stator MMF expressed as a function of stator angle θ_s. Further, a similar approach can be extended to the calculation of mutual flux, rotor to stator given as below.

$$\lambda_{sr} = \frac{\mu_0 rl}{g} \int_0^{\pi/p} \mathscr{N}_s(\theta_s)\mathscr{F}_r(\theta_s) d\theta_s \tag{3.23}$$

Extending the similar approach for rotor self and mutual flux the following can be obtained:

$$\lambda_{rr} = \frac{\mu_0 rl}{g} \int_0^{\pi/p} \mathscr{N}_r(\theta_r)\mathscr{F}_r(\theta_r) d\theta_r \tag{3.24}$$

$$\lambda_{rs} = \frac{\mu_0 rl}{g} \int_0^{\pi/p} \mathscr{N}_r(\theta_r)\mathscr{F}_s(\theta_r)d\theta_r \tag{3.25}$$

To make the further derivation easier, the stator flux linkages are expressed as a function of θ_s , whereas rotor flux linkages as as function of θ_r. It should be noted suitable caution should be taken care to transform the MMF and winding function from stator angle θ_s to rotor angle θ_r . To obtain the self and mutual flux linkages the winding function and the MMF function of both stator and rotor need to be derived.

3.2.4.1 Winding function

Stator winding function The proposed machine connects consecutive slots of a phase belt in series, and all phases in star fashion. The magnetics expressions for a conventional coil with go and return cannot be used for the proposed toroidal winding. However, it can be shown that the stator excitation scheme is similar to the induced currents inside a squirrel cage IM rotor, where each bar current is phase shifted by $\frac{2p\pi}{Q_r}$, where p is the pole pair number, and Q_r is the number of rotor bars. Hence the MMF developed by a single slot is to be derived rather than a closed coil.

Further, it should be emphasised, a conventional coil model was applied for the analytic derivation of stator and rotor flux in [63], which is not able to explain the fractional phase per pole cases. Hence this new analysis is needed to develop the expressions for stator and rotor MMFs analysing the slot current independently rather than as a coil with go and return.

The radial component of the flux created by a single slot conductor with N_s number of turns, at a stator position $\theta_s = 0$, carrying current i , is given as below [4]:

$$H_{sl}(\theta_s) = \frac{N_s i}{2g}(1 - \frac{\theta_s}{\pi}) \tag{3.26}$$

where g is the length of the air-gap. Due to symmetry i.e ($H_{sl}(0) = H_{sl}(2\pi)$), the MMF waveform takes shape of sawtooth waveform shown in Fig . 3.6. Hence for a phase belt of $q = 3$ conductors per phase, the net field will be the summation of three such waveforms, which are phase shifted slot pitch angle of α given as below:

$$\alpha = \frac{2\pi}{Q_S} \tag{3.27}$$

As an example case, a phase belt of 3 conductors in 36 stator slot machine is shown in Fig.

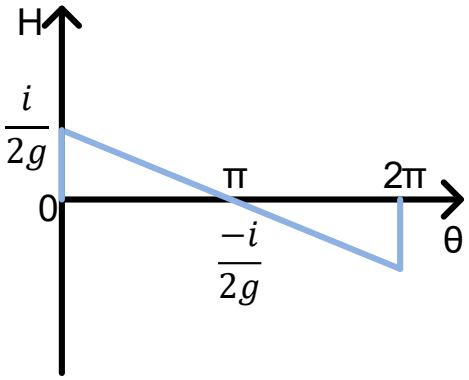

Figure 3.6: MMF of a single slot conductor [4]

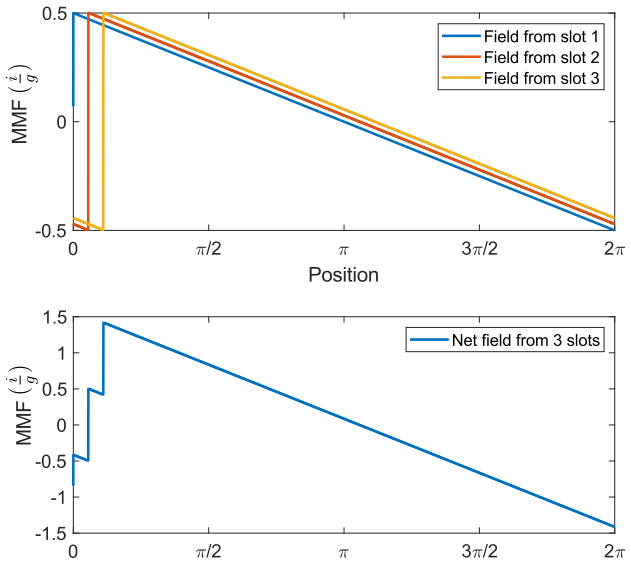

Figure 3.7: MMF of a phase belt of 3 conductors in 36 stator slot machine

3.7. For a generic case, the expression can be developed by taking the Fourier transform of the MMF waveform. The sawtooth waveform, shown in Fig. 3.6 can be expressed as

$$H_1(\theta_s) = \frac{N_s i}{\pi g} \sum_{\nu=1}^{\infty} \frac{1}{\nu}(\sin \nu\theta_s) \tag{3.28}$$

Hence the total MMF of a stator phase belt consisting q slots, which are phase shifted by slot pitch angle of α from each other, all carrying same current i, can be expressed as

$$\begin{aligned} H_s(\theta_s) &= \tfrac{N_s i}{\pi g} \sum_{j=0}^{q-1} \sum_{\nu=1}^{\infty} \tfrac{1}{\nu}(\sin(\nu\theta_s - j\alpha) \\ &= \tfrac{N_s i}{\pi g} \sum_{\nu=1}^{\infty} \tfrac{1}{\nu} \sum_{j=0}^{q-1} (\sin(\nu\theta_s - j\alpha) \end{aligned} \tag{3.29}$$

Eqn. 3.29 can be simplified as below:

$$\begin{aligned} H_s(\theta_s) &= \tfrac{N_s i}{\pi g} \sum_{\nu=1}^{\infty} \tfrac{1}{\nu} \sum_{j=0}^{q-1} (\sin(\nu\theta_s - j\alpha) \\ &= \tfrac{N_s i}{\pi g} \sum_{\nu=1}^{\infty} \tfrac{1}{\nu} \{\sin\nu\theta_s[1 + \cos\nu\alpha + ... + \cos\nu(q-1)\alpha] - \\ &\quad + \cos\nu\theta_s[\sin\nu\alpha + \sin 2\nu\alpha ... + \sin\nu(q-1)\alpha] \\ &= \tfrac{N_s i}{\pi g} \sum_{n=1}^{\infty} \tfrac{1}{\nu} \tfrac{\sin\nu q\frac{\alpha}{2}}{\sin\nu\frac{\alpha}{2}} \{\sin\nu\theta_s \cos\nu\tfrac{(q-1)\alpha}{2} - \cos\nu\theta_s \sin\nu\tfrac{(q-1)\alpha}{2}\} \\ &= \tfrac{qN_s i}{\pi g} \sum_{\nu=1}^{\infty} \tfrac{1}{\nu} \tfrac{\sin\nu q\frac{\alpha}{2}}{q\sin\nu\frac{\alpha}{2}} \sin\nu[\theta_s - \tfrac{(q-1)\alpha}{2}] \end{aligned} \tag{3.30}$$

If the origin of the coordinates are moved by an angle of $(\frac{(q-1)\alpha}{2})$, Eqn. 3.30 can be rewritten as below

$$H_s(\theta_s) = \frac{qN_s i}{\pi g} \sum_{\nu=1}^{\infty} \frac{1}{\nu} k_{q,\nu} \sin\nu\theta_s \tag{3.31}$$

where $k_{q,\nu}$ is the distribution factor for the ν th harmonic for a phase belt of q, given as

$$k_{q,\nu} = \frac{\sin\nu q\frac{\alpha}{2}}{q\sin\nu\frac{\alpha}{2}} \tag{3.32}$$

It should be noted, the above expressions, ν is the space harmonic as the Fourier transform was performed on the space domain. Eqn. 3.31 can be used to obtain the winding function of a stator phase belt ($\mathscr{N}_s(\theta_s)$) given as

$$H_s(\theta_s) = \frac{i\mathscr{N}_s(\theta_s)}{g} \tag{3.33}$$

From Eqn. 3.31, and 3.33, the winding function of stator phase belt can be given as

$$\mathscr{N}_s(\theta_s) = \frac{qN_s}{\pi} \sum_{\nu=1}^{\infty} \frac{1}{\nu} k_{q,\nu} \sin \nu\theta_s \tag{3.34}$$

Rotor winding function Conceptually the rotor bars can be modelled similar to the stator slots with only one turn and phase belt to be 1. Hence by setting q=1, and $N_s = 1$ in Eqn. 3.34, the winding function of a single rotor bar can be given as

$$\mathscr{N}_r(\theta_r) = \frac{1}{\pi} \sum_{\nu=1}^{\infty} \frac{1}{\nu} \sin(\nu\theta_r) \tag{3.35}$$

where θ_r is the angle in the rotor reference frame.

3.2.4.2 MMF function

Stator MMF function Having derived the winding function of a single phase belt of the stator (Eqn. 3.34) the MMF function of the stator ($\mathscr{F}_s(\theta_s)$) can be obtained as below

$$\mathscr{F}_s(\theta_s) = \sum_{k=0}^{M-1} i_{sk} \mathscr{N}_{sk}(\theta_{sk}) \tag{3.36}$$

where, M is the total number of the phases, and i_{sk} is the current in the kth stator phase, and $\mathscr{N}_{sk}$ is the winding function of the kth phase belt. Hence Eqn. 3.36 can be rewritten as

$$\mathscr{F}_s(\theta_s) = \sum_{k=0}^{M-1} I_s \sin(\omega_s t - \frac{k-1}{M} 2p\pi) \frac{qN_s}{\pi} \sum_{\nu=1}^{\infty} \frac{1}{\nu} k_{q,\nu} \sin(\nu(\theta_s - \frac{k-1}{M} 2\pi)) \tag{3.37}$$

where I_s is the peak of the stator current. Clearly Eqn. 3.37, consists of different space harmonics resulting from the winding function. However, for the fundamental, only the harmonic corresponding to the pole pair number ($\nu = p$) needs to be considered, given as

$$\mathscr{F}_{s1}(\theta_s) = \sum_{k=0}^{M-1} I_s \sin(\omega_s t - \frac{k-1}{M} 2p\pi) \frac{qN_s}{\pi} \frac{k_{q,p}}{p} \sin(p\theta_s - p\frac{k-1}{M} 2\pi) \tag{3.38}$$

Which can be simplified as below

$$\begin{aligned} \mathscr{F}_{s1}(\theta_e) &= \frac{qN_s I_s k_{q,p}}{p\pi} \sum_{k=0}^{M-1} \sin(\omega_s t - \tfrac{k-1}{M} 2p\pi) \sin(p\theta_s - \tfrac{k-1}{M} 2p\pi) \\ &= \frac{qN_s I_s k_{q,p}}{p\pi} \sum_{k=0}^{M-1} \tfrac{1}{2} \left[\cos(\omega_s t - p\theta_s) - \cos(\omega_s t + p\theta_s - \tfrac{k-1}{M} 4p\pi)\right] \end{aligned} \tag{3.39}$$

The second term under sum, converges to zero, giving the following

$$\mathscr{F}_{s1}(\theta_e) = \frac{qN_sI_sk_{q,p}}{p\pi}\frac{M}{2}\cos(\omega_s t - p\theta_s) \tag{3.40}$$

The phase belt q being defined as consecutive slots in series connection under one inverter leg, putting $Q_s = Mq$ in Eqn. 3.40 the following expression of the stator MMF is obtained as:

$$\mathscr{F}_{s1}(\theta_e) = \frac{Q_sN_sk_{q,p}}{2p\pi}I_s\cos(\omega_s t - p\theta_s) \tag{3.41}$$

Rotor MMF function A similar methodology can be developed to obtain the MMF function of the rotor. Hence the rotor MMF function can be defined as

$$\mathscr{F}_r(\theta_r) = \sum_{k=0}^{Q_r} i_{rk}\mathscr{N}_{rk}(\theta_{rk}) \tag{3.42}$$

where i_{rk} is the rotor current in k th bar, and Q_r is the total number of rotor bars. The winding function of a single bar has been already derived in Eqn. 3.35. The rotor current in the kth bar is given as

$$i_{rk} = I_r\sin(\omega_{sl}t - \frac{2p\pi}{Q_r}) \tag{3.43}$$

where I_r is the peak of the rotor current, ω_{sl} is the slip frequency, given as $\omega_{sl} = s\omega_s$ and s is the slip of the machine. Hence the fundamental rotor MMF, similar to stator winding function only the harmonic corresponding to the pole pair number ($\nu = p$) needs to be considered and is given as

$$\mathscr{F}_{r1}(\theta_r) = \sum_{k=0}^{Q_r} I_r\sin(\omega_{sl}t - \frac{2p\pi}{Q_r})\frac{1}{p\pi}\sin p(\theta_r - \frac{2\pi}{Q_r}) \tag{3.44}$$

which can be further simplified as below:

$$\begin{aligned}\mathscr{F}_{r1}(\theta_{re}) &= \frac{I_r}{p\pi}\sum_{k=0}^{Q_r}\sin(\omega_{sl}t - \tfrac{2p\pi}{Q_r})\sin(p\theta_r - \tfrac{2\pi p}{Q_r}) \\ &= \frac{I_r}{p\pi}\sum_{k=0}^{Q_r}\frac{1}{2}\left[\cos(\omega_{sl}t - p\theta_r) - \cos(\omega_{sl}t + p\theta_r - \tfrac{4p\pi}{Q_r})\right]\end{aligned} \tag{3.45}$$

The second term under sum converges to zero, hence the following can be obtained

$$\mathscr{F}_{r1}(\theta_{re}) = \frac{Q_r}{2p\pi}I_r\cos(\omega_{sl}t - p\theta_r) \tag{3.46}$$

Having obtained the winding function and MMF function for both stator and rotor the flux linkage quantities can be obtained.

3.2.4.3 Flux linkage

Flux linkage stator →stator (λ_{ss}) The stator to stator flux linkage or stator self flux linkage is defined as Eqn. 3.22 . Putting the expression from Eqn. 3.41 and 3.34 in Eqn. 3.21

$$\lambda_{ss} = \frac{\mu_0 rl}{g} \int_0^{\frac{\pi}{p}} \left\{ \frac{qN_s}{\pi} \sum_{\nu=1}^{\infty} \frac{1}{\nu} k_{q,\nu} \sin(\nu\theta_s) \right\} \left\{ \frac{Q_s N_s k_{q,p}}{2p\pi} I_s \cos(\omega_s t - p\theta_s) \right\} d\theta_s \tag{3.47}$$

Considering only the fundamental component ($\nu = p$) in the expression of winding function, and evaluating the integral the following is obtained:

$$\lambda_{ss} = \frac{\mu_0 rl}{g} \int_0^{\frac{\pi}{p}} \left\{ \frac{qN_s}{p\pi} k_{q,p} \sin(p\theta_s) \right\} \left\{ \frac{Q_s N_s k_{q,p}}{2p\pi} I_s \cos(\omega_s t - p\theta_s) \right\} d\theta_s \tag{3.48}$$

As the winding function and MMF functions are a function of $p\theta_s$, which is the electrical angle θ_e, hence the limits from Eqn 3.21 are used. Hence the flux linkage λ_{ss} can be further simplified as

$$\begin{aligned} \lambda_{ss} &= \frac{\mu_0 rl}{g} \frac{Q_s N_s^2 k_{q,p}^2}{2p^2\pi} \frac{q}{\pi} I_s \int_0^{\pi} \{\sin(\theta_e)\} \{\cos(\omega_s t - \theta_e)\} d\theta_s \\ &= \frac{\mu_0 rl}{g} \frac{Q_s N_s^2 k_{q,p}^2}{2p^2\pi} \frac{q}{\pi} \frac{I_s}{2} \int_0^{\pi} \{\sin(\omega_s t) + \sin(2\theta_e - \omega_s t)\} d\theta_s \\ &= \frac{\mu_0 rl}{g} \frac{Q_s N_s^2 k_{q,p}^2}{2p^2\pi} \frac{q}{\pi} \frac{\pi}{2} I_s \sin(\omega_s t) \\ &= \frac{\mu_0 Dl}{g} \frac{Q_s N_s^2 k_{q,p}^2}{2p^2\pi} \frac{q}{4} I_s \sin(\omega_s t) \end{aligned} \tag{3.49}$$

where D is the diameter of the machine at air-gap, given as $D = 2r$. The stator phase current being $I_s \sin(\omega_s t)$, the self inductance of stator L_{ss} is given as

$$L_{ss} = \frac{\mu_0 Dl}{g} \frac{Q_s N_s^2 k_{q,p}^2}{\pi} \frac{q}{8p^2} \tag{3.50}$$

Flux linkage rotor →rotor (λ_{rr}) Similar methodology can be used to find the rotor self flux linkage (λ_{rr}) and self inductance (L_{rr}). Putting the expression from Eqn. 3.46 and 3.35

in Eqn. 3.24

$$\lambda_{rr} = \frac{\mu_0 rl}{g} \int_0^{\frac{\pi}{p}} \left\{ \frac{1}{\pi} \sum_{\nu=1}^{\infty} \frac{1}{\nu} \sin(\nu\theta_r) \right\} \left\{ \frac{Q_r}{2p\pi} I_r \cos(\omega_{sl}t - p\theta_r) \right\} d\theta_r \tag{3.51}$$

Considering only the fundamental component in the expression of winding function, ($\nu = p$) the following is obtained:

$$\lambda_{rr} = \frac{\mu_0 rl}{p^2 g} \int_0^{\frac{\pi}{p}} \left\{ \frac{1}{\pi} \sin(p\theta_r) \right\} \left\{ \frac{Q_r}{2\pi} I_r \cos(\omega_{sl}t - p\theta_r) \right\} d\theta_r \tag{3.52}$$

Similar to stator flux linkage derivation changing the limits to $0 - \pi$, for the variable $\theta_{re} = p\theta_r$, the above expression can be further simplified as

$$\begin{aligned} \lambda_{rr} &= \frac{\mu_0 rl}{g} \frac{Q_r}{2p^2\pi} \frac{I_r}{\pi} \int_0^{\pi} \{\sin(\theta_{re})\} \{\cos(\omega_{sl}t - \theta_{re})\} d\theta_r \\ &= \frac{\mu_0 rl}{g} \frac{Q_r}{2p^2\pi} \frac{I_r}{2\pi} \int_0^{\pi} \{\sin(\omega_{sl}t) + \sin(\omega_{sl}t - 2\theta_{re})\} d\theta_r \\ &= \frac{\mu_0 rl}{g} \frac{Q_r}{2p^2\pi} \frac{I_r \pi}{2\pi} \sin(\omega_{sl}t) \\ &= \frac{\mu_0 Dl}{g} \frac{Q_r}{8p^2\pi} I_r \sin(\omega_{sl}t) \end{aligned} \tag{3.53}$$

The rotor bar current being $I_r \sin(\omega_{sl}t)$, the self inductance of stator L_{rr} is given as

$$L_{rr} = \frac{\mu_0 Dl}{g} \frac{Q_r}{8\pi p^2} \tag{3.54}$$

It has been shown before, conceptually the rotor can be modelled similar to the stator, with single turn and phase belt q=1, and a total number of Q_r slots. Hence the same expression of L_{rr} can be alternatively obtained directly from Eqn. 3.50, by setting $q = 1$, $N_s = 1$, and $k_{q,p} = 1$ and $Q_S = Q_r$.

Flux linkage rotor →stator (λ_{sr}) For calculating the mutual flux linkages, the transformation from the stator reference to the rotor reference frame needs to be established. Under steady sate operation, the stator and rotor coordinates are related as

$$\theta_s = \omega_r t + \theta_r \tag{3.55}$$

where ω_r is the rotor mechanical speed. Eqn. 3.55 along with Eqn. A.1, A.3 can be used to transform the rotor MMF function to stator co-ordinate and vice versa as below:

$$(\omega_{sl}t - p\theta_r) = (s\omega_s t - p\theta_r) = (\omega_s t - \omega_{re}t - p\theta_r) = (\omega_s t - p\omega_r t - p\theta_r) = (\omega_s t - p\theta_s) \tag{3.56}$$

Putting the expression from Eqn. 3.46 and 3.34 in Eqn. 3.25

$$\lambda_{sr} = \frac{\mu_0 rl}{g} \int_0^{\pi/p} \left\{ \frac{qN_s}{\pi} \sum_{\nu=1}^{\infty} \frac{1}{\nu} k_{q,\nu} \sin \nu\theta_s \right\} \left\{ \frac{Q_r}{2p\pi} I_r \cos(\omega_{sl}t - p\theta_r) \right\} d\theta_s \tag{3.57}$$

Considering the fundamental harmonic only ($\nu = p$), and transforming rotor to stator co-ordinate from Eqn. 3.56

$$\lambda_{sr} = \frac{\mu_0 rl}{g} \int_0^{\pi/p} \left\{ \frac{qN_s}{p\pi} k_{q,p} \sin p\theta_s \right\} \left\{ \frac{Q_r}{2p\pi} I_r \cos(\omega_s t - p\theta_s) \right\} d\theta_s \tag{3.58}$$

Changing the limit of integration to $0 - \pi$, for the variable $p\theta_s = \theta_e$, this can be simplified as

$$\begin{aligned} \lambda_{sr} &= \frac{\mu_0 rl}{g} \frac{qN_s}{\pi p^2} \frac{Q_r k_{q,p}}{2\pi} I_r \int_0^{\pi} \{\sin\theta_e\} \{\cos(\omega_s t - \theta_e)\} d\theta_s \\ &= \frac{\mu_0 rl}{g} \frac{qN_s}{\pi p^2} \frac{Q_r k_{q,p}}{2\pi} \frac{I_r}{2} \int_0^{\pi} \{\sin(\omega_s t) + \sin(2\theta_s - \omega_s t)\} d\theta_s \\ &= \frac{\mu_0 rl}{g} \frac{qN_s}{\pi p^2} \frac{Q_r k_{q,p}}{2\pi} \frac{I_r \pi}{2} \sin(\omega_s t) \\ &= \frac{\mu_0 rl}{g} \frac{qN_s}{\pi p^2} \frac{Q_r k_{q,p}}{8} I_r \sin(\omega_s t) \end{aligned} \tag{3.59}$$

Hence the mutual inductance between stator and rotor phases L_{sr} is defined as

$$\begin{aligned} L_{sr} &= \frac{\lambda_{rs}}{I_r \sin(\omega_s t)} \\ &= \frac{\mu_0 Dl}{g} \frac{Q_r k_{q,p} N_s}{\pi} \frac{q}{8p^2} \end{aligned} \tag{3.60}$$

Flux linkage stator $\rightarrow$rotor (λ_{rs}) Following similar methodology as before, putting the expression from Eqn. 3.41 and 3.35 in Eqn. 3.23

$$\lambda_{rs} = \frac{\mu_0 rl}{g} \int_0^{\pi/p} \left\{ \frac{1}{\pi} \sum_{\nu=1}^{\infty} \frac{1}{\nu} \sin(\nu\theta_r) \right\} \left\{ \frac{Q_s N_s k_{q,p}}{2p\pi} I_s \cos(\omega_s t - p\theta_s) \right\} d\theta_r \tag{3.61}$$

Considering the fundamental harmonic only $\nu = p$, and transforming rotor to stator coordinate from Eqn. 3.56

$$\lambda_{rs} = \frac{\mu_0 rl}{g} \int_0^{\pi/p} \left\{ \frac{1}{p\pi} \sin(p\theta_r) \right\} \left\{ \frac{Q_s N_s k_{q,1}}{2p\pi} I_s \cos(\omega_{sl} t - p\theta_r) \right\} d\theta_r \tag{3.62}$$

Changing the limit of integration to $0 - \pi$, for the variable $p\theta_r = \theta_{re}$, this can be simplified as

$$\begin{aligned} \lambda_{rs} &= \frac{\mu_0 rl}{g} \frac{1}{\pi} \frac{Q_s N_s k_{q,p}}{2p^2\pi} I_s \int_0^{\pi} \{\sin(\theta_{re})\} \{\cos(\omega_{sl} t - \theta_{re})\} d\theta_r \\ &= \frac{\mu_0 rl}{g} \frac{1}{\pi} \frac{Q_s N_s k_{q,p}}{2p^2\pi} \frac{I_s}{2} \int_0^{\pi} \{\sin(\omega_{sl} t) + \sin(\omega_{sl} t - 2\theta_r)\} d\theta_r \\ &= \frac{\mu_0 rl}{g} \frac{1}{\pi} \frac{Q_s N_s k_{q,1}}{2p^2\pi} \frac{\pi}{2} I_s \sin(\omega_{sl} t) \\ &= \frac{\mu_0 Dl}{g} \frac{Q_s N_s k_{q,p}}{8p^2\pi} I_s \sin(\omega_{sl} t) \end{aligned} \tag{3.63}$$

Hence the stator to rotor mutual inductance is given as

$$L_{rs} = \frac{\mu_0 Dl}{g} \frac{Q_s N_s k_{q,p}}{\pi} \frac{1}{8p^2} \tag{3.64}$$

3.2.4.4 Equivalent turns ratio

As it has been discussed earlier, the stator and rotor terms are represented in their respective per phase model, an equivalent turn ratio needs to be derived, to obtain the single per phase model as shown in Fig. 2.1 referred to the stator.

The stator flux, given in Eqn. 3.18 can be obtained by using the expressions of L_{ss} and L_{sr} obtained from Eqn. 3.50 and 3.60 as below

$$\lambda_s = L_{ls} I_s + \mathscr{P}_m \frac{Q_s N_s^2 k_{q,p}^2 q}{8p^2\pi} I_s + \mathscr{P}_m \frac{Q_r k_{q,p} N_s q}{8p^2\pi} I_r \tag{3.65}$$

This can be restructured as

$$\lambda_s = L_{ls} I_s + L_m (I_s + I_r^{'}) \tag{3.66}$$

Where $\mathscr{P}_m$ is defined as $\frac{\mu_0 Dl}{g}$, and $k_1$is defined as $\frac{L_{sr}}{L_m}$, given in Eqn. 3.67. The mutual inductance L_m is same as stator self inductance L_{ss}, as the equivalent circuit refers to stator.

$$k_1 = \frac{L_{sr}}{L_{ms}} = \frac{Q_r}{Q_s N_s k_{q,p}} \tag{3.67}$$

Further, Using $I_r^{'}$ in Eqn. 3.19

$$\lambda_r = \frac{L_{lr}I_r^{'}}{k_1} + \frac{L_{rr}}{k_1}I_r^{'} + L_m(\frac{L_{rs}}{L_{ss}})I_s \tag{3.68}$$

Using the expression of L_{ss}, L_{sr} L_{rs} and L_{rr} from Eqn. 3.50, 3.60, 3.64 and 3.54 respectively, along with k_1 from Eqn. 3.67 it can be shown

$$\begin{aligned} \lambda_r &= \frac{L_{lr}I_r^{'}}{k_1} + \frac{\mathscr{P}_m Q_s N_s k_{q,p}}{8\pi p^2}I_r^{'} + \frac{\mathscr{P}_m Q_s N_s k_{q,p}}{8\pi p^2}I_s \\ &= \frac{L_{lr}I_r^{'}}{k_1} + \frac{\mathscr{P}_m Q_s N_s k_{q,p}}{8\pi p^2}(I_r^{'} + I_s) \end{aligned} \tag{3.69}$$

This can be restructured to match the same mutual inductance L_m (in Eqn. 3.66) as below

$$k_2\lambda_r = \frac{k_2}{k_1}L_{lr}I_r^{'} + L_m(I_r^{'} + I_s) \tag{3.70}$$

where k_2 is defined as

$$\begin{aligned} k_2 &= \frac{\mathscr{P}_m Q_s N_s k_{q,p}}{8\pi p^2 L_m} \\ &= N_s k_{q,p} q \end{aligned} \tag{3.71}$$

Eqn. 3.70 gives the effective turn ratio for rotor to stator transformation as below

$$\begin{aligned} k_{rs} &= \frac{k_2}{k_1} \\ &= \frac{Q_s N_s^2 k_{q,p}^2 q}{Q_r} \end{aligned} \tag{3.72}$$

Hence the rotor leakage inductance and resistance referred to stator is given as below:

$$L_{lr}^{'} = k_{rs}L_{lr} \tag{3.73}$$

and

$$R_r^{'} = k_{rs}R_r \tag{3.74}$$

This completes the analytical derivation of the equivalent circuit elements (as shown in Fig. 2.1). As noted earlier, the quantities are obtained for a per leg model rather conventional per phase model as depending on the pole number the phase numbers change.

3.3 Finite Element Validation

In the previous section analytical expressions for all five parameters of per inverter leg circuit, as shown in Fig. 2.1 have been derived. However, due to the complexity of the derivation, it is also necessary to check the validity of the expressions obtained. In this section, a finite element method based simulation study has been performed to evaluate the same parameters numerically, which is then compared to the values obtained from these analytical expressions.

3.3.1 Finite Element Package

To implement finite element simulation, a two-dimensional finite element software FEMM [77] has been used. The software allows defining the geometry of the system, and material property of different parts of the problem along with boundary conditions. Further, the electrical circuit connection (series or parallel) can be defined, to set up excitation. The electrical current can be defined as an a.c. quantity (phasor representation for different phases) along with the frequency of the problem.

To study the proposed PPMIM, current at different stator slot is defined, with different phase belt current as given in Eqn 3.4. The software calculates induced rotor current in each of the rotor bars. The boundary condition is set as Coulomb gauge $\overrightarrow{A} = 0$ (being a low frequency electromagnetic problem, the wavelength is much longer than the machine dimensions) at double of the stator outer radius to include the outer toroidal return paths of the stator winding and enough outer air space. $\overrightarrow{A}$ denotes the magnetic vector potential given as below

$$\overrightarrow{B} = \nabla \times \overrightarrow{A} \tag{3.75}$$

and $\overrightarrow{B}$ is the flux density. The FEA package yields flux density, current density and magnetic vector potential over the geometry. It also gives a direct output for circuit properties, such as voltage drop, resistive loss, and flux linkage. The package further allows using the non-linear $B-H$ curve to model saturation in the magnetic material.

3.3.2 Circuit Parameters from FEA

As the modelled machine is a cage rotor IM the analysis is performed [78], using the above mentioned FEA package. The package allows only mechanically static configurations, hence the rotor speed cannot be modelled directly. Rather the system can be excited

through slip frequency, as in zero speed case, slip frequency equates to the excitation frequency. The steps for obtaining equivalent circuit parameters are shown below:

1. The machine is excited with balanced 1A (RMS) current in all phases (with the phase angles from Eqn.3.4) at a frequency ω.

2. The stator loss has been extracted from FEA.

3. Using stator current information, and total stator loss (by integrating power loss over all stator coils), stator resistance (R_s) is obtained as below

$$P_{sloss} = M|I_s|^2 R_s \tag{3.76}$$

4. Stator phase voltage has been obtained from the FEA result. Neglecting the core loss component, the stator voltage V_s is related to equivalent circuit parameters (shown in Fig. 2.1) as below:

$$V_s = I_s(R_s + j\omega L_s + \frac{j\omega L_m(\frac{R_r^{'}}{s} + j\omega L_r^{'})}{\frac{R_r^{'}}{s} + j\omega(L_m + L_r^{'})}) \tag{3.77}$$

5. It should be noted for a zero speed case, the slip s becomes 1, hence Eqn. 3.77 can be rewritten as below:

$$V_s = I_s(R_s + j\omega L_s + \frac{j\omega L_m(R_r^{'} + j\omega L_r^{'})}{R_r^{'} + j\omega(L_m + L_r^{'})}) \tag{3.78}$$

   As the injected current is $1\angle 0$ for the first phase, the induced voltage itself is the impedance Z. Although R_s can be obtained from Eqn. 3.76, 4 unknowns need to be found from Eqn. 3.77. However, solving the equation for real and imaginary parts separately will only result in two equations. Hence the simulation has been performed at two frequencies ω_1 and ω_2, giving net 4 equations, from which the circuit parameters can be obtained. The derivation of the circuit parameters is shown in the Appendix B.

It should be noted, this methodology of extraction of circuit parameters from the FEA simulation will enable to study the variation of the circuit parameters with frequency, by solving at different sets of (ω_1, ω_2), where ω_1 and ω_2 are relatively close to each other.

3.4 Results

The previous sections establish the analytical expressions of the equivalent circuit parameters and methodology to obtain the same from FEA of the proposed independent phase belt controlled PPMIM. However, for comparison of the numerical results with the analytical results, it is necessary to have actual machine details to work with. The machine details used for these results are given in 3.2. It is the same machine which has been fabricated for experimental verification of the proposed concept, which is discussed in detail in chapter 4 and 5.

Table 3.2: Details of the machine used for FEM and analytical study of PPMIM

Dimension	Value(in mm)
Stator Outer Dia	203.5
Stator Inner Dia	114.1
Rotor Outer Dia	113.3
Stator Slot Number	36
Rotor Slot Number	28
Stator Slot width (air gap side)	4.95
Stator Slot width (yoke side)	7.92
Stator Slot Depth	17.5
Rotor Slot width (air gap side)	5.15
Rotor Slot width (shaft side)	3.0
Rotor Slot Depth	11.15
Length of the machine	130

3.4.1 FEA Results

The machine described in Table 3.2, has been studied under 5 different pole -phase configuration as discussed in Table. 3.1. The flux density plots, with contours of A, are shown in the Figs. 3.8, 3.9, 3.10 3.11 and 3.12 for 2,4,6,8 and 10 pole configurations respectively. As the used FEM package can only handle static models, hence the rotor speed cannot be directly modelled. Hence for the FEM analysis, excitation frequency is kept at 1.5 Hz, which equates to 3% slip, considering 50Hz supply frequency. Exciting the system at slip frequency, in the static model is equivalent to analysing the system at rotor frame of reference.

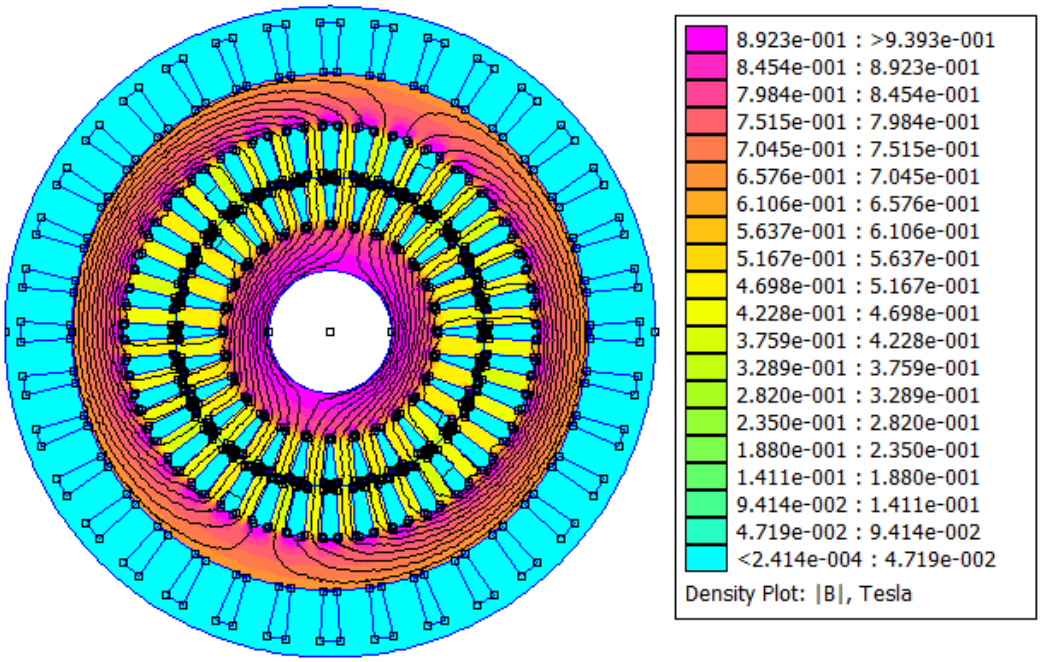

Figure 3.8: FEM result for 2 pole 6 phase configuration

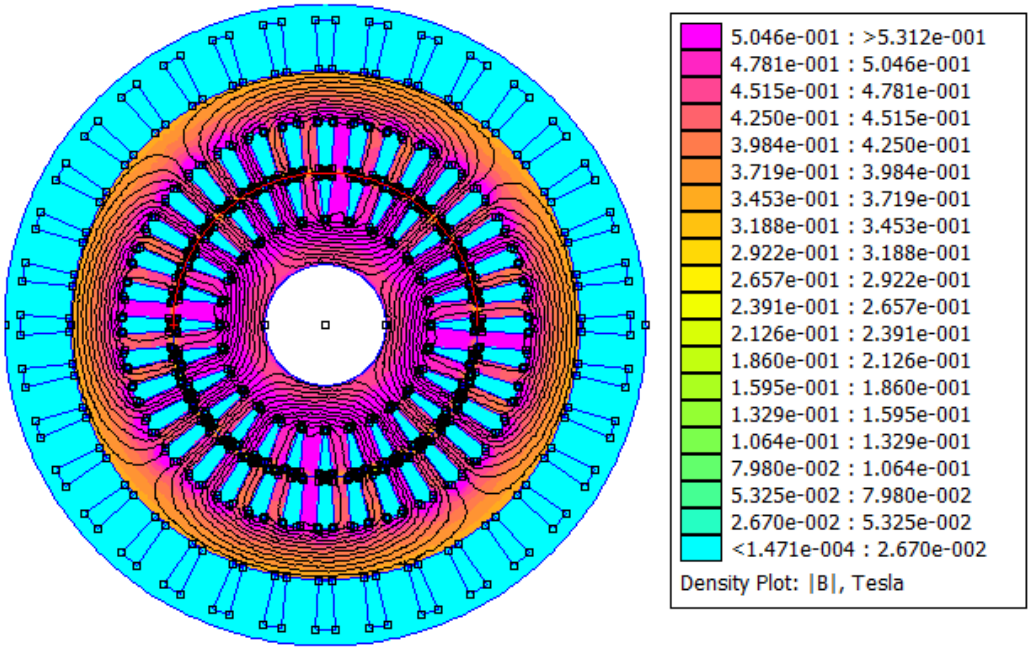

Figure 3.9: FEM result for 4 pole 3 phase configuration

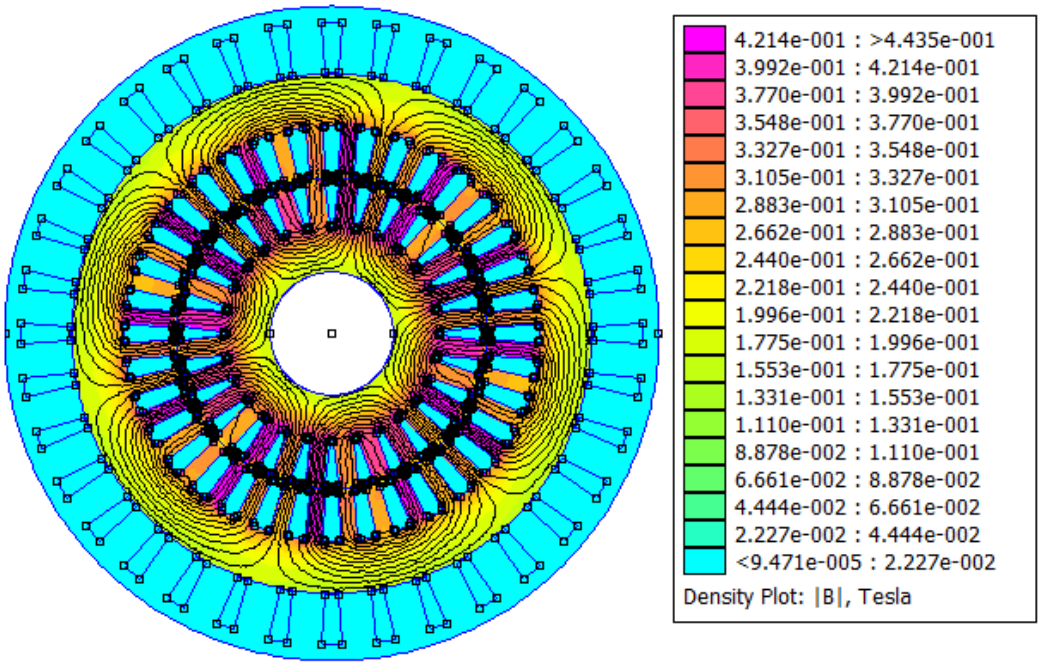

Figure 3.10: FEM result for 6 pole 2 phase configuration

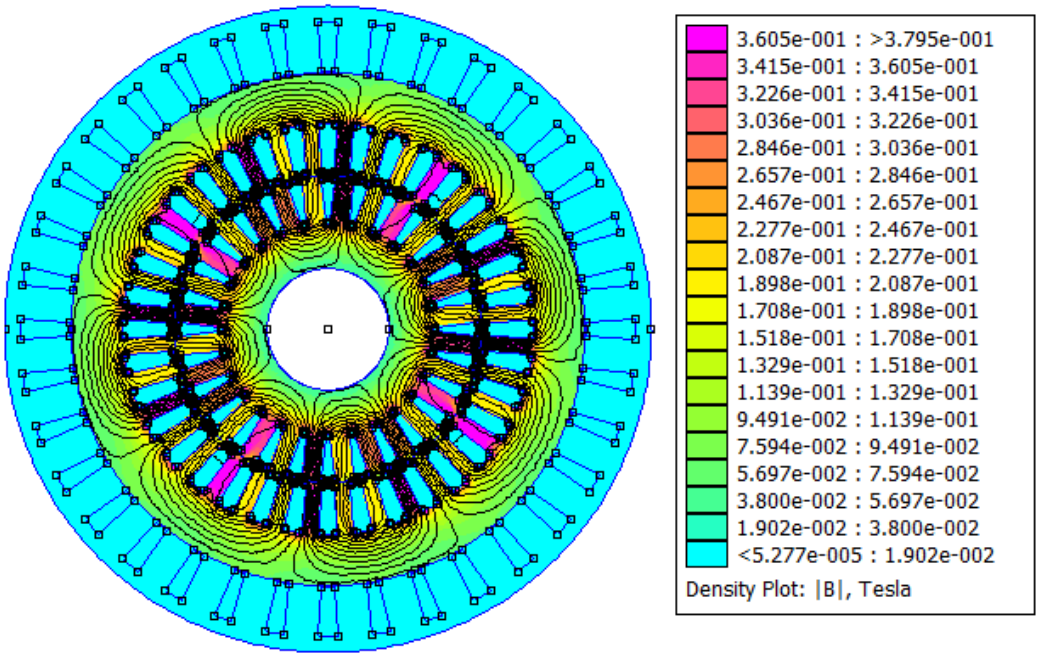

Figure 3.11: FEM result for 8 pole configuration

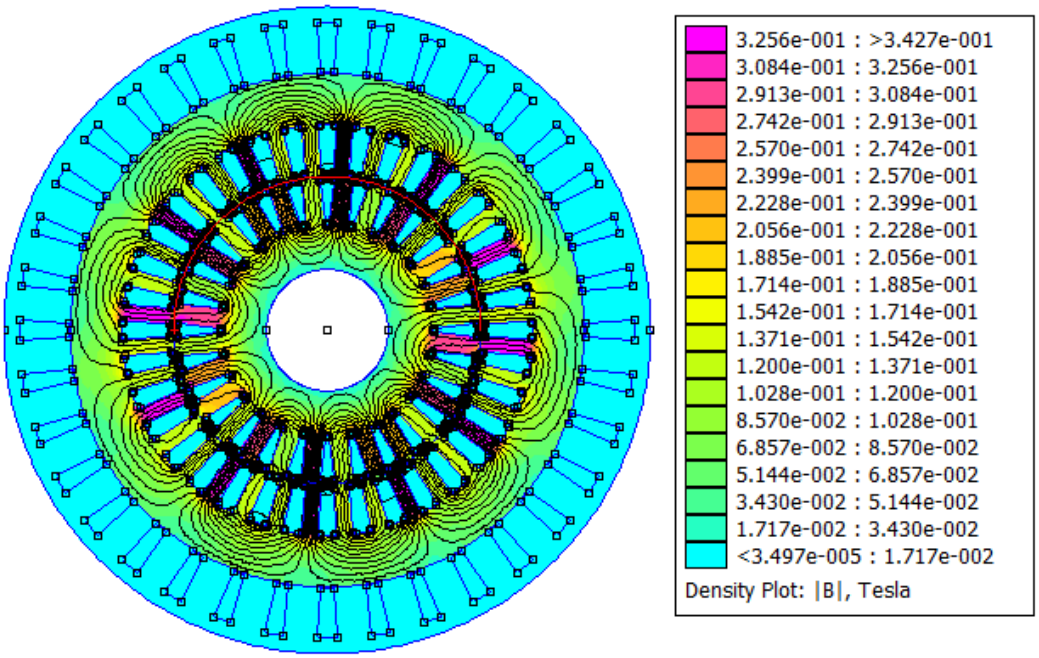

Figure 3.12: FEM result for 10 pole configuration

3.4.2 Circuit parameters

Following the method discussed under previous sub-section and derivation shown in Appendix A, the machine parameters are calculated from the FEA. Also using the analytical expressions developed in the previous section, the same parameters have been calculated. Both the results have been tabulated in Table.3.3 , for comparison. As the FEM simulation is done in two dimensions the end ring terms in the analytical result are neglected to emulate a similar condition. Initially it was found the analytical leakage terms are not matching well with the FEM results. A detailed investigation revealed this is due to the fact the analytical model does not include harmonic self inductance leakage terms [6, pp:66-78] for the stator. As the stator is modelled similar to the cage rotor of an IM here, following the methodology reported for the cage rotor in [6] the dominant harmonics can be found to be $M \pm p$ for the stator model, where M is the net number of inverter legs. The harmonics leakage term becomes important especially for the higher pole count. Including these harmonics along with the slot leakage terms gives a better estimate as shown in Table 3.3.

The difference in the result for these two methods is presented in Table 3.4, as a percentage of the analytical result. However, Table. 3.3 and Table 3.4 shows that the results obtained from FEM analysis are closely matching with analytical results, which proves the validity of the expressions obtained. It can be noted, as for FEM the leakage term was

Table 3.3: Equivalent circuit parameters from FEM and analytical method

Pole No.	Method	R_s (in $m\Omega$)	$R_r^{'}$ (in $m\Omega$)	L_s(in mH)	$L_r^{'}$ (in mH)	L_m (in mH)
2	FEM	89.8	214.2	1.4		137.5
	Analytical	89.8	215.1	1.6	0.3	123.3
4	FEM	89.8	201.0	1.2		34.4
	Analytical	89.8	199.6	1.7	0.3	30.8
6	FEM	89.8	178.1	1.4		13.9
	Analytical	89.8	180.0	1.7	0.6	13.7
8	FEM	89.8	152.2	1.0		7.2
	Analytical	89.8	153.2	1.8	0.3	7.7
10	FEM	89.8	111.3	1.3		4.4
	Analytical	89.8	115.2	1.8	0.8	4.9

Table 3.4: Percentage difference in equivalent circuit parameters from FEM and analytical method

Pole No.	R_s	$R_r^{'}$	L_m
2	0	0.41	11.5
4	0	0.72	11.7
6	0	1.07	1.1
8	0	0.65	6.6
10	0	3.35	10.9

derived assuming stator and rotor leakage to be the same.

3.4.3 Torque-speed characteristics

The circuit parameters obtained from the FEA and analytical model have been further used to find the torque-speed characteristics of the machine. For initial studies, it is assumed all the 12 phase belts are connected in star fashion, and excited by the 12 phase inverter from a 48V DC bus. For a balanced excitation, with l_n phases star connected, the phase voltage is given as

$$v_{ph} = \frac{v_{dc}}{2\sqrt{2}} \tag{3.79}$$

Hence for the given case phase voltage v_{ph} becomes 16.9 V. The torque-speed characteristics of the machine from the both FEA and analytical model are shown in Fig. 3.13. As the FEM simulation was done at particular slip frequencies, the corresponding torque and speed data points are also plotted in Fig. 3.13. It can be noted, that as expected from the good match of the circuit parameters from Table. 3.3, the torque-speed characteristics of the machine from both FEA and analytical model match closely. Although, there is slight mismatch of the FEM and analytical T-S characteristics, due to mismatch of the circuit parameters between FEA and analytical model, the T-S data points obtained for the steep part of the characteristics - where the machine operates nominally, matches very well. This close match ensures validity of the derived analytical expression of the circuit parameters. This can be attributed to the fact that, the analytical model considers flux created by the fundamental frequency only. This assumption match well with the FEM simulation under slip close to zero, as the FEM simulates the machine at slip frequency. However, when the slip frequency increases the flux distribution in the machine changes - leading to larger leakage. The torque-speed characteristics along with circuit parameters of the machine will be validated experimentally in the next chapters.

It can be noted, as the magnetising inductance is inversely proportional to the square of pole pair number, the magnetising inductance of the 10 pole configuration becomes similar to the leakage inductance, thus causing a drop in the peak torque. Fig. 3.13 shows peak torque available from the 10 pole configuration is lower than that obtained from 8 pole configuration. Hence for a practical operation, this configuration of this machine will not be used.

The efficiency of the machine under different pole configuration is shown in Fig. 3.14. It can be observed except, 10 pole configuration the efficiency is more than 80% in the practical operating range of slip. Furthermore, the efficiency drops with the increase of the pole number, which is due to the decreasing magnetising inductance. In higher pole number larger magnetising current is drawn, leading to poor power factor, higher phase current and lower efficiency. However, it should be noted, for the target application of starter alternator, the machine will operate in high pole count configuration for only short duration of time during starting.

Furthermore, conventional VVVF control can be applied along with PPMIM, as for VVVF the modulation depth (m) and frequency(f) of the inverter is changed, and for PPM the phase angle between the inverter legs (ϕ) is changed. The net torque-speed operating envelope of the developed machine under VVVF control is shown in Fig 3.15a. To demonstrate the enhanced capability of PPMIM to achieve wider torque-speed operating zone, the

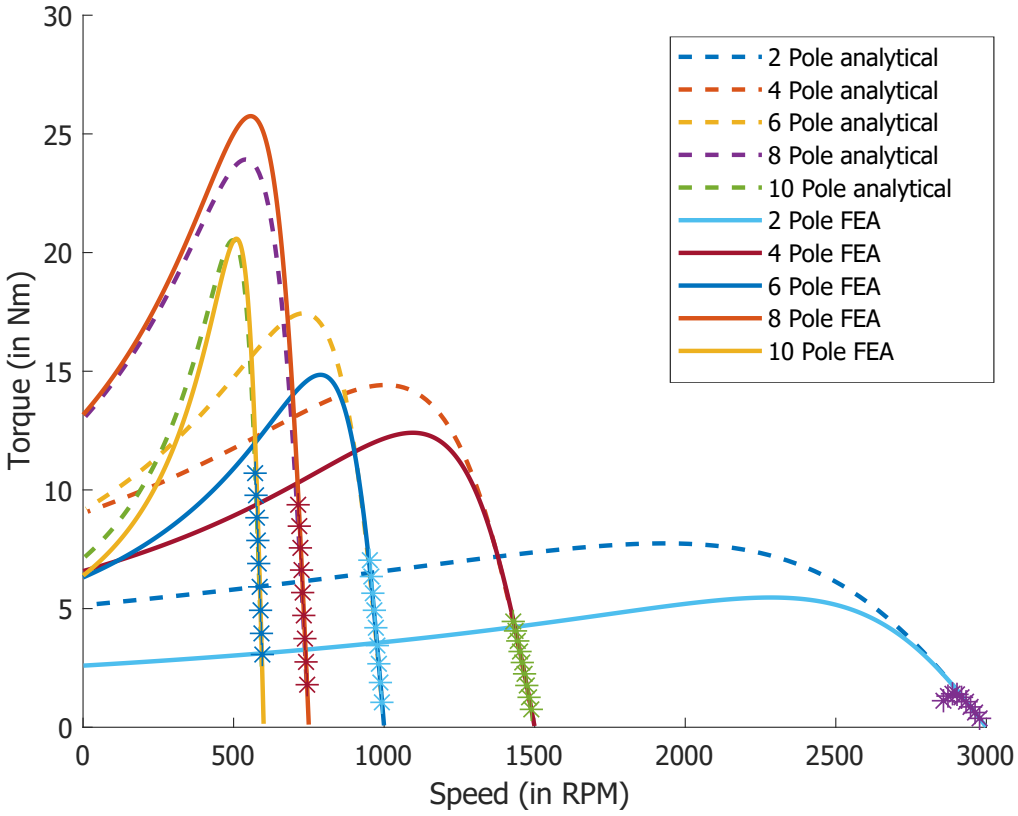

Figure 3.13: Torque - speed characteristics of the machine under different pole configurations from analytical and FEA circuit parameters. The * points on the curves denote the simulated points in the FEA.

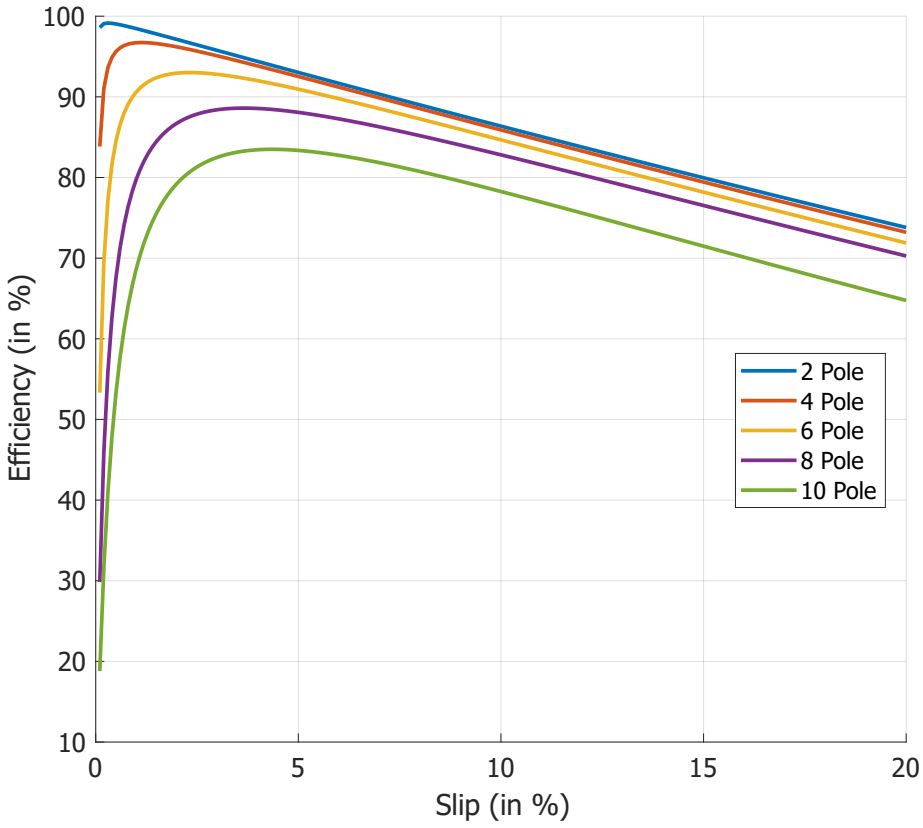

Figure 3.14: Efficiency of the machine under different pole configurations

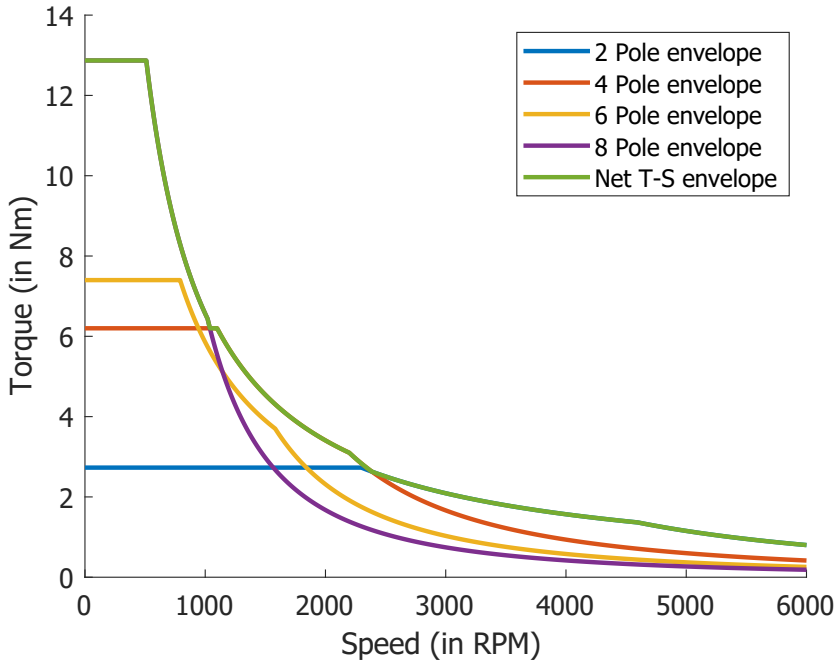

(a) T-S envelope of the PPMIM under VVVF

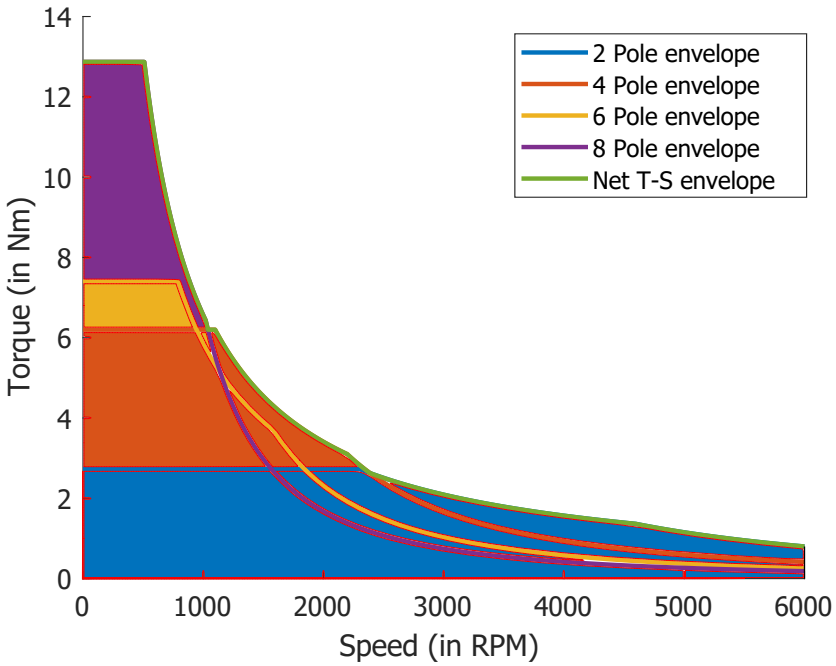

(b) T-S operating zones under different pole configuration

Figure 3.15: Torque - speed operation envelope of the PPMIM

developed machine has been compared against a conventional IM. As an example case of the torque-speed operating zone under VVVF of a conventional machine, the 6 pole configuration can be noted in Fig 3.15a. For both the PPMIM and conventional machine the rated torque has been taken as half of the peak torque. From the torque-speed envelope of the PPMIM and conventional machine, it can be seen that there is an improvement in the starting torque (due to the 8 pole configuration). Further the available torque at high speed is also increased due to reconfiguration into 2 pole. As shown in Fig. 2.5, for the 6 pole machine the rated torque at flux weakening zone is limited by the peak torque available, which is inversely proportional to the square of speed. Moreover, under the T-S operation envelope of the PPMIM different zones has been shown for different pole configurations in Fig. 3.15b. As the phase current remains low for lower pole count, the lowest pole count necessary to achieve the needed torque has been used, to keep the stator loss minimum.

It can be noted a significant zone of the achieved T-S envelope can be also achieved by only using 8 and 4 pole operation. The net T-S envelope achieved by VVVF operation of 4 pole, 8 pole configuration and combination of both are shown in Fig. 3.16a. This zone has been compared against the T-S zone achieved originally under all 4 possible configuration (shown in Fig. 3.15b) in Fig. 3.16b. The zone coloured in red in Fig. 3.16b denotes the compromised T-S zone for this restricted operation. Previously this zone was catered by 2 pole operation, where as under 4/8 pole operation this has to be catered by the flux weakening of 4 pole operation. As mentioned earlier due to the limitation of the peak torque available in extended flux weakening region (Fig. 2.5) the torque available from flux weakening of 4 pole operation is lower than that available from the 2 pole operation.

However, if this reduced T-S zone is acceptable for the load, this allows reduction of inverter legs by 50%, as 4 pole and 8 pole operation can be achieved by a 6 phase inverter. The phase belt diagram of 4 pole and 8 pole operation is shown in Fig. 3.17a. In this figure, phase a, b and c are 3 phases with phase difference of 120^o and a', b' and c' are 180^o phase-shifted from a, b and c respectively. It can be observed, phase-bands which are 180^o shifted in space are excited by same phase in both cases of 8 pole and 4 pole operation. Hence a 6 phase inverter will be sufficient to achieve these two pole configurations. This can be achieved by either series or parallel connection of the phase-bands which carry same phase. The wiring diagram for parallel and series connection has been shown in Fig. 3.17b and Fig. 3.17c respectively. Although this modified arrangement scheme proposes a PPMIM with two configurations only, like previous literatures, the 8 pole scheme of this 4/8 pole operation is achieved by application of the independent phase belt control which has not been reported earlier.

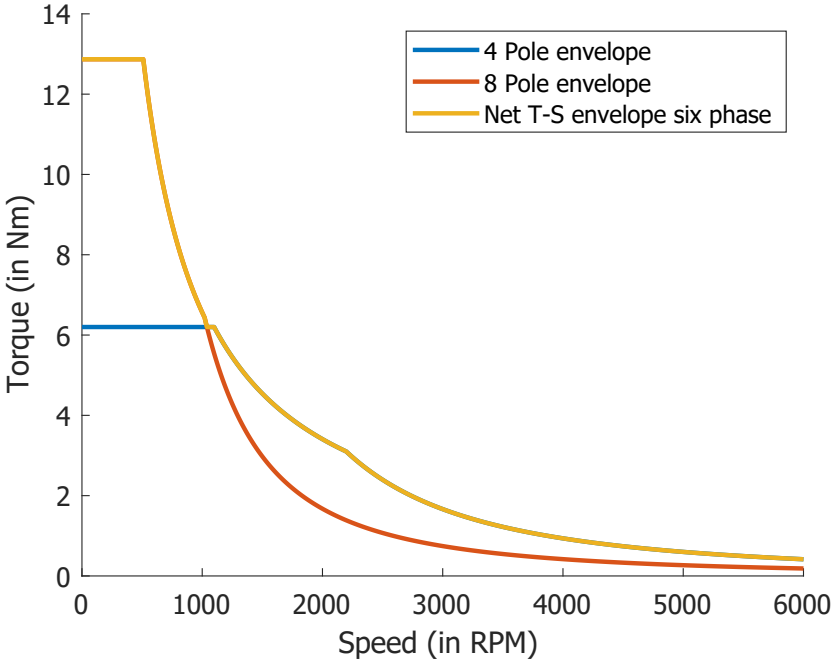

(a) T-S envelope of the PPMIM under VVVF with 4 pole and 8 pole operation

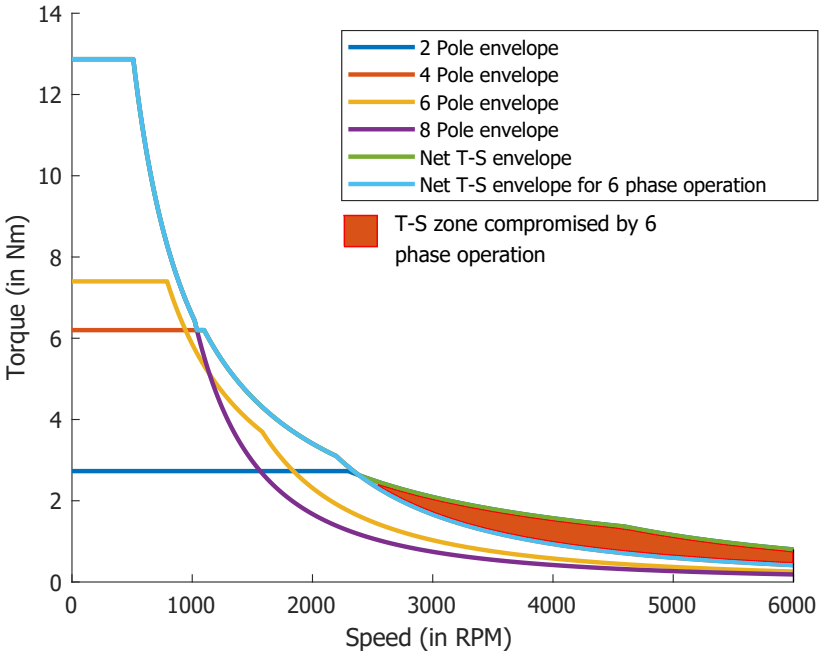

(b) Comparison of T-S zone by 6 phase and 12 phase operation

Figure 3.16: Torque - speed operation envelope of the PPMIM under 6 phase operation - 4 pole and 8 pole

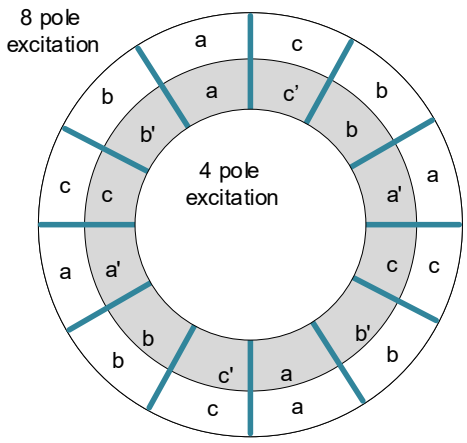

(a) Phase-band diagram of 4 pole and 8 pole operation

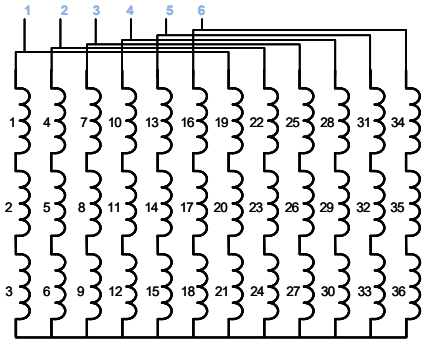

(b) Wiring diagram of the machine with parallel connection with 6 phase inverter for 4/8 pole operation

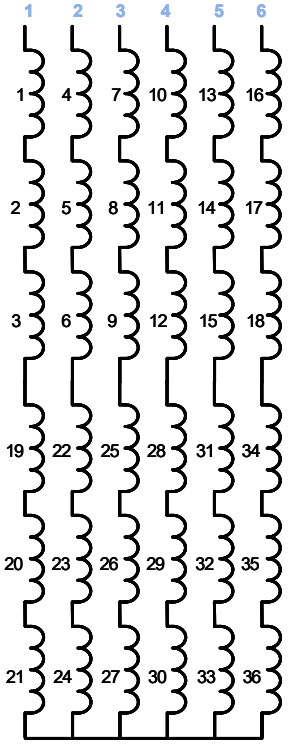

(c) Wiring diagram of the machine with series connection with 6 phase inverter for 4/8 pole operation

Figure 3.17: Torque - speed operation envelope of the PPMIM under 6 phase operation - 4 pole and 8 pole

3.5 Conclusions

The independent phase belt controlled PPMIM has been discussed in this chapter. The concept has been validated by both analytical and FEA. Although previously reported coil model (a winding with return) works for the pole configurations with direct return - 2,4, and 6 pole configuration - where some of the phase belt current is exactly out of phase (180^o phase shifted), the model cannot explain the 8 pole and 10 pole configurations where the phase angle difference between two phase belts is not a submultiple of π, which has not been investigated before. Hence a novel analytical model has been developed which accurately models independent stator slots for the toroidally wound machine, unlike previously reported winding with the return.

The analytical model matches closely with the FEA. The accuracy of the model is certainly limited by the several simplifying assumptions made in the course of the derivation. However, the closed-form expressions of the circuit parameters enable quick evaluation of the machine characteristics without needing a computationally heavy FEA. These closed-form expressions of the circuit parameters are useful particularly for design optimisation for a given design space. For a given machine dimensions, voltage, current and desired torque-speed envelope many different machine configurations are needed to be examined in order to optimise the design.

The proposed PPPMIM achieves a wider T-S operating envelope not only compared to a conventional VVVF controlled conventional machine but also from previously reported PPMIM. In [63] a 9 phase inverter has been used for 2/6 pole PPMIM. For a similar sized machine, the proposed methodology of independent phase belt controlled PPMIM increases the peak torque by 60% with the expense of 3 more inverter legs (33% increase). Further, it has been shown if a lower torque is acceptable at higher speed, the proposed machine can be achieved by a 6 phase inverter, restricting the operation in 8 pole and 4 pole only. This restricted operation still allows the same starting torque, but lowers the torque available at higher speed. The proposed concept has been verified experimentally as well. The experimental results of the discussed machine has been reported in the next chapter along with the details of the circulating power test-bench.

Chapter 4

Experimental Set up Development

The previous chapters discussed the theory of operation of the independent phase belt controlled PPMIM. To validate the proposed concept an experimental set up has been built including the poly-phase inverter and toroidally wound machine. Details of the machine winding design along with fabrication of the prototype machine have been reported in this chapter. This chapter also reports the hardware details of the poly-phase inverter design. Further the bus-bar design for low voltage high current inverter, DC bus capacitor selection, isolated gate-driver design for MOSFETs has been reported. To test the machine under load on both motor and generator operation, a circulating power test bed is developed by coupling another off the shelf 3 phase induction motor, driven by a commercially available 48 V inverter.

The independent phase belt controlled PPMIM discussed in the previous chapter has been fabricated for experimental verification. The schematic of the complete power circulating power test bench is shown in Fig. 4.1. The test bed consists of the fabricated 12 phase PPMIM prototype, which is driven by a laboratory developed 12 phase inverter. The prototype machine under test is coupled with one off the shelf 48V IM to perform load test of the machine. This off the shelf IM is driven by one commercially available low voltage inverter. The PPMIM is designed to be driven by the 12 phase inverter from a 48 V DC bus.

To implement a circulating power test bed, so that only the net system loss has to be supplied by the external DC source, the other IM and inverter is also rated to be driven by the same 48V supply. Hence the DC bus connects to both the inverters, forming a circulating power test bed, as shown in Fig. 4.1. The 12 phase inverter is controlled by a TI28379D DSP control card [79]. The following sections reports each of the subsystems: the developed prototype machine, the poly phase inverter along with the control, and the power cycling test bench in details.

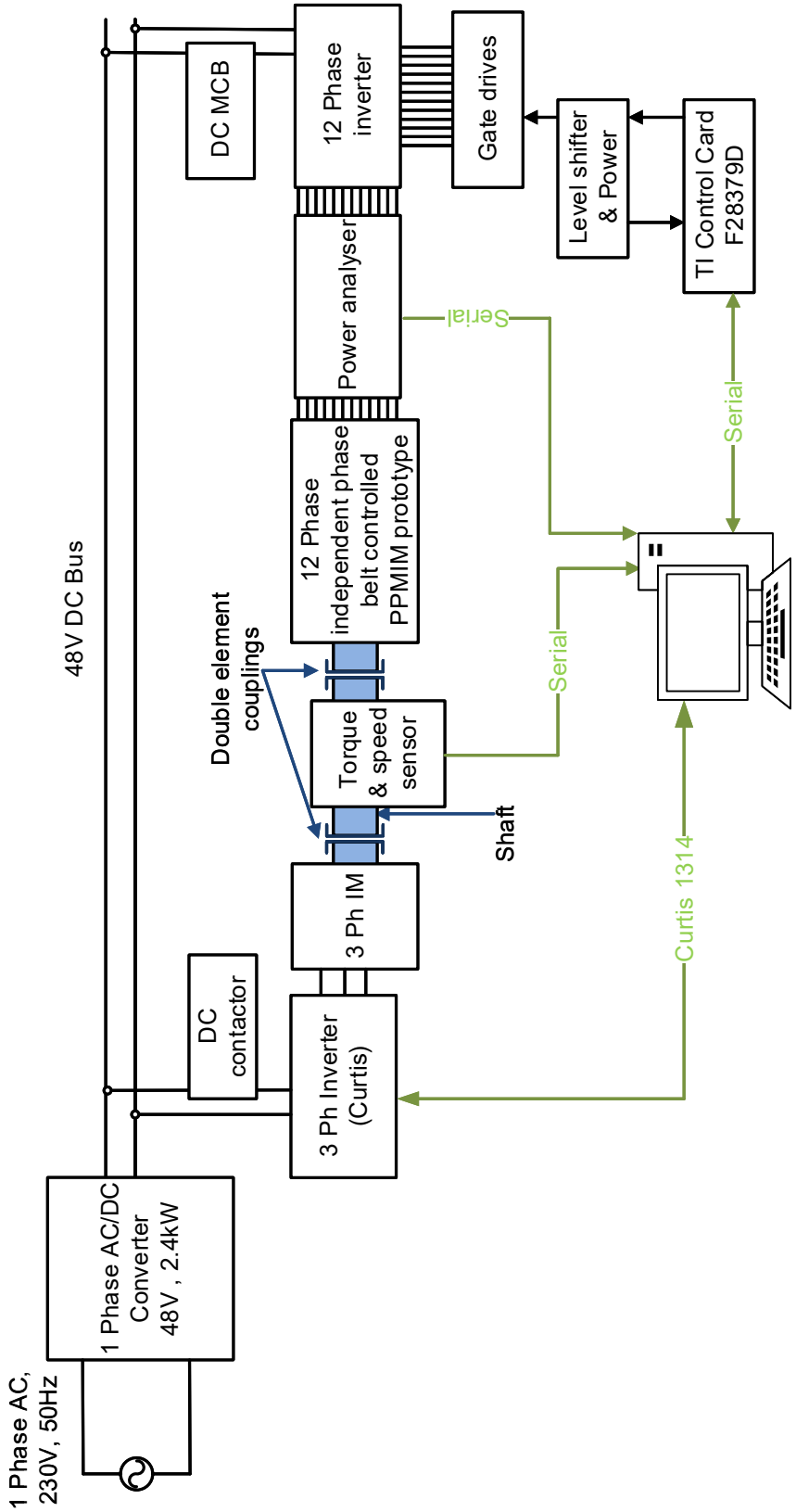

Figure 4.1: Circulating power experimental test bed schematic

Figure 4.2: Removal of the stator winding of an existing IM

Figure 4.3: Rotor of the existing machine

4.1 Machine Development

In the previous chapter the analytical results along with FEA results were compared for a specific machine (given in Table 3.2). This thesis aims to demonstrate the advantage of independent phase belt controlled PPMIM for widening the torque speed characteristics of IM drive. Hence to meet the timeline of the research, an existing 3 phase machine was modified to the required machine. A 5.5 HP (4kW) machine of IEC 112 frame was used for this purpose. The stator winding was removed to avail the stator core. Fig. 4.2 shows the stator in the process of removing the stator coil. The dimension details of the stator core are given in Appendix E. The 28 slot cage rotor of the machine was kept aside to be installed later with the new winding in place as shown in Fig. 4.3.

Figure 4.4: Modified stator before putting toroidal winding

To mount this experimental prototype machine with the test bed frame, four counterbores were made, as shown in Fig 4.4. The counterbores hold the stack of the stator core, as well as providing mechanical support for the machine to be mounted with the end plates. The end plates arrangement is shown later in Fig. 4.6.

4.1.1 Toroidal winding design

It has been discussed in previous chapters, the proposed independent phase belt controlled PPMIM utilises a toroidal winding. Hence the winding of the prototype machine has to be designed to meet the required bus voltage level (48V) and required power.

For the design of the machine, the magnetic loading (flux density) and electric loading (ampere conductor loading) need to be calculated. Hence the flux density at different locations of the stator and rotor need to be calculated.

Fig. 4.5 shows the flux density distribution at different location of the stator. The radial air-gap flux density of the machine can be given as

$$B_{\delta}(\phi_{sm},t) = \sum_{\nu=1}^{\infty} \hat{B}_{\delta,\nu} \sin(\omega_e t - \nu p \phi_{sm}) \tag{4.1}$$

where ν represents the space order of the harmonics. Hence the flux density through the

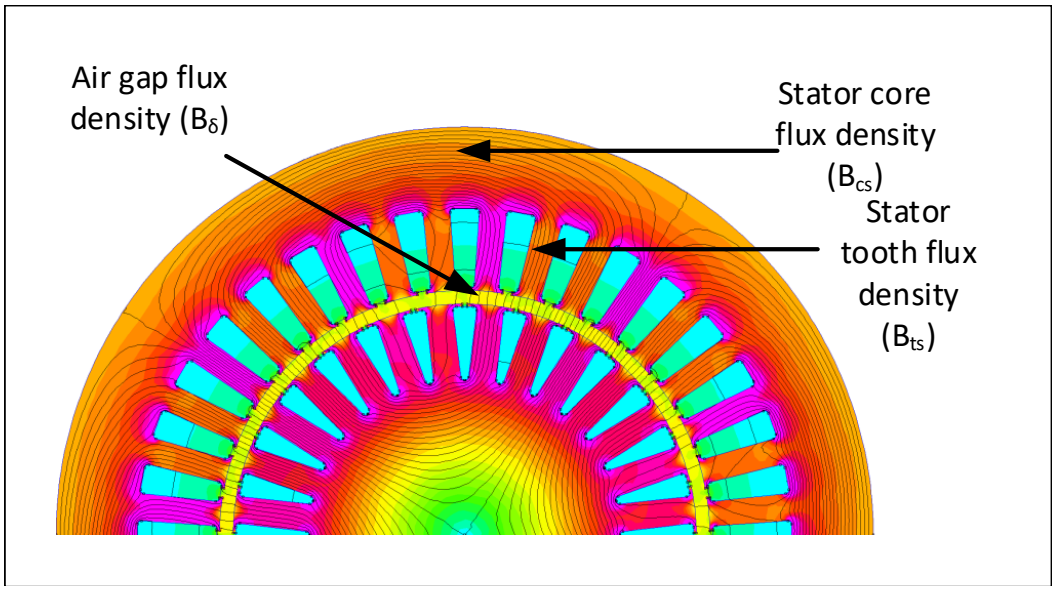

Figure 4.5: Flux density at different locations of the stator

stator tooth ψ_{ts} can be found by integrating the air-gap radial flux over a slot pitch, where the radial air-gap flux density is maximum, given below

$$\begin{aligned} \psi_{ts} &= \int_{\frac{-\pi}{Q_s}}^{\frac{\pi}{Q_s}} B_\delta(\phi_{sm},t) lr\, d\phi_{sm} \\ &= \int_{\frac{-\pi}{Q_s}}^{\frac{\pi}{Q_s}} \left\{\sum_{\nu=1}^{\infty} \hat{B}_{\delta,\nu} \sin(\omega_e t - \nu p\phi_{sm})\right\} lr\, d\phi_{sm} \end{aligned} \tag{4.2}$$

Considering the fundamental harmonic only, the maximum flux density occurs at $\omega_e t = \frac{-\pi}{2}$. Setting the limits of the integration to $\frac{\pi}{2}+\frac{\pi}{Q_s}$ to $\frac{\pi}{2}-\frac{\pi}{Q_s}$, ψ_{ts} can be simplified as

$$\begin{aligned} \hat{\psi}_{ts} &= \int_{\frac{\pi}{2}-\frac{\pi}{Q_s}}^{\frac{\pi}{2}+\frac{\pi}{Q_s}} \left\{\hat{B}_\delta \sin(\omega_e t - p\phi_{sm})\right\} lr\, d\phi_{sm} \\ &= \frac{2\hat{B}_\delta lr}{p} \sin(\tfrac{p\pi}{Q_s}) \end{aligned} \tag{4.3}$$

where $\hat{B_\delta}$ is the peak air-gap flux density. Hence the maximum tooth flux density is given as

$$\begin{aligned} \hat{B}_{ts} &= \frac{\hat{\psi}_{ts}}{l(1-\chi_s)\tau_s} \\ &= \frac{2\hat{B}_\delta r}{p(1-\chi_s)\tau_s} \sin(\tfrac{p\pi}{Q_s}) z \end{aligned} \tag{4.4}$$

where, χ_s is the ratio of slot width to tooth width and τ_s is the slot pitch. Further putting

$\tau_s = \frac{2\pi r}{Q_s}$ in the above equation, the following is obtained.

$$\hat{B}_{ts} = \frac{\hat{B}_\delta Q_s}{p(1-\chi_s)\pi} \sin(\frac{p\pi}{Q_s}) \tag{4.5}$$

This can be rearranged to find the expression of the peak air-gap flux density in terms of tooth flux density as below:

$$\hat{B}_\delta = \frac{\hat{B}_{ts} p(1-\chi_s)\pi}{Q_s \sin(\frac{p\pi}{Q_s})} \tag{4.6}$$

Having obtained the expression for tooth flux density, Eqn. 4.1 can be used to obtain the core (stator yoke) flux density. It can be observed from Fig. 4.5, the flux under the pole divides in two paths through the core. Hence the flux through the core ψ_{cs} is given as $\frac{\psi_p}{2}$, where ψ_p is the flux under one pole. ψ_p is given as

$$\begin{aligned} \psi_p &= \int_0^{\tau_p} B_\delta(\phi_{sm}, t) lr \, d\phi_{sm} \\ &= \int_0^{\tau_p} \sum_{\nu=1}^{\infty} \hat{B}_{\delta,\nu} \sin(\omega_e t - \nu p \phi_{sm}) lr \, d\phi_{sm} \end{aligned} \tag{4.7}$$

Taking the fundamental component only, the flux in the core is given as

$$\begin{aligned} \psi_{cs} &= \frac{1}{2} \int_0^{\frac{\pi}{p}} \hat{B}_\delta \sin(\omega_e t - p\phi_{sm}) lr \, d\phi_{sm} \\ &= \frac{rl\hat{B}_\delta}{p} \cos(\omega_e t) \end{aligned} \tag{4.8}$$

Hence the core flux density $B_{cs}$is given as

$$B_{cs} = \frac{\psi_{cs}}{l h_{cs}} \tag{4.9}$$

where h_{cs} is the depth of the stator core. Combining Eqn. 4.9, 4.5 and 4.8 the peak stator core flux density is given as

$$\begin{aligned} \hat{B}_{cs} &= \frac{r\hat{B}_\delta}{p h_{cs}} \\ &= \frac{\hat{B}_{ts} r(1-\chi_s)\pi}{h_{cs} Q_s \sin(\frac{p\pi}{Q_s})} \end{aligned} \tag{4.10}$$

Further, the expression of the core flux can be used to obtain the voltage in each of the phases. As the machine is wound toroidally, the core flux passes through the phase coil turns. Although the PPMIM mentioned in [63] uses a toroidally wound stator, as each of the coils has go and return directions, the flux linkage was double (the go side coil linking with north pole flux through core, and the other coil linking the south pole core flux diagonally

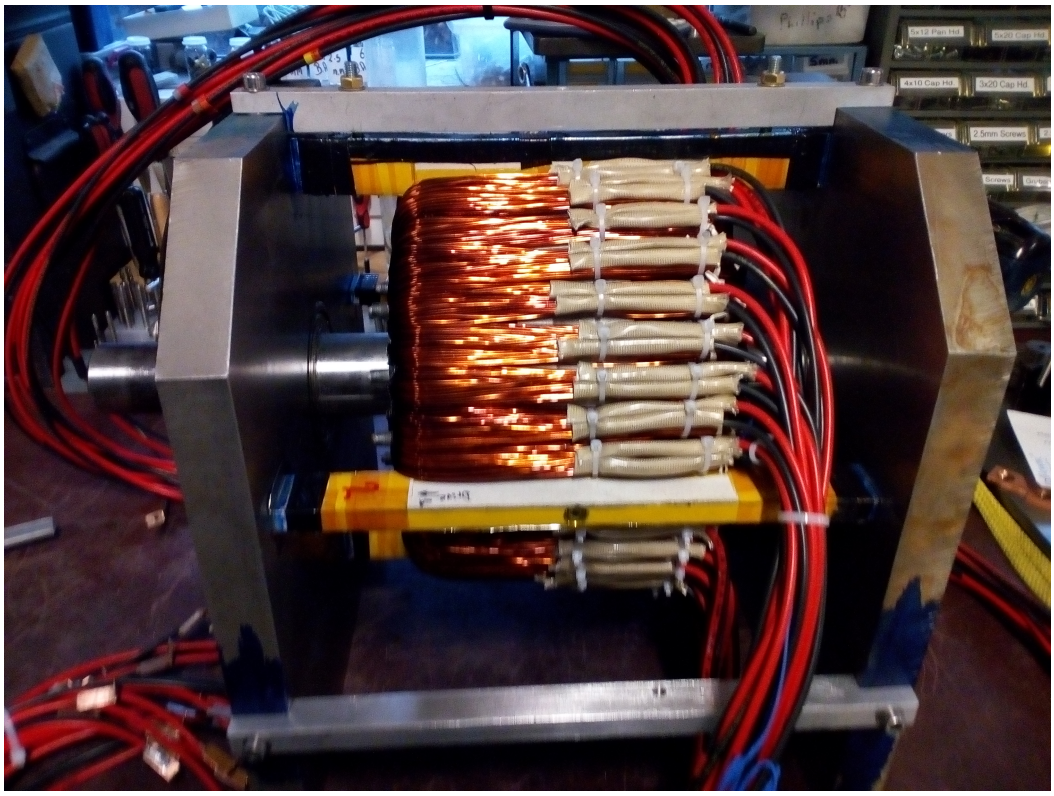

Figure 4.6: Fabricated prototype machine

opposite). Hence for the machine in this thesis, the air-gap voltage is given as

$$v_{gap} = \frac{\partial}{\partial t}\{qN_s k_w \psi_{cs}\} \tag{4.11}$$

where N_s is the number of turns per slot, q is the phase belt number and k_w is the winding factor. Substituting ψ_{cs} from Eqn. 4.8, the rms air-gap voltage is given as

$$V_{ph} = \frac{\omega_e q N_s k_w}{\sqrt{2}} \frac{rl\hat{B}_\delta}{p} \tag{4.12}$$

Substituting the expression for $\hat{B}_\delta$ from Eqn. 4.6

$$V_{ph} = \frac{\omega_e q N_s k_w B_{ts} rl(1-\chi_s)\pi}{\sqrt{2}Q_s \sin(\frac{p\pi}{Q_s})} \tag{4.13}$$

The dimensions of the stator core (presented in 3.2, and Appendix E) and Eqns. 4.6, 4.10 and 4.13, the number of turns in the stator coil (N_s) has been designed to be 22. The maximum flux density (B_{max}) was set to 1.4T. The flux density of the stator core under

Table 4.1: Stator tooth, air-gap and core flux density under different pole configurations

Pole no.	Tooth flux density (at 50Hz) ($\hat{B}_{ts}$) [T]	Air-gap density (at 50Hz) ($\hat{B}_{\delta}$) [T]	Stator core density (at 50Hz) ($\hat{B}_{cs}$) [T]	Maximum frequency (Hz)
2	0.28	0.20	0.46	152
4	0.57	0.41	0.46	120
6	0.85	0.61	0.46	80
8	1.13	0.82	0.46	60
10	1.4	1.03	0.46	50

different pole configuration, at the 48 V DC bus voltage, 50Hz frequency and modulation $m = 1$, is shown in Table. 4.1. As shown in Eqn 4.6, 4.10 and 4.13, for a fixed voltage, the stator core (yoke) flux density ($\hat{B}_{cs}$) remains constant, however air-gap flux density ($\hat{B}_{\delta}$) and tooth flux density ($\hat{B}_{ts}$) is proportional to the pole pair number. The maximum flux density is met in the 10 pole configuration at the tooth. Clearly for a customised stator stamping design of this type machine, the yoke depth (h_{cs}) should be reduced to increase iron utilization.

It can be argued that the utilization of the core is low for low pole configuration, as the flux density is below saturation level. However, this can be leveraged to allow injection of higher frequency (without decreasing the voltage) in the low pole count, thus increasing the operating speed range. Indeed this will lead to higher yoke flux density ($\hat{B}_{cs}$) and the yoke depth (h_{cs}) should be designed to ensure the yoke does not saturate. The maximum frequency, for the given machine dimensions, under each pole configuration is calculated by setting the maximum stator flux density to B_{max}, as shown in the last column of Table. 4.1. The frequency is limited by the tooth flux density ($\hat{B}_{ts}$) for pole configurations 4 to 10. However, for the 2 pole configuration this is limited by the yoke flux density ($\hat{B}_{cs}$).

Having designed the turns number of the coils, the coil wire gauge need to be decided. Using the stator slot cross section and the designed number of turns $N_s = 22$, the conductor size was chosen to be two strands of 19 SWG. The window space factor was calculated to be 0.7. As the laboratory fabricated machine would be air cooled, the current density in stator conductor was chosen to be $8\,A/mm^2$. The outer side of the toroidal winding increases cooling effectiveness, hence slightly higher current density can be used. The specific electric loading for this current density was found to be ~25000 ampere conductor/m.

The constructed machine with the designed toroidal winding is shown in Fig. 4.6. Additionally, to measure the flux density in the stator core, 3 search coils were placed at 30^o each around stator teeth. Four thermocouples are also placed on the constructed machine

- two directly in the stator core - below the return of the toroidal winding, and two on the stator winding to measure the temperature of the machine at different locations.

4.2 Poly Phase Inverter Design

Having designed the machine, the polyphase inverter has to be designed. The individual phase current limit can be calculated from the machine design to be ~15A RMS. The DC bus voltage has been decided to be 48V. For the purpose of this thesis, the machine design assumes three consecutive slot windings to be connected in series to form one phase. However it was decided to design the inverter capable to run the machine also at higher current by connecting slot windings in parallel. Hence a simple estimate shows that the per phase impedance in parallel connection will be $\frac{1}{9}$ of the series-connected impedance compared to the series connection. Hence high current MOSFETs in 4-Pin SOT-227B package were used to construct the inverter. Further, to allow fewer phases by connecting more slot windings in series the device was overrated in voltage as well. Finally, 150V, 150A MOSFET - IXFN 180N15P [80] was used to construct the inverter. To summarise, the inverter was deliberately over designed to allow future experiments on the reconfigurable IM drive, by allowing both series and parallel connection of the slot windings. To cater for the high current of the inverter, a sandwiched busbar was designed by using Autodesk Fusion 360 [81]. As the designed machine needs a 12 phase inverter, two identical 6 phase inverters were developed. Each 6 phase inverter has 3 inverter legs in each side of the busbar as shown in the inverter CAD model in Fig. 4.9. By putting inverter legs at both sides of the bus bar, the net length required for the bus bar was reduced. Fig. 4.10 shows the fabricated 6 phase inverter with the heat-sink.

4.2.1 DC bus capacitor design

The VSC needs a DC bus capacitor to maintain the DC bus voltage. The variation of DC bus voltage is generally caused by the VSI power unbalance [82].The DC bus capacitor size can be obtained from the design specification of the voltage ripple at the steady state operation, power rating, and switching frequency given as

$$C_{dc} = \frac{P_{max}}{(V_{dc}\triangle V + \frac{1}{2}\triangle V^2) f_{sw}} \tag{4.14}$$

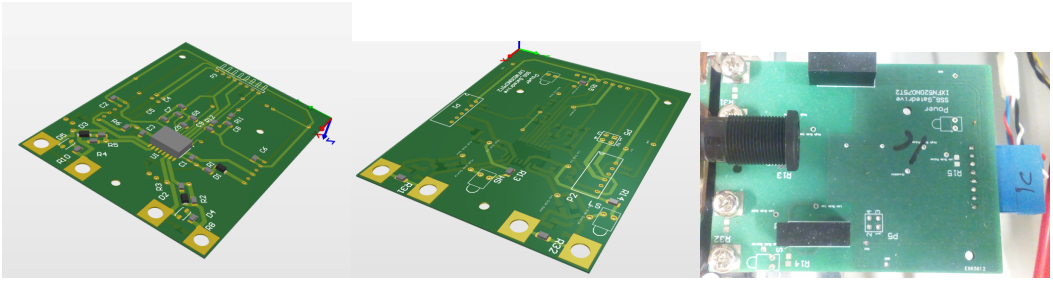

Figure 4.7: Designed gate drive circuit PCB model (in 3d) and fabricated prototype

where P_{max} is the maximum power delivered by the inverter, V_{dc} is the rated DC bus voltage, $\triangle V$ is the allowed voltage fluctuation at the DC bus, and f_{sw} is the switching frequency of the inverter. For the design of the inverter, putting $V_{dc} = 48$ V, $\triangle V = 2$ V, and setting $f_{sw} =$ 20 kHz, the DC bus capacitance was obtained to be 1 mF. Hence three 330 μF capacitors were used. These large bus capacitors was connected at the end of the DC bus, as shown in the converter model in Fig. 4.9. Due to large stray inductance from the long DC bus bar, large C_{oss} of the low voltage high current devices and high ESL of the the electrolytic capacitors there was switching noise coupling from one leg to another. Hence additional small DC bus capacitors (4.7nF film capacitor and 10μF electrolytic capacitor) were placed physically very close to the devices, providing the current path during switching transients.

4.2.2 Gate drive design

An isolated dual channel gate driver - UCC21520 [83] was used to drive each leg of the inverter. The gate driver provides isolation between the input signal side, high side gate drive and low side gate drive. The top and bottom sides were supplied by two isolated 5V-15V DC/DC converters. The PCB layout, as shown in Fig. 4.7 was optimised to have minimum loop length from the output of the driver to the gate of the device as this path carries high frequency pulsed gate current. Further, the gate driver is capable of sourcing 4A during turn on, and sinking 6A during turn off. Hence for a 15V gate drive voltage, the turn on resistance is set to be 4.7 Ω. During turn off an additional 6.8 Ω resistance is connected in parallel to achieve faster turn off utilising extra current sinking capability of the driver. The detailed circuit diagram of the complete gate driver board is shown in Appendix C. The gate driver allows incorporation of hardware forced dead time by setting a resistor and capacitor at the dead time pin. Although the dead time will be implemented by the software controlled PWM generation, to safeguard against accidental mistake, a 1μs dead time was set in the gate drive. This hardware enabled dead time is not an additional dead

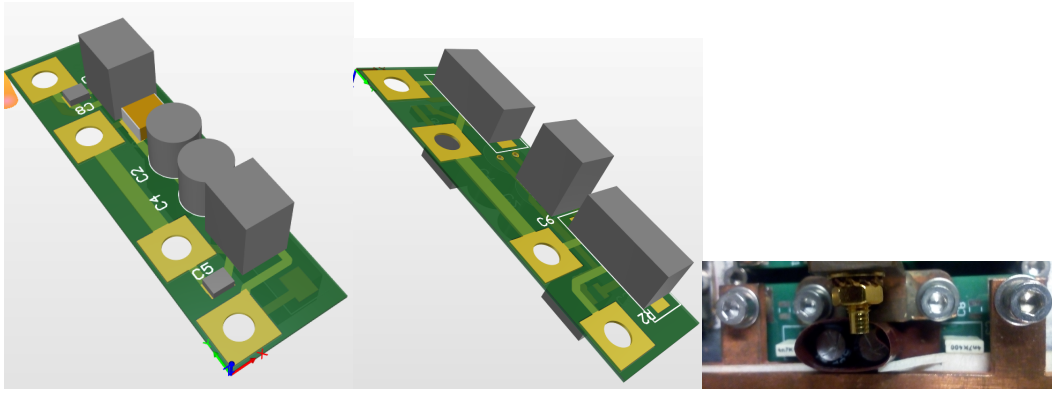

Figure 4.8: Designed snubber circuit PCB model(in 3d) and fabricated prototype

time applied by the software generated PWM, rather it applies when the software applied dead time is lower than the set value of $1\mu s$, and ensures both top and bottom switches are never switched on simultaneously. The chosen 4-Pin SOT-227B package of the devices allows the gate drive to be connected on the device directly from the other side of the bus bar - as the package has gate and source in one side of the device, and drain and source on the other side of the package. This ensures gate drive placement does not interfere with the sandwiched bus bar design. The gate drive PCB shape was designed from the CAD model of the inverter, so that it can be directly bolted on the devices as shown later in Fig. 4.9 and 4.10.

4.2.3 Snubber circuit design

As this inverter deploys sandwiched bus bar to handle large current rating of the inverter - this leads to larger DC bus inductance compared to PCB based inverter design. This larger DC bus inductance leads to ringing during switching transients. Hence an RC snubber circuit was designed to protect the devices from over voltage during switching transients. As discussed in [84] the snubber capacitor was selected to be twice the device output capacitance. The device being low voltage, high current has high output capacitance of 2.2 nF [80]. Hence a 4.4 nF capacitor was selected. The net snubber loss in the capacitor is given as

$$P_{loss} = CV^2 f \tag{4.15}$$

where C is the snubber capacitor, V is the DC bus voltage and f is the switching frequency. It should be noted, this includes both turn on and off energy in one device, each being equal to $\frac{1}{2}CV^2$. Hence for a 48 V DC bus, and 20 kHz switching frequency, 4.4 nF snubber

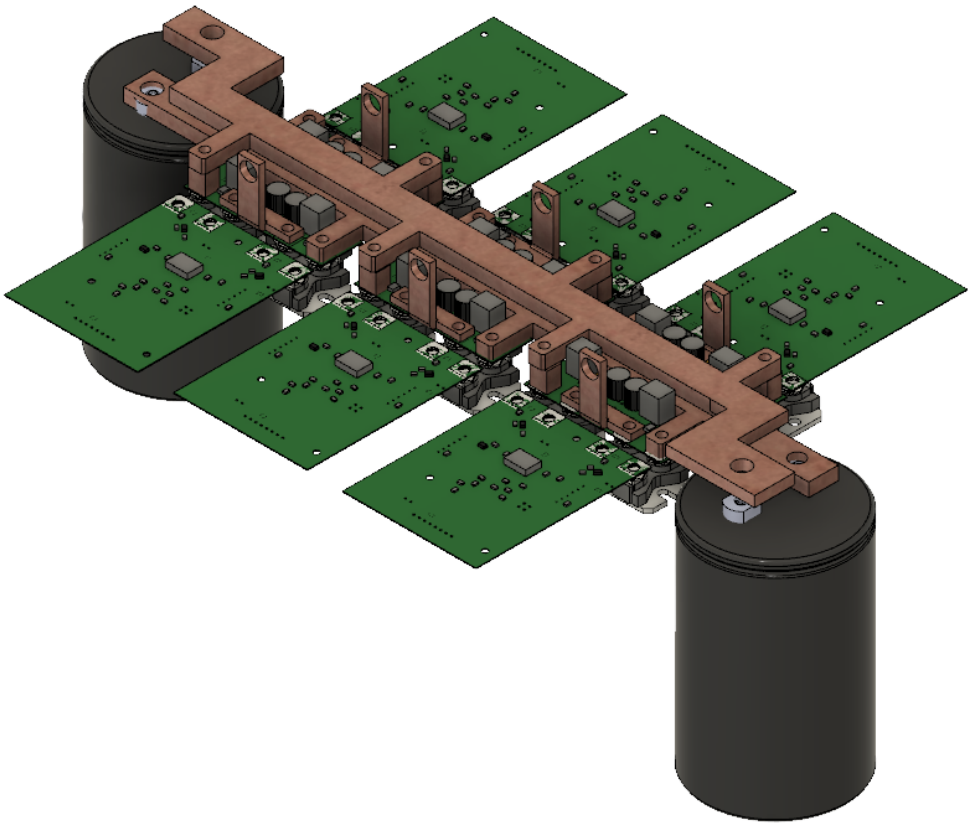

Figure 4.9: designed 6 phase inverter CAD model

capacitor causes individual snubber loss to be 0.22W. A 2 Ω, 2 W resistor was used, as this limits the initial current to 24A. Further the net loss for the 12 phase inverter (24 devices) is 5.8 W, which is significantly small compared to the power rating of the drive. The designed snubber circuit is shown in Fig. 4.8. Special care was taken to make the snubber PCB small, and directly mountable on the device terminals of the inverter legs to reduce stray inductance in the connection as shown in the complete inverter assembly in Fig. 4.9 and 4.10.

4.2.4 Inverter control software

A TI TMS320F28379D [79] processor based control card was used to generate the PWM for the 12 phase inverter by implementing a phase shifted sine PWM by comparing against a triangular carrier. EPWM modules of the controller were used to generate the pulses, along with dead time. The switching frequency was kept at 10kHz, and a dead time of 1 μs, between top and bottom device of the inverter legs was applied. The program allows

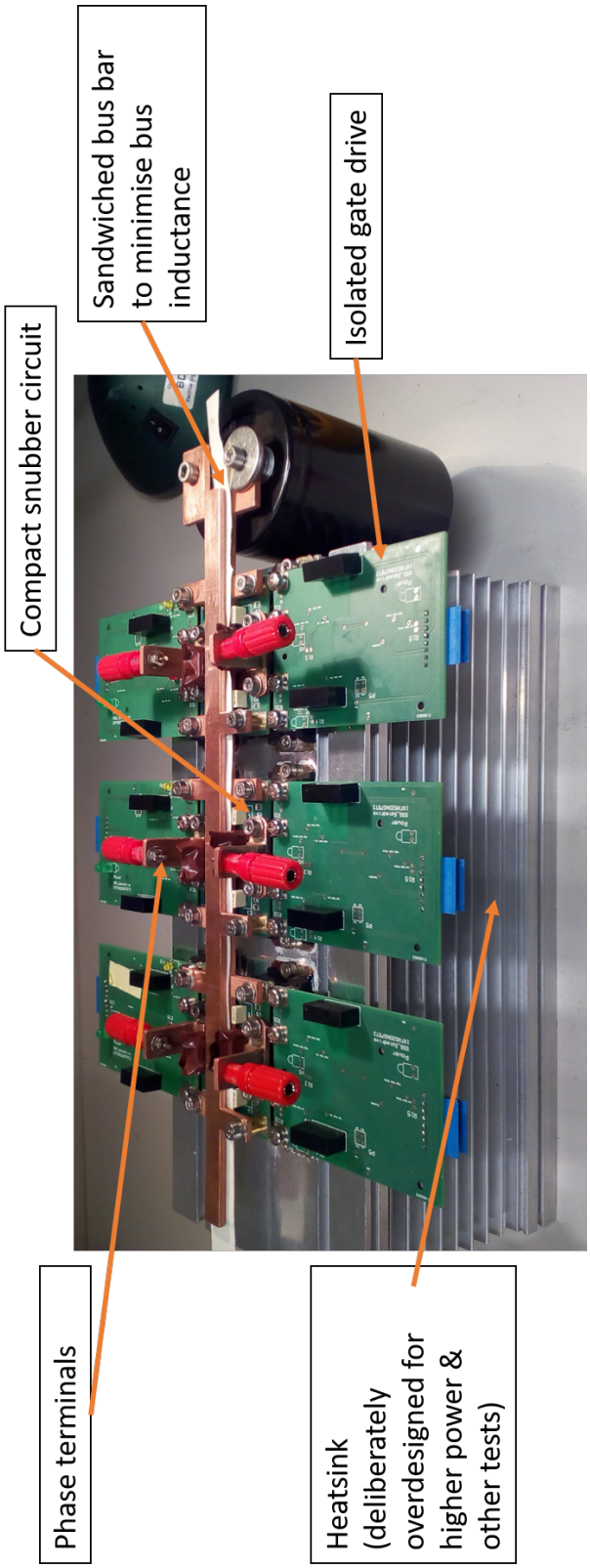

Figure 4.10: Fabricated 6 phase inverter

to change the modulation index (m), fundamental frequency (f) and the phase angle (ϕ) in between consecutive inverter phases in open loop.

Further, a simple modification in the program allows keeping the modulation index proportional to frequency, thus allowing testing the machine performance under VVVF control. A serial communication based graphical user interface as shown in Fig. 4.11 was developed based on MATLAB - Simulink, to control the the modulation index, fundamental frequency and the phase angle in between consecutive inverter phases.

4.3 Power cycling test bench

To test the machine under load condition, i.e. different torque-speed operating conditions, another load/drive machine is needed. Further, this load machine should be torque and / or speed controlled, so that the operating point can be set from the load/drive machine, while the prototype machine is operated without any closed loop control. Hence an inverter controlled machine is needed to be mechanically coupled with the prototype machine. Moreover, if this machine is chosen to be driven from the same DC bus voltage (48 V) as the prototype machine, a circulating power test bench can be developed. The load machine will be in generator mode, while the prototype machine will be motor operation and vice-versa. As the DC source needs to supply the loss of the system only (net loss of both the drives), this circulating power test bench would allow to test the prototype machine at higher power than that available from the DC source.

Hence another off the shelf induction machine was bought and its shaft was coupled directly with the prototype machine through a torque transducer [85]. The details of the commercially available IM used in the test bench is given in Appendix E. The inverter [86] for the load machine was connected to the same 48 V DC bus, as shown in Fig. 4.1. The user interface software of the inverter allows to set the maximum torque and speed of the machine. The complete circulating power test bench hardware photograph is shown in the Fig. 4.12.

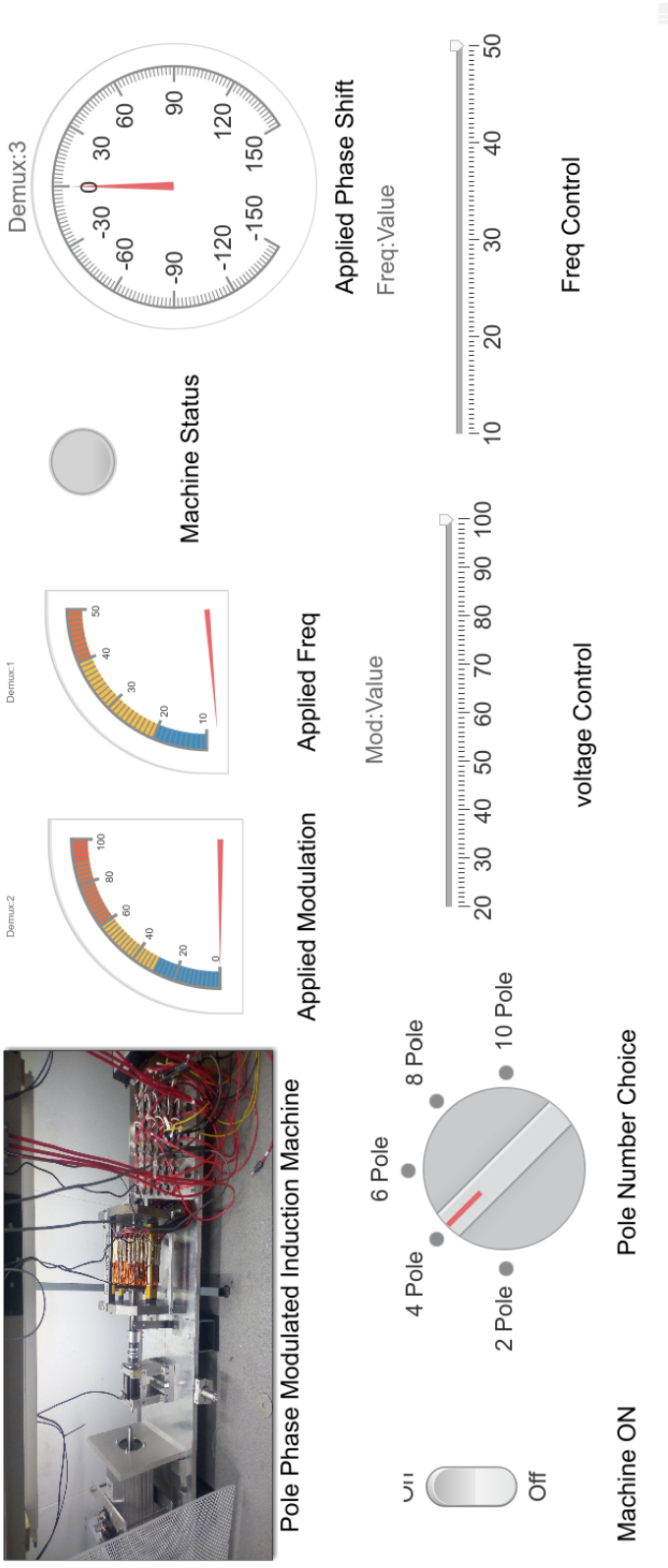

Figure 4.11: Serial communication user interface

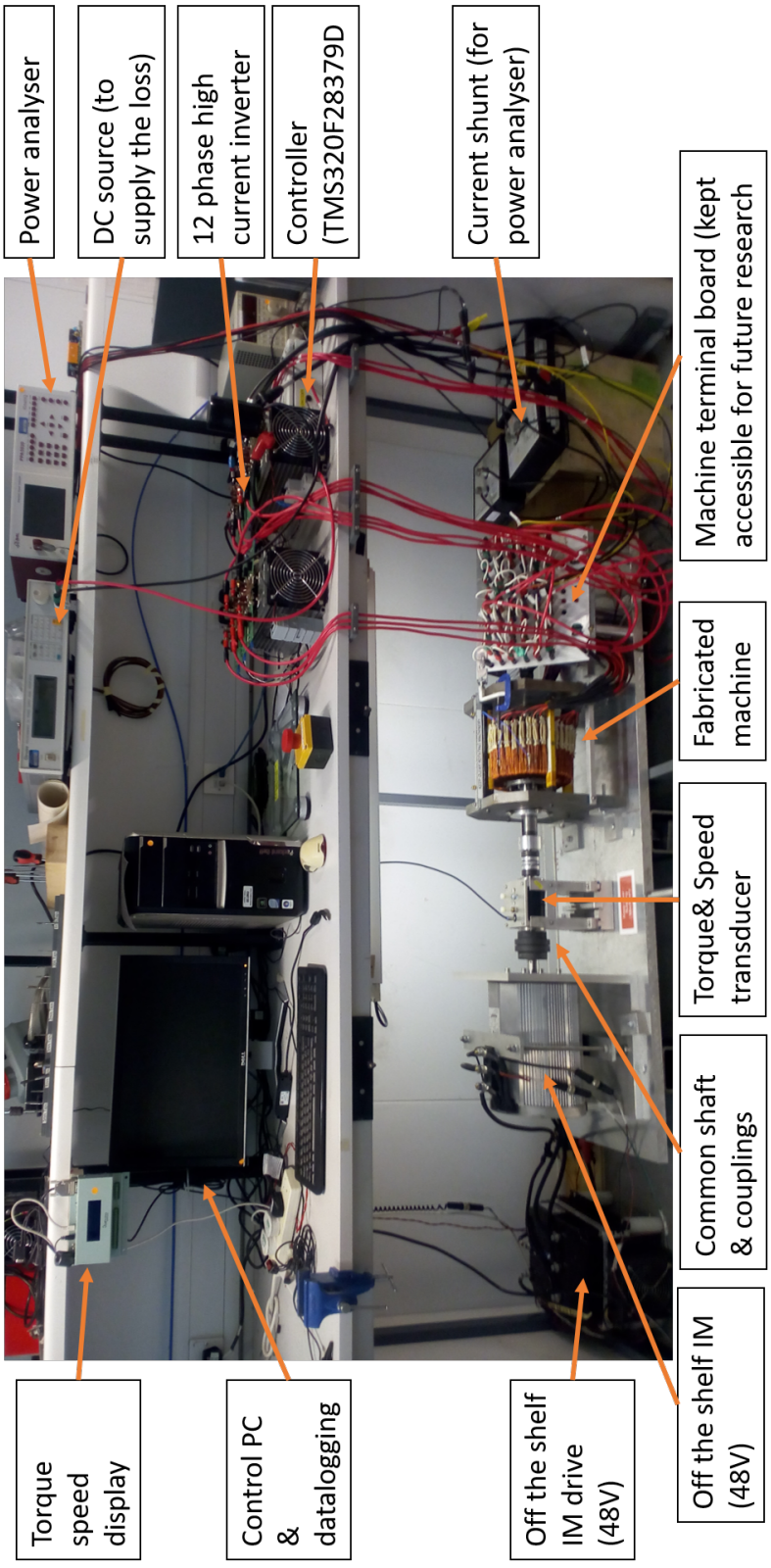

Figure 4.12: Fabricated circulating power experimental test bed

Chapter 5

Experimental Results - Steady state operation

The previous chapter discussed details of the experimental prototype machine design, inverter design and circulating power setup development, along with necessary control software. Having developed the test bench, experimental tests were performed on the fabricated machine. This chapter reports the experimental results of the machine from no-load test, blocked rotor test and load test under different pole configurations. Further, no-load test and blocked rotor test data has been used to calculate the machine parameters and have been compared against those parameter values obtained from FEA and analytical calculation presented in chapter 3. Finally the load test results on T-S characteristics of the machine under different pole configurations has been compared against the calculated machine torque-speed characteristics reported in chapter 3.

5.1 No load test

To estimate the machine parameters experimentally, no load test and blocked rotor test need to be performed at rated frequency. The control software was configured to apply a modulation index of 0.95 and frequency of 50 Hz, where the DC bus was kept at rated 48 V. The modulation index was kept at 0.95, instead of 1, to ensure the pulses at the peak of the sine wave are not too narrow leading to pulse dropping at peak due to the dead-time. A 0.95 modulation index at 10 kHz switching frequency would produce minimum width of pulse to be 5 μs, which will appear as 4 μs pulse at the device after application of the set dead time (1 μs).

Table 5.1: No load experimental results

Pole No.	Power (3 phase measured) (Watt)	Power (Total) (Watt)	VA (3 Phase measured) (VA)	VA (Total) (VA)	Power Factor	Phase Angle (Degree)	Phase Voltage (RMS) (V)	Phase Current (RMS) (A)	Speed (RPM)	Slip (%)	Magnetising inductance (L_m) (mH)
2	36.8	147.4	264.4	1057.5	0.14	82.0	16.7	5.3	2937	2.1	48.3
4	16.8	67.3	261.7	1046.8	0.06	85.0	16.7	5.2	1480	1.33	20.8
6	29.8	119.1	367.6	1470.5	0.08	85.5	16.8	7.3	988	1.2	15.0
8	79.9	319.7	579.2	2196.7	0.15	85.0	16.5	11.1	741	1.2	9.8
10	201.6	806.5	740.5	2961.8	0.27	84.0	16.4	15.1	589	1.83	7.4

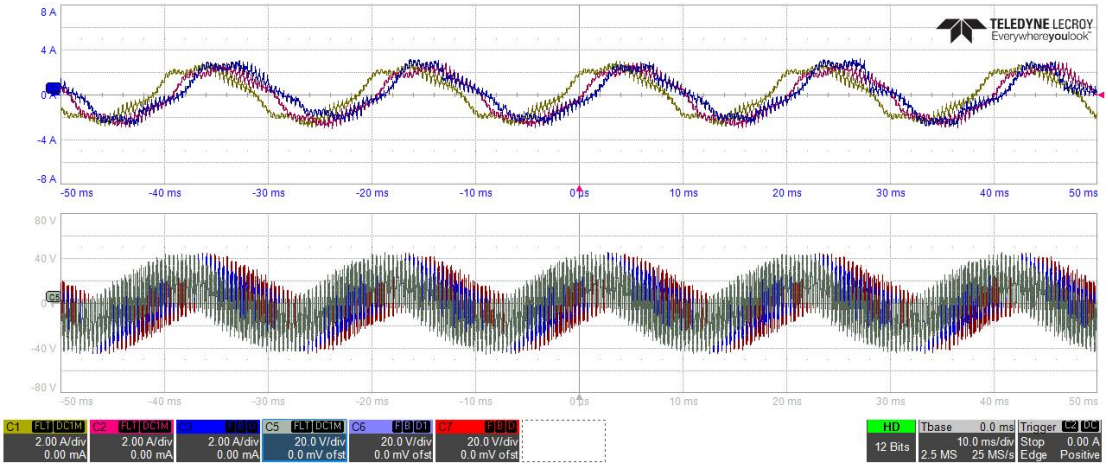

Figure 5.1: 2 pole operation (30^ophase shift)

The input DC power to the inverter was measured directly from the 48V DC power supply, which gives the input power to the inverter. The AC power output was measured using a 3 phase power analyser N4L PPA5530 [87]. Due to the difficulty of instrumentation to measure all 12 phases simultaneously, the power analyser was connected at three phases first, and then changed to other three phases to make sure all phases are balanced. Simultaneously the phase voltage and current waveforms were recorded too. Similar to the difficulty of measurement of the AC power, it is challenging to measure 12 phase voltage and current simultaneously. A Lecroy 8 channel MDA 800 oscilloscope [88] was used to observe 3 phase voltage and current at a time. Further, similar to power analyser measurement, the voltage and current waveforms of the other phases were checked to ensure the phases are balanced. By changing the phase angle between consecutive legs of the inverter, different pole pairs were realised. The experimental results of the no load test under different pole configuration are reported in table 5.1. The voltage and current waveforms of three consecutive phases were recorded using the oscilloscope, for five different pole configurations and are presented in Fig. 5.1 - 5.5

It can be observed, the slip of the machine under no load condition, is not very close to zero. This can be attributed to the presence of the load machine and friction and windage loss of the machine for the low pole high speed operation, and torque ripple present in the high pole low speed operation. Hence if magnetising inductance is calculated from this result, this would not be very close to accurate estimate as shown in Table 5.1. This error in the slip, is particularly large for the two pole operation, as the friction and windage loss is higher at higher speed. Hence to accurately estimate the magnetising inductance, a syn-

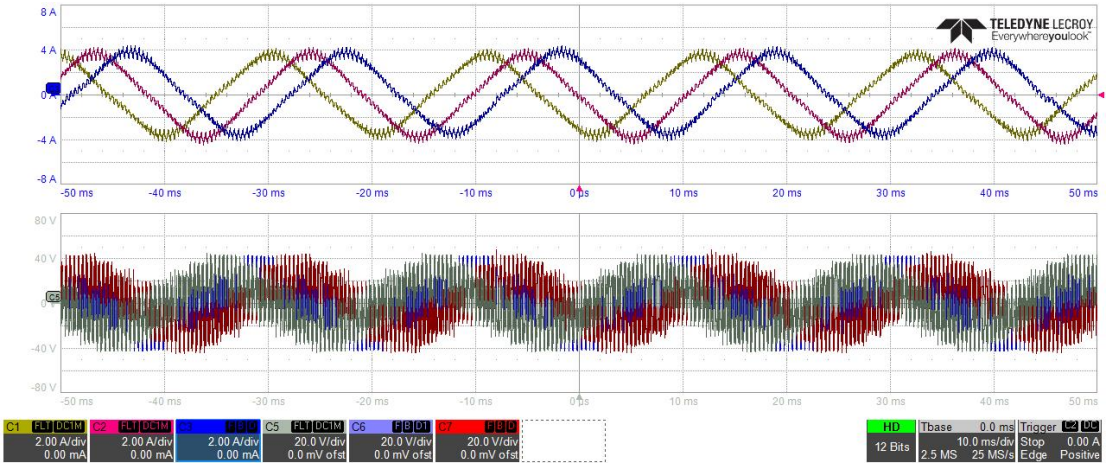

Figure 5.2: 4 pole operation (60^ophase shift)

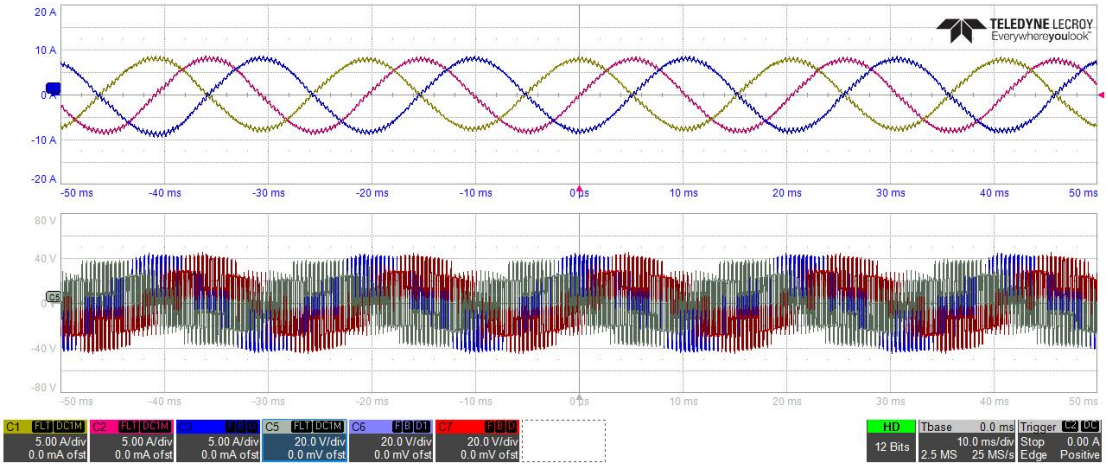

Figure 5.3: 6 pole operation (90^ophase shift)

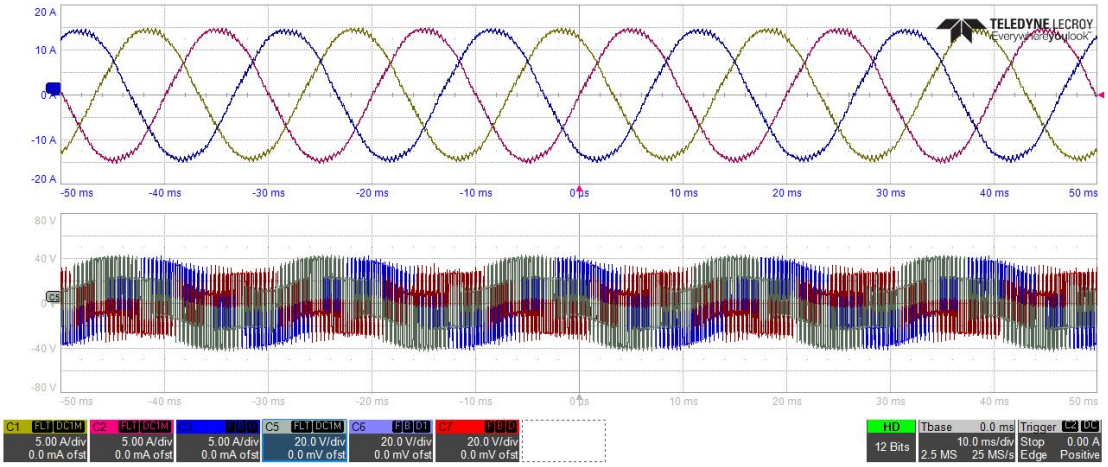

Figure 5.4: 8 pole operation (120^ophase shift)

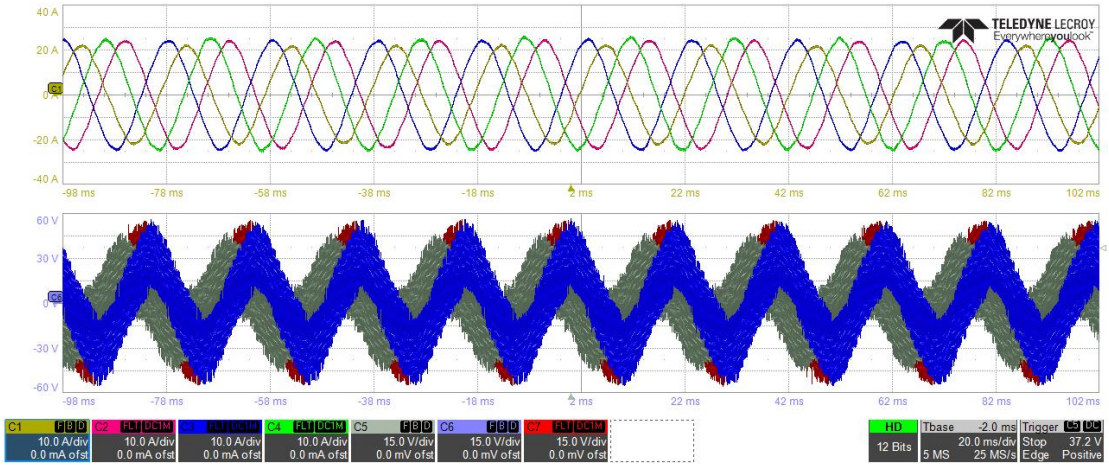

Figure 5.5: 10 pole operation (150^ophase shift)

chronous speed test of the machine was performed. This was achieved by running the load machine under speed control, by setting the speed of the rotor to be same as synchronous speed. The results of this test under different pole configuration is presented in table 5.2. Calculated magnetising inductance of the machine under different pole configuration has been presented too. Due to the counter used in the control software, the actual frequency of the supply was 49.4 Hz, rather than 50Hz. Hence the speed was adjusted to match the corresponding synchronous speed under different pole configuration, as shown in table 5.2.

5.2 Blocked rotor test

To estimate the stator and rotor leakage inductance and resistance, a blocked rotor test need to be performed. A customised rotor blocking arrangement was made which allows the shaft of the machine clamped by two pieces of hollow blocks and then bolted to the machine base, as shown in Fig 5.6. For this blocked rotor test, after blocking the rotor, the DC bus voltage was increased until the rated current of 13 A RMS phase current was reached, while the modulation index was kept at 0.95 as before. The experimental results has been reported in table 5.3. Further, the rotor and stator resistance and leakage inductances have been calculated and shown in the same table, for different pole configurations.

The stator resistance of a phase was measured by connecting a phase sensitive multimeter (N4L PSM 3750) [89], since the stator resistance is very small, and can be easily affected by the lead connection. Hence at first the resistance of the connected leads with the PSM were measured to be 265 $m\Omega$ (at 50Hz). Then the leads were connected across

Table 5.2: Synchronous speed experimental results

Pole No.	Power (3 phase measured) (Watt)	Power (Total) (Watt)	VA (3 Phase measured) (VA)	VA (Total) (VA)	Power Factor	Phase Angle (Degree)	Phase Voltage (RMS) (V)	Phase Current (RMS) (A)	Speed (RPM)	Magnetising inductance (L_m)(mH)
2	2	8	21.9	87.9	0.09	84.7	16.8	0.436	2965	123.16
4	9.1	36.4	91.2	364.8	0.1	84.3	16.8	1.81	1482	29.7
6	23	92	248.5	993.88	0.09	84.7	16.8	4.93	988	10.9
8	70	280	428.4	1713.6	0.16	80.6	16.8	8.5	741	6.4
10	130	520	720.7	2882.8	0.18	79.6	16.8	14.3	593	3.8

Table 5.3: Blocked rotor experimental results

Pole No.	Power (3 phase measured)	Power (Total)	VA (3 Phase measured)	VA (Total)	Power Factor	Phase Angle	Phase Voltage (RMS)	Phase Current (RMS)	Leakage inductance ($L_s + L_r'$) (mH)	Resistance ($R_s + R_r'$) (mΩ)
2	144.7	578.9	419.3	1677.4	0.35	69.8	11.64	12	2.9	335
4	133.9	535.7	364.8	1459.7	0.37	68.5	10.1	12	2.5	310
6	122.3	489.0	297.7	1190.8	0.41	65.8	8.2	12	2	283
8	118.4	473.5	333.8	1335.4	0.35	69.2	9.2	12	2.3	274
10	103.8	415.1	420.2	1680.7	0.25	75.7	11.7	12	3	240.2

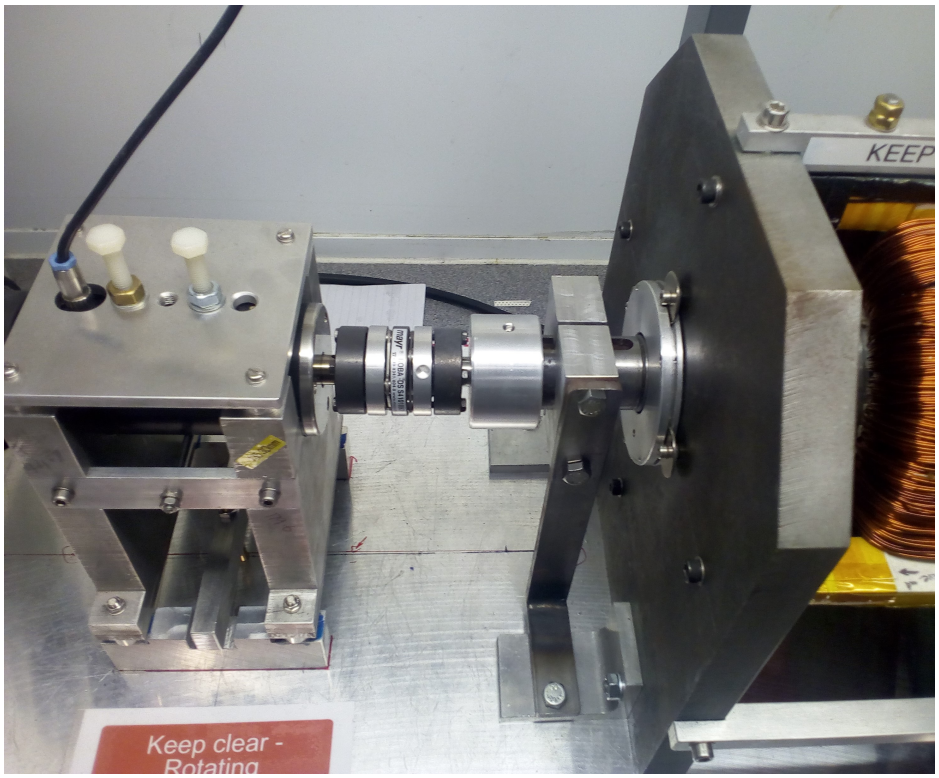

Figure 5.6: Blocked rotor test arrangement

one stator phase and the resistance were measured to be 383 $m\Omega$, giving each stator phase resistance to be 118 $m\Omega$, which is slightly higher than the stator resistance estimated to be 89.8 $m\Omega$, from the calculation in chapter 3. This can be attributed to connecting lead wires, and terminal junctions. However, as this is a low voltage high current machine, this small extra stator resistance will affect the machine torque and output, which is shown in the next section of load test of the machine.

Subtracting stator resistance from the net resistance obtained from the blocked rotor test would give the equivalent rotor resistance. The experimental values of the equivalent circuit parameters and the values obtained from the analytical and FEA calculation in chapter 3 have been tabulated in table 5.4 for comparison. It can be observed that for low pole numbers, the values agree very closely. However, for the larger pole number (8 and 10), due to the presence of the larger harmonics, the values diverge more as the analytical results were obtained for the fundamental frequency only.

Table 5.4: Equivalent circuit parameters of machine

Pole No.	Method	R_s (in $m\Omega$)	$R_r^{'}$ (in $m\Omega$)	L_s(in mH)	$L_r^{'}$ (in mH)	L_m (in mH)
2	Experimental	118	217	1.45		123.16
	FEM	89.8	214.2	1.4		137.5
	Analytical	89.8	215.1	1.6	0.3	123.3
4	Experimental	118	192	1.25		28.16
	FEM	89.8	201.0	1.2		34.4
	Analytical	89.8	199.6	1.7	0.3	30.8
6	Experimental	118	165	1		11.23
	FEM	89.8	178.1	1.4		13.9
	Analytical	89.8	180.0	1.7	0.6	13.7
8	Experimental	118	156	1.15		6.37
	FEM	89.8	152.2	1.0		7.2
	Analytical	89.8	153.2	1.8	0.3	7.7
10	Experimental	118	122	1.5		3.55
	FEM	89.8	111.3	1.3		4.4
	Analytical	89.8	115.2	1.8	0.8	4.9

5.3 Load test under different pole configurations

Having obtained the machine parameters from the experimental results, the torque-speed characteristics of the machine were obtained by load testing of the machine. As mentioned earlier, the 10 pole operation leads to large torque ripple, hence has not been studied under load test. This was achieved by operating the load machine under speed control, thus setting the operating speed of the machine under test. The machine input power was measured similar to the no load and blocked rotor experiments. The inverter input power and efficiency was measured as well. Table 5.5 - 5.8 reports the experimental data.

The T-S load data of the machine under different pole configurations is shown w.r.t the T-S characteristics obtained from the analysis in chapter 3 in Fig. 5.7. Fig. 5.7 shows good match of the experimental results and the estimated T-S characteristics obtained from the analysis in chapter 3. The efficiency and power factor of the machine under different pole configurations are also shown against the same estimated from the analysis in Figs. 5.8 and 5.9. As discussed in the previous section, the power factor and efficiency drop with the increase of the pole numbers due to increase in magnetising current caused by decrease in magnetising inductance. This is validated by experimental results as well.

Table 5.5: 2 Pole load test experimental results

Sl No	Speed (RPM)	DC input current (A)	DC input power (W)	AC input power (W)	Power Factor (pf)	Phase Current (RMS)	Torque (Nm)	Machine output (W)	Machine efficiency (%)	Inverter efficiency (%)
1	2900	3.2	152.3	138.9	0.9	0.8	0.4	132.1	95.2	91.2
2	2851	13.5	648.1	598.2	0.92	3.3	1.8	531.8	88.9	92.3
3	2800	13.9	669.0	624.9	0.92	3.5	1.9	563.5	90.2	93.4
4	2750	23.0	1101.9	1010.4	0.91	5.7	2.8	818.1	81.0	91.7
5	2700	28.7	1378.0	1274.6	0.91	7.3	3.7	1054.8	82.8	92.5
6	2650	34.1	16.38.2	1500.6	0.89	8.7	4.0	1120.8	74.7	91.6
7	2600	39.1	1874.6	1700.2	0.89	9.9	4.8	1315.7	77.4	90.7

Table 5.6: 4 Pole load test experimental results

Sl No	Speed (RPM)	DC input current (A)	DC input power (W)	AC input power (W)	Power Factor (pf)	Phase Current (RMS)	Torque (Nm)	Machine output (W)	Machine efficiency (%)	Inverter efficiency (%)
1	1450	5.9	282.6	257.4	0.65	2.0	1.5	233.9	90.9	91.1
2	1400	15.4	740.6	682.9	0.82	4.3	4.0	585.9	85.8	92.2
3	1350	28.8	1382.9	1284.7	0.84	7.9	7.4	1049.6	81.7	92.9
4	1300	35.1	1683.5	1542.1	0.83	9.6	8.3	1136.7	73.7	91.6
5	1250	47.1	2261.0	2086.9	0.82	13.2	10.7	1395.4	66.9	92.3
6	1200	49.1	2355.5	2157.6	0.79	14.2	11.2	1407.3	65.2	91.6

Table 5.7: 6 Pole load test experimental results

Sl No	Speed (RPM)	DC input current (A)	DC input power (W)	AC input power (W)	Power Factor (pf)	Phase Current (RMS)	Torque (Nm)	Machine output (W)	Machine efficiency (%)	Inverter efficiency (%)
1	971	7.3	350.4	323.6	0.44	3.8	2.5	254.2	78.6	92.4
2	950	13.0	622.8	574.9	0.56	5.3	4.9	488.9	85.0	92.3
3	925	19.3	924.7	855.4	0.67	6.5	7.4	719.3	84.1	92.5
4	900	28.4	1360.9	1248.0	0.71	9.0	10.2	957.9	76.8	91.7
5	870	34.3	1648.4	1523.1	0.71	11.0	12.2	1112.7	73.1	92.4
6	850	40.4	1936.9	1772.3	0.71	12.9	13.7	1219.3	68.8	91.5

Table 5.8: 8 Pole load test experimental results

Sl No	Speed (RPM)	DC input current (A)	DC input power (W)	AC input power (W)	Power Factor (pf)	Phase Current (RMS)	Torque (Nm)	Machine output (W)	Machine efficiency (%)	Inverter efficiency (%)
1	732	7.3	348.3	322.2	0.3	5.5	3.4	256.8	79.7	92.5
2	712	11.4	546.0	500.6	0.41	6.2	5.7	424.0	84.7	91.7
3	702	16.9	809.2	747.7	0.5	7.8	8.4	617.4	82.6	92.4
4	680	23.5	1127.8	1031.9	0.59	9.0	11.5	818.4	79.3	91.5
5	660	36.0	1727.2	1570.0	0.63	12.8	16.2	1116.8	71.1	90.9
6	640	37.5	1800.8	1635.1	0.64	13.2	17.4	1169.2	71.5	90.8

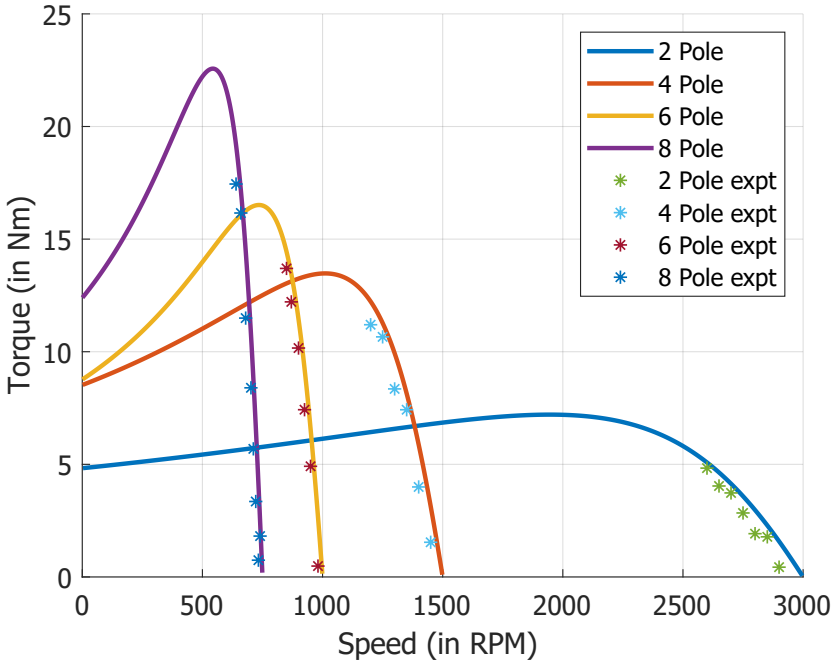

Figure 5.7: Experimental results on T-S characteristics of the machine under different pole configurations

5.4 Conclusions

In this chapter the experimental results of the fabricated prototype are presented. A good match of the equivalent circuit parameters obtained from the experimental results, with the same obtained by analytical model and FEA is reported. Further the T-S characteristics of the machine under different pole configuration is reported. Although there is a good match of the experiential T-S characteristics and analytical and FEA based characteristics presented in previous chapter there is slight mismatch as well. Several reasons can be identified for these discrepancies. One of them is that both analytical and FEM model analysed the machine with a 2D model neglecting the end ring effect of the rotor and end windings of the stator. Further, in the actual hardware prototype, the rotor bars were skewed by 1 slot. This reduces the net flux linkage [63] and thus the net torque produced. However, given the presence of the harmonics in the air-gap mmf, this skewing helps to reduce the torque ripple.

Furthermore, due to the nature of the laboratory prototyping, large lead connections were used to connect the stator terminals with the inverter. The terminal board, containing individual terminal of the slot windings also add extra resistance in the stator. The above

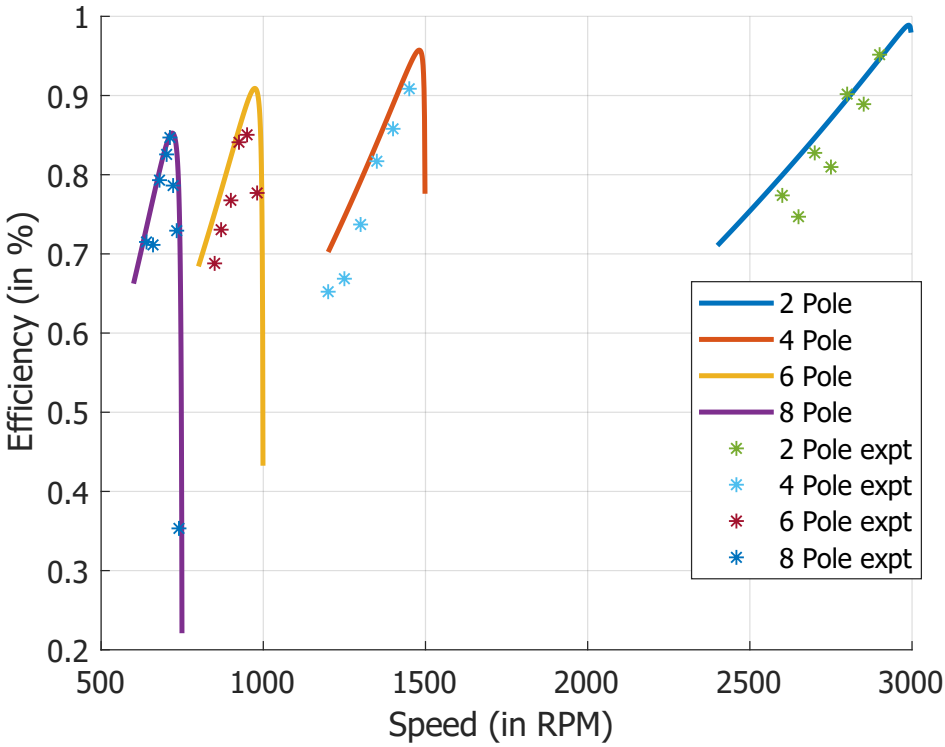

Figure 5.8: Experimental results on efficiency of the machine under different pole configurations

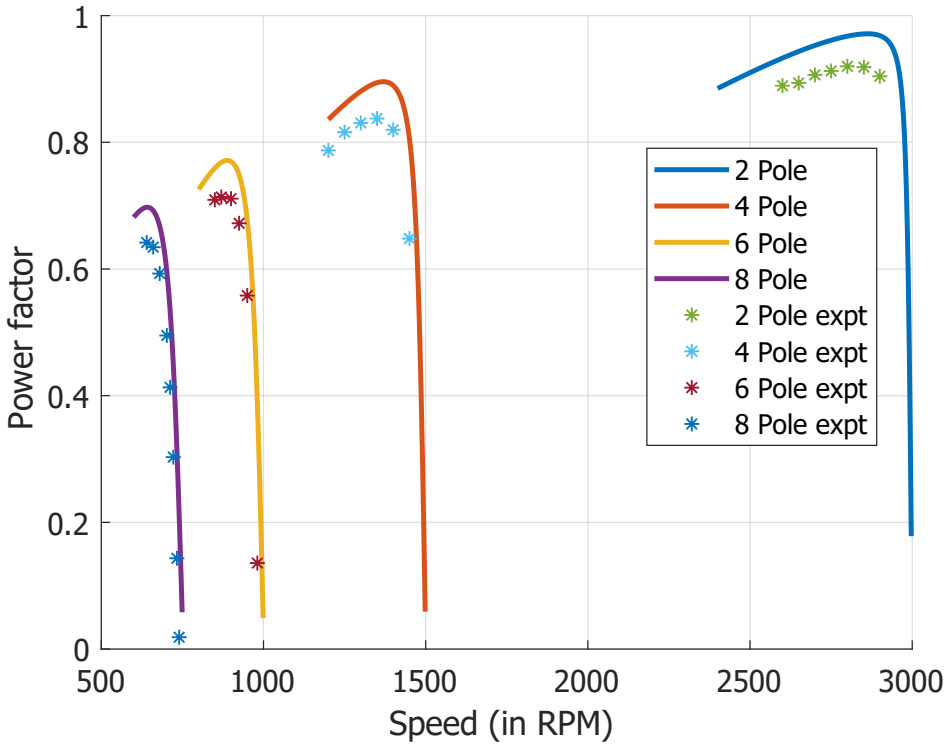

Figure 5.9: Power factor of the machine under different pole configurations

mentioned reasons explains slightly lower torque output of the machine under different pole configuration. Furthermore, the friction and windage loss of the system also reduces the torque output. However, the friction and windage loss of the system was found to be mostly negligible (less than 100 W) except 2 pole operation due to lower speed. At 3000 rpm friction and windage loss was measured to be 125 W.

Moreover, as discussed in last chapter, due to fabrication constraint, the toroidal winding was retrofitted on an off the shelf 3 phase 4 pole induction machine, hence the stator of the machine is not particularly designed and / or optimised for a pole changing operation. A complete design optimisation of the whole machine will be helpful to improve efficiency and power factor. However, the main objective of this thesis is to establish the theory of independent phase belt controlled pole-phase modulation and increase in the net torque-speed operating zone due to that. The results provided in this chapter experimentally validates the proposed concept.

Chapter 6

Dynamic Model of PPMIM and Online Pole Changing

The previous chapter experimentally validates the proposed concept of independent phase belt controlled PPMIM. Chapters 3 and 4 demonstrates the unprecedented flexibility in pole combination achievable from the proposed independent phase belt control of the PPMIM. However, the steady-state model developed in chapter 3 does not suffice to model the dynamic behaviour of the proposed machine during transients. The dynamic model is important for understanding transients during pole changing. This chapter focuses on the development of the dynamic model of the machine. The developed model has been used to understand the dynamics of the machine during pole changing. Further a closed loop speed control scheme along with a ramp transition from one pole configuration to another has been simulated by using the dynamic model of the machine. Finally experimental results have been reported for the online pole changing of the PPMIM.

6.1 Introduction

The dynamic model of conventional three phase induction machine is given as (in term of an arbitrary d and q axis quantities) [90]

$$v_{ds} = i_{ds}R_s + \frac{d}{dt}\lambda_{ds} - \dot{\Theta}_s\lambda_{qs} \tag{6.1}$$

$$v_{qs} = i_{qs}R_s + \frac{d}{dt}\lambda_{qs} + \dot{\Theta}_s\lambda_{ds} \tag{6.2}$$

$$v_{dr} = 0 = i_{dr}R_r + \frac{d}{dt}\lambda_{dr} - \dot{\Theta}_r\lambda_{qr} \tag{6.3}$$

$$v_{qr} = 0 = i_{qr}R_r + \frac{d}{dt}\lambda_{qr} + \dot{\Theta}_r\lambda_{dr} \tag{6.4}$$

where λ denotes the flux linkage, given as below:

$$\lambda_{ds} = L_s i_{ds} + M i_{dr} \tag{6.5}$$

$$\lambda_{qs} = L_s i_{qs} + M i_{qr} \tag{6.6}$$

$$\lambda_{dr} = L_r i_{dr} + M i_{ds} \tag{6.7}$$

$$\lambda_{qr} = L_r i_{qr} + M i_{qr} \tag{6.8}$$

L_s, and L_r are stator and rotor self inductances given as below

$$L_s = M + L_{ls} \tag{6.9}$$

$$L_r = M + L_{lr} \tag{6.10}$$

$\dot{\Theta}_s$ and $\dot{\Theta}_r$ are the derivative of the angle between stator and rotor axes with the reference axis [78] respectively. R_s and R_r are the stator and rotor resistance respectively, L_{ls} and L_{lr} are leakage inductance, and M is the mutual inductance term. The electromagnetic torque produced by the machine is given as

$$T_{em} = \frac{3}{2}p(\lambda_{ds}i_{qs} - \lambda_{qs}i_{ds}) \tag{6.11}$$

It is well known that for a conventional three phase machine, the Park transformation can be used to obtain the DQ machine parameters [6]. [76] discusses the derivation of these transformations for a generalized PPM IM by looking at the winding function of stator and rotor phases. The model derived in [76] cannot be directly applied due to the inherent difference of the winding connection of the proposed machine compared to the previously reported PPMIM, which is discussed in [63]. However, a similar approach can be taken for the proposed machine by using the winding functions derived in the chapter 3. Furthermore,

as discussed later, [63] does not provide a closed-form expression of the rotor inductance terms, which has been derived here as well to obtain a set of complete analytical closed-form expressions.

6.2 Dynamic model of the machine

The development of the dynamic model of the PPMIM can be studied as a two step process - first the dynamic model of the machine is developed in terms of the phases (*abc* domain), and then transformation of the obtained *abc* domain model into a stationary orthogonal reference frame ($\alpha\beta$ domain) through vector space decomposition [76] to simplify the phase domain model. Further the $\alpha\beta$ domain model can be transformed to a rotating reference frame (dq domain) by the suitable transformation.

6.2.1 Dynamic model in phase domain

A generic machine dynamic model of the proposed machine in *abc* reference frame can be given as [90]

$$v_s = R_s i_s + \frac{d}{dt}\lambda_S \tag{6.12}$$

$$v_r = 0 = R_r i_r + \frac{d}{dt}\lambda_r \tag{6.13}$$

$$\lambda_s = L_s i_s + L_{sr} i_r \tag{6.14}$$

$$\lambda_r = L'_{sr} i_s + L_r i_r \tag{6.15}$$

where v_s and v_r are stator and rotor voltage vectors, i_S and i_r are stator and rotor current vectors (in *abc* reference frame) respectively. Further, λ_s and λ_r are stator and rotor flux linkages. R_s is the diagonal matrix with stator phase resistance and R_r is the diagonal matrix with rotor phase resistance. L_s is the self inductance matrix of the machine, where diagonal terms presents stator phase self inductance, and non-diagonal entries represent mutual inductance of the stator phases. Similarly L_r is defined as the self inductance matrix of the rotor, and L_{sr} is the stator - rotor mutual inductance matrix. Further, L_s and L_r can be separated into the leakage inductance and mutual inductance terms as below:

$$L_s = L_{ls} + L_{ms} \tag{6.16}$$

and

$$L_r = L_{lr} + L_{mr} \tag{6.17}$$

where L_{ls} and L_{lr} are diagonal matrices with the stator and rotor leakage terms respectively. L_{ms} and L_{mr} are the mutual inductance terms of the stator and rotor respectively. Given the machine has m number of stator phases, the vectors of stator quantities (v_s, i_s and λ_s) has the dimension of m. However, for squirrel cage IM, the number of rotor phase is not specifically defined, which need to be fixed to obtain the dimensions of the vectors of rotor quantities (v_r, i_r and λ_r). It has been argued that given there are sufficient number of rotor phases, it is convenient to assume the number of rotor phases is the same as for the stator [76, 90], as that will make the transformation matrices for both stator and rotor the same, making the derivation simpler. However, as mentioned in [6], this approach is not strictly mathematically correct - as it fails to take cage structure of the rotor into account. Further, [76] clearly acknowledges due to this approximation of the same rotor phases, the winding function of the rotor can not be obtained in a closed analytical form. Hence in this thesis, the rotor is modelled more accurately by treating each of the bars. Taking the number of rotor bars to be Q_r the dimension of the vectors of rotor quantities become Q_r. Further, the stator to rotor mutual inductance matrix takes a dimension of $m \times Q_r$. By modelling the rotor with actual physical cage bars, this model enables the study of the effects from higher harmonics. As the proposed PPMIM is intended to operate under different pole configuration, this model will enable design of the number of rotor bars for an optimal design. For the rest of the derivation of the dynamic model of the machine, the matrices are represented as bold upper case letters, scalar quantities as lower case letters and vectors with lowercase letters with arrowhead ($\rightarrow$) on top. Further the matrix and vector dimensions are mentioned at subscript when they are defined. The parameter matrices in the Eqn. 6.12 - 6.17 can be expressed as below :

$$R_s = \begin{bmatrix} r_s & 0 & \cdots & 0 \\ 0 & r_s & \cdots & 0 \\ \vdots & \vdots & \ddots & 0 \\ 0 & 0 & 0 & r_s \end{bmatrix}_{m \times m} \tag{6.18}$$

$$R_r = \begin{bmatrix} r_r & 0 & \cdots & 0 \\ 0 & r_r & \cdots & 0 \\ \vdots & \vdots & \ddots & 0 \\ 0 & 0 & 0 & r_r \end{bmatrix}_{Q_r \times Q_r} \tag{6.19}$$

$$L_s = \begin{bmatrix} l_{ls} & 0 & \cdots & 0 \\ 0 & l_{ls} & \cdots & 0 \\ \vdots & \vdots & \ddots & 0 \\ 0 & 0 & 0 & l_{ls} \end{bmatrix}_{m \times m} + \begin{bmatrix} l_{sm} & l_{s1,2} & \cdots & l_{s1,m} \\ l_{s2,1} & l_{sm} & \cdots & l_{s2,m} \\ \vdots & \vdots & \ddots & l_{sm-1,m} \\ l_{sm,1} & l_{sm,2} & \cdots & l_{sm} \end{bmatrix}_{m \times m} \tag{6.20}$$

$$L_r = \begin{bmatrix} l_{lr} & 0 & \cdots & 0 \\ 0 & l_{lr} & \cdots & 0 \\ \vdots & \vdots & \ddots & 0 \\ 0 & 0 & 0 & l_{lr} \end{bmatrix}_{Q_r \times Q_r} + \begin{bmatrix} l_{rm} & l_{r1,2} & \cdots & l_{r1,m} \\ l_{r2,1} & l_{rm} & \cdots & l_{r2,m} \\ \vdots & \vdots & \ddots & l_{m-1,m} \\ l_{rm,1} & l_{rm,2} & \cdots & l_{rm} \end{bmatrix}_{Q_r \times Q_r} \tag{6.21}$$

and

$$L_{sr} = \begin{bmatrix} l_{srm} & l_{sr1,2} & \cdots & l_{sr1,m} \\ l_{sr2,1} & l_{srm} & \cdots & l_{sr2,m} \\ \vdots & \vdots & \ddots & l_{srm-1,m} \\ l_{srm,1} & l_{srm,2} & \cdots & l_{srm} \end{bmatrix}_{m \times Q_r} \tag{6.22}$$

The voltage, current and flux-linkage vectors of the stator are m dimensional vector and for rotor they are Q_r dimensional vectors. The terms in the Eqn. 6.18 - 6.22 has already been derived in chapter 3, except the stator and rotor phase - phase mutual inductance terms and stator-rotor phase mutual inductances. The stator phase i to phase j mutual inductance can be defined as [76]:

$$l_{si,j} = \frac{\mu_0 r L_e}{g} \int_0^{2\pi} \mathscr{N}_{si}(\theta_s) \mathscr{N}_{sj}(\theta_s) d\theta_s \tag{6.23}$$

where $\mathscr{N}_{sk}(\theta_s)$ is the winding function of the k^{th} stator phase. Modifying the stator winding function given in Eqn. 3.34 for k^{th} phase $\mathscr{N}_{sk}(\theta_s)$ is given as:

$$\mathscr{N}_{sk}(\theta_s) = \frac{qN_s}{\pi} \sum_{\nu=1}^{\infty} \frac{1}{\nu} k_{q,\nu} \sin \nu(\theta_s - (k-1)\frac{2\pi}{m}) \tag{6.24}$$

Hence $l_{si,j}$ can be obtained as:

$$\begin{aligned} l_{si,j} &= (\tfrac{qN_s}{\pi})^2 \tfrac{\mu_0 r L_e}{g} \pi \sum_{\nu=1}^{\infty} (\tfrac{k_{q,\nu}}{\nu})^2 \cos \nu \tfrac{2\pi}{m}(j-i) \\ &= l_{sm} \sum_{\nu=1}^{\infty} (\tfrac{k_{q,\nu}}{\nu})^2 \cos \nu \tfrac{2\pi}{m}(j-i) \end{aligned} \tag{6.25}$$

where l_{sm} is given as

$$l_{sm} = (\frac{qN_s}{\pi})^2 \frac{\mu_0 r L_e}{g} \pi \tag{6.26}$$

Following the same methodology and using the rotor winding function derived in Eqn. 3.35 the rotor phase i to phase j mutual inductance can be obtained as

$$l_{ri,j} = l_{rm} \sum_{\nu=1}^{\infty} \frac{1}{\nu} \cos \nu \frac{2\pi}{Q_r}(j-i) \tag{6.27}$$

where l_{rm} is given as

$$l_{rm} = (\frac{1}{\pi})^2 \frac{\mu_0 r L_e}{g} \pi \tag{6.28}$$

Following the similar definition of the inductance, the stator - rotor mutual inductance can be defined as

$$l_{sri,j} = \frac{\mu_0 r L_e}{g} \int_0^{2\pi} \mathscr{N}_{si}(\theta_s) \mathscr{N}_{rj}(\theta_r) d\theta_s \tag{6.29}$$

The relationship between stator and rotor angle is given as

$$\theta_r = \theta_s + \theta_{rm} \tag{6.30}$$

where θ_{rm} is the angle between stator and rotor. Hence 6.29 can be evaluated as

$$l_{sri,j} = \frac{\mu_0 r L_e}{g} \frac{qN_s}{\pi} \sum_{\nu=1}^{\infty} (\frac{k_{q,\nu}}{\nu^2}) \cos \nu \left(\frac{2\pi}{m}(i-1) - \frac{2\pi}{Q_r}(j-1) + \theta_{rm} \right) \tag{6.31}$$

It should be noted the quantities in both stator and rotor self inductance L_s and L_r are independent of the stator to rotor relative position, whereas the stator to rotor mutual inductances are varying with respect to stator to rotor angle (θ_{rm}). This is valid under the assumption of smooth air-gap and if the slot effect is neglected. Further, the rotor quantities are obtained by taking each of the rotor bars as a phase, hence the obtained expressions do not involve an effective turns ratio.

6.2.2 Dynamic model in the stationary reference frame (α, β)

Having obtained the dynamic model of the machine in the phase domain, the vector space transformation is to be obtained to transform the derived dynamic model of the machine from the phase domain to $\alpha\beta$ domain. As it can be seen from the dimensions of the equation matrices in the phase model there are m stator equations and Q_r rotor equations. The stationary reference frame model transforms both stator and rotor equations into a set of m orthogonal vectors. Hence the stator transformation matrix would have a dimension of $m \times m$. Furthermore, as [91] points out, the transformation matrix would have a dimension of $Q_r \times Q_r$ for the rotor.

For a generic machine with m independent phase belts, $\frac{m}{2} - 1$ pole pair combinations can be achieved. Hence $m-2$ orthogonal basis vectors can be defined (2 vector for each pole configuration - one with α and the other with β) from these pole configurations for the stator transformation matrix. These basis vectors directly correspond to electromagnetic energy conversion. Taking the first stator phase as the reference, α_i and β_i transformation vector for i^{th} pole pair for the m phase machine are given as below:

$$\left\{ \begin{array}{c} \alpha_i \\ \beta_i \end{array} \right\}_{stator} = \left\{ \begin{array}{ccccc} \cos(0) & \cos(\frac{2\pi}{m})i & \cos 2(\frac{2\pi}{m})i & \cdots & \cos(m-1)(\frac{2\pi}{m})i \\ \sin(0) & \sin(\frac{2\pi}{m})i & \sin 2(\frac{2\pi}{m})i & \cdots & \sin(m-1)(\frac{2\pi}{m})i \end{array} \right\} \tag{6.32}$$

where $i = 1, 2, \ldots, \frac{m}{2} - 1$. At least two zero vectors which are orthogonal to the rest (α_i and β_i) are needed for an even number of phases [92] . The inner product of the zero vectors with a balanced machine variable must be zero. These two zero vectors can be easily formulated by setting $i = \frac{m}{2}$ and $i = m$ in the following:

$$\overrightarrow{z_i} = \left\{ \begin{array}{ccccc} \cos(0) & \cos(\frac{2\pi}{m})i & \cos 2(\frac{2\pi}{m})i & \cdots & \cos(m-1)(\frac{2\pi}{m})i \end{array} \right\} \tag{6.33}$$

Hence the stator transformation matrix $K_{s(abc-\alpha\beta)}$ is given as

$$K_{s(abc-\alpha\beta)} = \begin{bmatrix} \cos(0) & \cos(\frac{2\pi}{m}) & \cos 2(\frac{2\pi}{m}) & \cdots & \cos(m-1)(\frac{2\pi}{m}) \\ \sin(0) & \sin(\frac{2\pi}{m}) & \sin 2(\frac{2\pi}{m}) & \cdots & \sin(m-1)(\frac{2\pi}{m}) \\ \cos(0)2 & \cos(\frac{2\pi}{m})2 & \cos 2(\frac{2\pi}{m})2 & \cdots & \cos(m-1)(\frac{2\pi}{m})2 \\ \sin(0)2 & \sin(\frac{2\pi}{m})2 & \sin 2(\frac{2\pi}{m})2 & \cdots & \sin(m-1)(\frac{2\pi}{m})2 \\ \vdots & \vdots & \vdots & \vdots & \vdots \\ \cos(0) & \cos(\frac{2\pi}{m})(\frac{m}{2}-1) & \cos 2(\frac{2\pi}{m})(\frac{m}{2}-1) & \cdots & \cos(m-1)(\frac{2\pi}{m})(\frac{m}{2}-1) \\ \sin(0) & \sin(\frac{2\pi}{m})(\frac{m}{2}-1) & \sin 2(\frac{2\pi}{m})(\frac{m}{2}-1) & \cdots & \sin(m-1)(\frac{2\pi}{m})(\frac{m}{2}-1) \\ \frac{1}{\sqrt{2}} & -\frac{1}{\sqrt{2}} & \frac{1}{\sqrt{2}} & \cdots & -\frac{1}{\sqrt{2}} \\ \frac{1}{\sqrt{2}} & \frac{1}{\sqrt{2}} & \frac{1}{\sqrt{2}} & \cdots & \frac{1}{\sqrt{2}} \end{bmatrix}_{m\times m} \tag{6.34}$$

Adding the $\sqrt{2}$ scaling factor at the zero vectors allows the following to be written

$$K_{s(abc-\alpha\beta)} \times K'_{s(abc-\alpha\beta)} = (\frac{m}{2})I_{m\times m} \tag{6.35}$$

where $I_{m\times m}$ is the identity matrix of order m. This will be later used to find the inverse of the transformation. Following the similar approach the orthogonal basis vector for the i th pole pair in the rotor transformation matrix can be defined as

$$\begin{Bmatrix} \alpha_i \\ \beta_i \end{Bmatrix}_{rotor} = \begin{Bmatrix} \cos(0) & \cos(\frac{2\pi}{Q_r})i & \cos 2(\frac{2\pi}{Q_r})i & \cdots & \cos(Q_r-1)(\frac{2\pi}{Q_r})i \\ \sin(0) & \sin(\frac{2\pi}{Q_r})i & \sin 2(\frac{2\pi}{Q_r})i & \cdots & \sin(Q_r-1)(\frac{2\pi}{Q_r})i \end{Bmatrix} \tag{6.36}$$

This will construct $m-2$ rows of the rotor transformation matrix. As the transformation intends to transfer the rotor quantities corresponding to the stator pole pairs, the rest of the rows of the rotor transformation matrix have to be zero vectors. Here as well the zero vectors will take a form similar to stator given as

$$\overrightarrow{z_i} = \begin{Bmatrix} \cos(0) & \cos(\frac{2\pi}{Q_r})i & \cos 2(\frac{2\pi}{Q_r})i & \cdots & \cos(Q_r-1)(\frac{2\pi}{Q_r})i \end{Bmatrix} \tag{6.37}$$

which can be found by suitable choice of i in the above expression. Assuming Q_r to be even (which is the case for most of the rotor), a similar strategy as for the stator can be taken to

construct the transformation matrix for the rotor as below:

$$K_{r(abc-\alpha\beta)} = \begin{bmatrix} \cos(0) & \cos(\frac{2\pi}{Q_r}) & \cos 2(\frac{2\pi}{Q_r}) & \cdots & \cos(Q_r-1)(\frac{2\pi}{Q_r}) \\ \sin(0) & \sin(\frac{2\pi}{Q_r}) & \sin 2(\frac{2\pi}{Q_r}) & \cdots & \sin(Q_r-1)(\frac{2\pi}{Q_r}) \\ \cos(0)2 & \cos(\frac{2\pi}{Q_r})2 & \cos 2(\frac{2\pi}{Q_r})2 & \cdots & \cos(Q_r-1)(\frac{2\pi}{Q_r})2 \\ \sin(0)2 & \sin(\frac{2\pi}{Q_r})2 & \sin 2(\frac{2\pi}{Q_r})2 & \cdots & \sin(Q_r-1)(\frac{2\pi}{Q_r})2 \\ \vdots & \vdots & \vdots & \vdots & \vdots \\ \cos(0) & \cos(\frac{2\pi}{Q_r})(\frac{m}{2}-1) & \cos 2(\frac{2\pi}{Q_r})(\frac{m}{2}-1) & \cdots & \cos(Q_r-1)(\frac{2\pi}{Q_r})(\frac{m}{2}-1) \\ \sin(0) & \sin(\frac{2\pi}{Q_r})(\frac{m}{2}-1) & \sin 2(\frac{2\pi}{Q_r})(\frac{m}{2}-1) & \cdots & \sin(Q_r-1)(\frac{2\pi}{Q_r})(\frac{m}{2}-1) \\ \vdots & \vdots & \vdots & \vdots & \vdots \\ \cos(0) & \cos(\frac{2\pi}{Q_r})(\frac{Q_r}{2}-1) & \cos 2(\frac{2\pi}{Q_r})(\frac{Q_r}{2}-1) & \cdots & \cos(Q_r-1)(\frac{2\pi}{Q_r})(\frac{Q_r}{2}-1) \\ \sin(0) & \sin(\frac{2\pi}{Q_r})(\frac{Q_r}{2}-1) & \sin 2(\frac{2\pi}{Q_r})(\frac{Q_r}{2}-1) & \cdots & \sin(Q_r-1)(\frac{2\pi}{Q_r})(\frac{Q_r}{2}-1) \\ \frac{1}{\sqrt{2}} & -\frac{1}{\sqrt{2}} & \frac{1}{\sqrt{2}} & \cdots & -\frac{1}{\sqrt{2}} \\ \frac{1}{\sqrt{2}} & \frac{1}{\sqrt{2}} & \frac{1}{\sqrt{2}} & \cdots & \frac{1}{\sqrt{2}} \end{bmatrix}_{Q_r \times Q_r} \tag{6.38}$$

Similar to stator transformation, the rotor transformation also satisfies

$$K_{r(abc-\alpha\beta)} \times K_{r(abc-\alpha\beta)}{}' = (\frac{Q_r}{2}) I_{Q_r \times Q_r} \tag{6.39}$$

This model is an extension of the complex vector model of 3 phase squirrel cage IM reported in [91] for a generalized *m* phase pole phase modulated machine. Using this transformation Eqn. 6.12 can be transformed in $\alpha\beta$ space as

$$\begin{aligned} \overrightarrow{v}_{s(\alpha\beta)} &= R_s \overrightarrow{i}_{s(\alpha\beta)} + \tfrac{d}{dt} K_{s(abc-\alpha\beta)} (L_s \overrightarrow{i}_s + L_{sr} \overrightarrow{i}_r) \\ &= R_s \overrightarrow{i}_{s(\alpha\beta)} + \tfrac{d}{dt} K_{s(abc-\alpha\beta)} (L_{ls} \overrightarrow{i}_s + L_{ms} \overrightarrow{i}_s + L_{sr} \overrightarrow{i}_r) \\ &= R_s \overrightarrow{i}_{s(\alpha\beta)} + \tfrac{d}{dt} (L_{ls} \overrightarrow{i}_{s(\alpha\beta)} + K_{s(abc-\alpha\beta)} L_{ms} K^{-1}_{s(abc-\alpha\beta)} \overrightarrow{i}_{s(\alpha\beta)} \cdots \\ &\qquad \cdots + K_{s(abc-\alpha\beta)} L_{sr} K^{-1}_{r(abc-\alpha\beta)} \overrightarrow{i}_{r(\alpha\beta)}) \end{aligned} \tag{6.40}$$

Similarly Eqn. 6.13 can be transformed as

$$\begin{aligned} \overrightarrow{v}_{r(\alpha\beta)} &= R_r \overrightarrow{i}_{r(\alpha\beta)} + \tfrac{d}{dt} K_{r(abc-\alpha\beta)} (L'_{sr} \overrightarrow{i}_s + L_r \overrightarrow{i}_r) \\ 0 &= R_r \overrightarrow{i}_{r(\alpha\beta)} + \tfrac{d}{dt} (L_{lr} \overrightarrow{i}_{r(\alpha\beta)} + K_{r(abc-\alpha\beta)} L_{mr} K^{-1}_{r(abc-\alpha\beta)} \overrightarrow{i}_{r(\alpha\beta)} \cdots \\ &\qquad \cdots + K_{r(abc-\alpha\beta)} L'_{sr} K^{-1}_{s(abc-\alpha\beta)} \overrightarrow{i}_{s(\alpha\beta)}) \end{aligned} \tag{6.41}$$

Eqn. 6.40 and 6.41 can be rewritten as

$$\overrightarrow{v}_{s(\alpha\beta)} = R_s \overrightarrow{i}_{s(\alpha\beta)} + \frac{d}{dt}\overrightarrow{\lambda}_{s(\alpha\beta)} \tag{6.42}$$

where

$$\overrightarrow{\lambda}_{s(\alpha\beta)} = L_{ls} \overrightarrow{i}_{s(\alpha\beta)} + L_{ms-\alpha\beta} \overrightarrow{i}_{s(\alpha\beta)} + L_{sr-\alpha\beta} \overrightarrow{i}_{r(\alpha\beta)} \tag{6.43}$$

and

$$\overrightarrow{v}_{r(\alpha\beta)} = 0 = R_r \overrightarrow{i}_{r(\alpha\beta)} + \frac{d}{dt}\overrightarrow{\lambda}_{r(\alpha\beta)} \tag{6.44}$$

where

$$\overrightarrow{\lambda}_{r(\alpha\beta)} = L_{lr} \overrightarrow{i}_{r(\alpha\beta)} + L_{mr-\alpha\beta} \overrightarrow{i}_{r(\alpha\beta)} + L_{rs-\alpha\beta} \overrightarrow{i}_{s(\alpha\beta)} \tag{6.45}$$

The new inductance matrices are defined as below:

$$\begin{cases} L_{ms-\alpha\beta} = K_{s(abc-\alpha\beta)} L_{ms} K^{-1}_{s(abc-\alpha\beta)} \\ L_{sr-\alpha\beta} = K_{s(abc-\alpha\beta)} L_{sr} K^{-1}_{r(abc-\alpha\beta)} \\ L_{mr-\alpha\beta} = K_{r(abc-\alpha\beta)} L_{mr} K^{-1}_{r(abc-\alpha\beta)} \\ L_{rs-\alpha\beta} = K_{r(abc-\alpha\beta)} L'_{sr} K^{-1}_{s(abc-\alpha\beta)} \end{cases} \tag{6.46}$$

Utilising the Eqn 6.35 and 6.39 the equivalent inductances in Eqn. 6.46 can be rewritten as

$$\begin{cases} L_{ms-\alpha\beta} = (\frac{2}{m}) K_{s(abc-\alpha\beta)} L_{ms} K'_{s(abc-\alpha\beta)} \\ L_{sr-\alpha\beta} = (\frac{2}{Q_r}) K_{s(abc-\alpha\beta)} L_{sr} K'_{r(abc-\alpha\beta)} \\ L_{mr-\alpha\beta} = (\frac{2}{Q_r}) K_{r(abc-\alpha\beta)} L_{mr} K'_{r(abc-\alpha\beta)} \\ L_{rs-\alpha\beta} = (\frac{2}{m}) K_{r(abc-\alpha\beta)} L'_{sr} K'_{s(abc-\alpha\beta)} \end{cases} \tag{6.47}$$

Further, due to the structure of the stator self inductance matrix, it can be shown $L_{ms-\alpha\beta}$

and $L_{mr-\alpha\beta}$ will take the following forms

$$L_{ms-\alpha\beta} = \begin{bmatrix} m_{s1} & 0 & 0 & 0 & \cdots & 0 & 0 & 0 & 0 \\ 0 & m_{s1} & 0 & 0 & \cdots & 0 & 0 & 0 & 0 \\ 0 & 0 & m_{s2} & 0 & \cdots & 0 & 0 & 0 & 0 \\ 0 & 0 & 0 & m_{s2} & \cdots & 0 & 0 & 0 & 0 \\ \vdots & \vdots & \vdots & 0 & \ddots & 0 & 0 & 0 & 0 \\ 0 & 0 & 0 & 0 & 0 & m_{s(\frac{m}{2}-1)} & 0 & 0 & 0 \\ 0 & 0 & 0 & 0 & 0 & 0 & m_{s(\frac{m}{2}-1)} & 0 & 0 \\ 0 & 0 & 0 & 0 & 0 & 0 & 0 & 0 & 0 \\ 0 & 0 & 0 & 0 & 0 & 0 & 0 & 0 & 0 \end{bmatrix}_{m\times m} \tag{6.48}$$

and

$$L_{mr-\alpha\beta} = \begin{bmatrix} m_{r1} & 0 & 0 & 0 & \cdots & 0 & 0 & 0 & \cdots & 0 \\ 0 & m_{r1} & 0 & 0 & \cdots & 0 & 0 & 0 & \cdots & 0 \\ 0 & 0 & m_{r2} & 0 & \cdots & 0 & 0 & 0 & \cdots & 0 \\ 0 & 0 & 0 & m_{r2} & \cdots & 0 & 0 & 0 & \cdots & 0 \\ \vdots & \vdots & \vdots & 0 & \ddots & 0 & 0 & 0 & \cdots & 0 \\ 0 & 0 & 0 & 0 & 0 & m_{r(\frac{m}{2}-1)} & 0 & 0 & \cdots & 0 \\ 0 & 0 & 0 & 0 & 0 & 0 & m_{r(\frac{m}{2}-1)} & 0 & \cdots & 0 \\ 0 & 0 & 0 & 0 & 0 & 0 & 0 & 0 & \cdots & 0 \\ \vdots & \vdots & \vdots & \vdots & \vdots & \vdots & \vdots & \vdots & \ddots & \vdots \\ 0 & 0 & 0 & 0 & 0 & 0 & 0 & 0 & \cdots & 0 \end{bmatrix}_{Q_r\times Q_r} \tag{6.49}$$

where m_{si} and m_{ri} are the stator and rotor self mutual inductance respectively for the i^{th} harmonic, given as below

$$m_{si} = \frac{m}{2}(\frac{qN_s}{\pi})^2 \frac{\mu_0 r L_e}{g} \pi (\frac{k_{q,i}}{i})^2 \tag{6.50}$$

and

$$m_{ri} = \frac{Q_r}{2} \frac{1}{\pi^2} \frac{\mu_0 r L_e}{g} \pi \frac{1}{i^2} \tag{6.51}$$

Further, $L_{sr-\alpha\beta}$ and $L_{rs-\alpha\beta}$ takes the following form

$$L_{sr-\alpha\beta} = \frac{m}{2} A \tag{6.52}$$

and

$$L_{rs-\alpha\beta} = \frac{Q_r}{2} A' \tag{6.53}$$

where A is given in Eqn. 6.54. m_{sri} is the stator to rotor mutual inductance for the i th harmonic given as

$$m_{sri} = \frac{\mu_0 r L_e}{g} \frac{q N_s}{\pi} \frac{k_{q,i}}{i^2} \tag{6.55}$$

In this simplification, in Eqn. 6.48 - 6.54, the harmonics orders higher than $\frac{m}{2}-1$ has been neglected as the model intends to model all $\frac{m}{2}-1$ pole configurations. To study the effect of harmonics (which will be more dominant under higher pole count - higher harmonic orders) further harmonics (higher than $\frac{m}{2}-1$) can be considered in the model. For example to study the effect of rotor bar harmonics, or stator slot harmonics, the simplified winding functions can be suitably modified to incorporate the effects of those harmonics. As it can be seen if only harmonics up to $\frac{m}{2}-1$ are considered for both stator and rotor, the mutual inductance matrices become zero for the rotor $\alpha\beta$ matrices for $i > 2(\frac{m}{2}-1)$. Hence for simplifying the calculations, the extra dimensions $(Q_r - m)$ in the rotor matrices can be truncated making the both stator and rotor matrices of the same dimensions in $\alpha\beta$ reference frame. However, if a more generalized study is intended (as mentioned before - slot harmonics, rotor bar harmonics) these dimensions should be kept.

The most important observation can be made from the structure of the inductance matrices, under this $\alpha\beta$ transformation, all the pole configurations have become decoupled. As this thesis intends to establish an electronically pole changing induction machine, the problem can be studied as a two-part problem. First, a machine is needed which can be reconfigured to different pole configurations by changing the excitation electronically. Chapter 3 established that the proposed machine can operate under different pole configuration by changing the phase angle between consecutive inverter legs. However, to achieve online pole changing of the machine, different pole configurations need to be decoupled. As this model is derived under no assumption of the stator and rotor current waveforms (unlike steady state model derivation in chapter 3, which assumed sinusoidal current excitation), the individual pole configuration can be independently controlled for an online pole changing by simply de-exciting one pole configuration and exciting the other. Under the assumption of magnetic linearity (the machine is not being saturated by excitation of one pole) the machine can be studied as the superposition of different pole configurations. This will be utilised in a later section to achieve online transition from one pole to another pole configuration.

Further, as the model has been derived by treating individual rotor bars, it would be convenient to introduce an equivalent turns ratio to refer the rotor circuit directly into stator

$$
A = \begin{bmatrix}
m_{sr1}\cos\theta_{rm} & m_{sr1}\sin\theta_{rm} & 0 & 0 & \cdots & 0 & 0 & 0 & \cdots & 0 \\
-m_{sr1}\sin\theta_{rm} & m_{sr1}\cos\theta_{rm} & 0 & 0 & \cdots & 0 & 0 & 0 & \cdots & 0 \\
0 & 0 & m_{sr2}\cos 2\theta_{rm} & m_{sr2}\sin 2\theta_{rm} & \cdots & 0 & 0 & 0 & \cdots & 0 \\
0 & 0 & -m_{sr2}\sin 2\theta_{rm} & m_{sr2}\cos 2\theta_{rm} & \cdots & 0 & 0 & 0 & \cdots & 0 \\
\vdots & \vdots & \vdots & 0 & \ddots & 0 & 0 & 0 & \cdots & 0 \\
0 & 0 & 0 & 0 & 0 & m_{sr(\frac{m}{2}-1)}\cos(\frac{m}{2}-1)\theta_{rm} & m_{sr(\frac{m}{2}-1)}\sin(\frac{m}{2}-1)\theta_{rm} & 0 & \cdots & 0 \\
0 & 0 & 0 & 0 & 0 & -m_{sr(\frac{m}{2}-1)}\sin(\frac{m}{2}-1)\theta_{rm} & m_{sr(\frac{m}{2}-1)}\cos(\frac{m}{2}-1)\theta_{rm} & 0 & \cdots & 0 \\
0 & 0 & 0 & 0 & 0 & 0 & 0 & 0 & \cdots & 0 \\
0 & 0 & 0 & 0 & 0 & 0 & 0 & 0 & \cdots & 0
\end{bmatrix}_{m\times Q_r} \tag{6.54}
$$

circuits. Eqn. 6.40 can be rewritten as below

$$\overrightarrow{v}_{s(\alpha\beta)} = R_s \overrightarrow{i}_{s(\alpha\beta)} + \frac{d}{dt}(L_{ls} \overrightarrow{i}_{s(\alpha\beta)} + L_{ms-\alpha\beta} \overrightarrow{i}_{s(\alpha\beta)} + L_{ms-\alpha\beta} B \overrightarrow{i}_{r'(\alpha\beta)}) \tag{6.56}$$

where $\overrightarrow{i}_{r'(\alpha\beta)}$ is defined as $\overrightarrow{k}\overrightarrow{i}_{r(\alpha\beta)}$ and $\overrightarrow{k}$ is a row vector defined for i^{th}pole pair as

$$k_i = \frac{\frac{m}{2} m_{sri}}{m_{si}} = \frac{1}{qN_s k_{q,i}} \tag{6.57}$$

As the zero vectors do not have a mutual inductance term, k_i is defined for the electromagnetic energy conversion vectors - i.e. $i = 1, 2 ... \frac{m}{2} - 1$ only. Further, the matrix B is defined as

$$B = \begin{bmatrix} \cos\theta_{rm} & \sin\theta_{rm} & 0 & 0 & \cdots & 0 & 0 & 0 & 0 \\ -\sin\theta_{rm} & \cos\theta_{rm} & 0 & 0 & \cdots & 0 & 0 & 0 & 0 \\ 0 & 0 & \cos 2\theta_{rm} & \sin 2\theta_{rm} & \cdots & 0 & 0 & 0 & 0 \\ 0 & 0 & -\sin 2\theta_{rm} & \cos 2\theta_{rm} & \cdots & 0 & 0 & 0 & 0 \\ \vdots & \vdots & \vdots & 0 & \ddots & 0 & 0 & 0 & 0 \\ 0 & 0 & 0 & 0 & 0 & \cos(\frac{m}{2}-1)\theta_{rm} & \sin(\frac{m}{2}-1)\theta_{rm} & 0 & 0 \\ 0 & 0 & 0 & 0 & 0 & -\sin(\frac{m}{2}-1)\theta_{rm} & \cos(\frac{m}{2}-1)\theta_{rm} & 0 & 0 \\ 0 & 0 & 0 & 0 & 0 & 0 & 0 & 0 & 0 \\ 0 & 0 & 0 & 0 & 0 & 0 & 0 & 0 & 0 \end{bmatrix}_{m \times m} \tag{6.58}$$

Similarly the rotor equation (given in 6.41) can be rewritten as

$$0 = R_r \overrightarrow{i}_{r'(\alpha\beta)} + \frac{d}{dt}(L_{lr} \overrightarrow{i}_{r'(\alpha\beta)} + L_{mr-\alpha\beta} \overrightarrow{i}_{r'(\alpha\beta)} + kL_{rs-\alpha\beta} \overrightarrow{i}_{s(\alpha\beta)}) \tag{6.59}$$

It can be further shown that $m_{ri} = k_i \frac{Q_r}{2} m_{sri}$. Hence the above equation can be rewritten as

$$\begin{aligned} 0 &= R_r \overrightarrow{i}_{r'(\alpha\beta)} + \frac{d}{dt}(L_{lr} \overrightarrow{i}_{r'(\alpha\beta)} + L_{mr-\alpha\beta} \overrightarrow{i}_{r'(\alpha\beta)} + L_{mr-\alpha\beta} B \overrightarrow{i}_{s(\alpha\beta)}) \\ &= R_{r'} \overrightarrow{i}_{r'(\alpha\beta)} + \frac{d}{dt}(L_{lr'} \overrightarrow{i}_{r'(\alpha\beta)} + L_{ms-\alpha\beta} \overrightarrow{i}_{r'(\alpha\beta)} + L_{ms-\alpha\beta} B \overrightarrow{i}_{s(\alpha\beta)}) \end{aligned} \tag{6.60}$$

where $R_{r'}$ and $L_{lr'}$ is defined as $\overrightarrow{k}_2 R_r$ and $\overrightarrow{k}_2 L_{lr}$ respectively, where $\overrightarrow{k}_2$ is a row vector defined as

$$k_{2i} = \frac{m_{si}}{m_{ri}} = \frac{mN_s^2 k_{q,i}^2 q^2}{Q_r} = \frac{Q_s N_s^2 k_{q,i}^2 q}{Q_r} \tag{6.61}$$

It can be noted this turns ratio obtained here is exactly the same as the turns ratio k_{rs} derived

earlier in the steady state equivalent circuit model in Eqn. 3.72. Following the introduction of the turns ratio, the stator and rotor dynamic equations only contains one mutual inductance term given as $L_{ms-\alpha\beta}$. However, the $\alpha\beta$ reference frame equations contain the position dependent mutual coupling (between α and β of the corresponding pole pair) matrix B. Hence in the next section these equations are transferred to the rotating reference frame to eliminate the position dependent terms.

6.2.3 Dynamic model in rotating reference frame (dq)

It is well known that the position dependent mutual coupling terms (in B) can be eliminated by referring all the equations into a common reference frame - which is usually denoted as $dq0$ frame in conventional three phase machine model or arbitrary reference frame model. As the stator and rotor reference frames are rotating at different speeds, separate transformation matrices (from α,β to dq) have to be developed for the stator and the rotor. Furthermore, the speed of the dq reference frames corresponding to p pole pair is rotating at p times of the speed. Incorporating this information the transformation matrices can be defined as partial block diagonal format as below:

$$K_{s(\alpha\beta-dq)} = \begin{bmatrix} K_1 & 0 & \cdots & 0 & 0 & 0 \\ 0 & K_2 & \cdots & 0 & 0 & 0 \\ \vdots & \vdots & \ddots & 0 & 0 & 0 \\ 0 & 0 & \cdots & K_{(\frac{m}{2}-1)} & 0 & 0 \\ 0 & 0 & \cdots & 0 & 1 & 0 \\ 0 & 0 & \cdots & 0 & 0 & 1 \end{bmatrix}_{m\times m} \tag{6.62}$$

and

$$K_{r(\alpha\beta-dq)} = \begin{bmatrix} K_1 & 0 & \cdots & 0 & 0 & \cdots & 0 \\ 0 & K_2 & \cdots & 0 & 0 & \cdots & 0 \\ \vdots & \vdots & \ddots & 0 & 0 & \cdots & 0 \\ 0 & 0 & \cdots & K_{(\frac{m}{2}-1)} & 0 & \cdots & 0 \\ 0 & 0 & \cdots & 0 & 1 & \cdots & 0 \\ \vdots & \vdots & \vdots & \vdots & \vdots & \ddots & \vdots \\ 0 & 0 & \cdots & 0 & 0 & 0 & 1 \end{bmatrix}_{Q_r\times Q_r} \tag{6.63}$$

where K_i is the 2×2 rotational transformation matrix defined as

$$K_i = \begin{bmatrix} \cos(\phi_p) & \sin(\phi_p) \\ -\sin(\phi_p) & \cos(\phi_p) \end{bmatrix} \tag{6.64}$$

where ϕ_p is the angle between the rotating d axis of the p^{th} pole pair count and α axis. Hence ϕ_i for stator and rotor is defined as ϕ_{sp} and ϕ_{rp} as below

$$\phi_{sp} = p \int \omega_m \, dt \tag{6.65}$$

$$\phi_{rp} = p \int (\omega_m - \omega_{rm}) \, dt \tag{6.66}$$

where ω_m is the speed of the dq reference frame, and ω_{rm} is the speed of the rotor. Furthermore, as discussed earlier, if the harmonics effect of the machine is not being studied, the rotor matrix can be truncated to be $m \times m$ to make the stator and rotor matrices of same dimensions. Similar to previous transformations $K_{s(\alpha\beta-dq)}$ and $K_{r(\alpha\beta-dq)}$ are orthogonal i.e. their transpose is equal to their inverse. Using the stator transformation ($K_{s(\alpha\beta-dq)}$) on Eqn. 6.56 following can be derived:

$$\begin{aligned} \overrightarrow{v}_{s(dq)} &= R_s \overrightarrow{i}_{s(dq)} + K_{s(\alpha\beta-dq)}\left(\tfrac{d}{dt}\left(L_{ls} \overrightarrow{i}_{s(\alpha\beta)} + L_{ms-\alpha\beta} \overrightarrow{i}_{s(\alpha\beta)} + L_{ms-\alpha\beta} B \overrightarrow{i}_{r'(\alpha\beta)}\right)\right) \\ &= R_s \overrightarrow{i}_{s(dq)} + L_{ls} \tfrac{d}{dt} \overrightarrow{i}_{s(dq)} + L_{ms-\alpha\beta} \tfrac{d}{dt} \overrightarrow{i}_{s(dq)} \cdots \\ &\quad \cdots + L_{ms-\alpha\beta} K_{s(\alpha\beta-dq)} \tfrac{d}{dt} \left(B K'_{r(\alpha\beta-dq)} \overrightarrow{i}_{r'(dq)}\right) \end{aligned} \tag{6.67}$$

As the matrices $K_{s(\alpha\beta-dq)}$, $K_{r(\alpha\beta-dq)}$ and B are block diagonal, the last term of the above equation $L_{ms-\alpha\beta} K_{s(\alpha\beta-dq)} \frac{d}{dt} (B K'_{r(\alpha\beta-dq)} \overrightarrow{i}_{r'(dq)})$ can be simplified by looking into the block corresponding to p^{th} pole pair given as Eqn. 6.68. Putting $\theta_{rm} = -\int \omega_{rm} \, dt$, $(\phi_{sp} + p\theta_{rm} - \phi_{rp})$ can be found to be 0, hence the the expression in Eqn. 6.68 can be simplified as

$$-m_{sp}(i\omega_m) \begin{bmatrix} 0 & 1 \\ -1 & 0 \end{bmatrix} \begin{bmatrix} i_{rd_p} \\ i_{rq_p} \end{bmatrix} + m_{sp} \begin{bmatrix} 1 & 0 \\ 0 & 1 \end{bmatrix} \frac{d}{dt} \left(\begin{bmatrix} i_{rd_p} \\ i_{rq_p} \end{bmatrix} \right) \tag{6.69}$$

$$
\begin{aligned}
& m_{si}\begin{bmatrix}\cos(\phi_{si}) & \sin(\phi_{si})\\ -\sin(\phi_{si}) & \cos(\phi_{si})\end{bmatrix}\frac{d}{dt}\left(\begin{bmatrix}\cos(i\theta_{rm}) & \sin(i\theta_{rm})\\ -\sin(i\theta_{rm}) & \cos(i\theta_{rm})\end{bmatrix}\begin{bmatrix}\cos(\phi_{ri}) & -\sin(\phi_{ri})\\ \sin(\phi_{ri}) & \cos(\phi_{ri})\end{bmatrix}\begin{bmatrix} i_{r'd_i}\\ i_{r'q_i}\end{bmatrix}\right)\\
&= m_{si}\begin{bmatrix}\cos(\phi_{si}) & \sin(\phi_{si})\\ -\sin(\phi_{si}) & \cos(\phi_{si})\end{bmatrix}\frac{d}{dt}\left(\begin{bmatrix}\cos(i\theta_{rm}-\phi_{ri}) & \sin(i\theta_{rm}-\phi_{ri})\\ -\sin(i\theta_{rm}-\phi_{ri}) & \cos(i\theta_{rm}-\phi_{ri})\end{bmatrix}\begin{bmatrix} i_{r'd_i}\\ i_{r'q_i}\end{bmatrix}\right)\\
&= m_{si}\tfrac{d}{dt}(i\theta_{rm}-\phi_{ri})\begin{bmatrix}\cos(\phi_{si}) & \sin(\phi_{si})\\ -\sin(\phi_{si}) & \cos(\phi_{si})\end{bmatrix}\begin{bmatrix}-\sin(i\theta_{rm}-\phi_{ri}) & \cos(i\theta_{rm}-\phi_{ri})\\ -\cos(i\theta_{rm}-\phi_{ri}) & -\sin(i\theta_{rm}-\phi_{ri})\end{bmatrix}\begin{bmatrix} i_{r'd_i}\\ i_{r'q_i}\end{bmatrix}\\
&\quad + m_{si}\begin{bmatrix}\cos(\phi_{si}) & \sin(\phi_{si})\\ -\sin(\phi_{si}) & \cos(\phi_{si})\end{bmatrix}\begin{bmatrix}\cos(i\theta_{rm}-\phi_{ri}) & \sin(i\theta_{rm}-\phi_{ri})\\ -\sin(i\theta_{rm}-\phi_{ri}) & \cos(i\theta_{rm}-\phi_{ri})\end{bmatrix}\frac{d}{dt}\left(\begin{bmatrix} i_{r'd_i}\\ i_{r'q_i}\end{bmatrix}\right)\\
&= m_{si}\tfrac{d}{dt}(i\theta_{rm}-\phi_{ri})\begin{bmatrix}-\sin(\phi_{si}+i\theta_{rm}-\phi_{ri}) & \cos(\phi_{si}+i\theta_{rm}-\phi_{ri})\\ -\cos(\phi_{si}+i\theta_{rm}-\phi_{ri}) & -\sin(\phi_{si}+i\theta_{rm}-\phi_{ri})\end{bmatrix}\begin{bmatrix} i_{r'd_i}\\ i_{r'q_i}\end{bmatrix}\\
&\quad + m_{si}\begin{bmatrix}\cos(\phi_{si}+i\theta_{rm}-\phi_{ri}) & \sin(\phi_{si}+i\theta_{rm}-\phi_{ri})\\ -\sin(\phi_{si}+i\theta_{rm}-\phi_{ri}) & \cos(\phi_{si}+i\theta_{rm}-\phi_{ri})\end{bmatrix}\frac{d}{dt}\left(\begin{bmatrix} i_{rd_i}\\ i_{rq_i}\end{bmatrix}\right)
\end{aligned}
\tag{6.68}
$$

Following $\alpha\beta - dq$ transformation with $K_{r(\alpha\beta-dq)}$ transformation matrix, the rotor equations can be written as

$$\begin{aligned} \overrightarrow{v}_{r(dq)} &= R_{r'}\overrightarrow{i}_{r'(dq)} + K_{r(\alpha\beta-dq)}\left(\tfrac{d}{dt}\left(L_{lr'}\overrightarrow{i}_{r'(\alpha\beta)} + L_{ms-\alpha\beta}\overrightarrow{i}_{r'(\alpha\beta)} + L_{ms-\alpha\beta}B'\overrightarrow{i}_{s(\alpha\beta)}\right)\right) \\ 0 &= R_{r'}\overrightarrow{i}_{r'(dq)} + L_{lr'}\tfrac{d}{dt}\overrightarrow{i}_{r'(dq)} + L_{ms-\alpha\beta}\tfrac{d}{dt}\overrightarrow{i}_{r'(dq)}\cdots \\ &\quad \cdots + L_{ms-\alpha\beta}K_{r(\alpha\beta-dq)}\tfrac{d}{dt}\left(B'K'_{r(\alpha\beta-dq)}\overrightarrow{i}_{s(dq)}\right) \end{aligned} \tag{6.70}$$

Following similar matrix multiplication as shown for stator in Eqn. 6.68, the last term of Eqn. 6.70 can be simplified. Again, due to block diagonal nature of the matrices, the block corresponding to p^{th} pole pair is given in Eqn. 6.71. Putting $(\phi_{rp} - p\theta_{rm} - \phi_{sp}) = 0$ in the expression in Eqn. 6.71 can be simplified as

$$-m_{sp}\left(p(\omega_m - \omega_{rm})\right)\begin{bmatrix} 0 & 1 \\ -1 & 0 \end{bmatrix}\begin{bmatrix} i_{sd_p} \\ i_{sq_p} \end{bmatrix} + m_{si}\begin{bmatrix} 1 & 0 \\ 0 & 1 \end{bmatrix}\frac{d}{dt}\left(\begin{bmatrix} i_{sd_p} \\ i_{sq_p} \end{bmatrix}\right) \tag{6.72}$$

Hence the stator and rotor equations for p^{th} pole pair in an arbitrary reference frame rotating at speed ω_m can be summarised as

$$v_{sd_p} = i_{sd_p}r_s + \frac{d}{dt}\lambda_{sd_p} - p\omega_m\lambda_{sq_p} \tag{6.73}$$

$$v_{sq_p} = i_{sq_p}r_s + \frac{d}{dt}\lambda_{sq_p} + p\omega_m\lambda_{sd_p} \tag{6.74}$$

$$v_{r'd_p} = 0 = i_{r'd_p}r_{r'} + \frac{d}{dt}\lambda_{r'd_p} - p(\omega_m - \omega_{rm})\lambda_{r'q_p} \tag{6.75}$$

$$v_{r'q_p} = 0 = i_{r'q_p}r_{r'} + \frac{d}{dt}\lambda_{r'q_p} + p(\omega_m - \omega_{rm})\lambda_{r'd_p} \tag{6.76}$$

where λ denotes the flux linkage, given as below:

$$\lambda_{sd_p} = l_{ls}i_{sd_p} + m_{sp}(i_{sd_p} + i_{r'd_p}) \tag{6.77}$$

$$\lambda_{sq_p} = l_{ls}i_{sq_p} + m_{sp}(i_{sq_p} + i_{r'q_p}) \tag{6.78}$$

$$\lambda_{r'd_p} = l_{lr'}i_{r'd_p} + m_{sp}(i_{sd_p} + i_{r'd_p}) \tag{6.79}$$

$$
\begin{aligned}
& m_{si}\begin{bmatrix}\cos(\phi_{ri}) & \sin(\phi_{ri})\\ -\sin(\phi_{ri}) & \cos(\phi_{ri})\end{bmatrix}\frac{d}{dt}\left(\begin{bmatrix}\cos(i\theta_{rm}) & -\sin(i\theta_{rm})\\ \sin(i\theta_{rm}) & \cos(i\theta_{rm})\end{bmatrix}\begin{bmatrix}\cos(\phi_{si}) & -\sin(\phi_{si})\\ \sin(\phi_{si}) & \cos(\phi_{si})\end{bmatrix}\begin{bmatrix} i_{sd_i}\\ i_{sq_i}\end{bmatrix}\right)\\
&= m_{si}\begin{bmatrix}\cos(\phi_{ri}) & \sin(\phi_{ri})\\ -\sin(\phi_{ri}) & \cos(\phi_{ri})\end{bmatrix}\frac{d}{dt}\left(\begin{bmatrix}\cos(i\theta_{rm}+\phi_{si}) & -\sin(i\theta_{rm}+\phi_{si})\\ \sin(i\theta_{rm}+\phi_{si}) & \cos(i\theta_{rm}+\phi_{si})\end{bmatrix}\begin{bmatrix} i_{sd_i}\\ i_{rsq}\end{bmatrix}\right)\\
&= m_{si}\frac{d}{dt}(i\theta_{rm}+\phi_{si})\begin{bmatrix}\cos(\phi_{ri}) & \sin(\phi_{ri})\\ -\sin(\phi_{ri}) & \cos(\phi_{ri})\end{bmatrix}\begin{bmatrix}-\sin(i\theta_{rm}+\phi_{si}) & -\cos(i\theta_{rm}+\phi_{si})\\ \cos(i\theta_{rm}+\phi_{si}) & -\sin(i\theta_{rm}+\phi_{si})\end{bmatrix}\begin{bmatrix} i_{sd_i}\\ i_{sq_i}\end{bmatrix}\\
&\quad +m_{si}\begin{bmatrix}\cos(\phi_{si}) & \sin(\phi_{si})\\ -\sin(\phi_{si}) & \cos(\phi_{si})\end{bmatrix}\begin{bmatrix}\cos(i\theta_{rm}+\phi_{si}) & -\sin(i\theta_{rm}+\phi_{si})\\ \sin(i\theta_{rm}+\phi_{si}) & \cos(i\theta_{rm}+\phi_{si})\end{bmatrix}\frac{d}{dt}\left(\begin{bmatrix} i_{sd_i}\\ i_{sq}\end{bmatrix}\right)\\
&= m_{si}\frac{d}{dt}(i\theta_{rm}+\phi_{si})\begin{bmatrix}\sin(\phi_{ri}-i\theta_{rm}-\phi_{si}) & -\cos(\phi_{ri}-i\theta_{rm}-\phi_{si})\\ \cos(\phi_{ri}-i\theta_{rm}-\phi_{si}) & \sin(\phi_{ri}-i\theta_{rm}-\phi_{si})\end{bmatrix}\begin{bmatrix} i_{sd_i}\\ i_{sq_i}\end{bmatrix}\\
&\quad +m_{si}\begin{bmatrix}\cos(\phi_{ri}-i\theta_{rm}-\phi_{si}) & \sin(\phi_{ri}-i\theta_{rm}-\phi_{si})\\ -\sin(\phi_{ri}-i\theta_{rm}-\phi_{si}) & \cos(\phi_{ri}-i\theta_{rm}-\phi_{si})\end{bmatrix}\frac{d}{dt}\left(\begin{bmatrix} i_{sd_i}\\ i_{sq_i}\end{bmatrix}\right)
\end{aligned}
\tag{6.71}
$$

$$\lambda_{r'q_p} = l_{lr'} i_{r'q_p} + m_{sp}(i_{sq_p} + i_{r'q_p}) \tag{6.80}$$

As the mutual inductance matrix elements for zero vectors become 0, the k^{th} zero vector can be given as

$$v_{sz_k} = i_{sz_k} r_s + l_{ls} \frac{d}{dt} i_{sz_k} \tag{6.81}$$

and

$$v_{rz_k} = 0 = i_{r'z_k} r_s + l_{ls} \frac{d}{dt} i_{r'z_k} \tag{6.82}$$

Eqn. 6.73 - 6.82 represents the equivalent model of a generic m phase PPMIM. Eqn. 6.73 - 6.82 has been represented as equivalent circuit using complex notation in Fig. 6.1. Further, comparing with the dynamic model of a conventional three phase induction machine given in Eqn. 6.1 - 6.10, the proposed PPMIM machine can be studied as superposition of several machines with different pole-pairs.

Having derived the equivalent circuit of the dynamic model of the machine, the model can be used for calculation of torque. For p^{th} pole pair, combining the stator and rotor voltage equations and flux linkage equations given in Eqn. 6.73 - 6.80 for a stator reference frame (reference frame speed $\omega_m = 0$), following can be written

$$\begin{bmatrix} v_{sd_p} \\ v_{sq_p} \\ 0 \\ 0 \end{bmatrix} = \begin{bmatrix} r_s + l_{sp}\sigma & 0 & m_{sp}\sigma & 0 \\ 0 & r_s + l_{sp}\sigma & 0 & m_{sp}\sigma \\ m_{sp}\sigma & p\omega_{rm} m_{sp} & r_{r'} + l_{r'p}\sigma & p\omega_{rm} l_{r'p} \\ -p\omega_{rm} m_{sp} & m_{sp}\sigma & -p\omega_{rm} l_{r'p} & r_{r'} + l_{r'p}\sigma \end{bmatrix} \begin{bmatrix} i_{sd_p} \\ i_{sq_p} \\ i_{r'd_p} \\ i_{r'q_p} \end{bmatrix} \tag{6.83}$$

where σ is the $\frac{d}{dt}$ operator, $l_{ps} = l_{ls} + m_{sp}$ and $l_{r'p} = l_{lr'} + m_{sp}$. Eqn. 6.83 can be expanded as $\overrightarrow{v} = R\overrightarrow{i} + L\sigma\overrightarrow{i} + p\omega_{rm} G\overrightarrow{i}$. Hence the power can be found to be $P = \overrightarrow{i}'\overrightarrow{v} = \overrightarrow{i}' R\overrightarrow{i} + \overrightarrow{i}' L\sigma\overrightarrow{i} + p\omega_{rm}\overrightarrow{i}' G\overrightarrow{i}$. From this expression the electromagnetic power can be found to be $p\omega_{rm}\overrightarrow{i}' G\overrightarrow{i}$. Hence electromagnetic torque in dq reference frame is given as

$$\begin{aligned} T_{em_p(dq)} &= p \begin{bmatrix} i_{sd_p} \\ i_{sq_p} \\ i_{r'd_p} \\ i_{r'q_p} \end{bmatrix}^T \begin{bmatrix} 0 & 0 & 0 & 0 \\ 0 & 0 & 0 & 0 \\ 0 & m_{sp} & 0 & l_{r'p} \\ -m_{sp} & 0 & -l_{r'p} & 0 \end{bmatrix} \begin{bmatrix} i_{sd_p} \\ i_{sq_p} \\ i_{r'd_p} \\ i_{r'q_p} \end{bmatrix} \\ &= pm_{sp}(i_{sq_p} i_{r'd_p} - i_{sd_p} i_{r'q_p}) \end{aligned} \tag{6.84}$$

As the transformation matrices used to convert phase equations into dq reference frame, are not unimodular (determinant = 1), the obtained dq reference frame torque should be suitably

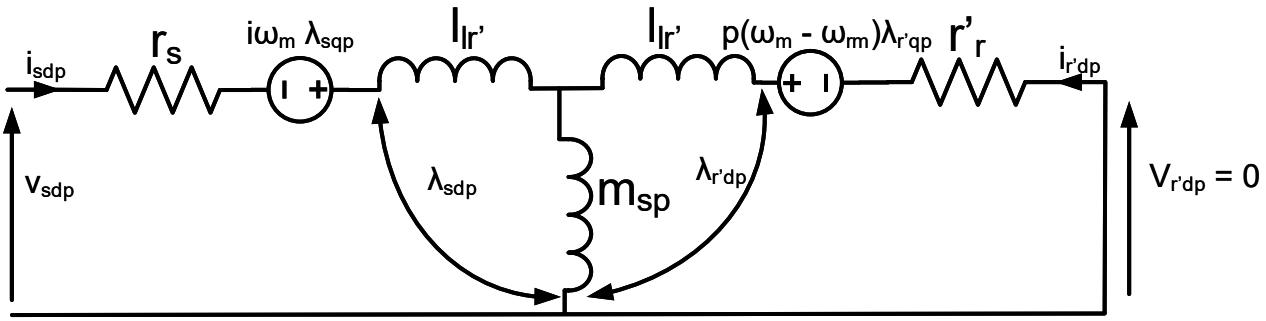

(a) D axis equivalent circuit stator and rotor for p^{th} pole pair

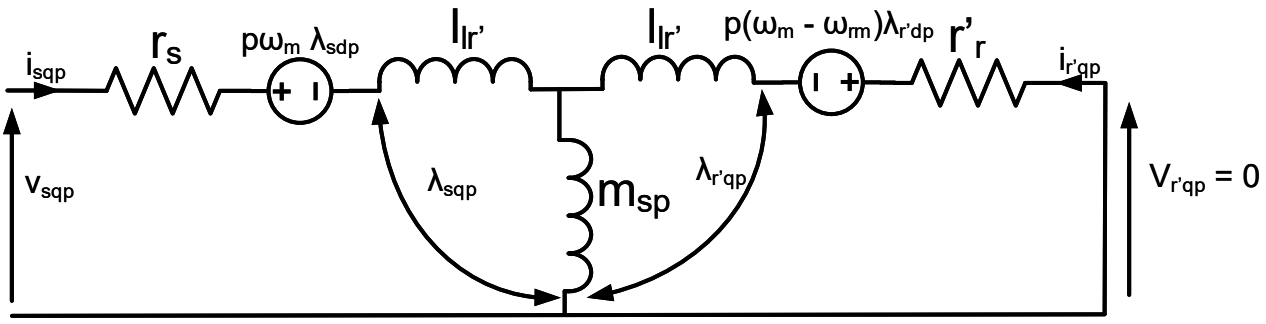

(b) Q axis equivalent circuit stator and rotor for p^{th} pole pair

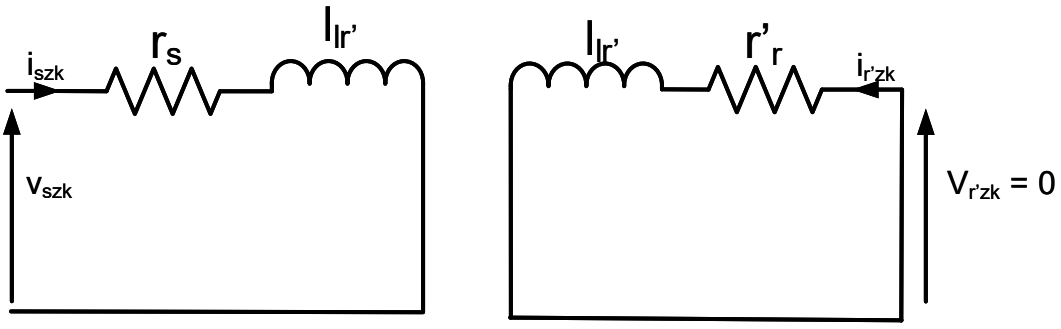

(c) k^{th} zero vector equivalent circuit stator and rotor

Figure 6.1: DQ Axis equivalent circuit model of PPMIM

scaled to get the actual torque of the machine, which can be obtained from similar treatment of power in phase reference frame given as $i'_{abc}v_{abc}$. This scaling factor can be obtained as

$$\begin{aligned} P_{dq} &= \overrightarrow{i}'_{dq}\overrightarrow{v}_{dq} = (K_{\alpha\beta-dq}K_{abc-\alpha\beta}\overrightarrow{i}_{abc})^T K_{\alpha\beta-dq}K_{abc-\alpha\beta}\overrightarrow{v}_{abc} \\ &= \overrightarrow{i}^T_{abc}(K_{\alpha\beta-dq}K_{abc-\alpha\beta})^T K_{\alpha\beta-dq}K_{abc-\alpha\beta}\overrightarrow{v}_{abc} \\ &= \overrightarrow{i}^T_{abc}K^T_{abc-\alpha\beta}K^T_{\alpha\beta-dq}K_{\alpha\beta-dq}K_{abc-\alpha\beta}\overrightarrow{v}_{abc} \\ &= \overrightarrow{i}^T_{abc}K^T_{abc-\alpha\beta}K_{abc-\alpha\beta}\overrightarrow{v}_{abc} \\ &= \tfrac{m}{2}\overrightarrow{i}^T_{abc}\overrightarrow{v}_{abc} = \tfrac{m}{2}P_{abc} \end{aligned} \tag{6.85}$$

Hence the machine torque for p^{th} pole pair operation is given as

$$T_{em_p} = \frac{2}{m}pm_{sp}(i_{sq_p}i_{r'd_p} - i_{sd_p}i_{r'q_p}) \tag{6.86}$$

In steady state operation, only one of the several pole configurations will be used. However, during online pole transition, as shown later in this chapter, one pole configuration will be gradually turned off, where as the other gradually activated. As discussed earlier, considering the machine as superposition of different pole configuration machine, the net torque of the machine is given as the summation of the torque produced by all pole configurations as below:

$$T_{em} = \frac{2}{m}\sum_{p=1}^{\frac{m}{2}-1} pm_{sp}(i_{sq_p}i_{r'd_p} - i_{sd_p}i_{r'q_p}) \tag{6.87}$$

Further the speed dynamics of a rotating machine can be given as

$$T_{em} = T_l + J\frac{d}{dt}\omega_{rm} \tag{6.88}$$

where T_l is the load torque and J is the combined inertia of the machine rotor and load. Additionally, if required the speed dynamics equation can be modified to incorporate the friction term as well. The obtained model of the machine will be used to find the dynamics of the machine during online pole changing in the next section.

6.3 Inverter Control

The above derived dynamic model of the machine can be used to implement an online pole changing control. As it has been shown earlier, the machine can be studied as the superposition of independent machines with different pole configurations. Hence to implement online pole changing, the machine with running pole configuration has to be de-energised

and the other machine (with desired pole numbers) has to be energised simultaneously. This can be achieved by a step change in these excitations or a change through ramp.

For conventional 3 phase induction machine it is known that, if the reference frame is set to be air-gap mmf, the dq axes quantities become DC. Hence the reference frame is set to be electrical frequency - which will correspond to the air gap mmf speed for $p = 1$. Furthermore, as the developed dynamic model takes into account the difference of reference frame speed at different pole configurations the reference frame speed will be adjusted to the corresponding air gap mmf accordingly.

A simple scalar closed-loop control scheme has been implemented as shown in Fig. 6.2. At first, a simple scalar function (as a function of speed) is defined for the modulation indices of different pole configurations to implement V/f control which ensures constant flux operation under base speed. The modulation index as a function of synchronous speed command is shown in Fig. 6.3. As the 10 pole configuration is intended not to be used, its modulation index is kept at zero throughout the range. The controller takes a speed command as an input. Further, the machine speed is sensed through a quadrature encoder. The machine speed (ω_{rm}) is subtracted from the reference speed and the error signal is passed to a PI controller to generate the synchronous speed command. The synchronous speed command is used to generate the modulation indices under different pole configurations. An independent control input is taken, which selects the pole number. The modulation index corresponding to the selected pole number is passed on from the v_{dq0} block to the next stage, while the modulation indices for other pole numbers and zero vectors are set to zero as shown by the selection switches in the block digram shown in Fig. 6.2. The v_{dq0} command is then passed through a rate limit block - which ensures a smooth transition from one pole configuration to another. When the pole select command changes - the modulation index of the previous pole is set to zero and the modulation index of the new pole is set to the desired value, based on the current synchronous speed of the machine. The rate limit block allows gradual change from existing command (zero for new pole configuration and non-zero for old pole configuration) to new commands (non-zero for new pole configuration and zero for old pole configuration). To generate the $\alpha\beta$ voltage commands the synchronous speed command is multiplied by corresponding pole pair numbers and integrated to generate ωt, $2\omega t$, $3\omega t$ etc. Taking sine of these generated angles the matrix to transform $dq0$ vector into $\alpha\beta$ reference frame is obtained. The obtained $v_{\alpha\beta}$ vector is then transformed into v_{abc} command by multiplying with the $K'_{abc-\alpha\beta}$ matrix. The generated v_{abc} command is finally passed to the inverter to generate the machine terminal voltages.

As an example case, the pole transition from 4 pole to 2 pole for the developed 12 phase

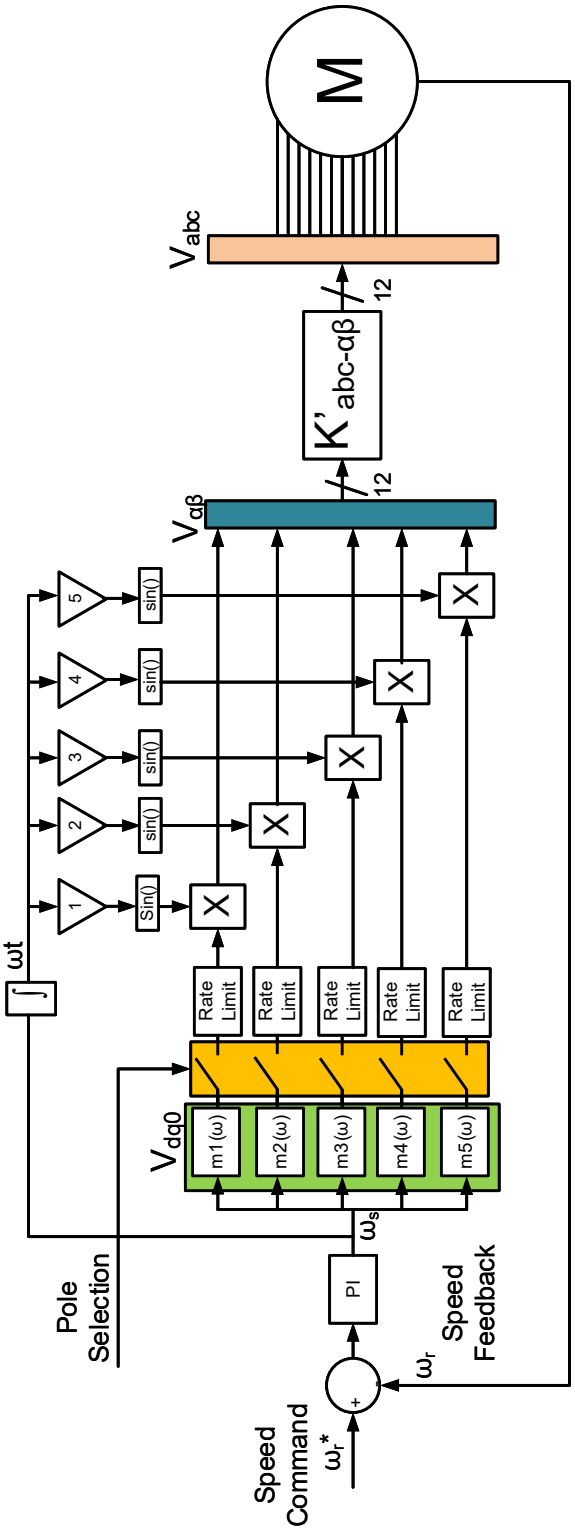

Figure 6.2: Machine control scheme

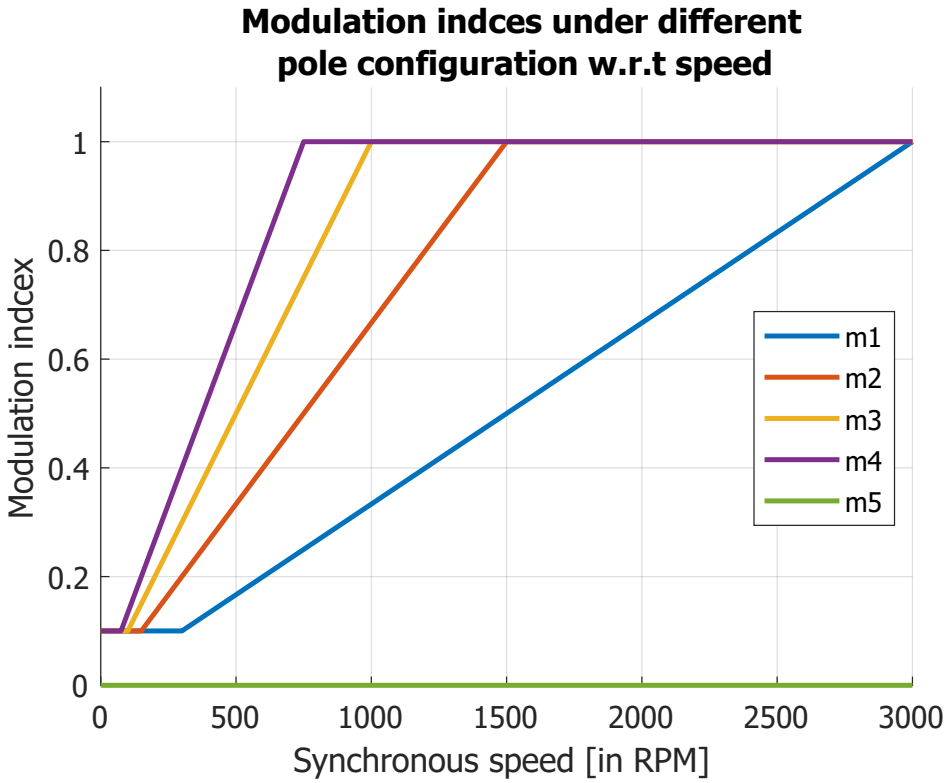

Figure 6.3: Modulation indices for V/f control

Table 6.1: 4 pole - 2 pole transition at 1500 RPM synchronous speed

Parameter	4 pole	2 pole
Frequency (Hz)	50	25
Modulation (%)	100	50
Phase difference (^{o})	$\frac{\pi}{3}$	$\frac{\pi}{6}$

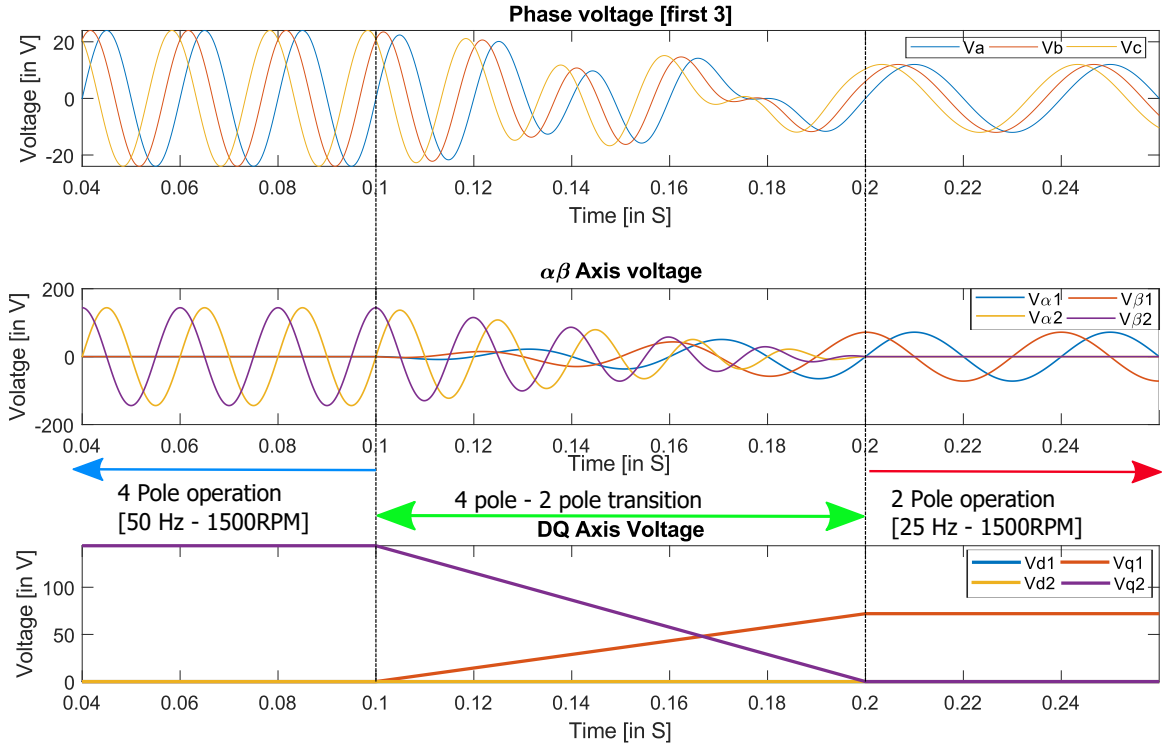

Figure 6.4: 4 pole to 2 pole transition at 1500 RPM

machine fed from 48V DC bus has been discussed here. The machine was previously running at 50Hz, 4 pole configuration. Hence the synchronous speed of the machine was 1500 RPM. At $t = 0.1$ the pole select is changed from 4 pole to 2 pole. As the machine synchronous speed is kept constant, the electrical frequency after the pole transition would be 25 Hz. The closed-loop speed control actually ensures rotor speed to be constant. However, the speed control acts at a slower speed than the pole transition - hence at first the pole transition will occur at a fixed synchronous speed, and thereafter the speed controller will adjust the synchronous speed to match the loss in rotor speed due to change in slip caused by the pole change. The drive configuration under 4 pole and 2 pole configuration is listed in table 6.1.

It can be noted during the transition, frequency, phase and modulation all 3 parameters of the inverter have to be changed simultaneously. The corresponding modulation indices (for 4 pole and 2 pole) is at first calculated through the modulation index function, as shown in Fig. 6.3. Next the controller ramps down the 4 pole modulation index (m_2) to zero from 100, while simultaneously gradually rising the two pole modulation index m_1 to 50 from zero through the rate limit block. The resulting v_{dq0} commands are shown in the Fig. 6.4. It can be noted for the 48V DC bus voltage the AC peak voltage is 24V. Hence the DQ0 and

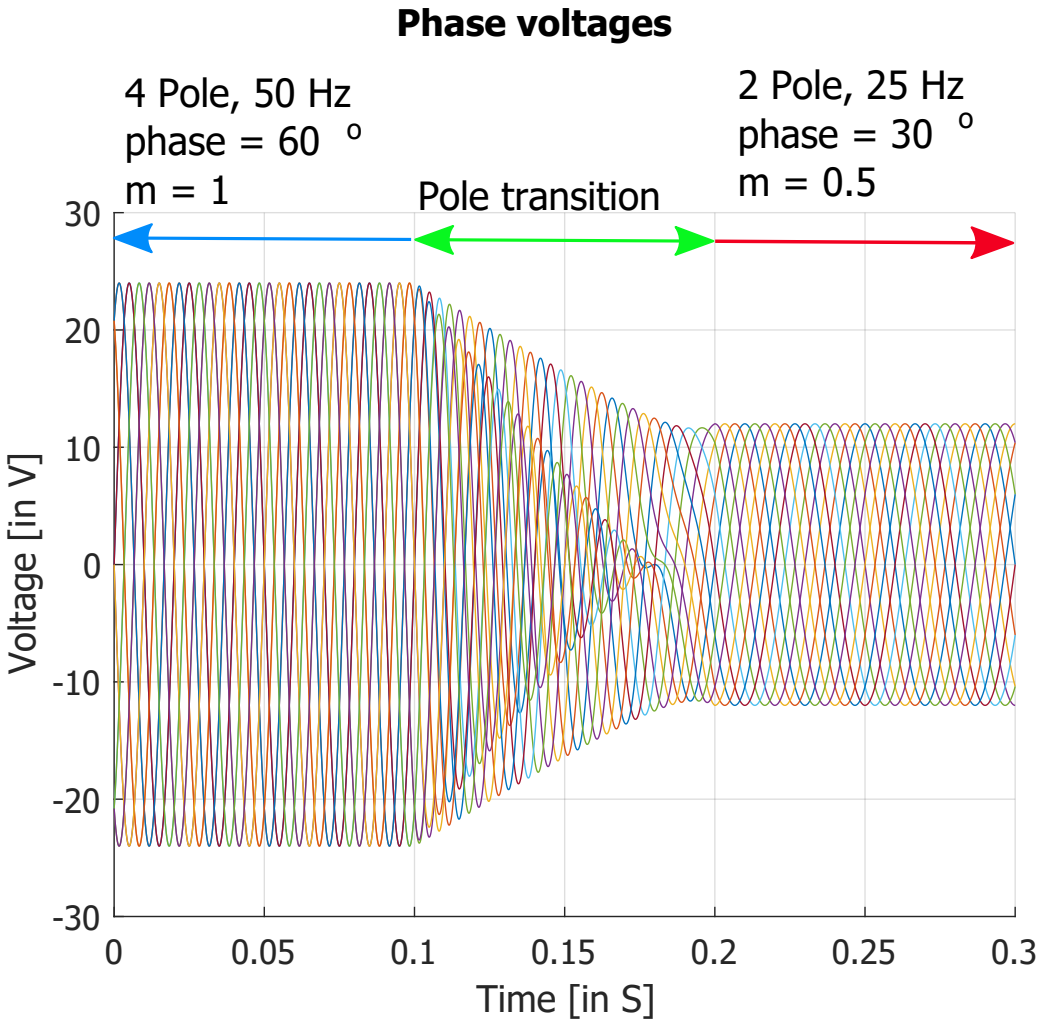

Figure 6.5: 4 pole to 2 pole transition at 1500 RPM - phase voltages

$\alpha\beta$ reference frame values correspond to 6 times 24V - 144V, due to the $\frac{m}{2}$ factor originated from the used $K_{abc-\alpha\beta}$ transformation matrix. Next using the DQ0-$\alpha\beta$ transformation, the $\alpha\beta$ commands are generated as shown in the middle of Fig. 6.4. As discussed earlier in the machine model development section - due to the decoupled nature of different poles in the $\alpha\beta$ reference frame, it can be observed during pole transition 4 pole excitation is gradually brought down to zero, while 2 pole excitation is gradually increased to the desired value (50%). Finally using the inverse of $K_{abc-\alpha\beta}$ matrix the $\alpha\beta$ vectors are transformed into phase voltages. For clarity, the waveforms of first three consecutive machine terminal voltages during this transition are shown in the top subplot of the Fig. 6.4. All 12 phase voltages of the machine during this pole transition are shown in Fig. 6.5.

6.4 Online pole changing - simulation results

Having developed the machine dynamic model and inverter control scheme, the same models have been implemented in the Matlab-Simulink platform to simulate online pole changing. Parameters of the developed experimental prototype, reported in chapter 4 has been used for this simulation model. The schematic block diagram of the implemented simulation model is shown in Fig 6.6. To emulate the actual experimental set up as closely as possible the same user interface to the DSP (TMS320F28379D) [79] and control code used to program the DSP has been used. The generated modulation index by the DSP has been passed to a linear model of the inverter - which generates machine terminal voltages. At first, the phase voltages applied to the machine have been transformed to stationary $\alpha\beta$ reference and then to the synchronously rotating reference frame ($dq0$). The $dq0$ voltages are fed into the machine model which is modelled by using Eqn. 6.83. This model generates the stator and rotor currents in the $dq0$ reference frame. Further using Eqn. 6.87 the electromagnetic torque generated by the machine has been calculated. Eqn. 6.88 has been modelled in the machine mechanical model to calculate rotor speed from electromagnetic torque and load torque. Finally, the stator currents are inverse transformed from $dq0$ frame to $\alpha\beta$ frame and then stator reference frame.

Using this simulation model the online pole changing of the machine has been studied. The waveforms of 8 pole - 6pole transition, 6 pole - 4 pole transition and 4 pole - 2 pole transition are shown in Fig 6.7, 6.8 and 6.9 respectively. The pole change command was initiated by using the user interface module. The serial communication link in between the user interface and the DSP is operated at 40 ms sampling frequency, hence there is a delay between the pole change command and the actual pole transition initiated by the DSP. The

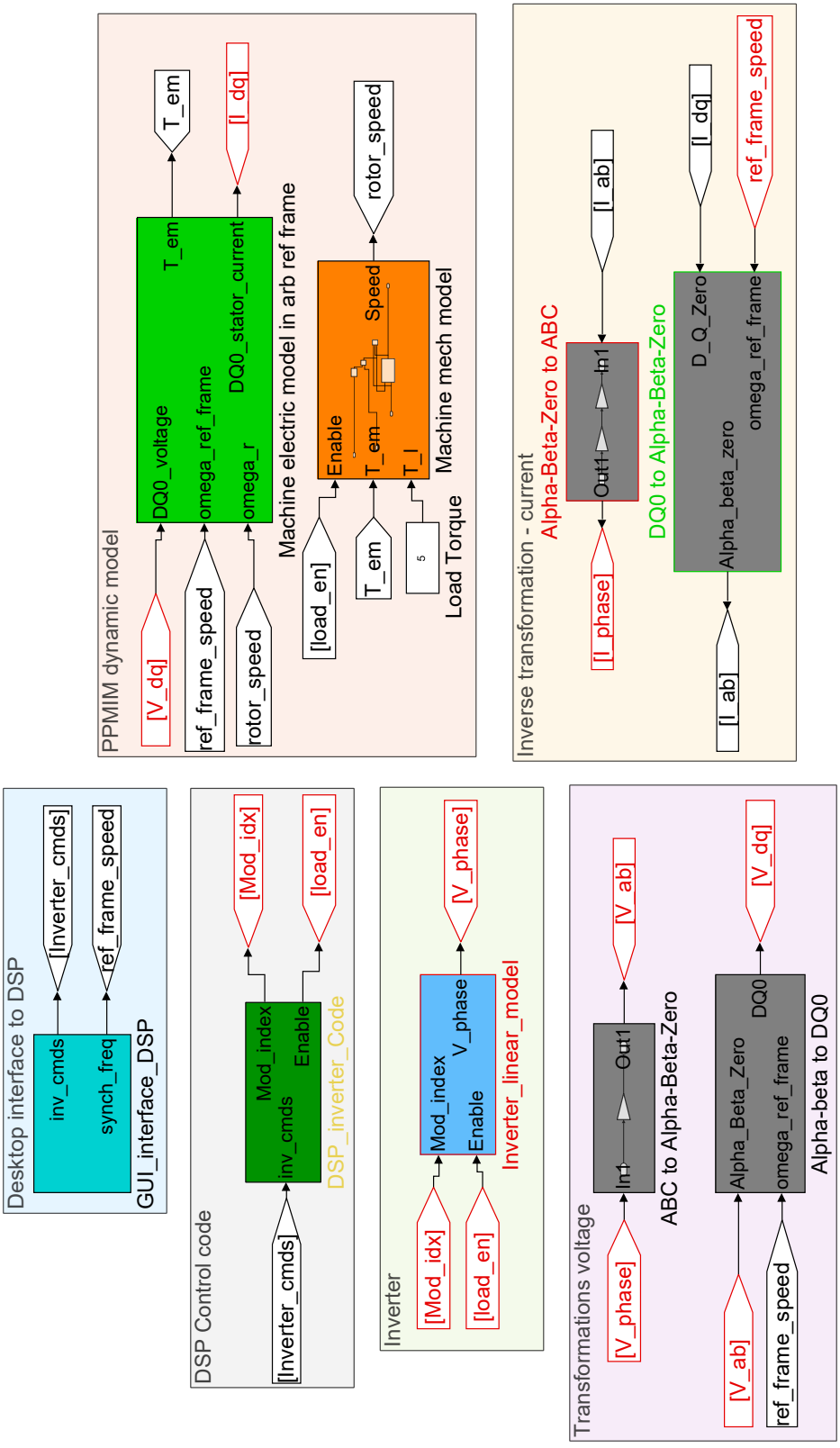

Figure 6.6: Dynamic model of the PPMIM for online pole changing in MATLAB-Simulink

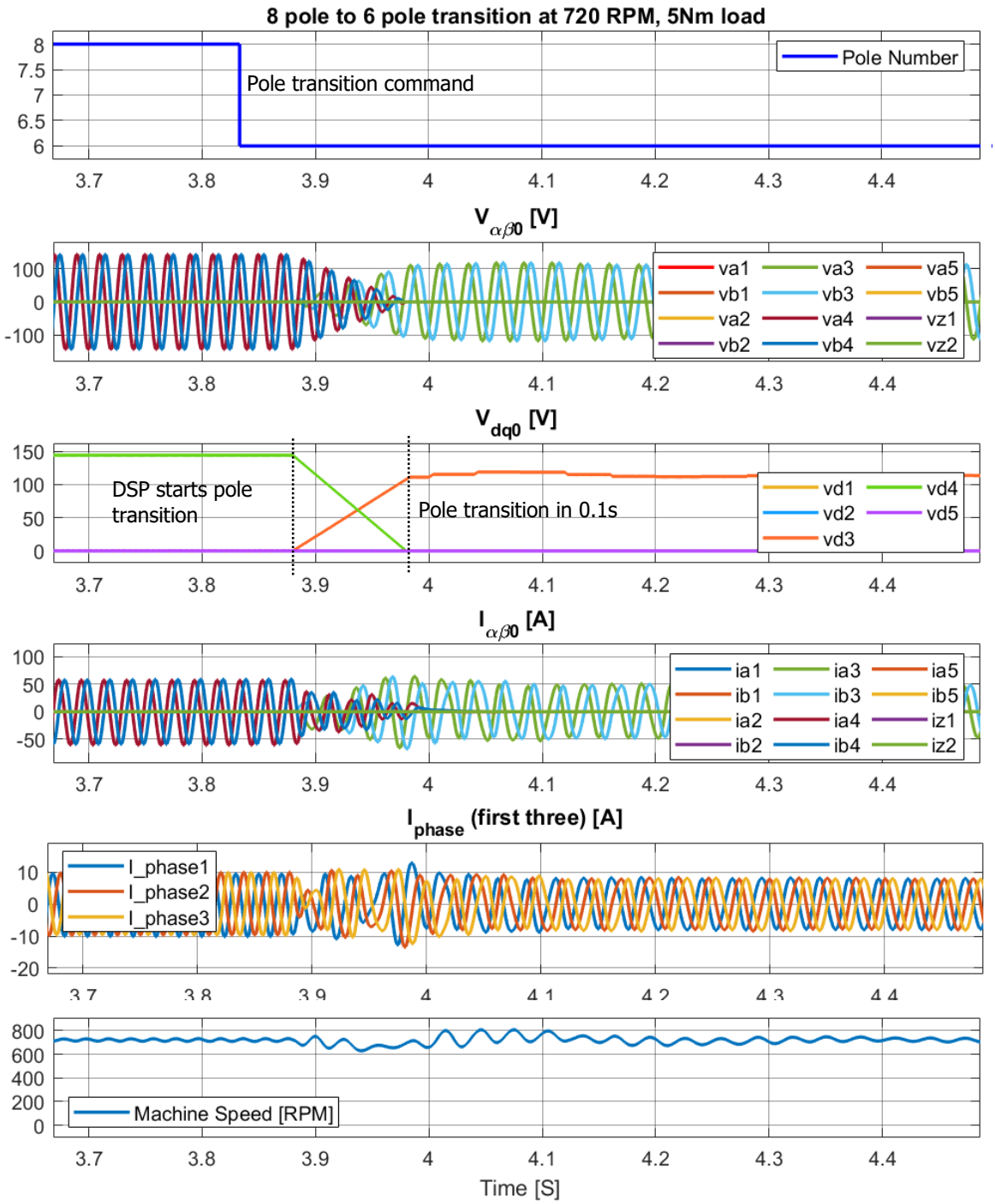

Figure 6.7: Simulation results of 8 pole to 6 pole transition

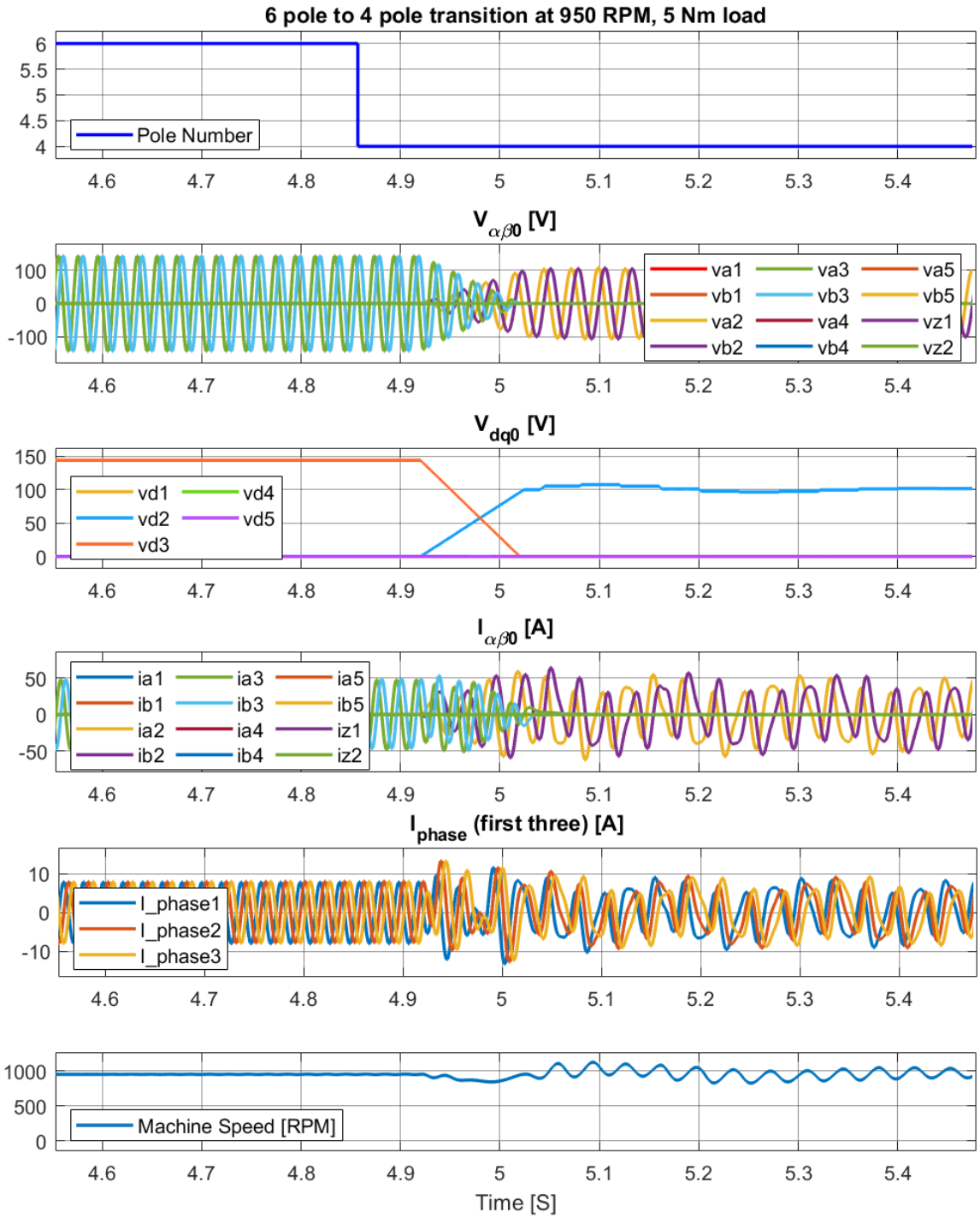

Figure 6.8: Simulation results of 6 pole to 4 pole transition

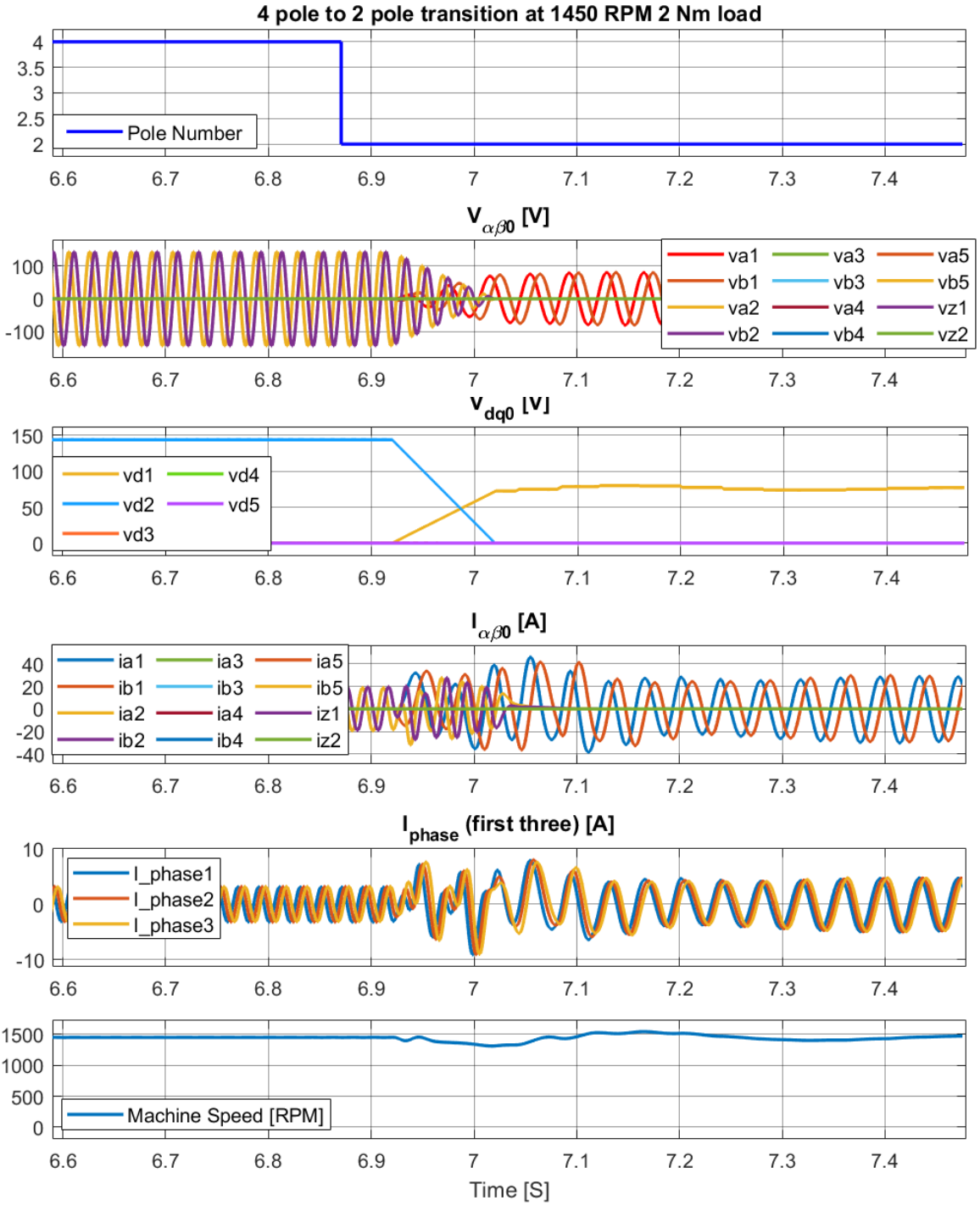

Figure 6.9: Simulation results of 4 pole to 2 pole transition

Table 6.2: Rotor time constant for different pole configurations

Pole No	2	4	6	8	10
Rotor resistance$R_r^{'}$ (in $m\Omega$)	214.2	201.0	178.1	152.2	111.3
Rotor leakage inductance$L_{lr}^{'}$ (in mH)	1.4	1.2	1.4	1.0	1.3
Mutual inductance L_m (in mH)	137.5	34.4	13.9	7.2	4.4
$\tau_r = \frac{L_r'}{R_r'} = \frac{L_m + L_{lr}'}{R_r'}$(in mS)	648.5	177.1	85.9	53.9	51.2

$\alpha\beta 0$ voltages show a gradual transition from one pole configuration to the other. Only 0.1 s has been given for the pole transition to complete. It can be seen, the speed waveform has some ripples, which is settled within 1 s from the pole transition. The current waveforms in $\alpha\beta$ reference frame indicate there is no significant oscillation during the pole transition.

As shown from the simulation results, the machine phase current has different dynamics during different pole transition. This can be attributed to the fact, the machine has different rotor time constant, under different pole configurations. The rotor time constant is given as given as the ratio of the rotor self inductance to rotor resistance. The rotor self inductance is given as sum of the rotor leakage inductance and mutual inductance. Using the FEM results obtained in chapter 3, the rotor time constant for different pole configurations are presented in table 6.2. The rotor time constant (τ_r) decides the rotor side flux dynamics. It can be observed from the simulation results, the current oscillation persists for longest for 6-4 pole transition compared to the other pole transitions. As 8 pole rotor time constant is very small, the rotor flux responds quickly as the excitation is controlled from the stator side. Whereas the 2 pole time constant is very large, hence the controller is able to act before the oscillation persists. However, the 4 pole and 6 pole time constants are neither too large to be controlled by the speed controller, nor too small to be settled quickly.

A minimal time period of 0.1 s has been given to complete the pole transition. For the target application of this drive - an electric or hybrid vehicle application the pole changing will emulate gear shifting, which is given 2s time in New European Driving Cycle. Hence to achieve a smoother transition the pole transition time can be increased to 1 s.

It has been reported in [63], a vector control (by taking the current feedback of the machine phases) will improve the transient during transition slightly compared to the implemented scalar control. However, the improvement achieved over the implemented scalar control by the vector control is not significant. If certain application has more stringent requirement on the transients i.e. stricter requirement in speed, torque and current oscillation and lesser time available for transition - vector control should be implemented by taking the phase current feedback.

6.5 Online pole changing - experimental results

The proposed pole changing control scheme has been implemented in the developed experimental hardware as well. The proposed inverter control scheme, discussed in section 6.3 has been implemented in the DSP control board (TMS320F28379D control card). A quadrature encoder has been fitted at the non driving end of the machine shaft to sense machine speed. The machine speed is fed back into the controller to achieve closed loop scalar control. A serial communication based graphical user interface (GUI) has been developed in Matlab-Simulink platform for easy communication with the DSP controller. The user interface allows to send the speed reference (ω_r^*) and pole selection command, as shown in Fig. 6.2. To perform the experiment, the machine is at first run at a certain speed under a specific pole configuration. Once the machine has achieved steady state the pole selection command is initiated from the GUI. The machine terminal voltage and current (first three phases), and machine speed is recorded during the transient.

Currents and phase voltages of three consecutive phases have been recorded in channel 1-3 and channel 5-7 respectively. Channel 4 shows the discrete signal indicating pole number and channel 8 shows the speed measurement as an analogue signal. The recorded waveforms for 8 pole to 6 pole at 750 RPM, 6pole to 4 pole at 1000 RPM and 4 pole to 2 pole transition at 1500 RPM under no load is shown in Fig. 6.10 - 6.12 respectively. It can be observed in all three cases of pole transitions, due to the ramped transition strategy from one pole configuration to another, the pole transition is completed within the given 0.1 s time, without any significant oscillation in the current, while the speed of the machine (channel 8) remained constant. As discussed earlier in the simulation results section, the phase voltages (and hence the phase currents) changes magnitude, phase and frequency simultaneously during online pole changing.

Due to the limitation of the hardware set up online pole changing under load condition could not be performed. As the load machine is controlled using an off the shelf inverter, the required control to program the load machine drive as a fixed torque load was not available to the end user. However, as shown in simulation, the developed control scheme is capable achieving online pole changing under load condition. A better dynamometer test bench set up, with capability to to control the load machine as a fixed torque load, will enable enable testing the developed machine under load condition.

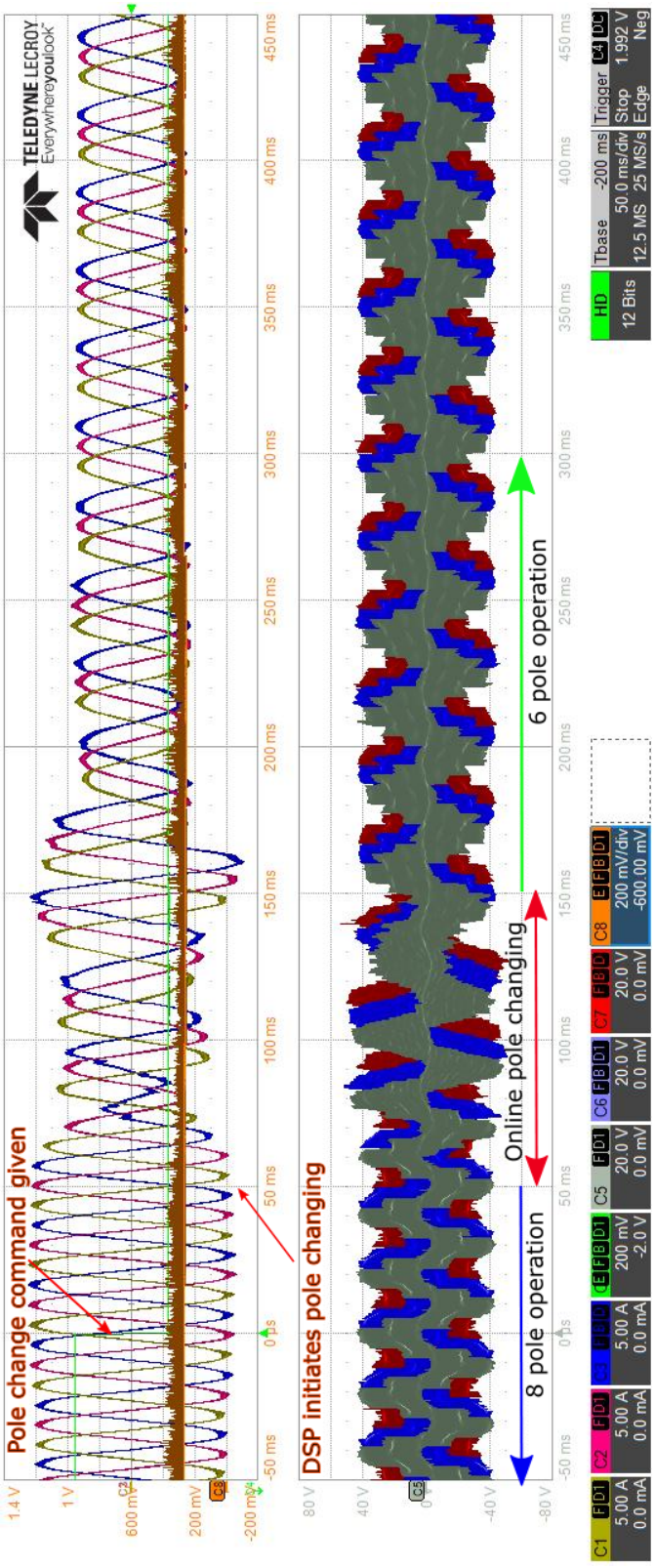

Figure 6.10: Experimental results of 8 pole to 6 pole transition

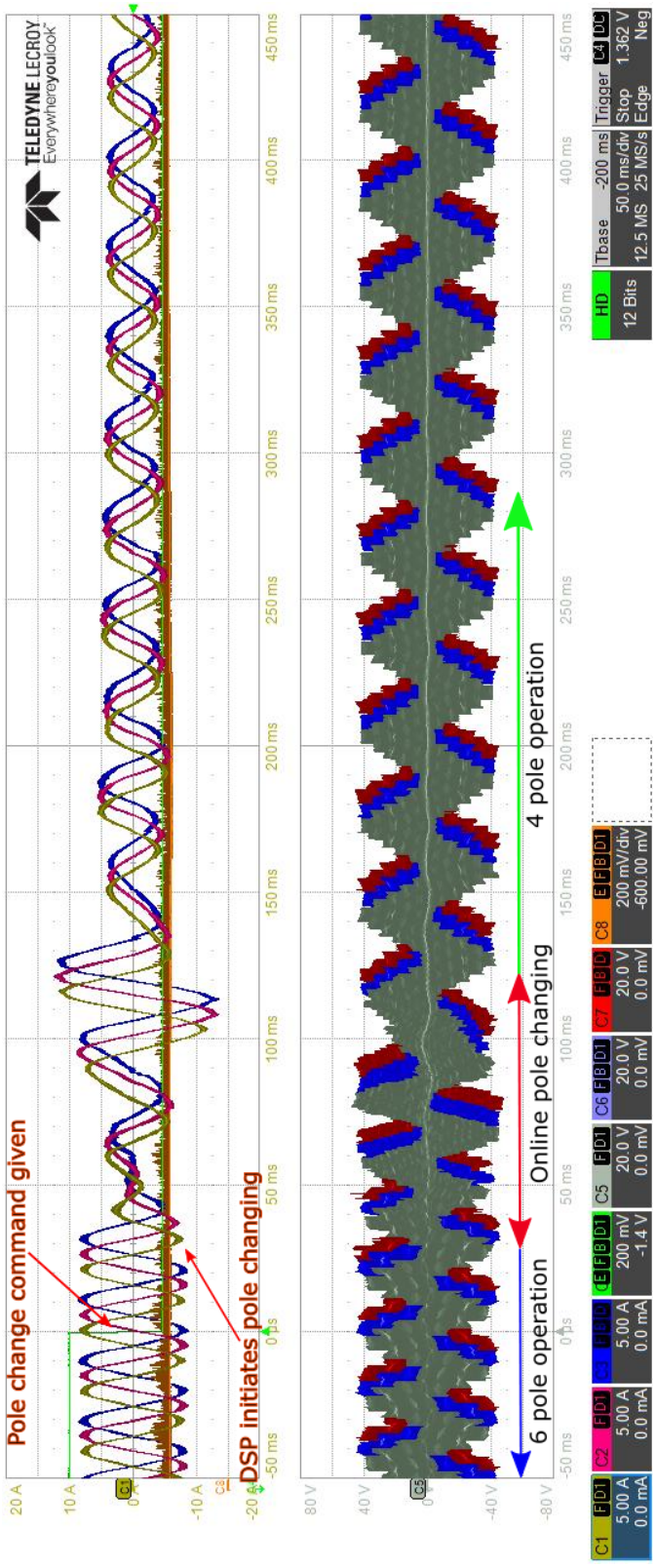

Figure 6.11: Experimental results of 6 pole to 4 pole transition

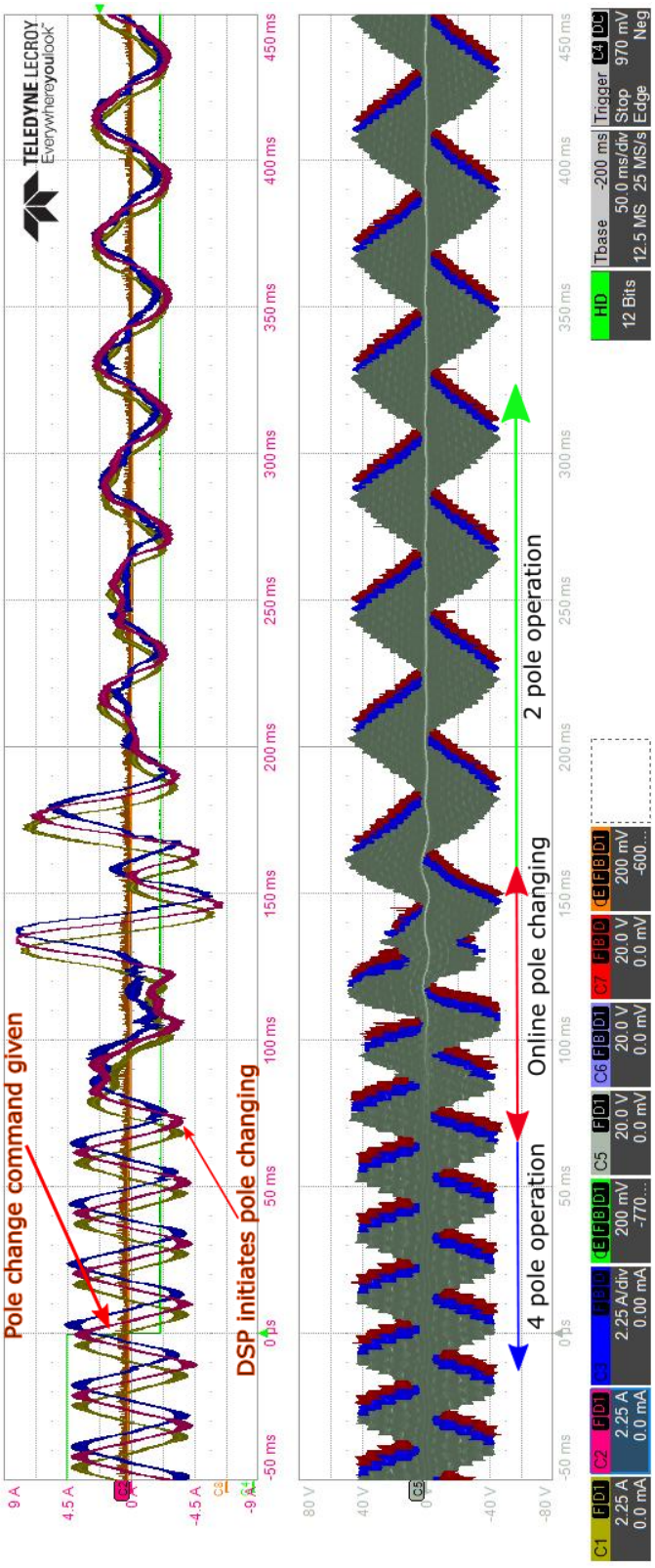

Figure 6.12: Experimental results of 4 pole to 2 pole transition

6.6 Conclusions

In this chapter a dynamic model of the independent phase belt controller PPMIM has been developed. It has been discussed previously the pole changing induction machine works with cage machine only, as the squirrel cage rotor adopts suitably to different mmf applied in the stator depending on the pole configuration. A rigorous mathematical approach has been taken to develop the machine model without approximating the rotor as stator phases - rather considering the rotor bars. The developed model shows that different pole configurations are independent of each other. Suitable reference frame transformation has been developed to model the machine in arbitrary reference frame - same as conventional thee phase induction machine. This enables the application of conventional flux oriented control (FOC) of the induction machine for the developed machine. To validate the dynamic model of the machine, an online pole changing strategy has been developed. A simple scalar control scheme has been designed as well. The model has been developed in Matlab - Simulink platform to study online pole changing and simulation results has been reported. Finally the developed online pole changing control scheme has been implemented on the hardware prototype. Experimental results of the transient during online pole changing for different pole pairs have been reported as well.

It should be noted the online pole changing scheme will work without the closed loop speed control. However, due to the change of torque available from new pole configuration, there will be a change in the slip in the machine, while the synchronous speed of the machine remain constant. Hence at the end of transition there would be slight change in the rotor speed . The simple scalar speed control solves this problem without introducing too much complexity in the control. Moreover if a FOC is implemented by taking current feedback, the dynamics in the current and speed oscillation would improve. For the target application of xEVs as online pole changing will emulate a gear shifting the achieved 0.1 s transition time is significantly lower than the allowed 2 s for gear shifting in standard drive cycle. Hence the oscillation can be further decreased by increasing the transition time.

Chapter 7

Conclusions and Future Works

The final chapter presents a summary of the work done in this thesis. Key contributions of this work and their implications with respect to the challenges identified in the introductory chapter have been discussed. Finally, the chapter concludes with the possible future extension of the presented work reflecting on the limitations of the work done in this project.

7.1 Thesis Summary

In this thesis, an independent phase belt controlled Pole Phase Modulated Induction Machine for electric and hybrid electric vehicles has been reported. Whereas conventional pole changing induction machines usually show the capability to reconfigure into two possible pole configurations - the proposed generalised machine allows an m phase machine into 2,4,6...$m-2$ pole configuration. As an example case, a 12 phase machine has been designed, fabricated and tested which can be configured into 5 possible pole configurations - 2/4/6/8/10. The concept is at first developed through analytical methods to study the proposed machine, and then validated by the FEA. Through this process the equivalent circuit model of the machine under steady-state operation is developed. Next the proposed machine is designed, fabricated along with the necessary power electronic converter and its controller. A complete circulating power test bench has been developed to test the fabricated machine under load conditions. The prototype has been tested under steady-state to show the capability of wide pole reconfigurability, and the torque-speed characteristics under different pole configuration are reported. Finally a dynamic model of the machine has been developed to achieve online pole changing of the machine. The dynamic model is implemented in Matlab-Simulink to study the transients during online pole changing. Further

based on the dynamic model of the machine an online pole changing scheme with a scalar speed control has been discussed. The proposed control scheme achieves online pole changing within 0.1 s, without large oscillation. Finally the online pole changing control scheme is implemented on the fabricated prototype machine and experimentally verified. A more detailed chapter wise summary of the thesis is presented below.

Chapter 1 starts with literature review on various electric drive technologies reported in the literature - induction machine, permanent magnet machine and switched reluctance motor for EVs and HEVs and presents a detailed discussion on advantage and disadvantages of each of these machines for xEVs. Based on this literature review the key technical requirement of the electric drive for xEV is found to be significantly wider torque-speed characteristics of the drive. This requirement arises from the various operating modes of the electric machine in xEV - such as high torque low speed during starting for EV or ICE cranking for HEV, high speed low torque during highway cruising in EV or alternator operation in HEV, and medium range of torque speed during city drive, torque boosting and regenerative braking in xEVs. Based on the literature survey and the technical challenge identified for the electric drive for xEVs, the chapter finally identifies pole changing induction machine to be most promising to offer a wide torque speed characteristics.

Chapter 2 looks more into induction machine drives and the limitation of conventional VVVF control of the machine in terms of torque-speed characteristics. It is identified that the breakdown torque of the machine is inversely proportional to the square of the speed of the machine under VVVF control (at speed higher than base speed) and thus becomes the limiting factor at high speed. The chapter also looks into previously reported techniques for pole changing of induction machines and identifies pole phase modulation to have highest potential for reconfigurability which has been explored further in the rest of the thesis.

Chapter 3 introduces a novel independent phase belt controlled PPMIM. By allowing control of each of the phase belts independently it has been shown for a generic m phase machine can be reconfigured into 2,4,6...$m-2$ pole configuration. Compared to previous literature the independent phase belt control enables a higher number of pole configuration using the same number of power electronics. As an example case a 12 phase machine has been studied and shown to be reconfigured into a 2/4/6/8/10 pole machine. The 8 and 10 pole operation achieves a fractional phase per pole (12 phase for 8 pole - 1.5 phase /pole and 12 phase for 10 pole - 1.2 phase / pole) as a first.

The chapter further delves into the development of the equivalent circuit model of the machine under different pole configurations. However as the proposed machine does not use standard winding configurations with go and return - hence the standard analytical model

for the winding function and mmf function of machine winding can not be used. An accurate mathematical approach has been developed to model the winding function and mmf function of the stator winding by considering each of the slot currents individually rather than in a loop. The rotor is also modelled by considering individual rotor bar current separately. Using the developed winding functions and mmf functions of the stator and rotor windings (under the assumption of sinusoidal excitation) the closed-form analytical expressions of the equivalent circuit parameters of the machine under different pole configuration has been obtained. The developed model also refers the rotor quantities w.r.t. stator through the derivation of an equivalent turns ratio for rotor to stator transformation. The machine has been then analysed by FEM simulation under different pole configurations. A simple mathematical process has been reported to extract the equivalent circuit parameters from the FEA results. The equivalent circuit parameters from FEA and analytical expressions show a good match, which has been used to obtain torque-speed characteristics of the machine. The net torque-speed operation envelope of the machine using VVVF control on each of the pole configurations has been reported and shown to be significantly increased compared to a machine with similar power rating and single pole configuration. Finally, the chapter concludes with a possible reduced flexibility PPMIM with only 6 phases allowing 4 pole and 8 pole operation - which still manages to cover a large portion of the torque-speed operating zone of the independent phase belt controlled PPMIM, using only half of the power electronics.

Chapter 4 reports the design and fabrication of the prototype 12 phase 1.5 kW machine. The details of the 12 phase low voltage high current sandwiched bus bar inverter design along with isolated gate driver circuits and snubber circuit design have been reported as well. The chapter also reports on the fabricated circulating power testbed using another off the shelf IM and commercially available low voltage IM inverter for load testing of the prototype. Finally, a serial communication based easy to use GUI software has been developed in Matlab- Simulink platform for testing the machine under different pole configuration.

Chapter 5 reports the experimental results of the developed machine. At first the no-load test and blocked rotor test have been performed on the machine. These results have been used to obtain the equivalent circuit parameters of the machine. A good match between the experimentally obtained values of the equivalent circuit parameter and the same obtained from analytical and FEA in chapter 3 has been shown. Utilising the previously reported circulating power testbed the fabricated prototype has been tested under different pole configuration. The torque-speed characteristics of the machine under different pole configurations have been reported along with the power factor of the machine and efficiencies of machine,

inverter and drive.

To effectively utilise the pole reconfigurability of the proposed drive, it is important to achieve an online pole changing - without causing significant oscillation in machine current, torque or speed. Hence having established the theory of steady-state operation of the proposed independent phase belt controlled PPMIM and experimentally verifying the same in previous chapters, chapter 6 focuses on the dynamic model of the proposed machine. The dynamic model of the machine has to cover all possible pole configurations. A novel mathematical approach has been introduced to model the cage rotor more accurately by treating individual rotor bars - rather than assuming the rotor to have the same number of phases as the stator. This treatment is particularly important as a cage rotor is important for electronic pole changing from stator exciting, as only a cage rotor can accommodate to different air-gap mmf generated by different pole configurations. Starting from the winding function expressions of the stator and rotor winding the dynamic model has been established at first in phase domain without any assumption of the excitation current/voltage waveforms. Then suitable transformation matrices have been derived to transform the dynamic model into stationary $\alpha\beta$ reference frame where each of the pole pair is represented by a pair of $\alpha\beta$ vectors. Finally, the dynamic model is transformed into an arbitrary reference frame (dq) allowing the elimination of the position dependent mutual inductance terms.

The dynamic model shows in $\alpha\beta$ frame of reference hence in dq frame of reference as well, each of the pole configurations are independent of each other. This allows the development of a simple online pole changing strategy by gradually turning off the current pole excitation vector and slowly ramping up the excitation vector for the new pole configuration while keeping the synchronous speed of the machine same. Coupled with V/f control of the machine this translates into a simultaneous change of magnitude, phase and frequency of the inverter modulation. The dynamic model of the machine (using the parameters of the fabricated prototype machine) along with inverter control strategy has been implemented in Matlab - Simulink platform. A simple scalar speed control loop has been implemented too. The simulation results of online pole changing - from 8 pole - 6 pole, 6 pole - 4 pole and 4 pole - 2 pole have been reported for the fabricated prototype. Finally, the proposed inverter control scheme has been implemented in the experimental hardware and the online pole changing has been successfully verified by experimental results as well. Although previous literature has reported on the dynamic model of the other PPMIM and simulation results of online pole changing, there has been no report on the experimental results of online pole changing. The experimental results of the transient during the pole transition from 8 pole - 6 pole, 6 pole - 4 pole and 4 pole - 2 pole have been reported in this thesis. The pole

transition has been achieved both in simulation and experiment within only 0.1 s without any significant oscillation in current, speed or torque. However there is plenty of headroom to slow down the transition by allowing more time - as online pole changing emulates gear shifting for the intended application of xEVs, which is given 2 s in a standard drive cycle.

7.2 Key Contributions

The key contributions of this thesis are now summarised below:

- A novel pole changing induction machine has been reported in this thesis. Using the proposed independent phase belt controlled pole phase modulation the proposed machine achieves higher reconfigurability compared to previously reported PPMIM. A single machine capable of 5 different pole configuration has been designed, fabricated and tested.

- The proposed machine removes the constraint of the magnetic space phase angle between two consecutive phase bands to be a submultiple of π as a first. In the conventional machines, the north and south poles are constructed by the go and return of the phase winding (i.e a and a'), which ensures integral phase per pole. This can be interpreted as the magnetic space phase angle between two consecutive phase bands to be a submultiple of π. For a conventional 3 phase machine, this magnetic space phase angle between two consecutive phase band can be found to be $\frac{\pi}{3}$. The proposed machine operates in 2/4/6/8/10 pole configuration. The 8 pole configuration achieves magnetic space phase angle between two consecutive phases to be $\frac{2\pi}{3}$ and for 10 pole machine this angle can be found to be $\frac{5\pi}{6}$.

- As the conventional winding structure with go and return is no more valid for some of pole configurations of an independent phase belt controlled PPMIM (8 and 10 pole for the prototype 12 phase machine) a new mathematical model of the winding function and mmf function of the toroidal winding machine has been reported. The mathematical model treats each of the slot currents independently thus allowing modelling of independent phase belt control. It has been further shown that the developed model can be easily extended to model the rotor bars as well accurately without making any approximation to model the rotor to have the same number of stator phases.

- Using the developed mathematical model of the stator and rotor winding functions, a complete set of closed-form expressions for the equivalent circuit parameters of the

machine (under steady-state operation - with sinusoidal excitation current) has been obtained. The analytical expressions are validated by FEA and later experimental validation of a prototype machine as well.

- It has been shown at the end of chapter 3 a significant portion of the torque-speed operation envelope can be achieved by only two modes of operation - 8 pole and 4 pole. It has been further shown these two operation modes can be achieved using only 6 leg inverter. Compared to a conventional 3 phase inverter, using only 3 more legs this combination offers a modification in the torque-speed operation zone of the machine. Although only two operation modes are used in this configuration, the 8 pole operation is obtained by use of the proposed independent phase belt control - which has not been reported earlier.

- The proposed 12 phase machine with 5 different pole configuration has been fabricated and experimentally validated using the developed circulating power testbed. Machine equivalent circuit parameters under different pole configuration have been obtained and show good match with the same obtained by analytical and FEA methods. The close match of the analytical expressions with FEA and experimental results will enable a robust design optimisation for a specific rating / torque-speed characteristics without using computationally intensive FEA for each of the design iterations. The torque-speed characteristics of the machine has been obtained at different pole configurations. In line with the proposed theory - the machine achieves a modified torque-speed operating zone.

- Similar to the steady-state analytical model of the machine, the dynamic model of the machine is also obtained using the mathematical model of the winding function. Unlike the steady-state model, the dynamic model does not use mmf function, as no approximation has been made for the excitation current. Moreover, the dynamic model of the rotor is also obtained by considering each of the rotor bars separately rather than approximating the rotor to have the same number of stator phases. Hence as a first, closed-form expressions for the complete dynamic model of the PPMIM have been derived.

- Through suitable transformations it has been shown that each of the pole configurations can be controlled independently. Thus utilising the dynamic model of the machine a simple gradual pole transition strategy has been devised which allows smooth online pole changing. The online pole changing has been validated both by simulation

model (in Matlab - Simulink platform) and experimental results as well.

7.3 Future Works

This thesis presents the possibility of reconfiguring a single machine into multiple pole configurations electronically by deploying independent phase belt controlled pole phase modulation. Several areas of the work presented in this thesis can be extended to pursue further research to maximise the benefit obtained from the proposed pole changing technique and optimise the drive performance. Some of the possible future works are listed below:

- Optimised machine design

As the proposed pole changing technique realises different air-gap mmf under different pole configurations, the stator core flux density changes inversely with the pole numbers for a fixed frequency and voltage. Further, the higher pole number causes higher flux density at stator teeth. This subjects the core to maximum flux density for the minimum pole pair configuration and the teeth to maximum flux density under maximum pole configuration. For the constraint of time and capability to manufacture custom machine stator, a radially wound induction machine stator was used to fabricate the prototype for this thesis. Detailed design optimisation can be pursued to optimise the stator design specifically taking into account of the toroidal winding and pole changing. An optimised design will result in the better design of the stator core yoke depth, slot width and depth design to maximize the net utilization of magnetic core under different pole configurations.

- Holistic drive design optimisation

Electric and hybrid vehicles pose as the most attractive application of the reported reconfigurable induction machine drive. Holistic design optimisation can be pursued by taking into account the intended torque-speed operating zone of the drive beforehand. Using existing vehicle driving profile data or standard drive cycles and vehicle details the most commonly used torque-speed zone of the drive can be found. Using this torque-speed operation zones an optimised machine with reduced phase legs (such as the 4/8 pole machine with 6 leg discussed in chapter 3) can be designed which specifically covers the intended operation zones. This will enable an optimum number of power electronic devices to cater the required operating zones.

- Study on the effect of stator slot harmonics, rotor bar harmonics

The air gap mmf of the machine in higher pole count (hence lower phase count) has higher harmonics. Hence the study of the harmonics on the machine performance is important. The mathematical model presented in chapter 3 can be extended to take into account of the effect of these harmonics - by modifying the simplified winding function to take into account the harmonics effect. The dynamic model too can be modified to take into account the harmonics as the same set of winding functions are used as a basis to obtain the inductance expressions. Furthermore, the machine design optimisation can be extended to take this into account as well. Furthermore, the phase shifted carrier technique can be applied to higher pole configurations to reduce the net phase harmonics.

- Vector controlled pole transition

By taking the phase current feedback of the phases the machine current in dq reference frame can be obtained by using the developed transformation matrices. Then a control scheme can be implemented to control the machine current in dq reference frame. As the dynamic model of the machine shows each of the pole configurations to be independent of each other, standard vector control scheme of three phase IM can be applied to control the machine for better dynamic performance. The control scheme can be further utilised to achieve online pole transition. This can be achieved by gradually reducing the i_d^* and i_q^* command of the current pole configuration and ramping up the i_d^* and i_q^* command for the intended pole configuration. In addition to this, online pole changing under different load condition can be performed, to find the optimal settings for the closed loop controller (either scalar / vector control) - which will ensure smooth transition without large oscillation in speed or current.

References

[1] M. Osama and T. A. Lipo, "Modeling and analysis of a wide speed range induction motor drive based on electronic pole changing," in *, Conference Record of the 1996 IEEE Industry Applications Conference, 1996. Thirty-First IAS Annual Meeting, IAS '96*, vol. 1, Oct. 1996, pp. 357–364 vol.1.

[2] J. M. Miller, V. Stefanovic, V. Ostovic, and J. Kelly, "Design considerations for an automotive integrated starter-generator with pole-phase modulation," in *Conference Record of the 2001 IEEE Industry Applications Conference, 2001. Thirty-Sixth IAS Annual Meeting*, vol. 4, Sep. 2001, pp. 2366–2373 vol.4.

[3] T. A. Lipo, *Introduction to AC machine design: Wisconsin power electronics research center*, 2004.

[4] B. Heller and V. Hamata, *Harmonic field effects in induction machines*. Elsevier Science & Technology, 1977.

[5] B. S. Umesh and K. Sivakumar, "Multilevel Inverter Scheme for Performance Improvement of Pole-Phase-Modulated Multiphase Induction Motor Drive," *IEEE Transactions on Industrial Electronics*, vol. 63, no. 4, pp. 2036–2043, Apr. 2016.

[6] H. W. Beaty, J. L. Kirtley, N. K. Ghai, R. Lyon, and S. Leeb, *Electric motor handbook*. McGraw-Hill California, 1998.

[7] IEA, "Energy Balances of Non-OECD Countries 2015 edition," Tech. Rep.

[8] O. US EPA, "Global Greenhouse Gas Emissions Data," Jan. 2016. [Online]. Available: https://www.epa.gov/ghgemissions/global-greenhouse-gas-emissions-data

[9] "Greenhouse gas emissions from transport in Europe." [Online]. Available: https://www.eea.europa.

eu/data-and-maps/indicators/transport-emissions-of-greenhouse-gases/transport-emissions-of-greenhouse-gases-11

[10] A. Emadi, K. Rajashekara, S. Williamson, and S. Lukic, "Topological overview of hybrid electric and fuel cell vehicular power system architectures and configurations," *IEEE Transactions on Vehicular Technology*, vol. 54, no. 3, pp. 763–770, May 2005.

[11] C. Chan, "The State of the Art of Electric, Hybrid, and Fuel Cell Vehicles," *Proceedings of the IEEE*, vol. 95, no. 4, pp. 704–718, Apr. 2007.

[12] "Hybrid and Electric Cars in the US: Two differing strategies," *Hybrid & Electric Cars in the U.S. - Two Differing Strategies*, pp. 1–29, Mar. 2014. [Online]. Available: http://search.ebscohost.com/login.aspx?direct=true&db=bth&AN=95761233&site=ehost-live&scope=site

[13] H. Turker, "Methodology hybridization of a vehicle," in *2015 IEEE Transportation Electrification Conference and Expo (ITEC)*, Jun. 2015, pp. 1–8.

[14] S. Raghavan and A. Khaligh, "Electrification Potential Factor: Energy-Based Value Proposition Analysis of Plug-In Hybrid Electric Vehicles," *IEEE Transactions on Vehicular Technology*, vol. 61, no. 3, pp. 1052–1059, Mar. 2012.

[15] J. Miller, A. Emadi, A. Rajarathnam, and M. Ehsani, "Current status and future trends in More Electric Car power systems," in *Vehicular Technology Conference, 1999 IEEE 49th*, vol. 2, Jul. 1999, pp. 1380–1384 vol.2.

[16] D. Mohr, N. Muller, A. Krieg, P. Gao, H. Kaas, A. Krieger, and R. Hensley, "The Road to 2020 and Beyond: What's Driving the Global Automotive Industry," *McKinsey & Company, Inc*, 2013.

[17] E. Efficiency and R. Energy, "Subcontract Report: Final Report on Assessment of Motor Technologies for Traction Drives of Hybrid and Electric Vehicles Subcontract No. 4000080341," 2011. [Online]. Available: http://info.ornl.gov/sites/publications/files/pub28840.pdf

[18] D. Dorrell, L. Parsa, and I. Boldea, "Automotive Electric Motors, Generators, and Actuator Drive Systems With Reduced or No Permanent Magnets and Innovative Design Concepts," *IEEE Transactions on Industrial Electronics*, vol. 61, no. 10, pp. 5693–5695, Oct. 2014.

[19] I. Boldea, L. Tutelea, and C. Pitic, "PM-assisted reluctance synchronous motor/generator (PM-RSM) for mild hybrid vehicles: electromagnetic design," *IEEE Transactions on Industry Applications*, vol. 40, no. 2, pp. 492–498, Mar. 2004.

[20] I. Boldea, V. Coroban-Schramel, G. Andreescu, F. Blaabjerg, and S. Scridon, "BEGA Starter/Alternator #x2014;Vector Control Implementation and Performance for Wide Speed Range at Unity Power Factor Operation," *IEEE Transactions on Industry Applications*, vol. 46, no. 1, pp. 150–158, Jan. 2010.

[21] D. Perreault and V. Caliskan, "Automotive power generation and control," *IEEE Transactions on Power Electronics*, vol. 19, no. 3, pp. 618–630, May 2004.

[22] W. Cai, "Comparison and review of electric machines for integrated starter alternator applications," in *Conference Record of the 2004 IEEE Industry Applications Conference, 2004. 39th IAS Annual Meeting*, vol. 1, Oct. 2004, p. 393.

[23] M. Ehsani, Y. Gao, and S. Gay, "Characterization of electric motor drives for traction applications," in *The 29th Annual Conference of the IEEE Industrial Electronics Society, 2003. IECON '03*, vol. 1, Nov. 2003, pp. 891–896 vol.1.

[24] L. Lorilla, T. Keim, J. Lang, and D. Perreault, "Topologies for future automotive generators. Part I. Modeling and analytics," in *Vehicle Power and Propulsion, 2005 IEEE Conference*, Sep. 2005, pp. 74–85.

[25] T. Lorilla, L.M. Keim, J. Lang, and D. Perreault, "Topologies for Future Automotive Generators - Part II: Optimization," in *Vehicle Power and Propulsion, 2005 IEEE Conference*, Sep. 2005, pp. 831–837.

[26] S. Chen, B. Lequesne, R. Henry, Y. Xue, and J. Ronning, "Design and testing of a belt-driven induction starter-generator," *IEEE Transactions on Industry Applications*, vol. 38, no. 6, pp. 1525–1533, Nov. 2002.

[27] M. Naidu and J. Walters, "A 4-kW 42-V induction-machine-based automotive power generation system with a diode bridge rectifier and a PWM inverter," *IEEE Transactions on Industry Applications*, vol. 39, no. 5, pp. 1287–1293, Sep. 2003.

[28] C. Mudannayake and M. Rahman, "Sensorless induction machine based integrated starter alternator for the 42 V powernet for automobiles," in *Vehicle Power and Propulsion, 2005 IEEE Conference*, Sep. 2005, pp. 479–486, 00001.

[29] J. Zhang and M. Rahman, "A Direct-Flux-Vector-Controlled Induction Generator With Space-Vector Modulation for Integrated Starter Alternator," *IEEE Transactions on Industrial Electronics*, vol. 54, no. 5, pp. 2512–2520, Oct. 2007.

[30] S. Jurkovic, K. Rahman, J. Morgante, and P. Savagian, "Induction Machine Design and Analysis for General Motors e-Assist Electrification Technology," *IEEE Transactions on Industry Applications*, vol. 51, no. 1, pp. 631–639, Jan. 2015.

[31] F. Caricchi, F. Crescimbini, E. Santini, and L. Solero, "High-efficiency low-volume starter/alternator for automotive applications," in *Conference Record of the 2000 IEEE Industry Applications Conference, 2000*, vol. 1, 2000, pp. 215–222 vol.1.

[32] Z. Fu, J. Xiang, W. Reynolds, and B. Nefcy, "Vector control of an IPM synchronous machine capable of full range operations for hybrid electric vehicle application," in *Industry Applications Conference, 2003. 38th IAS Annual Meeting. Conference Record of the*, vol. 3, Oct. 2003, pp. 1443–1450 vol.3.

[33] K. Chau, Y. Li, J. Jiang, and C. Liu, "Design and Analysis of a Stator-Doubly-Fed Doubly-Salient Permanent-Magnet Machine for Automotive Engines," *IEEE Transactions on Magnetics*, vol. 42, no. 10, pp. 3470–3472, Oct. 2006.

[34] L. Chedot, G. Friedrich, M. Biedinger, and P. Macret, "Integrated Starter Generator: The Need for an Optimal Design and Control Approach. Application to a Permanent Magnet Machine," *IEEE Transactions on Industry Applications*, vol. 43, no. 2, pp. 551–559, Mar. 2007.

[35] H. Mirahki and M. Moallem, "Design improvement of Interior Permanent Magnet synchronous machine for Integrated Starter Alternator application," in *Electric Machines Drives Conference (IEMDC), 2013 IEEE International*, May 2013, pp. 382–385.

[36] F. N. Jurca, M. Ruba, and C. Martis, "Analysis of permanent magnet synchronous machine for integrated starter-alternator-booster applications," in *2015 International Conference on Electrical Drives and Power Electronics (EDPE)*, Sep. 2015, pp. 272–276, 00000.

[37] M. Morandin, A. Faggion, and S. Bolognani, "Integrated Starter Alternator With Sensorless Ringed-Pole PM Synchronous Motor Drive," *IEEE Transactions on Industry Applications*, vol. 51, no. 2, pp. 1485–1493, Mar. 2015.

[38] S. Tang, D. Otten, T. Keim, and D. Perreault, "Design and Evaluation of a 42-V Automotive Alternator With Integrated Switched-Mode Rectifier," *IEEE Transactions on Energy Conversion*, vol. 25, no. 4, pp. 983–992, Dec. 2010, 00008.

[39] D. Torrey, "Switched reluctance generators and their control," *IEEE Transactions on Industrial Electronics*, vol. 49, no. 1, pp. 3–14, Feb. 2002.

[40] N. Schofield and S. Long, "Generator Operation of a Switched Reluctance Starter/Generator at Extended Speeds," *IEEE Transactions on Vehicular Technology*, vol. 58, no. 1, pp. 48–56, Jan. 2009.

[41] P. Watterson, W. Wu, B. Kalan, H. Lovatt, G. Prout, J. Dunlop, and S. Collocott, "A switched-reluctance motor/generator for mild hybrid vehicles," in *International Conference on Electrical Machines and Systems, 2008. ICEMS 2008*, Oct. 2008, pp. 2808–2813.

[42] K. Kiyota, T. Kakishima, and A. Chiba, "Comparison of Test Result and Design Stage Prediction of Switched Reluctance Motor Competitive With 60-kW Rare-Earth PM Motor," *IEEE Transactions on Industrial Electronics*, vol. 61, no. 10, pp. 5712–5721, Oct. 2014.

[43] Y. Hu, X. Song, W. Cao, and B. Ji, "New SR Drive With Integrated Charging Capacity for Plug-In Hybrid Electric Vehicles (PHEVs)," *IEEE Transactions on Industrial Electronics*, vol. 61, no. 10, pp. 5722–5731, Oct. 2014.

[44] C. Chan, "The state of the art of electric and hybrid vehicles," *Proceedings of the IEEE*, vol. 90, no. 2, pp. 247–275, Feb. 2002.

[45] J. Miller, "Multiple voltage electrical power distribution system for automotive applications," in *Energy Conversion Engineering Conference, 1996. IECEC 96., Proceedings of the 31st Intersociety*, vol. 3, Aug. 1996, pp. 1930–1937 vol.3.

[46] J. Miller and P. Nicastri, "The next generation automotive electrical power system architecture: issues and challenges," in *Digital Avionics Systems Conference, 1998. Proceedings., 17th DASC. The AIAA/IEEE/SAE*, vol. 2, Oct. 1998, pp. I15/1–I15/8 vol.2.

[47] A. Emadi, M. Ehsani, and J. Miller, "Advanced silicon rich automotive electrical power systems," in *Digital Avionics Systems Conference, 1999. Proceedings. 18th*, vol. 2, 1999, pp. 8.B.1–1–8.B.1–8 vol.2.

[48] S. Lukic and A. Emadi, "Performance analysis of automotive power systems: effects of power electronic intensive loads and electrically-assisted propulsion systems," in *Vehicular Technology Conference, 2002. Proceedings. VTC 2002-Fall. 2002 IEEE 56th*, vol. 3, 2002, pp. 1835–1839 vol.3.

[49] T. Neugebauer and D. Perreault, "Computer-aided optimization of DC/DC converters for automotive applications," *IEEE Transactions on Power Electronics*, vol. 18, no. 3, pp. 775–783, May 2003.

[50] L. Hao, C. Namuduri, S. Gopalakrishnan, and C. Freitas, "Comparison of the influence of PM drive system with voltage adaptation or machine winding reconfiguration on HEV/EV applications," in *2015 IEEE Energy Conversion Congress and Exposition (ECCE)*, Sep. 2015, pp. 6130–6138, 00000.

[51] T. Gerrits, J. Duarte, C. Wijnands, E. Lomonova, J. Paulides, and L. Encica, "Twelve-phase open-winding SPMSM development for speed dependent reconfigurable traction drive," in *2015 Tenth International Conference on Ecological Vehicles and Renewable Energies (EVER)*, Mar. 2015, pp. 1–7, 00000.

[52] R. Martin, J. D. Widmer, B. C. Mecrow, M. Kimiabeigi, A. Mebarki, and N. L. Brown, "Electromagnetic considerations for a six-phase switched reluctance motor driven by a three-phase inverter," in *2015 IEEE International Electric Machines Drives Conference (IEMDC)*, May 2015, pp. 280–286, iSSN: null.

[53] G. Martin, R. Moutoux, M. Myat, R. Tan, G. Sanders, and F. Barnes, "An Integrated Starter-Alternator System Using Induction Machine Winding Reconfiguration," in *IEEE Vehicle Power and Propulsion Conference, 2007. VPPC 2007*, Sep. 2007, pp. 677–681, 00003.

[54] D. Sarafianos, T. Logan, R. McMahon, T. Flack, and S. Pickering, "Alternator loss breakdown and use of alternative rectifier diodes for improvement of vehicle electrical power system efficiency," in *Power Electronics and Motion Control Conference and Exposition (PEMC), 2014 16th International*, Sep. 2014, pp. 502–507.

[55] D. Sarafianos, R. McMahon, T. Flack, and S. Pickering, "Characterisation and modelling of automotive Lundell alternators," in *2015 IEEE 11th International Conference on Power Electronics and Drive Systems (PEDS)*, Jun. 2015, pp. 928–933.

[56] T. Neugebauer and D. Perreault, "Computer-aided optimization of DC/DC converters for automotive applications," *IEEE Transactions on Power Electronics*, vol. 18, no. 3, pp. 775–783, May 2003, 00074.

[57] R. Gehring, J. Froschl, T. Kohler, and H. Herzog, "Modeling of the automotive 14 V power net for voltage stability analysis," in *IEEE Vehicle Power and Propulsion Conference, 2009. VPPC '09*, Sep. 2009, pp. 71–77.

[58] T. Kohler, T. Wagner, A. Thanheiser, C. Bertram, D. Buecherl, H.-G. Herzog, J. Froeschl, and R. Gehring, "Experimental investigation on voltage stability in vehicle power nets for power distribution management," in *2010 IEEE Vehicle Power and Propulsion Conference (VPPC)*, Sep. 2010, pp. 1–6.

[59] T. Kohler, R. Gehring, J. Froeschl, R. Dornmair, C. Schramm, F. Ruf, A. Thanheiser, D. Buecherl, and H.-G. Herzog, "Sensitivity analysis of voltage behavior in vehicular power nets," in *2011 IEEE Vehicle Power and Propulsion Conference (VPPC)*, Sep. 2011, pp. 1–6.

[60] F. Ruf, M. Schill, A. Barthels, T. Kohler, H.-U. Michel, J. Froeschl, and H.-G. Herzog, "Topology and Design Optimization of a 14 V Automotive Power Net Using a Modified Discrete PSO in a Physical Simulation," in *2013 IEEE Vehicle Power and Propulsion Conference (VPPC)*, Oct. 2013, pp. 1–7.

[61] F. Ruf, A. Neiss, A. Barthels, T. Kohler, H.-U. Michel, J. Froeschl, and H. Herzog, "Design optimization of a 14 V automotive power net using a parallelized DIRECT algorithm in a physical simulation," in *2012 13th International Conference on Optimization of Electrical and Electronic Equipment (OPTIM)*, May 2012, pp. 73–80.

[62] F. Ruf, A. Barthels, G. Walla, M. Winter, T. Kohler, H. Michel, J. Froeschl, and H. Herzog, "Autonomous load shutdown mechanism as a voltage stabilization method in automotive power nets," in *2012 IEEE Vehicle Power and Propulsion Conference (VPPC)*, Oct. 2012, pp. 1261–1265.

[63] M. Magill, "An investigation of electronic pole changing in high inverter count induction machines," Ph.D. dissertation, University of Illinois at Urbana-Champaign, 2015. [Online]. Available: https://www.ideals.illinois.edu/handle/2142/78380

[64] M. M. Swamy, T. Kume, A. Maemura, and S. Morimoto, "Extended high-speed operation via electronic winding-change method for AC motors," *IEEE Transactions on Industry Applications*, vol. 42, no. 3, pp. 742–752, May 2006.

[65] Y. Takatsuka, H. Hara, K. Yamada, A. Maemura, and T. Kume, "A wide speed range high efficiency EV drive system using winding changeover technique and SiC devices," in *2014 International Power Electronics Conference (IPEC-Hiroshima 2014 - ECCE ASIA)*, May 2014, pp. 1898–1903.

[66] G. H. Rawcliffe and R. F. Burbidge, "A 2:1 pole-changing induction motor of improved performance," *Proceedings of the IEE - Part A: Power Engineering*, vol. 104, no. 18, pp. 457–460, Dec. 1957.

[67] T. H. Barton, O. I. Butler, and H. Sterling, "The theory and characteristics of the 3:1 pole-changing induction motor," *Proceedings of the IEE - Part A: Power Engineering*, vol. 103, no. 9, pp. 285–294, Jun. 1956.

[68] F. C. Williams, J. F. Eastham, D. Tipping, and G. W. McLean, "A.C. diesel-electric drive system using consequential pole changing," *Proceedings of the Institution of Electrical Engineers*, vol. 113, no. 12, pp. 1957–1963, Dec. 1966.

[69] G. H. Rawcliffe, R. F. Burbidge, and W. Fong, "Induction-motor speed-changing by pole-amplitude modulation," *Proceedings of the IEE - Part A: Power Engineering*, vol. 105, no. 22, pp. 411–419, Aug. 1958.

[70] B. B. Jensen, A. G. Jack, G. J. Atkinson, and B. C. Mecrow, "Performance of a Folded-Strip Toroidally Wound Induction Machine," *IEEE Transactions on Industrial Electronics*, vol. 59, no. 5, pp. 2217–2226, May 2012.

[71] R. Qu and T. Lipo, "Design and optimization of dual-rotor, radial-flux, toroidally-wound, permanent-magnet machines," in *38th IAS Annual Meeting on Conference Record of the Industry Applications Conference, 2003.*, vol. 2, Oct. 2003, pp. 1397–1404, iSSN: null.

[72] M. Aoyama, K. Nakajima, and T. Noguchi, "Proposal of electrically reversal magnetic pole type variable magnetic flux PM motor," in *2016 IEEE Energy Conversion Congress and Exposition (ECCE)*, Sep. 2016, pp. 1–8, iSSN: null.

[73] C. Spargo, B. Mecrow, and J. Widmer, "Synchronous reluctance motors with toroidal windings," in *2014 IEEE Energy Conversion Congress and Exposition (ECCE)*, Sep. 2014, pp. 1374–1378, iSSN: 2329-3748.

[74] H.-I. Lee and M. D. Noh, "Optimal Design of Radial-Flux Toroidally Wound Brushless DC Machines," *IEEE Transactions on Industrial Electronics*, vol. 58, no. 2, pp. 444–449, Feb. 2011.

[75] R. Marlow, N. Schofield, and A. Emadi, "A Continuous Toroidal Winding SRM With 6- or 12-Switch DC Converter," *IEEE Transactions on Industry Applications*, vol. 52, no. 1, pp. 189–198, Jan. 2016.

[76] M. P. Magill and P. T. Krein, "A dynamic pole-phase modulation induction machine model," in *2015 IEEE International Electric Machines Drives Conference (IEMDC)*, May 2015, pp. 13–19.

[77] D. C. Meeker. Finite element method magnetics, version 4.0.1 (03dec2006 build) url: http://www.femm.info. [Online]. Available: http://www.femm.info

[78] D. Dolinar, R. de Weerdt, R. Belmans, and E. Freeman, "Calculation of two-axis induction motor model parameters using finite elements," *IEEE Transactions on Energy Conversion*, vol. 12, no. 2, pp. 133–142, Jun. 1997, 00059.

[79] Texas Instruments, "TMS320f28379d controlCARD Datasheet." [Online]. Available: http://www.ti.com/lit/ug/sprui76a/sprui76a.pdf

[80] IXYS, "IXFN 180n15p Datasheet." [Online]. Available: https://docs-emea.rs-online.com/webdocs/14b7/0900766b814b781d.pdf

[81] "Cloud Powered 3d CAD/CAM Software for Product Design | Fusion 360." [Online]. Available: https://www.autodesk.co.uk/products/fusion-360/overview

[82] R. Lai, F. Wang, R. Burgos, Y. Pei, D. Boroyevich, B. Wang, T. A. Lipo, V. D. Immanuel, and K. J. Karimi, "A Systematic Topology Evaluation Methodology for High-Density Three-Phase PWM AC-AC Converters," *IEEE Transactions on Power Electronics*, vol. 23, no. 6, pp. 2665–2680, Nov. 2008.

[83] Texas Instruments, "ucc21520 Datasheet." [Online]. Available: https://www.ti.com/lit/ds/symlink/ucc21520.pdf

[84] R. Severns and E. Reduce, "Design of snubbers for power circuits," *International Rectifier Corporation*, 2006.

[85] "Rotary Torque Sensor | Inline Contactless Torque Transducer | M425." [Online]. Available: https://datum-electronics.co.uk/product/rotary-torque-sensor-m425/

[86] Curtis Instruments, "123638e Datasheet." [Online]. Available: https://cdn.curtisinstruments.com/products/datasheets/123638E_datasheet_en.pdf

[87] N4L, "PPA45 - 5500 Datasheet." [Online]. Available: https://www.newtons4th.com/wp-content/uploads/2014/07/PPA45_5500-Brochure.pdf

[88] Lecroy, "MDA800a oscilloscopes datasheet.pdf." [Online]. Available: http://cdn.teledynelecroy.com/files/pdf/mda800a-oscilloscopes-datasheet.pdf

[89] N4L, "PSM3750 Datasheet." [Online]. Available: https://www.newtons4th.com/wp-content/uploads/2014/07/PSM3750_Brochure2.pdf

[90] A. M. Trzynadlowski, *Control of induction motors*. Academic press, 2000.

[91] A. R. Munoz and T. A. Lipo, "Complex vector model of the squirrel-cage induction machine including instantaneous rotor bar currents," *IEEE Transactions on Industry Applications*, vol. 35, no. 6, pp. 1332–1340, Nov. 1999.

[92] J. Figueroa, J. Cros, and P. Viarouge, "Generalized transformations for polyphase phase-Modulation motors," *IEEE Transactions on Energy Conversion*, vol. 21, no. 2, pp. 332–341, Jun. 2006.

Appendix A

Induction Machine Torque-Speed Characteristics

The three phase IM fed with fixed voltage and frequency can be studied by using a per phase equivalent circuit as shown in Fig. A.1. The circuit consists of stator winding resistance (R_s), stator leakage inductance (L_s), rotor winding resistance - referred to the stator ($R_r^{'}$), rotor leakage inductance - referred to the stator ($L_r^{'}$), magnetising inductance (L_m), and core loss resistance (R_m).

V_1 is the phase voltage, and s is the slip of the machine, given as below:

$$s = \frac{\omega_s - \omega_{re}}{\omega_s} = \frac{\omega - \omega_r}{\omega} \tag{A.1}$$

where ω_s is the supply electrical frequency (in rad/s), ω_{re} is rotor speed in electrical refer-

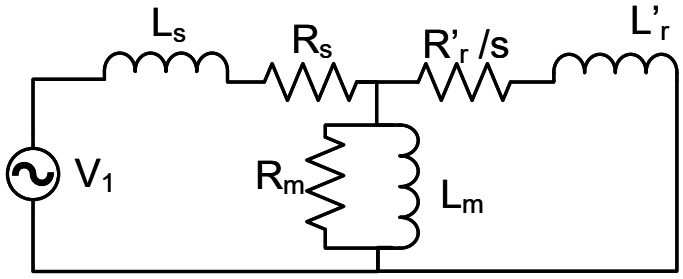

Figure A.1: IM per phase equivalent circuit

ence, and ω is the synchronous frequency. ω_s, ω_{re} and ω is given as below:

$$\omega_s = 2\pi f \tag{A.2}$$

$$\omega_{re} = \omega_r * p \tag{A.3}$$

$$\omega = \frac{2\pi f}{p} \tag{A.4}$$

where f is the supply frequency (in Hz), ω_r is the rotor speed (in rad/s), and p is the number of pole pair of the machine. The resistance $\frac{R_r^{'}}{s}$, represents both rotor winding loss and electromagnetic energy transferred. Hence this can be expressed as $\frac{R_r^{'}}{s} = R_r^{'} + \frac{1-s}{s}R_r^{'}$, where the first term $R_r^{'}$ represents rotor loss, and the second term $\frac{1-s}{s}R_r^{'}$ represents the electromagnetic energy transfer. The electromagnetic power transferred to the rotor is given as power consumed by the resistor $\frac{1-s}{s}R_r^{'}$. Hence the torque of the machine (T_{em}) is given as:

$$T_{em} = \frac{(I_2^{'})^2 \frac{1-s}{s} R_r^{'}}{\omega_r} \tag{A.5}$$

where $I_2^{'}$ is the current through the rotor, referred to stator. Using Eqn. A.1,A.2, A.3 and A.5, T_{em} can be expressed as:

$$T_{em} = \frac{p(I_2^{'})^2 R_r^{'}}{s\omega_s} \tag{A.6}$$

If the magnetising branch (L_m) and core loss component (R_m) is neglected, $I_2^{'}$ can be given as:

$$I_2^{'} = \frac{V_1}{\sqrt{(R_s + \frac{R_r^{'}}{s})^2 + (\omega_s(L_s + L_r^{'}))^2}} \tag{A.7}$$

Substituting $X_s = \omega_s L_s$, and $X_r^{'} = \omega_s L_r^{'}$, Eqn. A.7 can be rewritten as:

$$I_2^{'} = \frac{V_1}{\sqrt{(R_s + \frac{R_r^{'}}{s})^2 + (X_S + X_r^{'})^2}} \tag{A.8}$$

Substituting Eqn.A.8 in Eqn.A.6 T_{em} can be expressed as:

$$T_{em} = \frac{V_1^2}{(R_s + \frac{R_r^{'}}{s})^2 + (X_S + X_r^{'})^2} * \frac{pR_r^{'}}{s\omega_s} \tag{A.9}$$

Table A.1: Example IM [6]

	Symbol	Value	Unit
Number of phases		3	
Pole pair	p	3	
RMS terminal voltage (L-L)	V_{ll}	230	V
Frequency	f	60	Hz
Stator resistance	R_s	0.06	Ω
Stator leakage reactance	X_s	0.34	Ω
Rotor resistance	$R_r^{'}$	0.055	Ω
Rotor leakage reactance	$X_r^{'}$	0.33	Ω
Magnetising reactance	X_m	10.6	Ω

It is evident from Eqn. A.9, the torque produced in IM is proportional to square of line voltage, simple voltage control using variac does not allow smooth control over torque-speed characteristics of the machine. As an example case, IM parameters have been taken from [6], detailed in Table A.1. The torque-speed characteristics of this machine is shown in Fig. A.2.

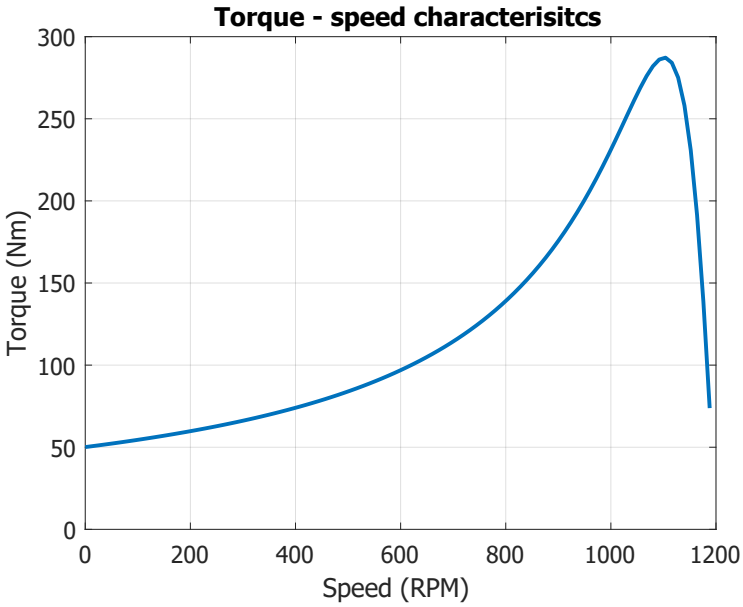

Figure A.2: IM torque-speed characteristics

Appendix B

Circuit Parameters from FEA

From Eqn. 3.77, the stator voltage, applied at one phase (one inverter leg) is related to the current of the same phase as below:

$$V_s = I_s(R_s + j\omega L_s + \frac{j\omega L_m(R_r^{'} + j\omega L_r^{'})}{R_r^{'} + j\omega(L_m + L_r^{'})}) \tag{B.1}$$

As mentioned earlier the current is set to be $1\angle 0$, for the first phase, and the next ones are phase shifted, as per Eqn. 3.4. Hence the phase impedance Z_S is same as the induced voltage, given as

$$Z_s = R_s + j\omega L_s + \frac{j\omega L_m(R_r^{'} + j\omega L_r^{'})}{R_r^{'} + j\omega(L_m + L_r^{'})} \tag{B.2}$$

This can be simplified by substituting $l_r = L_m + L_r^{'}$, $R_s = r_1$, $R_r^{'} = r_2$, $L_s = l_1$, $L_r^{'} = l_2$, $L_m = l_m$ as below

$$\begin{aligned}
Z_s &= r_1 + j\omega l_1 + \frac{j\omega l_m r_2 - \omega^2 l_m l_2}{r_2 + j\omega l_r} \\
&= r_1 + j\omega l_1 + \frac{(j\omega l_m r_2 - \omega^2 l_m l_2)(r_2 - j\omega l_r)}{r_2^2 + \omega^2 l_r^2} \\
&= r_1 + j\omega l_1 + \frac{j\omega l_m r_2^2 + \omega^2 l_m l_r r_2 - \omega^2 l_m l_2 r_2 + j\omega^3 l_m l_r l_2}{r_2^2 + \omega^2 l_r^2} \\
&= r_1 + j\omega l_1 + \frac{j\omega l_m r_2^2 + \omega^2 l_m^2 r_2 + j\omega^3 l_m l_r l_2}{r_2^2 + \omega^2 l_r^2} \\
&= r_1 + \frac{\omega^2 l_m^2 r_2}{r_2^2 + \omega^2 l_r^2} + j\omega\left\{l_1 + \frac{l_m r_2^2 + \omega^2 l_m l_r l_2}{r_2^2 + \omega^2 l_r^2}\right\} \\
&= r_1 + \frac{\omega^2 l_m^2 r_2}{r_2^2 + \omega^2 l_r^2} + j\omega\left\{l_1 + l_m\frac{r_2^2 + \omega^2 l_r(l_r - l_m)}{r_2^2 + \omega^2 l_r^2}\right\} \\
&= r_1 + \frac{\omega^2 l_m^2 r_2}{r_2^2 + \omega^2 l_r^2} + j\omega\left\{l_1 + l_m - \frac{\omega^2 l_r l_m^2}{r_2^2 + \omega^2 l_r^2}\right\} \\
&= r_1 + kr_2 + j\omega\{l_1 + l_m - kl_r\}
\end{aligned} \tag{B.3}$$

where k is given as

$$k = \frac{\omega^2 l_m^2}{r_2^2 + \omega^2 l_r^2} \tag{B.4}$$

Equating real and imaginary quantities separately the following can be obtained

$$r_1 + k r_2 = \Re(Z) \tag{B.5}$$

and

$$l_1 + l_m - k l_r = \frac{\Im(Z)}{\omega} \tag{B.6}$$

Where $\Re(Z)$ and $\Im(Z)$ represents real and imaginary part of the impedance Z. Z_1 and Z_2 are obtained for two frequencies ω_1 and ω_2, and the following is defined

$$a_i = \Re(Z_i) - r_1 \tag{B.7}$$

and

$$b_i = \frac{\Im(Z_i)}{\omega_i} \tag{B.8}$$

r_1 can be obtained from Eqn. 3.76. Combining with the Eqn. B.5 and B.6 following can be written

$$\begin{cases} k_1 r_2 & = & a_1 \\ k_2 r_2 & = & a_2 \\ l_1 + l_m - k_1 l_r & = & b_1 \\ l_1 + l_m - k_2 l_r & = & b_2 \end{cases} \tag{B.9}$$

where k_i is defined as

$$k_i = \frac{\omega_i^2 l_m^2}{r_2^2 + \omega_i^2 l_r^2} \tag{B.10}$$

From Eqn. B.9

$$\begin{array}{rcl} k_1 - k_2 & = & \frac{a_1 - a_2}{r_2} \\ k_2 - k_1 & = & \frac{b_1 - b_2}{l_r} \end{array} \tag{B.11}$$

Combining these two

$$\frac{l_r}{r_2} = \frac{b_1 - b_2}{a_2 - a_1} = \tau_1 (say) \tag{B.12}$$

Also

$$\begin{aligned} l_1 + l_m &= b_1 + k_1 l_r \\ &= b_1 + a_1 \tau_1 \\ &= b_1 + a_1 \frac{b_1 - b_2}{a_2 - a_1} \\ &= \frac{a_2 b_1 - a_1 b_2}{a_2 - a_1} \end{aligned} \tag{B.13}$$

Further, Lets assume $\frac{l_r}{r_2} = \tau_1$. Hence

$$\begin{aligned} a &= \frac{\omega^2 l_m^2}{r_2^2 + \omega^2 l_r^2} r_2 \\ &= r_2 (\frac{l_m}{r_2})^2 \frac{\omega^2}{1 + \omega^2 (\frac{l_r}{r_2})^2} \\ &= r_2 \tau_2^2 \frac{\omega^2}{1 + \omega^2 \tau_1^2} \\ \Rightarrow \tau_1^2 &= \frac{r_2 \tau_2^2 \omega^2 - a}{\omega^2 a} \end{aligned} \tag{B.14}$$

where $\tau_2 = \frac{l_m}{r_2}$. Combining two equations for two frequencies $a_1$for ω_1 and a_2 for ω_2

$$\frac{r_2 \tau_2^2 \omega_1^2 - a_1}{\omega_1^2 a_1} = \tau_1^2 = \frac{r_2 \tau_2^2 \omega_2^2 - a_2}{\omega_2^2 a_2} \tag{B.15}$$

Eqn B.15 can be solved as

$$\begin{aligned} r_2 \tau_2^2 (a_2 - a_1) \omega_1^2 \omega_2^2 &= a_1 a_2 (\omega_2^2 - \omega_1^2) \\ \Rightarrow r_2 \tau_2^2 &= \frac{a_1 a_2 (\omega_2^2 - \omega_1^2)}{(a_2 - a_1) \omega_1^2 \omega_2^2} \\ \Rightarrow \frac{l_m^2}{r_2} &= \frac{a_1 a_2 (\omega_1^2 - \omega_2^2)}{(a_1 - a_2) \omega_1^2 \omega_2^2} \\ &= \alpha \ (say) \end{aligned} \tag{B.16}$$

Also from Eqn. B.14

$$r_2 \tau_2^2 = \frac{a(1 + \omega^2 \tau_1^2)}{\omega^2} \tag{B.17}$$

Similarly combinng two equations for two frequencies $a_1$for ω_1 and a_2 for ω_2

$$\frac{a_1 (1 + \omega_1^2 \tau_1^2)}{\omega_1^2} = r_2 \tau_2^2 = \frac{a_2 (1 + \omega_2^2 \tau_1^2)}{\omega_2^2} \tag{B.18}$$

This can be solved as

$$\begin{array}{rcl} a_1(1+\omega_1^2\tau_1^2)\omega_2^2 & = & a_2(1+\omega_2^2\tau_1^2)\omega_1^2 \\ \Rightarrow \tau_1^2 & = & \frac{a_2\omega_1^2-a_1\omega_2^2}{(a_1-a_2)\omega_1^2\omega_2^2} \\ & = & \beta^2 \ (say) \end{array} \tag{B.19}$$

As τ_1 has been expressed in both Eqn. B.12 and B.19 in terms of the known quantities, hence the equations in B.9 can not be solved for all 4 unknowns. However, it is reasonable to assume for a practical induction machine, primary and secondary leakage inductance to be almost similar. Hence under the assumption $l_1 \approx l_2$, $l_r = l_1 + l_m$. Hence putting the values from Eqn. B.12 and B.13

$$\begin{array}{rcl} l_r & = & \frac{a_2b_1-a_1b_2}{a_2-a_1} \\ \Rightarrow \frac{l_r}{r_2}r_2 & = & \frac{a_2b_1-a_1b_2}{a_2-a_1} \\ \Rightarrow \tau_1 r_2 & = & \frac{a_2b_1-a_1b_2}{a_2-a_1} \\ \Rightarrow \frac{b_1-b_2}{a_2-a_1}r_2 & = & \frac{a_2b_1-a_1b_2}{a_2-a_1} \\ \Rightarrow r_2 & = & \frac{a_2b_1-a_1b_2}{b_1-b_2} \end{array} \tag{B.20}$$

From Eqn. B.20 and B.16 l_m can be given as

$$l_m = \sqrt{\frac{a_1a_2(\omega_1^2-\omega_2^2)}{(a_1-a_2)\omega_1^2\omega_2^2} * \frac{a_2b_1-a_1b_2}{b_1-b_2}} \tag{B.21}$$

Further, from Eqn. B.21 and B.13 $l_1$can be given as

$$l_1 = \frac{a_2b_1-a_1b_2}{a_2-a_1} - \sqrt{\frac{a_1a_2(\omega_1^2-\omega_2^2)}{(a_1-a_2)\omega_1^2\omega_2^2} * \frac{a_2b_1-a_1b_2}{b_1-b_2}} \tag{B.22}$$

These derivations are obtained under the assumption of $l_1 \approx l_2$. Table B.1 summarises the final expressions for the circuit parameters from FEA. R_s has been already obtained previously from the loss in the stator circuit, and explained previously in 3.3.2.

Quantity	Expression
$R_r^{'}$	$\frac{a_2b_1-a_1b_2}{b_1-b_2}$
L_m	$\sqrt{\frac{a_1a_2(\omega_1^2-\omega_2^2)}{(a_1-a_2)\omega_1^2\omega_2^2} * \frac{a_2b_1-a_1b_2}{b_1-b_2}}$
L_s	$\frac{a_2b_1-a_1b_2}{a_2-a_1} - \sqrt{\frac{a_1a_2(\omega_1^2-\omega_2^2)}{(a_1-a_2)\omega_1^2\omega_2^2} * \frac{a_2b_1-a_1b_2}{b_1-b_2}}$
$L_r^{'}$	

Table B.1: Expression for circuit parameters from FEA

Appendix C

PCB Designs

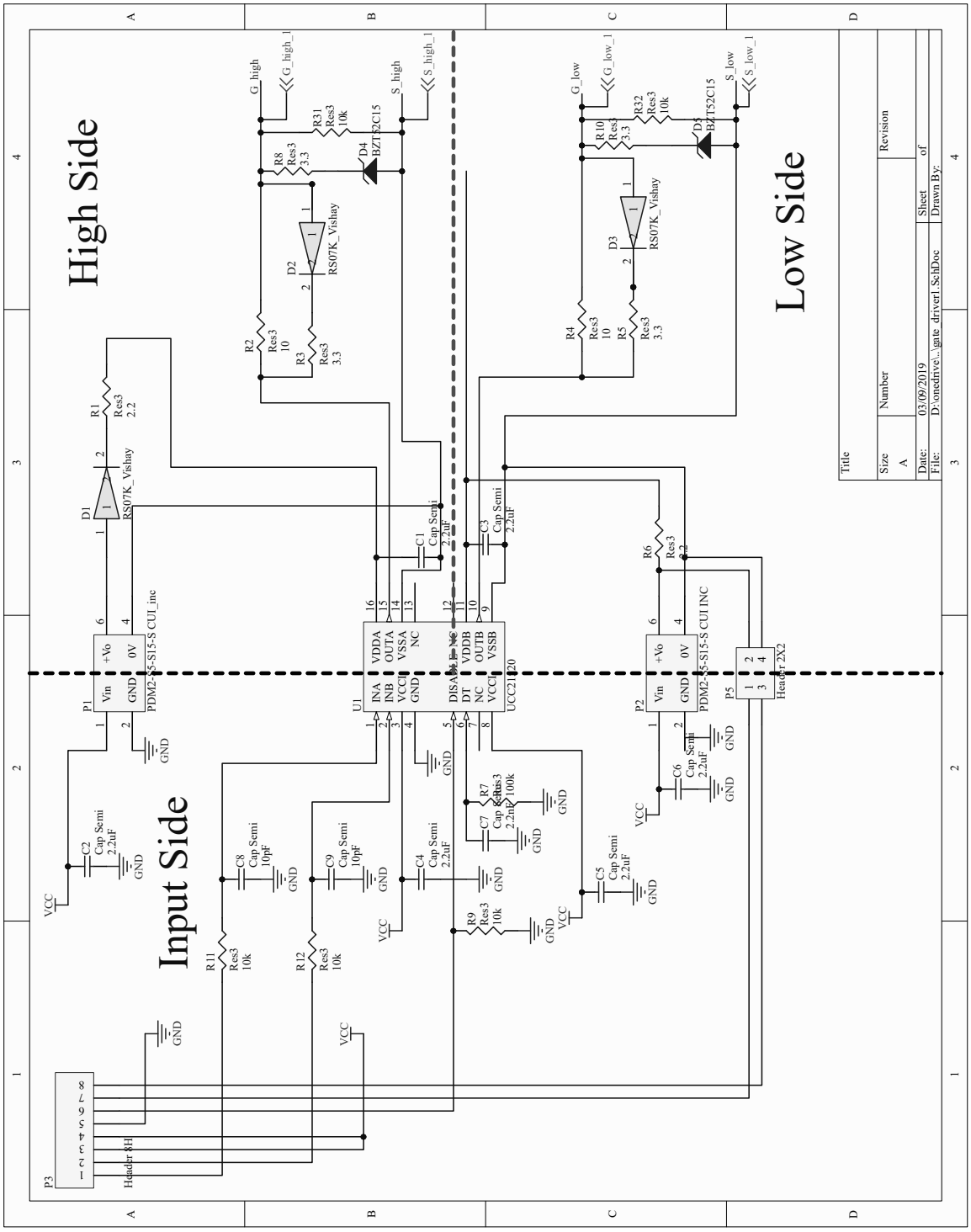

Figure C.1: Circuit schematic of gate driver (each leg - high side and low side device)

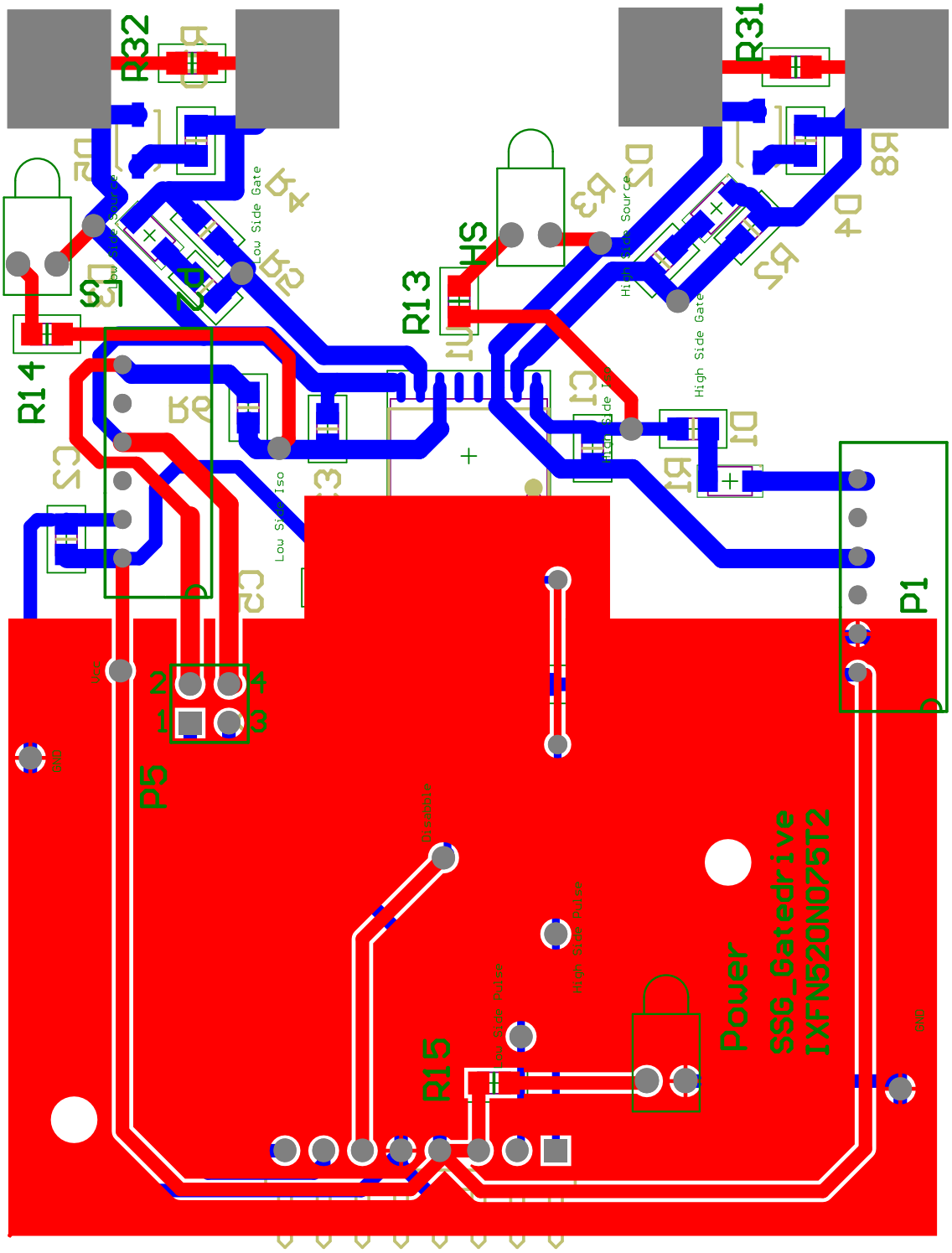

Figure C.2: PCB layout of gate driver

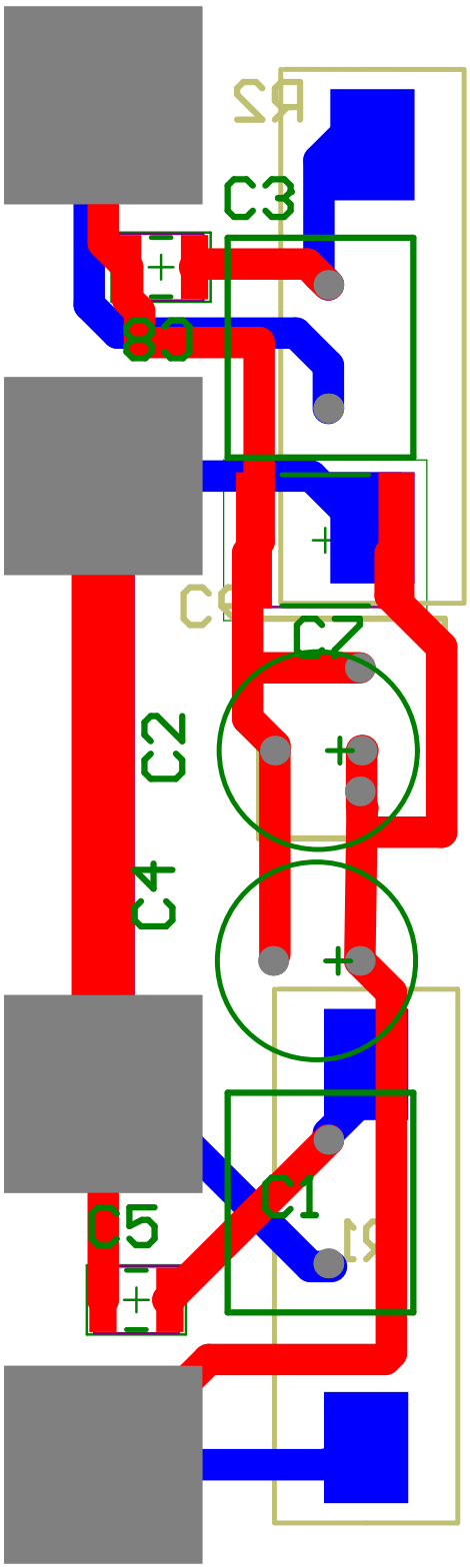

Figure C.3: PCB layout of the snubber circuit

Appendix D

Machine dimensions

The dimensions of the fabricated machine is given below. The same machine dimensions are used for FEA and analytical model for equivalent circuit parameters.

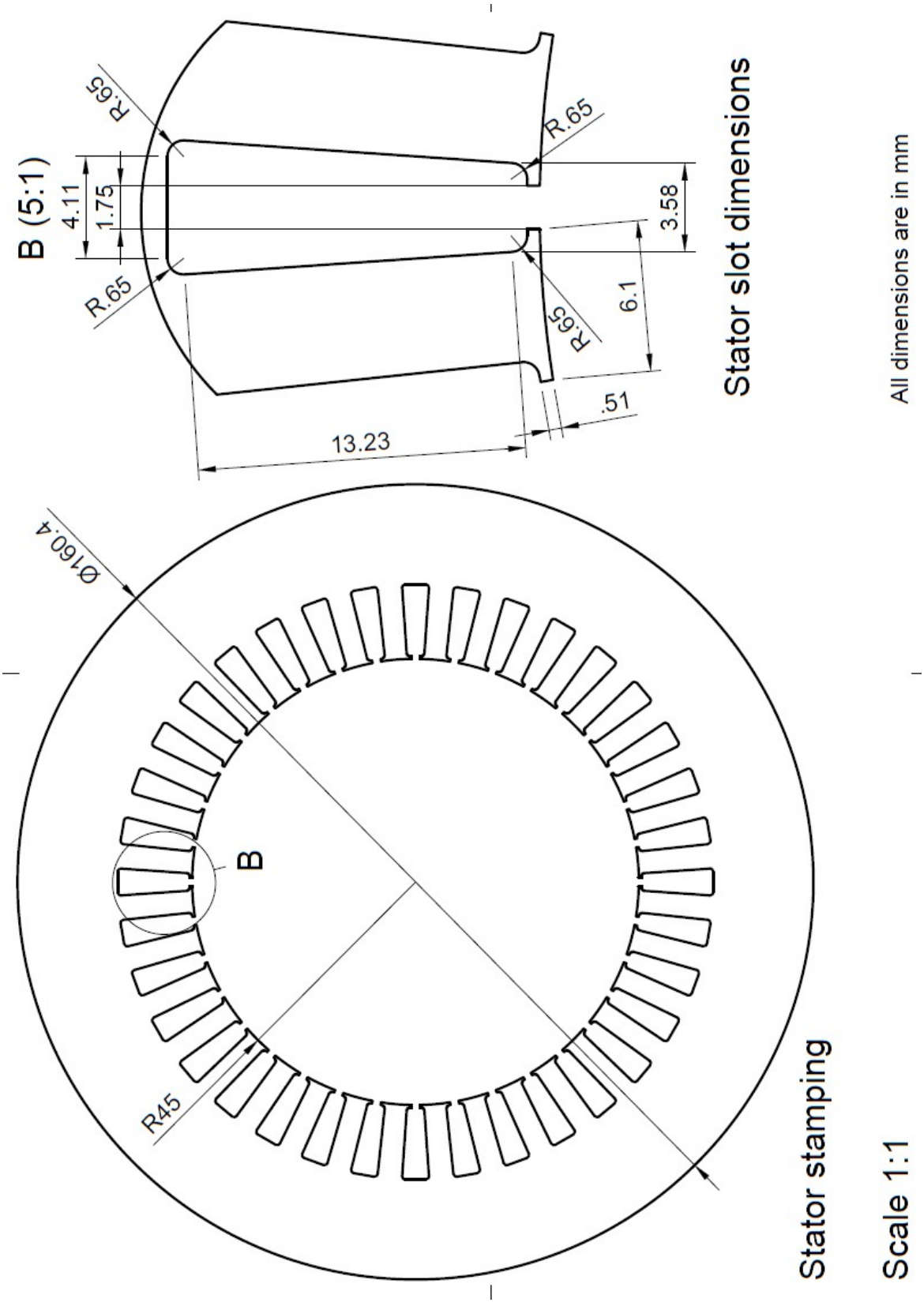

Figure D.1: Stator stamping dimensions

Figure D.2: Rotor stamping dimensions

Appendix E

Off the shelf machine details

The details of the commercially available IM used in the circulating power test bench are provided below.

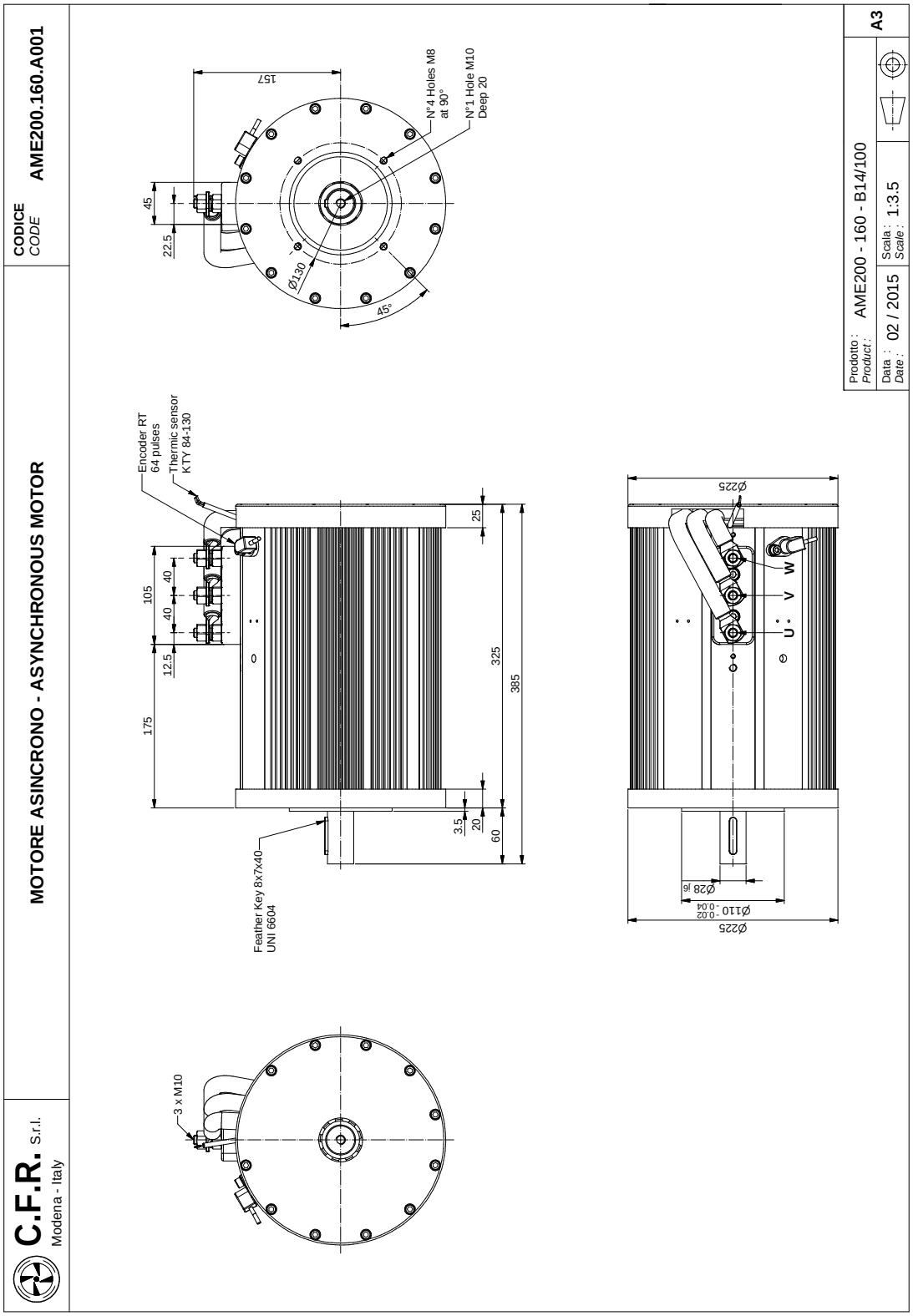

Figure E.1: Dimensions of the off the shelf IM used in the test bench.

C.F.R. s.r.l.
MODENA - Italy

PROVA MOTORE ASINCRONO
AC MOTOR DATA SHEET

N. File	A01169
Codice Motore	
Data	22/11/2016

PROVA A CARICO / TEST DATA

Tensione batt. *Battery voltage*	**Corrente batt.** *Battery current*	**Velocità** *Speed*	**Coppia** *Torque*	**Potenza resa** *Output power*	**Tensione fase** *Motor voltage*	**Corrente fase** *Motor current*	**Frequenza** *Frequency*	**Scorrimento** *Slip*	**Rend. totale** *Total eff.*	**Rend. motore** *Motor eff.*	**Rend. inv** *Inv. eff.*	**S2** *S2*	**S3** *S3*
V	A	rpm	Nm	kW	V	A	Hz	%	%	%	%	min	%
48,0	51,6	4009	4,86	2,05	33,7	64,2	134,2	0,5	82,5	84,7	97,4		
48,0	101,0	3997	10,19	4,27	33,9	97,3	134,4	0,9	88,1	89,9	97,9		
48,0	148,5	4000	14,97	6,28	33,7	133,7	135,2	1,4	88,1	90,2	97,7		
48,0	168,8	3893	17,57	7,17	33,6	150,9	131,9	1,6	88,5	90,7	97,6		
48,0	51,8	3508	5,80	2,13	33,7	68,6	117,4	0,3	85,7	87,7	97,7		
48,0	101,9	3501	11,90	4,37	33,9	99,7	117,8	0,8	89,3	91,0	98,1		
48,0	157,5	3497	18,35	6,72	33,7	142,9	118,3	1,5	89,0	91,2	97,6		
48,0	192,1	3388	22,91	8,13	33,5	169,7	115,1	1,8	88,3	90,7	97,3		
48,0	59,3	2995	7,58	2,38	34,2	82,8	100,3	0,5	83,5	85,9	97,3		
48,0	103,8	3001	13,94	4,38	33,9	107,7	100,9	0,9	87,9	90,2	97,6		
48,0	157,4	3000	21,25	6,68	33,8	146,2	101,5	1,5	88,5	90,7	97,6		
47,8	219,6	2900	30,10	9,14	33,3	197,4	98,8	2,1	87,1	89,7	97,0		
48,0	155,1	2850	22,01	6,57	33,8	146,0	96,4	1,4	88,3	90,5	97,5		
48,0	67,3	2506	10,12	2,66	33,7	99,7	84,0	0,6	82,3	84,9	96,9		
47,9	126,5	2497	20,20	5,29	33,7	132,5	84,2	1,2	87,2	89,6	97,4		
47,9	188,3	2498	30,07	7,87	33,5	177,1	84,8	1,8	87,3	89,8	97,2		
47,9	258,8	2402	42,17	10,61	33,2	234,8	82,2	2,6	85,7	88,6	96,7		
48,0	89,4	2005	16,76	3,52	31,3	133,4	67,4	0,9	82,2	85,6	96,0		
47,9	176,5	2003	34,11	7,16	33,5	194,4	67,9	1,6	84,7	87,8	96,5		
47,9	264,3	2004	50,68	10,64	33,3	251,1	68,6	2,6	84,2	87,5	96,2		
47,8	318,8	1897	63,27	12,57	33,0	298,1	65,4	3,3	82,5	86,2	95,7		
48,0	95,3	1477	23,73	3,67	24,7	162,7	50,0	1,6	80,4	84,7	94,9		
47,9	183,7	1504	44,38	6,99	28,2	251,3	51,4	2,4	79,4	84,1	94,4		
47,8	278,8	1504	65,40	10,31	30,3	337,8	51,8	3,2	77,3	82,6	93,6		
47,8	365,6	1464	84,84	13,02	31,4	422,2	50,9	4,1	74,7	80,6	92,6		
48,0	66,5	1022	22,56	2,42	17,4	159,3	34,8	2,2	75,8	81,3	93,2		
48,0	138,6	1001	46,39	4,87	19,7	261,1	34,7	3,7	73,2	79,4	92,2		
47,9	215,4	1001	69,04	7,24	21,3	353,3	35,1	5,0	70,2	77,0	91,1		
47,8	300,1	1005	91,34	9,61	22,7	444,0	35,7	6,1	67,0	74,5	89,9		

Figure E.2: Test results (supplied by the manufacturer) of the off the shelf IM used in the test bench.